POLYPUBLIE
Polytechnique Montréal

Titre: Title:	Development of in-Vivo Histology with Quantitative Magnetic Resonance Imaging to Resolve Fine Neurodegenerative Features
Auteur: Author:	Gabriel Mangeat
Date:	2021
Type:	Mémoire ou thèse / Dissertation or Thesis
Référence: Citation:	Mangeat, G. (2021). Development of in-Vivo Histology with Quantitative Magnetic Resonance Imaging to Resolve Fine Neurodegenerative Features [Thèse de doctorat, Polytechnique Montréal]. PolyPublie. https://publications.polymtl.ca/6280/

Document en libre accès dans PolyPublie
Open Access document in PolyPublie

URL de PolyPublie: PolyPublie URL:	https://publications.polymtl.ca/6280/
Directeurs de recherche: Advisors:	Julien Cohen-Adad, & Tobias Granberg
Programme: Program:	Génie biomédical

POLYTECHNIQUE MONTRÉAL

affiliée à l'Université de Montréal

Development of in-vivo histology with quantitative magnetic resonance imaging to resolve fine neurodegenerative features

GABRIEL MANGEAT

Institut de génie biomédical

Thèse présentée en vue de l'obtention du diplôme de *Philosophiæ Doctor*

Génie biomédical

Avril 2021

POLYTECHNIQUE MONTRÉAL

affiliée à l'Université de Montréal

Cette thèse intitulée :

Development of in-vivo histology with quantitative magnetic resonance imaging to resolve fine neurodegenerative features

présentée par **Gabriel MANGEAT**

en vue de l'obtention du diplôme de *Philosophiæ Doctor*

a été dûment acceptée par le jury d'examen constitué de :

Nikola STIKOV, président

Julien COHEN-ADAD, membre et directeur de recherche

Tobias GRANBERG, membre et codirecteur de recherche

Delphine PERIE-CURNIER, membre

Christine TARDIF, membre externe

DEDICATION

To Frédérique, Frédéric, Aline, Thomas, Johanna et Blanche.

ACKNOWLEDGEMENTS

RÉSUMÉ

La sclérose en plaques (SEP) est une maladie dévastatrice qui touche 2 à 3 millions de personnes dans le monde. La SEP se caractérise par la formation d'inflammations ou de plaques, qui endommagent la gaine de myéline, un composant clé des cellules neuronales. Ces dommages perturbent la capacité des régions du cerveau et de la moelle épinière à communiquer entre elles, ce qui entraîne des déficits fonctionnels tels que la paralysie et la douleur chronique, affectant les activités sociales et professionnelles des patients atteints de SEP. Alors que l'imagerie par résonance magnétique (IRM) a été le principal outil de diagnostic et d'étude de la progression de la SEP, l'IRM actuellement utilisé en cliniques ne peut pas mesurer le contenu en myéline ou l'intégrité des neurones. Des méthodes avancées d'IRM quantitative (IRMq) nous permettent de caractériser plus précisément les tissus microstructuraux. Par exemple, *"l'IRM de diffusion"* permet d'étudier la perte ou les dommages subis par les axones, tandis que *"l'IRM de transfert de magnétisation"* (MT) permet d'étudier la perte de myéline. Toutefois, lorsque chacune de ces techniques est utilisée séparément, elles sont souvent entravées par une faible spécificité. L'IRMq montre toute sa puissance lorsque plusieurs de ces techniques sont combinées pour examiner et caractériser le même tissu.

Au cours de ma maîtrise, j'ai proposé une méthode permettant de combiner plusieurs méthodes d'IRM afin de gagner en spécificité dans l'estimation de la myéline et j'ai démontré le potentiel de cette approche chez les patients atteints de SEP.

Bien que ces travaux passés fussent prometteurs, ils avaient plusieurs limites : 1) Ils ne comprenaient que des mesures quantitatives dans la matière grise corticale dont les caractéristiques neurodégénératives sont différentes de celles de la matière blanche. 2) La méthode n'était pas applicable en clinique car elle nécessitait des scanners IRM de pointe (7 teslas), de longues acquisitions (~2 h) et un post-traitement complexe. 3) Enfin, l'étude a été entravée par l'absence d'un étalon : nous n'avons pu obtenir que des mesures relatives, et non absolues, de la teneur en myéline.

L'objectif de ce projet de doctorat était de s'attaquer à ces limites et, plus généralement, d'étudier le potentiel de l'IRMq pour caractériser les mécanismes neurodégénératifs du système nerveux central. Pour ce faire, j'ai mis au point des méthodes permettant de combiner et plusieurs séquences d'IRMq dans un contexte académique et dans un contexte clinique axés sur la SEP. Ensuite, j'ai

validé la précision des biomarqueurs quantitatifs dans des conditions cliniques réelles. Finalement, j'ai développé un protocole basé sur la microscopie optique pour valider la précision des biomarqueurs IRMq proposés. Plus précisément, la question générale de recherche de ce projet était *"Quel est le potentiel de l'IRM quantitative multimodale pour étudier les mécanismes neurodégénératifs subtils de la SEP, dans un contexte de recherche et clinique. Et quels sont les défis pour passer de l'IRM quantitative multimodale à l'histologie in-vivo ?"*

La première contribution de ce projet est le développement d'un cadre algorithmique permettant de combiner plusieurs techniques d'IRMq de pointe afin de détecter des caractéristiques pathologiques subtiles chez des patients récemment atteints de SEP. J'ai combiné les cartographies haute résolution (7 teslas) T1 et T2* afin d'estimer un marqueur de myélinisation corticale (CME). En plus de ces mesures de relaxométrie dans le cortex, j'ai traité, sur la même cohorte de sujets, les données d'IRM de diffusion à haute résolution angulaire d'un scanner Connectome (300 mT/m) et modélisé la tractographie de la matière blanche afin de calculer des métriques de connectivité neuronale issues de la théorie des graphs. Cette étude a permis de découvrir une nouvelle association entre la pathologie corticale et la réorganisation du réseau cérébral à un stade précoce de la SEP. Plus précisément, des co-variations significatives entre l'estimation de la myéline et les mesures de connectivité dans matière blanche ont été observées : Les coefficients de corrélation Rho de Spearman étaient de 0,52 (p=0,0003), 0,55 (p=0,0001) et 0,53 (p=0,0001) pour *l'intensité de connexion*, *l'efficacité locale* et le *regroupement neuronal*, respectivement. Ce travail a été publié dans la revue Human Brain Mapping (Gabriel Mangeat et al., 2018) et j'ai ensuite été invité à la conférence ARSEP 2019 à Paris (Fondation pour l'aide à la recherche sur la sclérose en plaques) pour présenter ces résultats.

La deuxième contribution de ce projet est le développement d'une approche d'apprentissage machine capable de distinguer deux maladies neurodégénératives radiologiquement similaires : la SEP et la leucoencéphalopathie héréditaire. La leucoencéphalopathie héréditaire est une maladie rare par rapport à la SEP et est souvent diagnostiquée à tort comme une SEP. Cette situation est très problématique car le pronostic et le traitement de la SEP et de la HDLS diffèrent largement. Mon modèle est basé sur une nouvelle technique d'IRMq, appelée IRM synthétique (SyMRI) qui a récemment été certifiée (marquage CE) pour un usage clinique en Suède. J'ai démontré que combinaison des outils cliniques d'IRMq et de l'apprentissage machine est pertinente pour faciliter

le difficile diagnostic différentiel de la HDLS par rapport à la SEP. Le modèle développé atteint une classification 100% correcte des données brutes, en validation croisée. Lorsque le bruit d'incertitude maximum a été inséré dans le modèle, le taux de vrais positifs de leucoencéphalopathie héréditaire était de 97,2%, tandis que le taux de vrais positif de SEP était de 99,6%. Ce travail a été publié dans le Journal of Neuroimaging (Gabriel Mangeat et al., 2020).

La troisième contribution de ce projet est l'évaluation de la répétabilité et la reproductibilité des biomarqueurs utilisés dans l'étude précédente. Au cours d'un stage de recherche à Stockholm, en Suède, j'ai recruté 5 sujets témoins sains et effectué plus de 165 acquisitions avec le protocole SyMRI, en utilisant 9 IRM différentes provenant de 3 fournisseurs (Siemens, GE et Phillips) et 2 puissances de champ (1,5 teslas et 3 teslas). Les cartes quantitatives de densité de protons (PD), T1, T2 et d'estimation rapide de myéline (REMyDI) ont été extraites et moyennées dans la matière grise et blanche du cerveau. Nous avons constaté que le coefficient de variation intra-scanner variait de 0,10 % pour PD à 1,97 % pour T1 dans la matière blanche et de 0,10 % pour PD à 3,38 % pour la REMyDI dans la matière grise. Les coefficients de variation inter-scanner étaient plus grands, allant de 1,60% et 1,08% pour PD dans la matière blanche et grise respectivement à 4,84% et 20,2% pour REMyDI dans matière blanche et grise respectivement. Ce travail permet aux cliniciens d'évaluer la possibilité de comparer les images et les biomarqueurs provenant de différents scanners. Par exemple, il montre que les algorithmes aidant au diagnostic différentiel de la leucoencéphalopathie héréditaire par rapport à la SEP peuvent être, sous certaines mesures, utilisés à partir de données multicentriques. Ce travail a été soumis dans la revue Neuroimage.

Enfin, la quatrième contribution de ce projet est le développement d'un protocole basé sur l'histologie pour calibrer des techniques d'IRMq avec un biais minimum. Pour cela, j'ai étudié trois techniques d'histologie notables, dont deux techniques sans marqueurs : la microscopie CARS (*Raman Scattering Coherent Anti-Stokes*) et l'auto-fluorescence hyperspectrale, et une technique utilisant des marqueurs fluorescents. En outre, j'ai proposé et testé un protocole impliquant l'imagerie IRMq *in-vivo* et *ex-vivo* de la moelle épinière d'un cochon, suivie d'une extraction de tissus et d'une étude histologique. Une partie de cette étude a été publiée dans la conférence internationale ISMRM 2019 (G. Mangeat et al., 2019). Les résultats montrent que l'histologie d'auto-fluorescence hyperspectrale corrèle avec MTR, MTsat et qT1 (r = 0,64, 0,62 et 0,51 respectivement). Mon expérience avec des protocoles d'histologie m'a amené à collaborer avec des

collègues travaillant sur d'autres études de validation d'IRMq via l'histologie. Par exemple, j'ai contribué à une étude visant à valider l'estimation rapide de la myéline REMyDI, dérivée du protocole SyMRI. Cette étude a été publiée dans la revue Annals of Neurology (Ouellette et al., 2020).

L'impact de ce projet de Ph.D. est triple : pour les chercheurs en SEP, l'étude de l'interaction entre les mesures de la matière grise et blanche peut conduire à l'élaboration de biomarqueurs sensibles aux altérations précoces de la SEP dans le cerveau ; pour les médecins, les outils informatiques cliniques basés sur l'IRMq peuvent être utiles pour faciliter les diagnostics différentiels difficiles (par exemple leucoencéphalopathie héréditaire *vs* SEP), ce qui permet d'économiser du temps et des ressources, et pour les patients, un diagnostic plus précis et plus précoce pourrait être réalisé, ce qui ouvrirait la porte à des traitements plus personnalisés et plus efficaces.

ABSTRACT

Multiple Sclerosis (MS) is a devastating disease affecting 2-3 millions people in the world. MS is characterized by the formation of inflammations or plaques, damaging the myelin sheath, a key component of neuronal cells. This damage disrupts the ability of regions in the brain and spinal cord to communicate with each other, resulting in functional deficits such as paralysis and chronic pain, affecting the social and professional activities of MS patients. While Magnetic Resonance Imaging (MRI) has been the main tool for diagnosing and studying MS progression, MRI currently used in clinics cannot provide reliable measures of myelin content or neuronal health. Advanced quantitative MRI (qMRI) methods enable us to go deeper into the characterization of tissue microstructure. For example, *"diffusion MRI"* can probe axonal loss while *"magnetization transfer"* (MT) can probe myelin loss. However, this is not enough: when each of these techniques is used separately, they only provide minimum added information and are hampered by poor specificity. qMRI exhibits its full power when several of these techniques are combined to look at the same tissue.

During my master's, I proposed a method to combine several MRI methods to gain specificity in myelin estimation and demonstrated the potential of this approach in MS patients. While this past work showed promises, it had several limitations: 1) It only included quantitative measurements in the cortical grey matter (GM) in which the neurodegenerative features are different than in the white matter (WM). 2) The method was not applicable in clinics since it required state-of-the-art MRI scanners (7 tesla), long scanning procedures (~2 h) and complex post processing. 3) Finally, the study was hampered by the absence of a gold standard: we could only get relative, not absolute, measures of myelin content.

The objective of this PhD project was to tackle those limitations and more generally to investigate the potential of qMRI to characterize neurodegenerative mechanisms in the central nervous system. This was achieved by 1) developing methods to combine and analyze multimodal quantitative MRI in research and 2) clinical setups focused on MS, 3) validating the precision of the quantitative biomarkers in clinical conditions and 4) developing a microscopy-based protocol to validate the accuracy of the proposed qMRI biomarkers. More specifically, the general research question of the project was *"What is the potential of multimodal quantitative MRI to decipher subtle*

neurodegenerative mechanisms of MS, in a research and clinical setups. And what does it take to bring multimodal quantitative MRI to in-vivo histology?".

For the first contribution, I developed a framework that combines several qMRI techniques to detect subtle pathological features in early MS patients. I combined high resolution 7 tesla T1 and T2* mapping in order to extract a marker of cortical myelination (CME). In addition to these relaxometry measures in the cortex, I processed, on the same cohort of subjects, the high angular resolution diffusion MRI data of a Connectome scanner (300 mT/m), computed the white matter tractography and extracted several brain connectivity metrics from the graph theory. This study enabled us to discover a new association between cortical pathology and brain network reorganization at an early stage of MS. More specifically, significant co-variations between myelin estimation and white matter connectivity metrics were observed: Spearman's Rho correlation coefficients were 0.52 (p=0.0003), 0.55 (p=0.0001), and 0.53 (p=0.0001) for strength, local efficiency, and clustering, respectively. This work was published in the journal Human Brain Mapping (Gabriel Mangeat et al., 2018) and I was later invited to the ARSEP 2019 conference in Paris (equivalent of French MS society) to present these findings.

For the second contribution, I developed a machine learning approach capable of distinguishing two radiologically similar neurodegenerative conditions: MS and HDLS (Hereditary Diffuse Leukodystrophy with Spheroids). HDLS is a rare disorder compared to MS, which is often misdiagnosed as MS. This is highly problematic since the prognosis and treatment of MS and HDLS largely differ. My model was based on a new qMRI technique, called Synthetic MRI, which had recently been approved (CE-marked) for clinical use in Sweden. Combining clinical qMRI tools and machine learning prove to be relevant in aiding the challenging differential diagnosis of HDLS versus MS. The model gave a 100% correct classification of the raw cross-validation data. When the maximum uncertainty noise was inserted in the model, the true positive rate of HDLS was 97.2%, while the true positive rate of MS was 99.6%. This work was published in the Journal of Neuroimaging (Gabriel Mangeat et al., 2020).

The third contribution was to assess the repeatability and reproducibility of the synthetic MRI biomarkers used in the HDLS vs. MS study. During a research internship in Stockholm, Sweden, I recruited 5 healthy controls and performed about 165 acquisitions with the Synthetic MRI protocol, using 9 different MRI from 3 vendors (Siemens, GE and Phillips) and 2 field strengths

(1.5 tesla and 3 tesla). The quantitative proton density (PD), T1, T2 and Rapid Estimation of Myelin (REMyDI) maps were extracted and averaged across the WM and GM. Results showed that intra-scanner coefficient of variation ranged from 0.10% for PD to 1.97% for T1 in the WM and 0.10% for PD to 3.38% for REMyDI in the GM. The inter-scanner coefficients of variations were larger, from 1.60% and 1.08% for PD in the WM and GM respectively to 4.84% and 20.2% for REMyDI in the WM and GM respectively. This work enables clinicians to assess the possibility to compare quantitative images and biomarkers acquired from different scanners. For example, it shows that the algorithms aiding the differential diagnosis of HDLS versus MS can be applied to multicentric data under certain conditions. This work has been submitted in the journal Neuroimage.

The fourth and last contribution focused on the development of a histology-based protocol to calibrate qMRI techniques with minimum bias. For this, I have investigated three histology techniques of interest: two stain-free techniques: Coherent Anti-Stokes Raman Scattering (CARS) microscopy and hyperspectral auto-fluorescence, and one technique using fluorescent markers. In addition, I have proposed and tested a protocol involving *in-vivo* and *ex-vivo* qMRI imaging of a pig spinal cord, followed by tissues extraction and histology. A part of this study was published in the international conference ISMRM 2019 (G. Mangeat et al., 2019). I reported that hyperspectral auto-fluorescence histology correlates with MTR, MTsat and qT1 with r = 0.64, 0.62 and 0.51 respectively. My experience with histology protocols led me to collaborate with colleagues working on other histology validation studies. For example, I have contributed to a study aiming to validate the myelin estimation REMyDI, derived from SyMRI. This study was published in the journal Annals of Neurology (Ouellette et al., 2020).

The impact of this project is threefold: for researchers, investigating the interplay between WM and GM metrics can lead to sensitive and early biomarkers of MS alterations in the brain; for doctors, clinical qMRI based tools may be helpful in aiding challenging differential diagnoses, (e.g. HDLS *vs* MS) saving time and resources, and for patients, a more accurate and earlier diagnosis could be achieved, resulting in more personalized and effective treatments.

TABLE OF CONTENTS

LIST OF TABLES

LIST OF FIGURES

LIST OF SYMBOLS AND ABBREVIATIONS

BA   Brodmann area

BASC Bootstrap analysis of stable clusters

BBB   Blood-brain barrier

CARS Coherent anti-Stokes Raman scattering

CME Combined myelin estimation

CNS   Central nervous system

CoV   Coefficient of variance

CSF   Cerebrospinal fluid

DIR   Double inversion recovery

DOF   Degrees of freedom

DTI   Diffusion tensor imaging

DWI   Diffusion-weighted images

EDSS Expanded disability status scale

FLAIR Fluid attenuated inversion recovery

FSL   FMRI software library

GM   Grey matter

HDLS Hereditary Diffuse Leukodystrophy with Spheroids

LDA   Linear discriminant analysis

LFB   Luxol fast blue

MPRAGE   Magnetization-prepared rapid acquisition gradient echo

MRI   Magnetic resonance imaging

MS   Multiple sclerosis

MT   Magnetization transfer

MTR   Magnetization transfer ratio

MWF   Myelin water fraction

NAWM   Normal-appearing white matter

NAGM   Normal-appearing grey matter

NODDI   Neurite orientation dispersion and density imaging

OD   Optical density

PD   Proton density

PET   Positron emission tomography

PPMS   Primary progressive multiple sclerosis

qMRI   quantitative magnetic resonance imaging

REMyDI   Rapid estimation of myelin for diagnostic imaging

RRMS   Relapsing–remitting multiple sclerosis

SD   Standard deviation

SPMS   Secondary progressive multiple sclerosis

T   Tesla

WM   White matter

LIST OF APPENDICES

CHAPTER 1   INTRODUCTION

Multiple Sclerosis (MS) is a devastating disease affecting more than 100,000 people in Canada (*MS Society of Canada*) and 2-3 millions people in the world (Thompson, Baranzini, et al., 2018). MS is characterized by the formation of inflammations or plaques, damaging the myelin sheath, a key component of neuronal cells. This damage disrupts the ability of regions in the brain and spinal cord to communicate with each other, resulting in functional deficits such as paralysis and chronic pain, affecting the social and professional activities of MS patients. The socio-economic cost of MS is colossal: firstly, life quality of MS patients and that of their family members can be drastically hampered. Secondly, existing treatments that reduce handicapping effects of MS are expensive, with an annual cost estimated in billions of dollars in Canada (Karampampa et al., 2012) and in the USA (Hartung et al., 2015).

While Magnetic Resonance Imaging (MRI) has been the main tool for diagnosing and studying MS progression, MRI currently used in clinics cannot provide reliable measures of myelin content or neuronal health (Polman et al., 2011; Thompson, Banwell, et al., 2018). Advanced quantitative MRI methods, including those that I have developed during my Master's (G. Mangeat, Govindarajan, et al., 2015), enable us to go deeper into the characterization of tissue microstructure. For example, "diffusion MRI" is based on the quantification of the water diffusion in tissues and can probe axonal loss (Schneider et al., 2017; H. Zhang et al., 2012) in WM and in the spinal cord. "Magnetization transfer" (MT) is based on the difference between the water and macromolecules absorption spectra and can probe myelin loss (Levesque & Pike, 2009; Schmierer et al., 2004) and macromolecules in the brain. Moreover, the MR longitudinal relaxation time (called T1) has been shown to be closely related to myelin volume in- and ex-vivo (Lutti et al., 2014; Schmierer et al., 2008; Sereno et al., 2013; Stüber et al., 2014) and the transverse relaxation (called T2*) at 7 tesla was shown to be a sensitive marker of pathology and disease progression of MS patients (Cohen-Adad et al., 2011, 2012; Mainero et al., 2015).

However, this is not enough: when each of these techniques is taken separately, they only provide minimum added information and are hampered by poor specificity. Quantitative MRI exhibits its full power when several of these techniques are combined to probe the same tissue: together, they can reveal the true underlying state of neuronal tissue health.

Histology is another leading piece of the puzzle that needs to be bridged with MRI. Imaging tissue with molecular selectivity typically requires the introduction of specific staining, such as Luxol Fast Blue, Hematoxylin and Eosin, or Proteolipid. It should be noted, however, that the inhomogeneous penetration of the staining agents can introduce biases (Vincze et al., 2008). Recent, label-free histology techniques have shown an interesting potential to quantify myelin with less bias than labeling techniques. For example, coherent anti-Stokes Raman scattering (CARS) microscopy technique demonstrated the feasibility to obtain outstanding contrast to myelin (Evans et al., 2005; Imitola et al., 2011). Given that the myelin signal is an endogenous contrast to CARS, the tissue does not need to be fixed or stained. In addition, hyperspectral auto-fluorescence microscopy demonstrated interesting performances in label-free histology. As different tissues emit different autofluorescence spectra, it is possible to unmix the contribution of each tissue when a multi-spectral microscopy image is recorded. This technique can separate the myelin, the axons and the background on multi-spectral, one photon confocal images (Christensen et al., 2014).

During my master's, I proposed a method to combine several MRI methods to gain precision in myelin estimation (G. Mangeat, Govindarajan, et al., 2015), and demonstrated the potential of this approach in MS patients (G. Mangeat et al., 2013; G. Mangeat, Louapre, et al., 2015).

While this past work showed promises, it had several limitations: 1) It only included quantitative measurements in the cortical GM, in which the neurodegenerative features are different than in the WM tissues. 2) The method was not applicable in clinics since it required state of the art MRI scanners (7 Tesla), long scanning procedures (~2h) and complex post processing. 3) Finally, the study was hampered by the absence of a gold standard: we could only get relative, not absolute, measures of myelin content.

The objective of my PhD was to tackle these limitations and more generally to investigate the potential of qMRI to monitor MS mechanisms. This was achieved by i) developing methods to combine and analyze multimodal quantitative MRI in research and ii) clinical setups focused on MS, iii) validating the precision of the quantitative biomarkers in actual clinical conditions and iv) evaluating and testing a protocol to improve the accuracy of histological measurements derived from qMRI. More specifically, the general research question of the project was *"What is the potential of multimodal quantitative MRI to decipher subtle neurodegenerative mechanisms of MS,*

in a research and clinical setups. And what does it take to bring multimodal quantitative MRI to in-vivo histology?".

Chapter 2 will present a critical review of the literature on the potential of qMRI to study MS. Chapter 3 will describe the methodology followed to answer the research questions, while Chapters 4, Chapter 4, Chapter 6 and Chapter 7 will present published results related to this project, including method combing state of the art qMRI techniques in research and clinical setups, validation of the precision of several biomarkers across different clinical setups and testing of protocols to calibrate qMRI with label-free histology.

Non-invasive and accurate quantification of demyelination is one of the missing pieces of the pathophysiology puzzle in MS. A potential impact of this work is a more accurate and earlier diagnosis of MS, resulting in more personalised treatment, thus potentially more effective.

CHAPTER 2   LITERATURE REVIEW

2.1   Anatomy of the brain

The Human brain is one of the most complex organs of the human body. It is the central organ of the nervous system, and along with the spinal cord makes up the central nervous system (CNS). The brain controls most activities of the body, processing, integrating and coordinating the information it receives from the sensorial organs. It is composed of more than 100 billion neurons that communicate in trillions of connections called synapses (Tang et al., 2001). The main components of the brain are 1) the cerebral cortex, part of the GM, the outermost layer of brain cells, where most of the neural connexions are made. 2) The cerebral WM, contains most of the axons, grouped in the form of tracts, that are wiring the areas mentioned above. 3) The brain stem is between the spinal cord and the rest of the brain. Basic functions like breathing and sleep are controlled here. 4) The basal ganglia, part of the GM, are a cluster of structures in the center of the brain. The basal ganglia coordinate messages between multiple other brain areas. 5) The cerebellum is at the base and the back of the brain. The cerebellum is responsible for coordination and balance. Figure 2.1 is showing different components of the brain imaged with MRI.
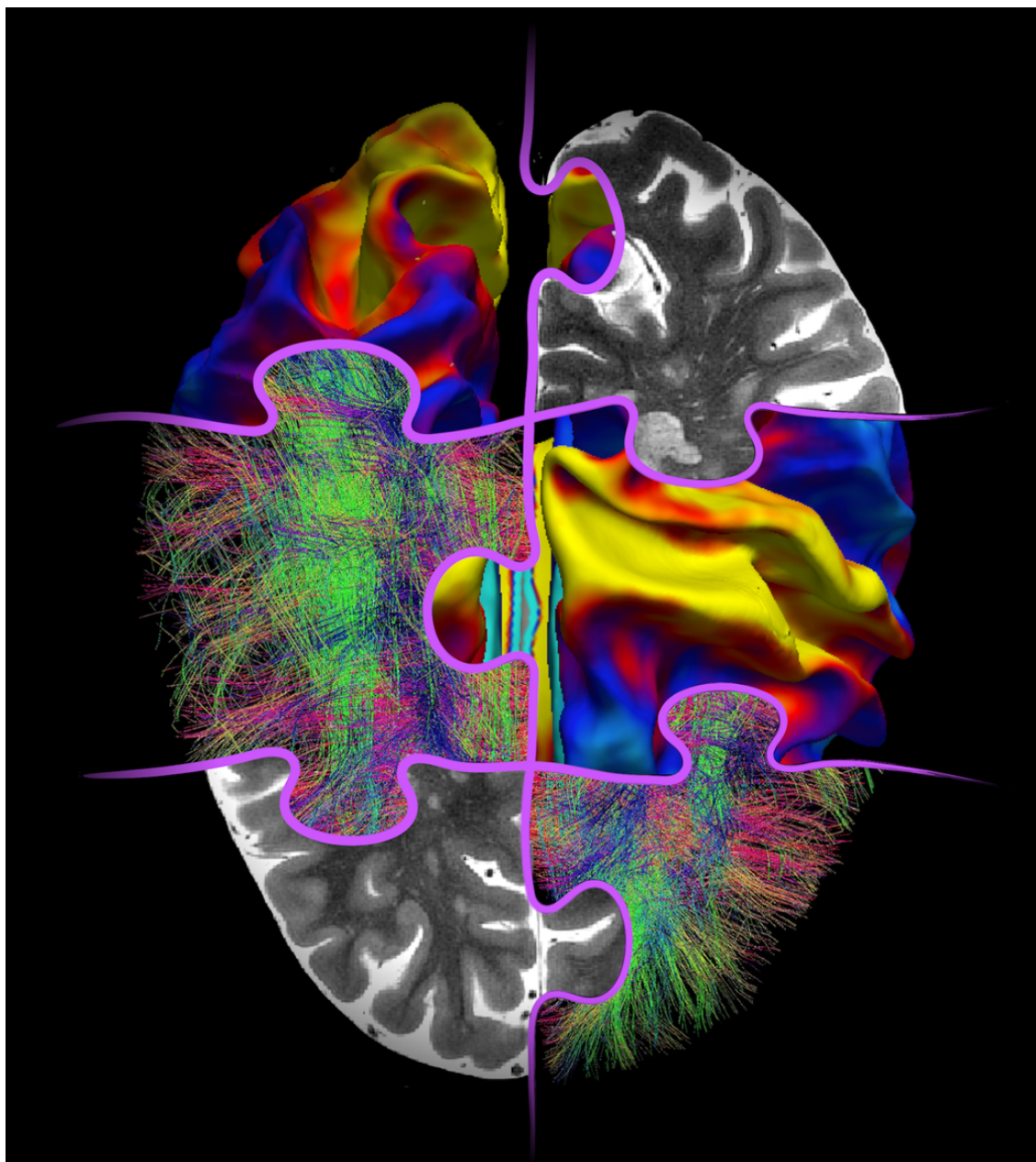
Figure 2.1 Representation of the Human brain through several modality of MRI imaging. The surfacic imaging (blue-red-yellow) is used to image the cortical ribbon; the high field MRI imaging (black and white) enables to image the gray and white matter with high resolution; and diffusion MRI permits to image the axonal tracts of the white matter (red-green-blue fibers). Multimodal MRI allows to study the brain structure and mechanisms from several points of views and is the tool of choice to solve the puzzle of neurodegeneration. Image created by G. Mangeat, 2018 for the *"Genie en Image"* prize of Polytechnique. *Note: to improve the aesthetic the picture, the brain was flipped upside down compared to the radiological convention.*

2.1.1 Neurons, axons and myelin

Neurons appear in a wide range of sizes and shapes; however, all share dendrites and axon terminals used to receive and transmit the nervous information. Moreover, all neurons have a cell body, referred to as soma, and a wiring system, referred to as axon, that convey the electrical information through the nervous system. Figure 2.2 A shows a representation of a neuron and its basic components as well as the shape of a neuron observed through a microscope. As in other types of cells, a neuron contains a nucleus in its cell body (or soma) that encloses the genetic information. The dendrites are a series of highly branched outgrowths linked to the soma. their role is to receive the inputs from other neurons. In average a neuron has 1,000 dendrites, but some neurons may have as many as 400,000 dendrites (Widmaier et al., 2013). The number of dendrites increases the cell capacity to receive signals from many afferent neurons. The component that actually transmits the information are the axons terminals. Under the command of an action potential, axon terminals are releasing the neurotransmitters through the synaptic terminals that reach another neuron or an excitatory cell. Finally, the part of the neuron which links the soma with the axons terminals is a kind of organic wire called axon. An axon can be some micrometers to many centimeters long. Axons are encompassed by sheaths of myelin, a macromolecule produced by a cell called oligodendrocyte, Figure 2.2 B. Axons transmit the action potentials from the cell body to the axon's terminals using ionic currents.
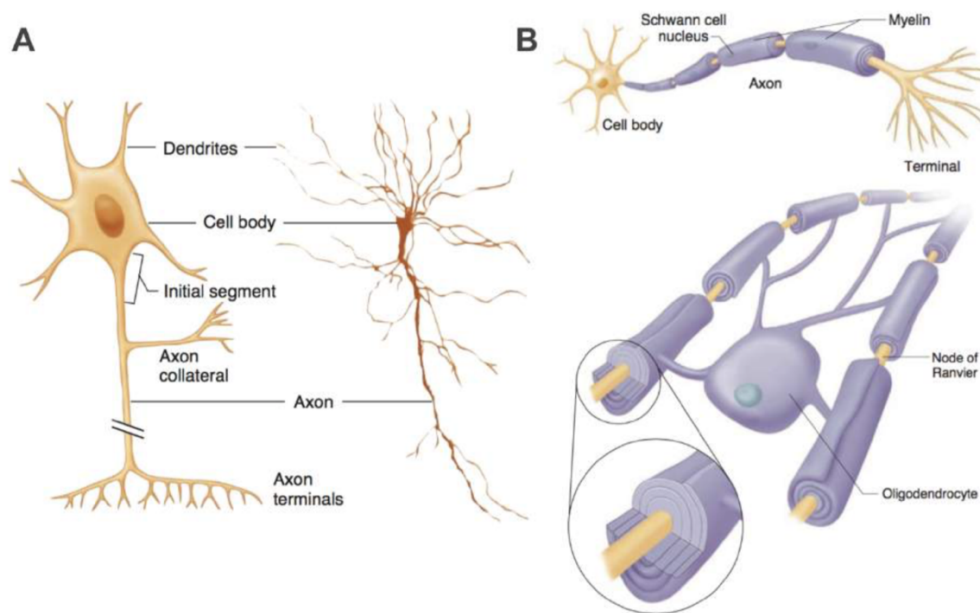
Figure 2.2 Adjusted from (Widmaier et al. 2013, Fig. 6-1 & 6-2). A) Representation of a neuron and its essential components as well as the shape of a neuron watched through a microscope. B) Representations of axons enveloped by macromolecules of myelin. Myelin is delivered by oligodendrocytes cells within the CNS and by Schwann cell within the Peripheral Nervous System (PNS).

The myelin is responsible for the velocity with which an action potential propagates along the axon, or myelinated fiber. Myelin acts as an insulator that decreases the membrane permeability to ions. Because there is less flux of charge across the myelin, a local current can spread farther along an axon (Widmaier et al., 2013). Furthermore, the concentration of voltage-gated sodium channels in the myelinated region of axons is low. Therefore, action potentials occur only at the nodes of Ranvier, where the myelin coating is interrupted and the concentration of voltage-gated sodium channels is high, Figure 2.3. Thus, action potentials jump from one node to the next as they propagate along a myelinated fiber, such propagation is called saltatory conduction.

Propagation via saltatory conduction is faster than propagation in unmyelinated fibers of the same axon diameter because less charge leaks out through the myelin-covered sections of the membrane.

More charge arrives at the node adjacent to the active node, and an action potential is generated there sooner than if the myelin were not present. Moreover, because ions cross the membrane only at the nodes of Ranvier, the membrane pumps need to restore fewer ions. Myelinated axons are therefore metabolically more efficient than unmyelinated ones. In this way, myelin adds speed, reduces metabolic cost, and saves room in the nervous system because the axons can be thinner.
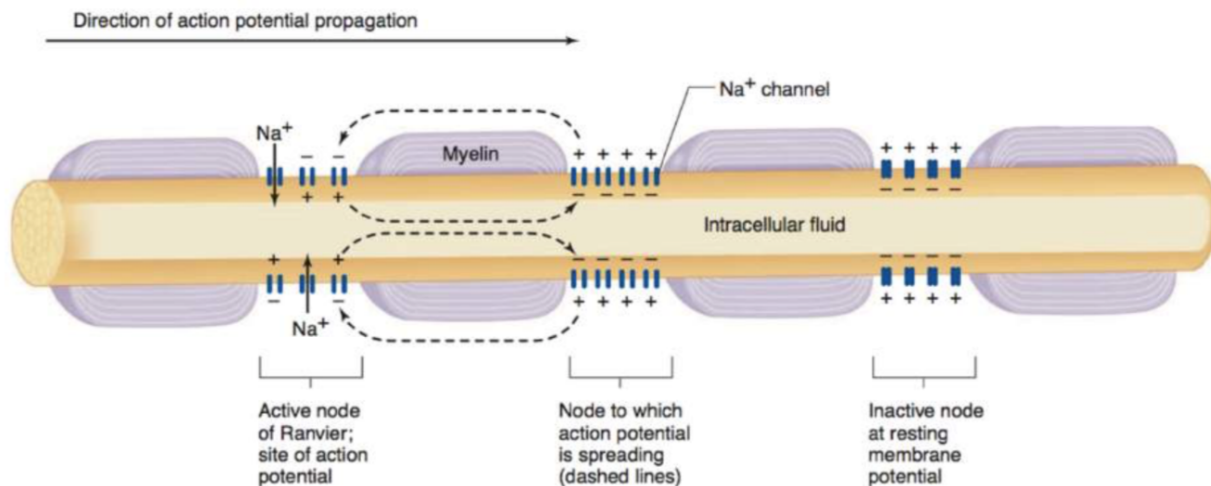
Figure 2.3 Adapted from (Widmaier et al., 2013) Representation of the saltatory conduction. Concentration of voltage-gated sodium channels is low in the myelinated regions. Action potentials occur only at the nodes of Ranvier, where axon is bare and the concentration of voltage-gated sodium channels is high. Action potentials thus "jump" from one node to the next as they propagate along a myelinated fiber.

2.1.2 White matter and grey matter

The upper brain can be separated into two distinct structures: the white matter (WM) and the grey matter (GM). Grey matter is distinguished from white matter in that it contains numerous cell bodies and relatively few myelinated axons, while white matter contains relatively few cell bodies and is composed chiefly of long-range myelinated axons. The colour difference arises mainly from the whiteness of myelin. Figure 2.4 shows an MRI image highlighting a clear distinction between the WM and GM tissues.
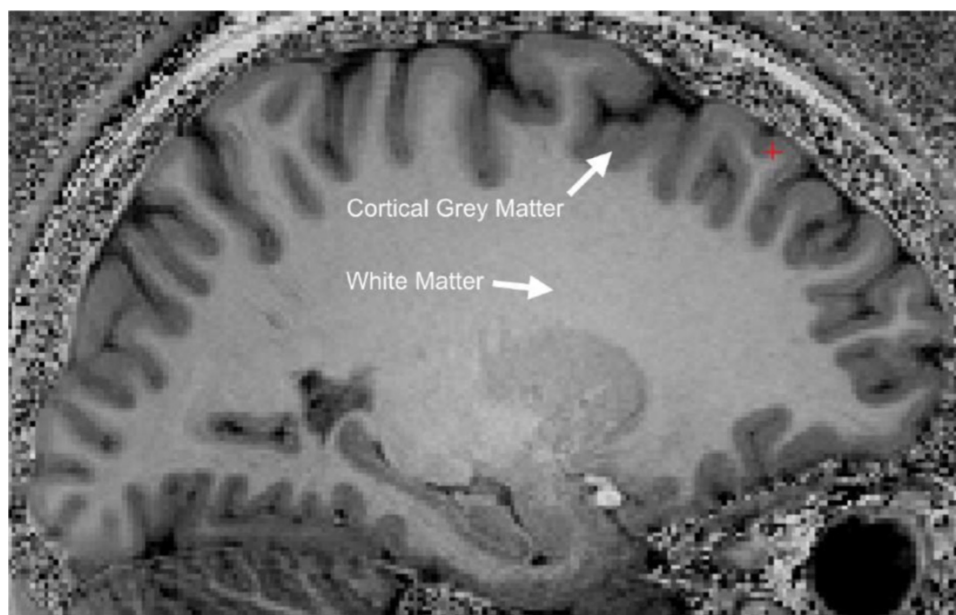
Figure 2.4 Sagittal view of a Human brain, imaged with magnetic resonance imaging (MRI) highlighting a clear distinction between the WM and GM tissues.

The cerebral cortex is the main component of the GM. It is a 2 to 4 mm thick ribbon that contains the cell bodies and the dendrites of the cerebral neurons. Moreover, neurons account for only 28% of the cells in the cerebral cortex (Azevedo et al., 2009), the 72% remaining cells are the glial cells, also called neuroglial cells (glia = glue). Glial cells surround the soma, axons and dendrites, one of their roles is to provide them with metabolic support. The main glial cells are the astrocytes, microglia, ependymal cells and oligodendrocytes, Figure 2.5. The astrocytes help regulate the composition of the extracellular fluid and sustain the neurons metabolically, for example by providing glucose and removing ammonia. Astrocytes also stimulate the formation of tight junctions between the wall cells of the capillaries in order to form the so- called blood-brain barrier (BBB), which prevents toxins and other undesired substances from entering the brain. Microglia are macrophage cells that perform immune function in the cortex and in the central nervous system in general. Ependymal cells form the boundaries between the brain matter and the cerebrospinal fluid. Lastly, the oligodendrocytes produce the myelin sheaths that cover the axons. As we saw in the precedent section, the myelin sheaths are essential for the propagation of the action potentials. Therefore, death of oligodendrocytes in a region of the cortex leads to a demyelination of axons that hampers the afferent communications between neurons. The demyelination processes and

effects will be discussed in more details in the next section. So far, glial cells are known to play a secondary role in the information processing, but they are critical for the synergy of the central nervous system. Moreover, as well as neurons, they are contributing to the MRI signal, thus, a change in the neuroglial composition implies a change in an MRI image.
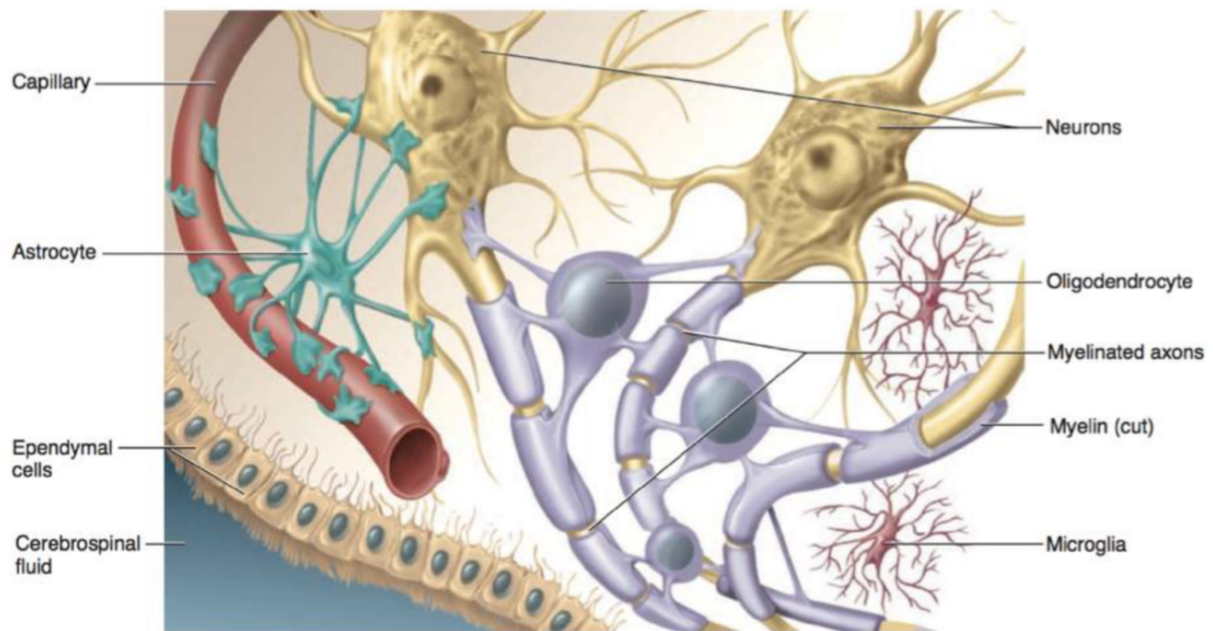
Figure 2.5 Adapted from (Widmaier et al., 2013). Representation of the main glial cells of the central nervous system.

WM is composed of bundles, which connect various grey matter areas of the brain to each other and carry nerve impulses between neurons. Long thought to be passive tissue, white matter affects learning and brain functions, modulating the distribution of action potentials, acting as a relay and coordinating communication between different brain regions (Douglas Fields, 2009). Myelin is only partially formed at birth and gradually develops in different regions throughout our 20s. The timing of growth and degree of completion can affect learning, self-control, and mental illnesses such as schizophrenia, autism and even pathological lying (Douglas Fields, 2009). Figure 2.6 shows the different tracts of myelinated axons observed in the white matter of a Human brain. Those tracts were computed from diffusion MRI data and tractography techniques.
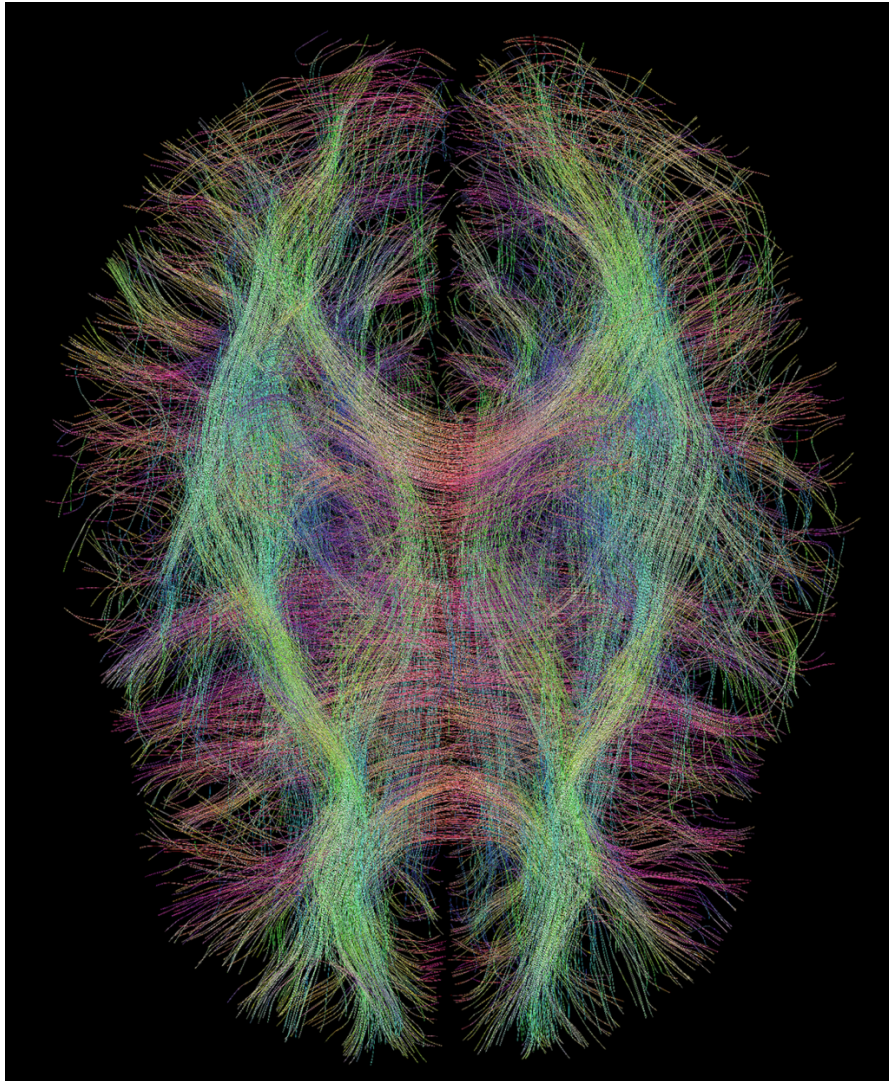
Figure 2.6 White matter tracts computed from diffusion MRI data and tractography techniques. Every line represents a bundle of myelinated fiber, connecting various GM areas of the brain to each other. The different colours show the average direction of the fibers (green = antero-posterior, red = lateral, blue = dorsoventral). Here, only a fraction of the fiber tracts are displayed for clarity.

2.2 Neurodegenerative diseases and MRI

2.2.1 Multiple Sclerosis

MS is a devastating disease of the CNS, affecting more than 100,000 people in Canada (*MS Society of Canada*) and 2-3 millions people in the world (Thompson, Baranzini, et al., 2018). MS is

characterized by the formation of inflammations or plaques, damaging the myelin sheath, a key component of neuronal cells. This damage disrupts the ability of regions in the brain and spinal cord to communicate with each other, resulting in functional deficits such as paralysis and chronic pain, affecting the social and professional activities of MS patients. As MS often affects individuals in their early adult life, it has a huge impact functionally, financially, and on quality of life. The socio-economic cost of MS is colossal. Firstly, life quality of MS patients and those of their family members can be drastically hampered. Secondly, existing treatments that reduce handicapping effects of MS are expensive, rising with increasing disability (Kobelt et al., 2017), with an annual cost estimated in billions of dollars in Canada (Karampampa et al., 2012) and in the USA (Hartung et al., 2015).

2.2.2 Causes of MS

Despite the causes of multiple sclerosis are still unclear, studies are mostly reporting environmental and genetic factors (Compston & Coles, 2008). The global distribution of multiple sclerosis can be generalised as increasing with distance north or south of the equator, but some countries do have a higher incidence of MS, e.g. Canada, UK, Sweden, Finland or New Zealand. In Canada, a significant increase in incidence of MS has been reported in Canadian women over the past 30 years (Orton et al., 2006), causing a change in the female to male ratio to more than 3:1. Moreover, hygiene can be a negative indirect factor, indeed, individuals not exposed to infections early in life, because of a clean environment, make aberrant responses to infections as young adults (Levin et al., 2010). In particular, an inadequate immune response to the Epstein-Barr virus can cross-reacts with myelin and induce demyelination, because several T-cell receptor peptide contacts are identical for myelin basic protein and Epstein-Barr virus (Lang et al., 2002). Some studies suggested other environmental triggers such as low sunlight, vitamin D deficiency, diet, geomagnetism, air pollutants, radioactive rocks, cigarettes, and toxins (Marrie, 2004).

2.2.3 MS pathophysiological processes in the CNS

While the causes of MS are still under investigation, the effects of the disease on the central nervous system (CNS) are widely understood and acknowledged (Thompson, Baranzini, et al., 2018). MS

is characterized by an autoimmune inflammation of the CNS. Why immune responses are initiated against CNS antigens and maintained in MS is unclear. Several acute and chronic mechanisms are present, such as 1) infiltration of macrophages (T cell and B cell) in the CNS via disruption of the blood-brain barrier (BBB), 2) activation of the resident immune system (microglia and astrocytes), 3) autoimmune disruption of the myelin sheaths (demyelination), 4) axonal degeneration leading to irreversible axonal injury. The relation between the inflammatory (1, 2 and 3) and neuro-degenerative (4) processes is still a subject of investigation. Some studies propose the hypothesis of a detrimental circle of events: tissue damage leads to release of antigens to the periphery, which primes new immune responses in the lymphoid tissue, followed by the invasion of lymphocytes into the CNS (Thompson, Baranzini, et al., 2018).

2.2.4 Treatments

The emergence of an increased number of disease-modifying treatments over the last 5 years is a major development, Figure 2.7. In general, treatments target neuroinflammation and could have an indirect effect on neurodegeneration; however, their efficacy for reducing the development of brain atrophy in clinical trials has been moderate at best. Only one disease-modifying treatment (ocrelizumab) has been shown to slow progression in patients with primary progressive multiple sclerosis (Mulero et al., 2018; Thompson, Baranzini, et al., 2018). The emergence of effective treatments has created an impetus to diagnose as early as possible.
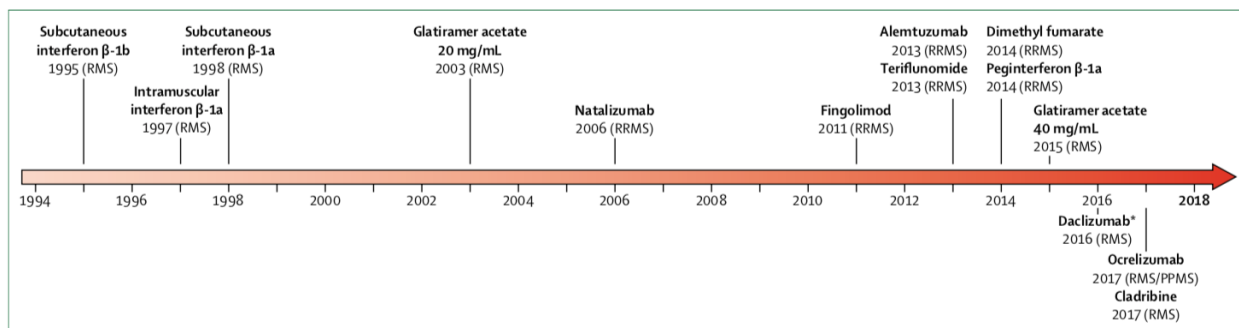
Figure 2.7 Adapted from (Thompson, Baranzini, et al., 2018). Disease modifying treatments and their year of discovery.

2.2.5 MS and clinical MRI

Magnetic Resonance Imaging (MRI) has been the main tool for diagnosing and studying MS progression. Indeed, the pathological hallmark of MS diagnosis is focal demyelination in regions called plaques or lesions. Using the fluid-attenuated inversion recovery (FLAIR) sequence, MS lesions appear as focal areas of signal increase. Lesion appearance and location gives additional pathological insights. MS lesions in the brain are commonly round or ovoid and range from a few mm to more than 1 cm in size and have a high propensity to locate in the brainstem, cerebellum, and periventricular white matter. While FLAIR hyperintensities is the hallmark for MS diagnosis, the specificity of the underlying mechanism (causing the hyperintensity) is very low. Indeed, different types of MRI contrasts might highlight different types of lesions. For example, when considering a FLAIR image, 10-30% of the lesions appear as low signal intensity on Gadolinium-enhanced T1-weighted images, also called hypointense black holes (green arrow on Figure 2.8). Moreover, lesions can show a rimmed signal intensity pattern (Figure 2.8). Suggesting different pathological mechanisms behind the observed hyper hyperintensities.
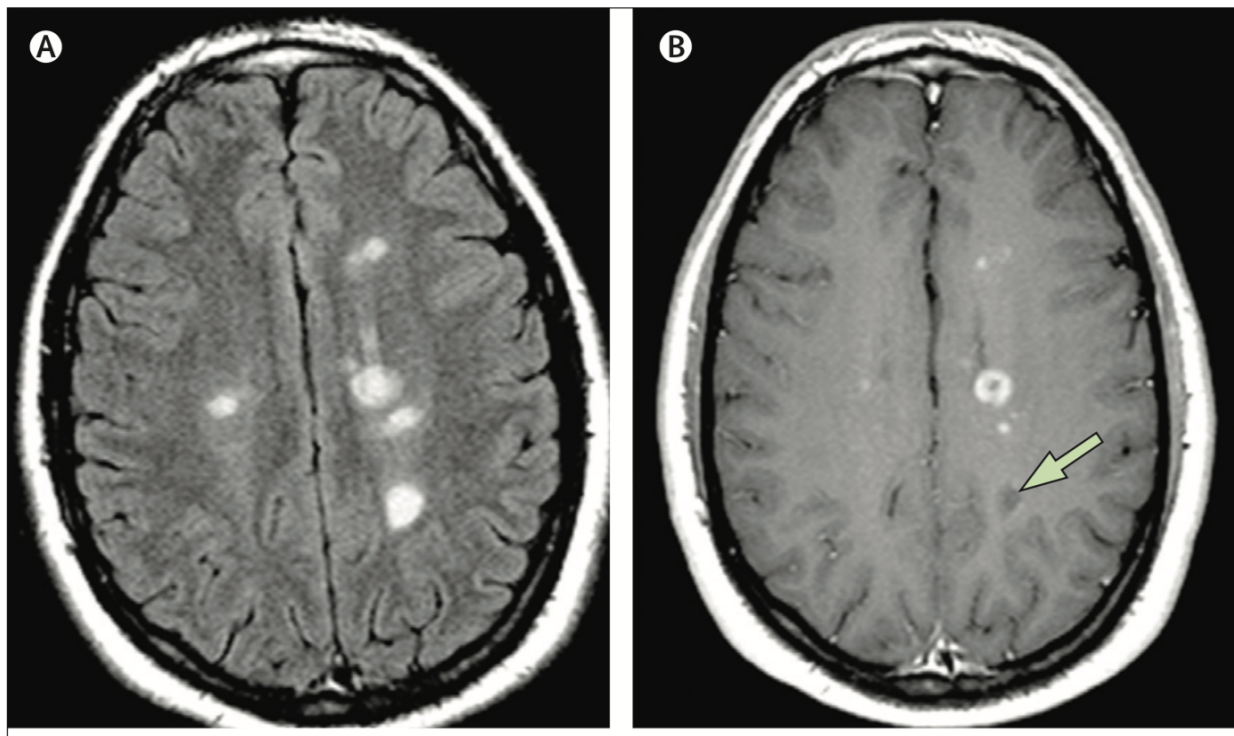
Figure 2.8 Adapted from (Massimo Filippi et al., 2012). (A) FLAIR sequence shows multiple round-to-ovoid lesions in the periventricular and deep white matter. (B) Gadolinium-enhanced

T1-weighted scan shows enhancement of most of these lesions with either a nodular or a ring-like pattern; one lesion (arrow) is not enhancing and appears dark.

Pathological insights into MS lesions are mainly based on studies of archival autopsy tissues. Different MS mechanisms (described above) can be found in lesions, such as macrophages infiltration, microglia activation or myelin debris. Some lesions can be inflammatory only, sometimes with demyelination and/or axonal injury and/or remyelination. More problematic is that most of these mechanisms can be found in non-lesion areas, also called normal appearing regions on MRI. For example, gliosis, demyelination, macrophage infiltration, axonal injury or microglia activation can be found in the normal appearing white matter (NAWM).

Consequently, <u>clinical MRI only provides an indirect measurement of the underlying microstructure</u>, i.e., the MRI signal at each voxel includes contribution from multiple healthy and pathological structures (chemical composition, tissue orientation, flow, etc.) and is poorly specific to e.g., the presence of demyelination. This poor specificity drastically hampers the ability of clinicians to draw an accurate picture of disease diagnosis and progression.

2.2.6 Quantitative MRI for MS

While clinical MRI lacks specificity to decipher all pathological processes of MS, quantitative MRI (qMRI) techniques have the potential to distinguish between the different pathogenic mechanisms. Figure 2.9 shows some examples of disease mechanisms of MS and their imaging modalities. In particular, neuroaxonal degeneration can be measured by determining whole brain atrophy and compartment-specific atrophy (eg, white, grey, and deep grey matter). MTR is sensitive to demyelination. Microstructural changes involving neurons and axons can be measured with DWI, ODI, and NDI. Specific molecular PET and metabolic MRS targets for astrocyte activation, neuroaxonal degeneration, microglia activation, energy failure, glutamate excitotoxicity, and demyelination have been developed.
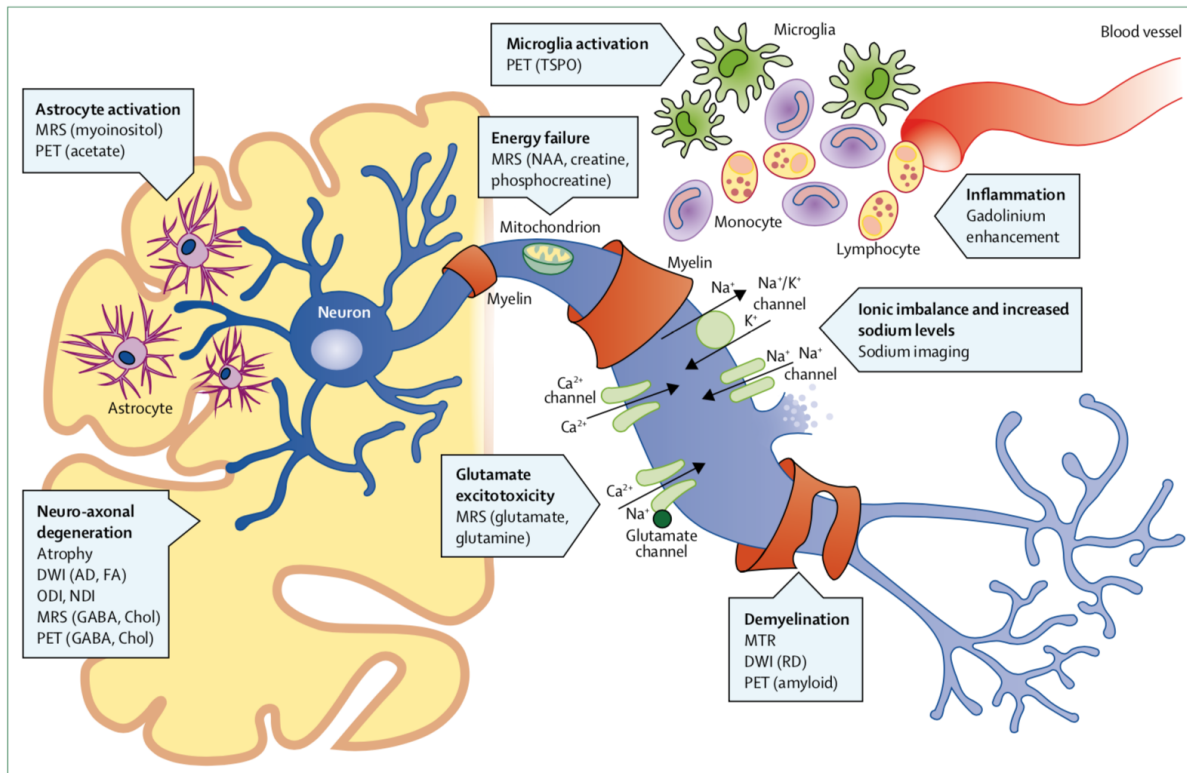
Figure 2.9 Adapted from (Thompson, Baranzini, et al., 2018). Pathogenic mechanisms of multiple sclerosis and their imaging modalities.

The link between MS pathophysiological features and quantitative MRI has been an extensive topic of research of the last decade. Table 2-1 summarises how the most relevant qMRI modalities are used to measure the different pathophysiological mechanisms of MS, and what are the associated challenges. Those qMRI modalities will be presented in more detail in the next section.

Table 2.1 Main qMRI modalities used to measure the different pathophysiological features of MS, and their associated challenges. We note that most of the qMRI modalities are not specific to one MS feature, and reciprocally, a high number of MS features can be detected with several qMRI modalities. This highlights the usefulness of multimodal qMRI acquisitions to unmix the contributions of specific MS mechanisms.

qMRI modality	MS pathophysiological features	Main challenges	References
qT1	NAWM changes NAGM changes Type III subpial lesions Cortical demyelination WM lesions Oedemas Remyelination	Several sequences available, the quantification depends on the sequence. Flip angle and B1 homogeneity.	(Vrenken et al., 2006) (Manfredonia et al., 2007) (Tardif et al., 2012) (Blystad et al., 2016) (Bonnier et al., 2017) (Ma et al., 2020) (Galbusera et al., 2020)
qT2	NAWM changes Type III subpial lesions Cortical demyelination WM lesions		(Tardif et al., 2012) (Bonnier et al., 2017) (Blystad et al., 2016) (Ma et al., 2020)
qT2*	Diffuse cortical changes. Acute cortical lesions of type III Cortical demyelination Rimmed WM lesions Rimmed GM lesions	Long scan times. Signal affected by iron, fiber orientation and susceptibility variations.	(Mainero et al., 2009) (Cohen-Adad et al., 2011) (Mainero et al., 2012) (Mainero et al., 2015) (Pitt et al., 2010)
qPD	NAGM changes WM lesion Type III subpial lesions	Low sensitivity	(Tardif et al., 2012) (Gracien et al., 2016) (Chong et al., 2016)

	Cortical demyelination Oedemas		
Diffusion MRI	WM lesions Alterations of the structural connectivity Network plasticity	Low image resolution. Long scan times.	(M. Filippi et al., 2001) (Shu et al., 2011) (Schneider et al., 2017) (Nigro et al., 2015) (Lashkari et al., 2020) (Fleischer et al., 2016)
MTR	NAWM changes NAGM changes Demyelination Remyelination	Partial specificity to the macromolecular components of myelin.	(Schmierer et al., 2004) (Schmierer et al., 2008) (Chen et al., 2013) (Bonnier et al., 2017) (Giacomini et al., 2009)
qMT	NAWM changes Demyelination Remyelination WM lesions	Long scan times. Partial specificity to the macromolecular components of myelin.	(Schmierer et al., 2007) (Cercignani et al., 2009) (Fooladi et al., 2020) (Tozer et al., 2003) (Levesque et al., 2010)
ihMT	NAWM changes WM lesions Demyelination	Low SNR Product sequence not available	(L. Zhang et al., 2020) (Van Obberghen et al., 2018)
QSM	Rimmed WM lesions WM local lesions	Long scan time Sensitive and complex post processing.	(Harrison et al., 2016) (Jang et al., 2020)
SyMRI	NAWM changes NAGM changes	Low in-plane resolution	(A. Hagiwara, Hori, Yokoyama, Nakazawa, et al., 2017; A. Hagiwara, Hori, Yokoyama,

	Demyelination Edema WM lesions Parenchymal fraction		Takemura, Andica, Kumamaru, et al., 2017; A. Hagiwara, Hori, Yokoyama, Takemura, Andica, Tabata, et al., 2017; Akifumi Hagiwara et al., 2017) (Vaughn et al., 2013) (Vågberg et al., 2013) (Granberg et al., 2016)
MWI	NAWM changes NAGM changes Demyelination	High variability Difficult processing due to the low SNR of the short component. Long scan times.	(Levesque et al., 2010) (C. Laule et al., 2006) (Cornelia Laule et al., 2008) (S. Kolind et al., 2012)

2.3   Quantitative MRI

QMRI is a subclass of MRI techniques that measures the absolute value of intrinsic MR properties of tissue with the best possible repeatability and precision across scans sessions, scanners, and over time (Cohen-Adad et al., 2012; Mainero et al., 2015; Stikov et al., 2014; Vaughn et al., 2013). Thus, qMRI has the capability to provide more specificity to tissue microstructure, including demyelination. This section presents the most promising qMRI techniques as well as their advantages and limitations.

2.3.1 Diffusion MRI

Diffusion MRI is amongst the more popular qMRI techniques. It is sensitive to the preferential directions of water diffusion and can be used to reconstruct the tracts of neural fibers in the brain and spinal cord. Thus, diffusion MRI can probe axonal loss (Schneider et al., 2017; H. Zhang et al., 2012), white matter connectivity (Betzel et al., 2016; Bullmore & Sporns, 2009; Fornito et al., 2015), and other quantitative derived indexes, such as fractional anisotropy or mean diffusivity. In addition, multi-shell diffusion can probe others neural properties, such as "neurites density" or "neurites dispersion index" (Schneider et al., 2017; H. Zhang et al., 2012). The reconstruction of

neural fiber tracts is called tractography (Li et al., 2013; Rilling et al., 2011) and allows to compute the brain's connectivity graphs, out of which several Graph Theory based indexes can be computed (Mohan et al., 2016). Connectivity measurements have been promising to study neurodegenerative diseases, such as Parkinson, ALS or MS (Betzel et al., 2016; Griffa et al., 2013; Kocevar et al., 2016). Diffusion MRI typically requires long scan times (typically > 30 min) and is hampered by a poor image resolution (typically > 1.5 mm isotropic).
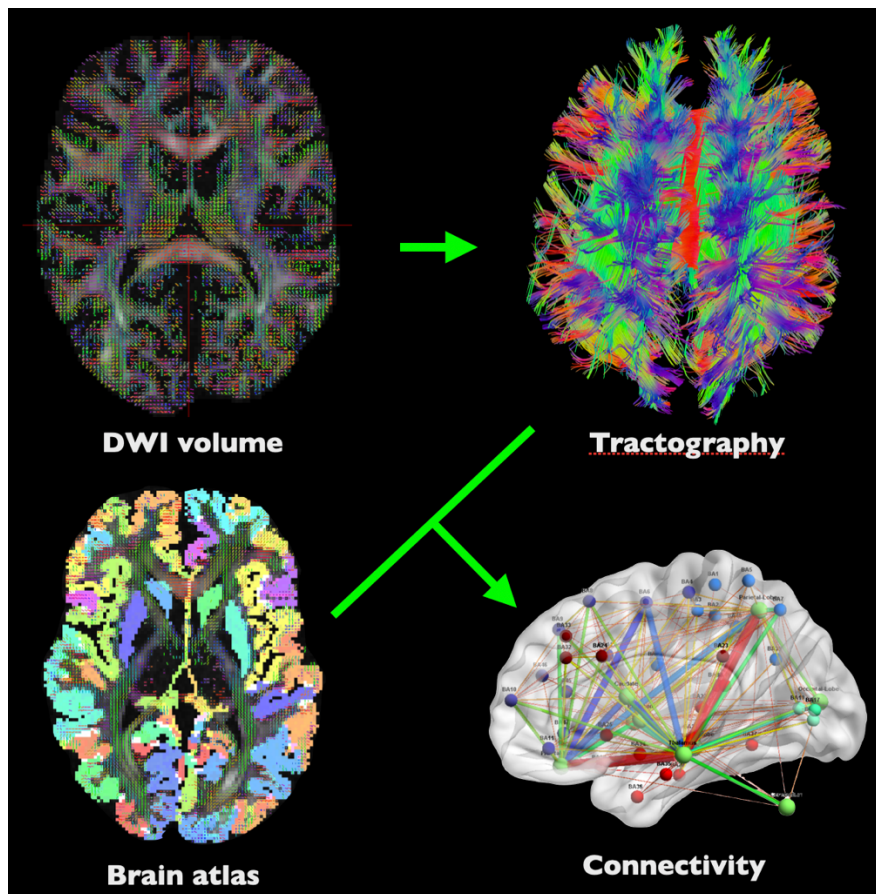
Figure 2.10 Illustration of some diffusion-derived modalities. Top left is a representation of a Diffusion Weighted Imaging (DWI) volume. The color represents the direction of preferential diffusion of water. From this DWI volume, it is possible to compute a tractography volume (top right), which represents the main fiber tracts of the brain. When the tractography is combined with a well registered brain atlas (bottom left), it is possible to compute the connectivity matrix of the brain studied, as well as any graph theory metric derived from this connectivity matrix.

2.3.2 Magnetization transfer

The "magnetization transfer" (MT) technique is another MRI contrast that can probe myelin loss (Levesque & Pike, 2009; Schmierer et al., 2004). The MT effect results from the interaction between two kinds of hydrogen nucleus. Protons in a liquid state (free state) associated with water molecules and protons in semisolid state associated with macromolecules (Henkelman et al., 2001). Macromolecular spins cannot be imaged by conventional MRI method, because of their very short T2 (<1ms). However, macromolecular spins can be indirectly imaged by off-resonance saturation. Different models, such as the 2-pools model (Henkelman et al., 1993; Samsonov et al., 2012) or the 4-pools model (Levesque & Pike, 2009), can then be applied to recover the parameters involved in the MT effect, such as macromolecular volume or rate of exchange. As myelin sheath are composed of macromolecules (~20% proteins and ~80% lipids), the MT measurements will be sensitive to myelin changes in the brain and spinal cord. The specificity of MT to probe myelin is hampered by the presence of non-myelin macromolecules, such as collagen (Berry et al., 1999; Pampel et al., 2015).
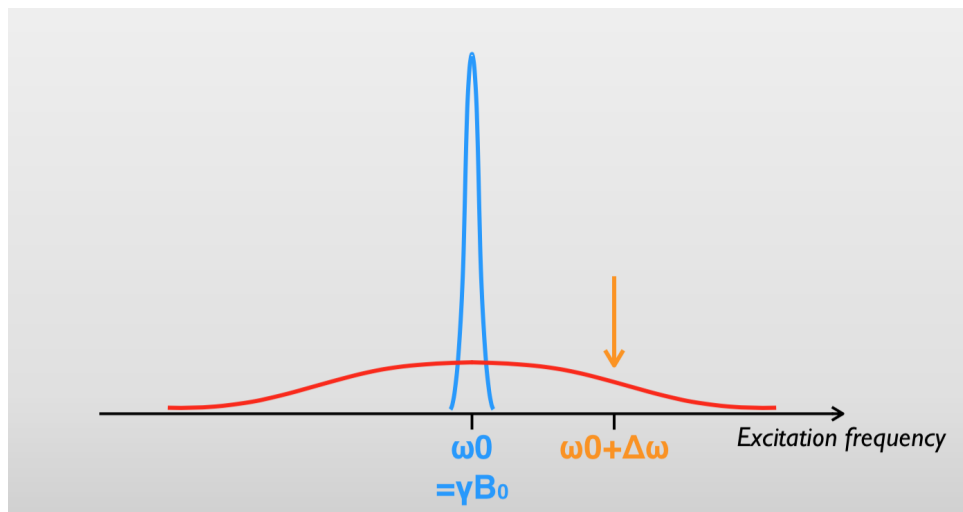
Figure 2.11 Representation of the absorption profiles of water protons (or free protons, blue line) and proteins bound to macromolecules (semi-solid proteins, red line). The bound protons have a much wider excitation range and can thus be excited by an off-resonance pulse before imaging. They will then transfer their magnetization to the close-by free protons. The most popular modalities derived from the MT effect are Magnetisation Transfer Ratio (MTR) and quantitative Magnetisation Transfer (qMT).

2.3.2.1 The MTR, 2-pool and 4-pool models

Magnetisation Transfer Ratio (MTR) is a semi-quantitative MT-derived modality. It only requires two scans, one with and one without the MT saturation pulse. The ratio between those scans is then computed to obtain the MTR volume (Figure 2-12, left). MTR has the advantage to be a fast technique and is sometimes used in clinics (Chen et al., 2013; Giacomini et al., 2009). MTR was shown to correlate with myelin content (Henkelman et al., 2001; Schmierer et al., 2004), but lacks specificity. Indeed, it is also sensitive to other macromolecules in the brain, like collagen, B1 profile and T1 relaxation. The qMT 2-pool (Henkelman et al., 2001) and 4-pool (Levesque & Pike, 2009) models aim at modeling several tissue compartments (myelin: liquid and semi-solid and non-myelin: liquid and semi-solid). The unknown parameters are the compartments volumes and their magnetic interactions with each other. These models are able to separate the signal contribution of different compartments inside a voxel, making them more specific than others monoexponential qMRI modalities. However, qMT modeling is data and time consuming as it requires a large amount of scans, making it difficult to use for clinical studies.
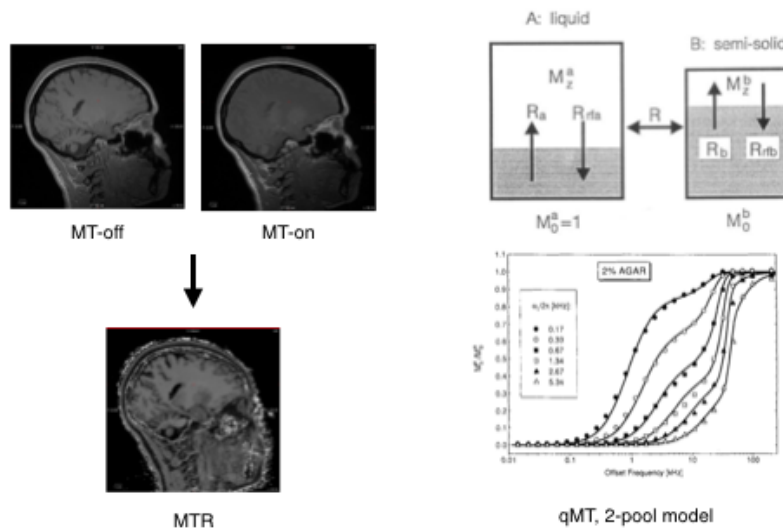
Figure 2.12 Left: Raw MRI images with and without MT saturation pulse used to calculate MTR. Right: Illustration of the 2-pool model, adapted from (Henkelman et al., 1993). Here, several off-resonance images with different saturation pulses in order to fit experimental curves and recover the MT parameters.

2.3.2.2 Inhomogeneous magnetization transfer

Recently, a new MR contrast mechanism, namely inhomogeneous magnetization transfer (ihMT), has been proposed (Girard et al., 2015; Taso et al., 2016; Varma et al., 2015) and has shown high capabilities in discriminating highly myelinated WM tissues and other tissues. The technique relies on the ability to isolate the components with inhomogeneously-broadened lines from the broad MT macromolecular pool, these inhomogeneous lines presumably arising from large structured membranes such as lipid bilayers (main components of the myelin sheath), because of motion restriction and reduced spin diffusion.

2.3.3 Quantitative relaxometry

Quantitative relaxometry is another type of qMRI modality. The longitudinal relaxation time T1 (Lutti et al., 2014; Stikov et al., 2014; van der Kouwe et al., 2008), the transverse relaxation times T2 (Ben-Eliezer et al., 2015) and T2* (Cohen-Adad, 2014; Cohen-Adad et al., 2011, 2012; Stüber et al., 2014) and the proton density PD are four orthogonal parameters driving the MR relaxation. Every tissue can be characterised by its own relaxation parameters (T1, T2, T2* and PD) as well as its rate of magnetization exchange with others surrounding tissues. As a single voxel usually contains several types of neural tissues, a multi-exponential modeling can be used to recover the relaxation parameters of each tissue. For example, the myelin water fraction (MWF) technique uses the intensities ratio of the multiexponential T2 decay to estimate the myelin fraction in a voxel (Mackay et al., 1994; Stewart et al., 1993), see Figure 2.13, A. While this technique has been used to study myelin damaging diseases (S. H. Kolind & Deoni, 2011; C. Laule et al., 2006; Vavasour et al., 2009) its specificity to myelin is hampered by the room temperature, as well as the geometry of the cells (axons sizes, density and shapes) (Does, 2018).

The monoexponential relaxometry parameters have also been shown of interest to probe the brain microstructure. Indeed, if the intra voxel magnetisation exchange is occurring relatively fast compared to the measurement time, the MR relaxation can be approximated to a monoexponential model. The MR longitudinal relaxation time, T1, has been shown to be closely related to myelin content in vivo (Bjarnason et al., 2005; Koenig et al., 1990) and ex vivo (Mottershead et al., 2003; Schmierer et al., 2004) and has been widely used to study myelin modifying diseases. Several

techniques can be used to compute T1 maps (see Figure 2.13, B). Recently, high-resolution T1 maps were used to study the myeloarchitecture of the entire cortical ribbon (Lutti et al., 2014; Sereno et al., 2013). The specificity of T1 maps to myelin can be hampered by B1 inhomogeneities, flip angle variations or water content in tissues.

In addition, the transverse relaxation (called T2*, see Figure 2.13, C) at 7 Tesla was shown to be a sensitive marker of pathology and disease progression of MS patients (Cohen-Adad et al., 2011, 2012; Deistung et al., 2013; Mainero et al., 2015). The use of quantitative T2* to map cortical integrity can reveal changes in myelin content beyond visible focal cortical lesions (Mainero et al., 2015). These findings have been corroborated by histopathological-MRI correlations in ex vivo samples from patients with multiple sclerosis imaged at 7T (Kilsdonk et al., 2016; Pitt et al., 2010). Despite its sensitivity to myeloarchitecture, T2* is influenced by several confounds, such as B0 field inhomogeneities (Hines et al., 2012), fiber orientation with respect to B0 (Cohen-Adad et al., 2012), and iron levels in tissue (Fukunaga et al., 2010).

The PD based technique: macromolecular volume fraction (MVF) imaging (Mezer et al., 2013; Stikov et al., 2011; West et al., 2018) has also shown promising results in terms of specificity to myelin.
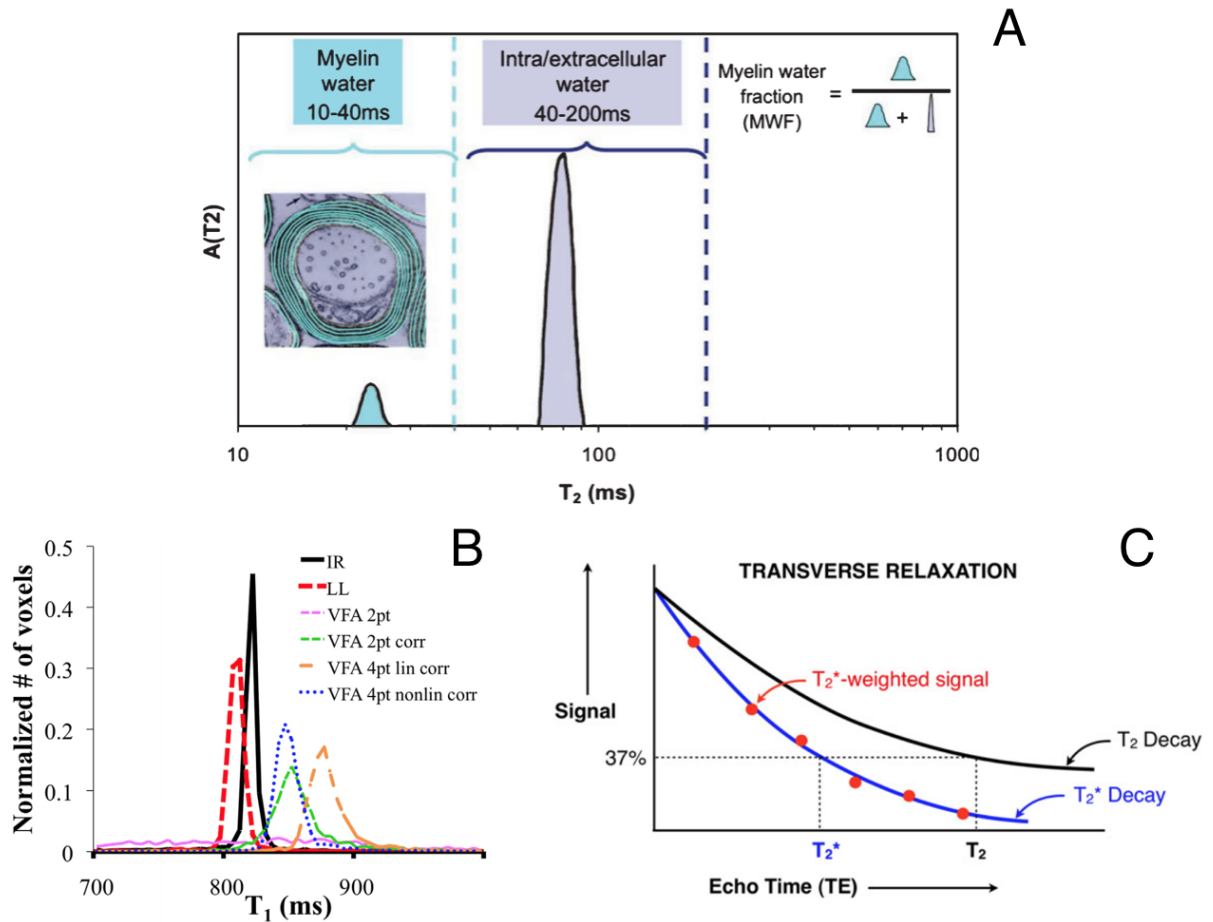
Figure 2.13 Quantitative relaxometry. A: Adapted from (MacKay & Laule, 2016) Illustration of the concept on Myelin Water Imaging (MWI). A multiexponential modelisation of T2 is used to create a marker of myelin. B: Adapted from (Stikov et al., 2014). Histograms of different T1 mapping techniques, highlighting that quantitative T1 maps differ depending on the imaging sequence used. C: adapted from (Cohen-Adad, 2014), illustrating the fitting procedure to obtain the quantitative T2* parameter from a series of T2*-w images with different echo times.

2.3.4 Synthetic MRI

Synthetic MRI (SyMRI) is an emerging technique aiming to provide the absolute quantification of the T1, T2, PD and B1 inhomogeneities in a single scan (J. B. M. Warntjes et al., 2008). The SyMRI pulse sequence is a 2D fast spin-echo (FSE) multi-dynamic, multi-echo (MDME) sequence, which is performed using an interleaved slice-selective 120 degrees saturation and multi-echo acquisition. Each MDME acquisition is 8 (complex) images per slice: 4 saturation delays, at 2 echo times (J.

B. M. Warntjes et al., 2008). The MDME images all exhibit different effects of the T1 and T2 relaxation times and the proton density PD of the imaged tissues. The SyMRI algorithm does a least-square fir on the signal intensity of each pixel of the 8 images per slice to compute the quantitative T1, T2 and PD maps.

In addition to the advantages associated with the single acquisition (e.g., no co-registration required), synthetic MRI has been validated as a time-efficient imaging method for a number of clinical applications (typically <7min for a full brain image), (A. Hagiwara, Hori, Yokoyama, Nakazawa, et al., 2017; A. Hagiwara, Hori, Yokoyama, Takemura, Andica, Kumamaru, et al., 2017; Akifumi Hagiwara et al., 2017; Vågberg et al., 2013) and recently received the CE-mark for clinical use.

In addition to the quantitative T1, T2 and PD maps, SyMRI proposes a "Rapid Estimation of Myelin" map: REMyDI (M. Warntjes et al., 2016). In this model, four pools (myelin water, extracellular water, free water, and excess parenchymal water, Figure 2.14) are used, and their magnetic properties are calibrated from the data of 20 healthy controls and 20 MS patients. After this calibration, the Warntjes model outputs the respectives volumes of each pool based on the inputs of the three relaxometry parameters: T1, T2 and PD.

Advantages of REMyDI: 1) Unlike qMT or MWF, there is a calibration step done once and for all and does not need to be redone after each scan. Thus, it increases its SNR by averaging the data of 20 ctrl on and voxels of 2x2x2mm and will therefore have more sensitivity than a technique whose fit is done on the data of a scan alone. 2) It assumes a mono-exponential T1 signal and a mono-exponential T2 signal because its sequence cannot capture the fast component T2. This makes the SyMRI T2 images more repeatable because the mono-exponential model is more robust and repeatable than the multi-exponential (Does, 2018). However, SyMRI T2 data cannot be used alone to predict myelin because the mono-exponential signal is not specific to the volume of myelin. SyMRI will take advantage of the non-linear combination of T1, T2 and PD to predict myelin, which greatly increases its specificity.

Disadvantages of REMyDI: 1) The REMyDI model (M. Warntjes et al., 2016) is an approximation of the 4 pool qMT model (Levesque & Pike, 2009), the 2 main pools of Warntjes V_MY and V_CL are an average of the myelin water and myelin semisolid pools; and extracellular water and non-myelin semi-solid respectively from the qMT model. This implies a potential loss of

specificity. A more complex model would generate too many degrees of freedom in its fit, which would limit convergence. 2) The fact that the model was trained on 20 healthy controls only, this limits the specificity of measurements on a larger population. 3) The two studies aiming to validate REMyDI (Ouellette et al., 2020; J. B. M. Warntjes et al., 2017) only show a correlation between REMyDI and myelin histology, the accuracy was not validated.
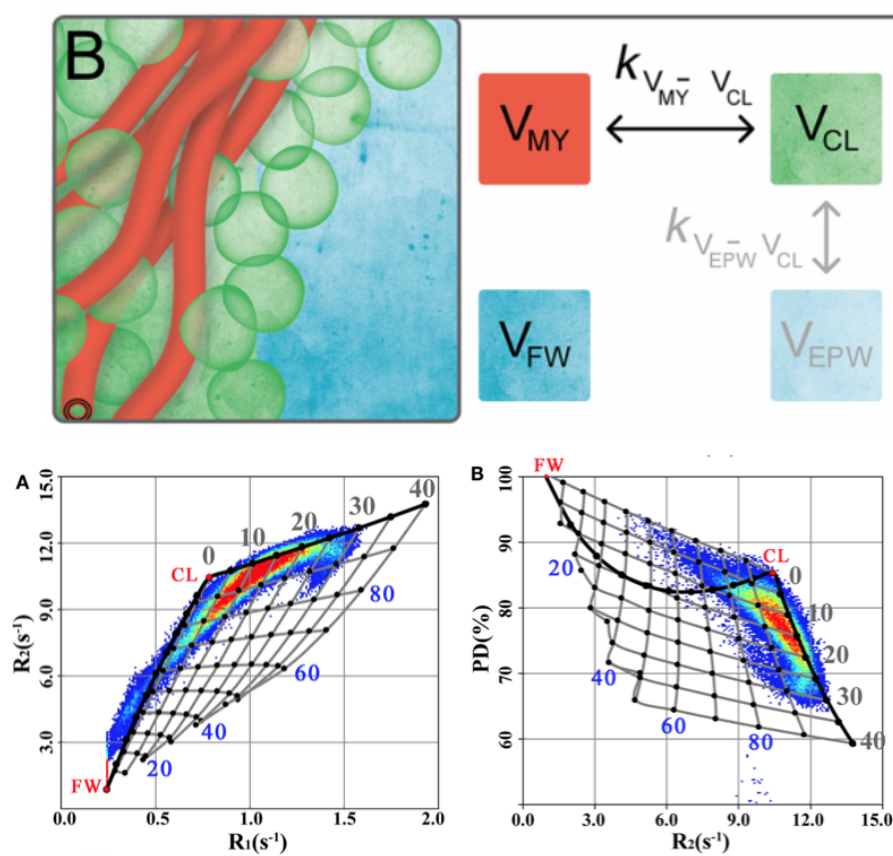
Figure 2.14 Adapted from (M. Warntjes et al., 2016). SyMRI provides three quantitative maps in a single acquisition: T1, T2 and PD maps. A: a four-pool model (top) was developed to provide a Rapid Estimation of Myelin (REMyDI) map. REMyDI is calculated from a non-linear combination of T1, T2 and PD (bottom). Vmy = myelin partial volume; Vcl = cellular partial volume; Vfw = free water partial volume and Vepw = excess parenchymal water partial volume.

2.4 Neural tissue histology

2.4.1 Optical stains

Imaging tissue with molecular selectivity typically requires the introduction of specific staining, such as Luxol Fast Blue (LFB), Proteolipid Protein (PLP), or Myelin Basic Protein (MBP) stain. Table 2-2 summarises the results of previous studies aiming to compare qMRI and histology images. We note that the studies using common absorption stainings (like LFB, PLP or MBP) show correlations ranging from 0.50 to 0.80 (R and Rho, average ~0.65). It should be noted that the specificity of the staining technique and inhomogeneous penetration of the staining agents can introduce biases (Vincze et al., 2008). Moreover, we note a high variability in the claimed performances of the different studies, as also reported in studies specifically aiming to measure myelin content (Mancini et al., 2020). Finally, the staining procedures are typically time and cost consuming, limiting their accessibility. Stain-free or label-free histology techniques aim to overcome the biases linked to the staining procedure. We note that the label-free techniques of Table 2-2 (polarised OCT, polarised light and PIXE) show much higher correlations with qMRI: 0.81 to 0.93 (Nieminen et al., 2001; Stüber et al., 2014; Hui Wang et al., 2014). Of course, different microstructural features are targeted in these different studies, so their direct comparison needs to be discussed. Polarised light-based techniques are efficient for detecting fiber-like features. PIXE Is a sort of X-ray fluorescence technique (very sensitive and specific to individual atoms), whose spatial specificity is assured by a focal ion beam scanning the sample. Despite promising, those techniques have a limited field of view (FOV) and their complicated set up also limits their accessibility.

Table 2.2 Results of previous histology studies aiming to validate qMRI measurements.

qMRI modality	Histology technique	Result	References
Diffusion MRI (tractography)	Polarized OCT	R = 0.9	(Hui Wang et al., 2014)
qMT	LFB	R = 0.8	(Schmierer et al., 2007)

MWF	LFB	R = 0.77 to 0.95	(C. Laule et al., 2006; Cornelia Laule et al., 2008)
SyMRI (REMyDI)	LFB and PLP	R = 0.67 to 0.69	(Ouellette et al., 2020)
SyMRI (REMyDI)	LFB	Rho = 0.74	(J. B. M. Warntjes et al., 2017)
qT1	MBP	R = -0.58, rho = -0.77	(Tardif et al., 2012)
SyMRI (qT1)	LFB	Rho = 0.63	(J. B. M. Warntjes et al., 2017)
qR1	PIXE (Fe, P, S)	R = 0.87	(Stüber et al., 2014)
qT2	MBP	R = -0.51, rho = -0.65	(Tardif et al., 2012)
qT2 (high field, 9.4T)	Polarised light (fiber structure)	R = 0.91	(Nieminen et al., 2001)
qR2*	PIXE (Fe, P, S)	R = 0.93	(Stüber et al., 2014)
qPD	MBP	R = -0.61, rho = -0.59	(Tardif et al., 2012)
SyMRI (qPD)	LFB	Rho = -0.73	(J. B. M. Warntjes et al., 2017)
MTR	MBP	R = 0.56, rho = 0.6	(Tardif et al., 2012)
QSM	PIXE (Fe, P, S)	R = 0.81	(Stüber et al., 2014)

2.4.2 Label-free histology

Recent development in vibrational microscopy allows the use of biomolecules as natural labels by measuring their molecular vibration spectra in living cells and tissues (Cheng & Xie, 2015). Specifically, coherent Raman scattering microscopy has emerged as a high-speed vibrational imaging platform. Single-frequency coherent anti-Stokes Raman scattering (CARS) and stimulated Raman scattering (SRS) microscopes have reached a video-rate imaging speed (Min et al., 2011).

CARS and SRS microscopy demonstrated the feasibility to obtain outstanding contrast to myelin (Evans et al., 2005; Fu et al., 2007; Imitola et al., 2011; Tian et al., 2016; Haifeng Wang et al., 2005). Despite a fiber orientation dependence of the CARS and SRS signals (Fu et al., 2008), corrections can be applied to obtain bias free myelin specific images (Duboisset et al., 2015; Fu et al., 2008). Overall, the SRS modality will be preferred over CARS, as it offer many advantages, such as: The absence of nonreasoning background, the shot-noise-limited sensitivity, the linear concentration dependence or even the existence of a point spread function that can be used to deconvolute the high resolutions images (Min et al., 2011).

While hyperspectral vibrational microscopy is demanding in terms of scan time, multi-color vibrational microscopy can be an interesting alternative to increase the specificity to the observed tissue. For example, the CH2 group, present in the lipid macromolecules, can be vibrationally excited at 2,845 cm-1; and the CH3 group, present in proteins can be excited at 2,950 cm-1. As the myelin is composed of ~20% of proteins and ~80% of lipids, one could compute the ratio of a two-color vibrational image at 2,845 and 2,950cm-1 to increase its specificity to myelin.

Another label-free microscopy technique of interest is the autofluorescence unmixing. As different tissues emit different autofluorescence spectra, it is possible to unmix the contribution of each tissue when a multi-spectral microscopy image is recorded. This technique has been shown to successfully separate the myelin, the axons and the background on multi-spectral, one photon confocal images (Christensen et al., 2014). The advantage of the method is the simplicity of implementation, as it is working on any confocal microscope equipped with a multispectral detector. The drawback is the potential lack of specificity due to an unperfect unmixing procedure.
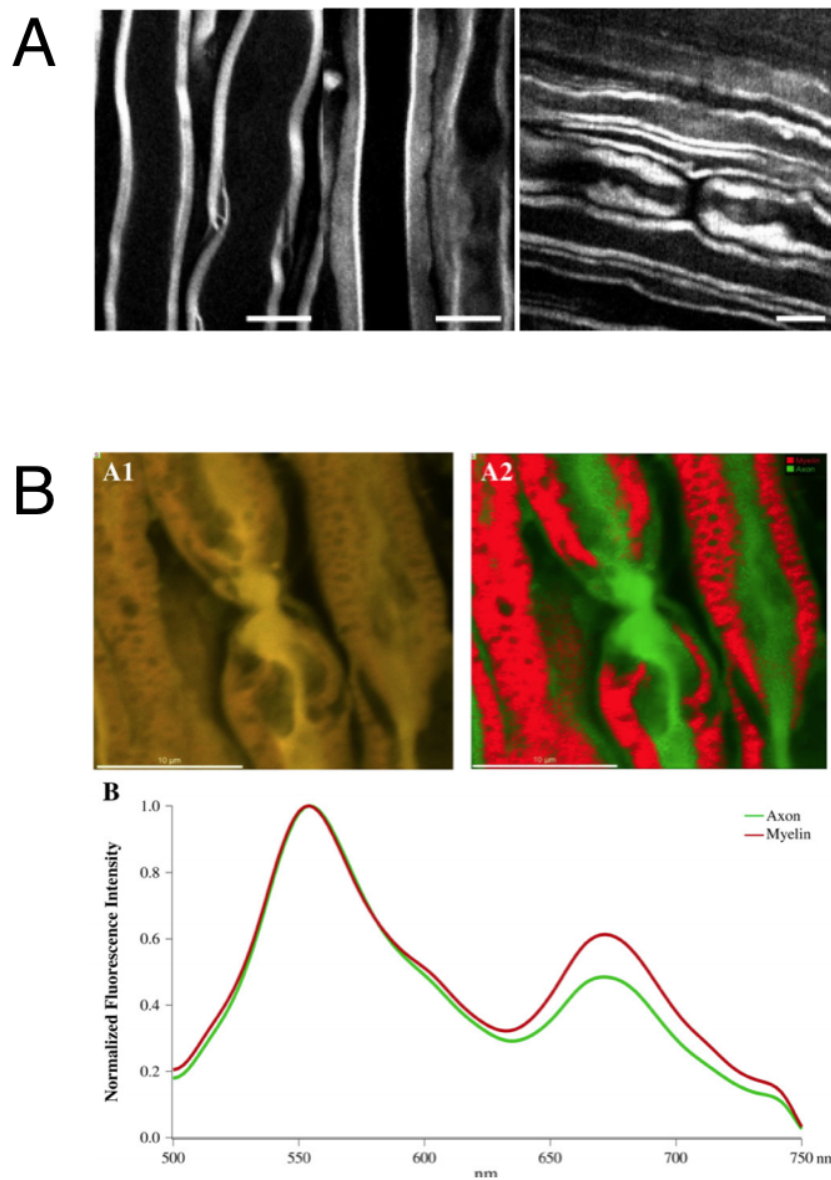
Figure 2.15 A: adapted from (Cheng & Xie, 2015). CARS imaging of chemically induced myelin sheath swelling in a rat spinal cord tissue. Scale bars, 10 micrometers. B: adapted from (Christensen et al., 2014). Principle of the hyperspectral autofluorescence unmixing. As different tissues emit different autofluorescence spectra, it is possible to unmix the different tissues from a stain-free hyperspectral autofluorescence image. Scale bars, 10 micrometers.

2.4.3 Fixation

Tissue fixation is another potential source of bias that can induce geometrical distortions such as tissue shrinkage. In theory, the two techniques described above (vibrational and autofluorescence) could work on fresh tissues. However, the challenge is in the sectioning step, which is more challenging on un-fixed tissues. Cryo-microtome sectioning can be a solution to image unfixed tissues (Frank et al., 2002). Tissue sectioning is also a source of geometrical distortions. While rigid distortions are easy to correct, non-linear distortions or damages are difficult to properly account for, leading to inaccuracies in the gold standard images. Recent tissue clearing techniques, such as CLARITY (Chung et al., 2013; Morawski et al., 2018) of purely chemical clearing (Quintá et al., 2015) could be use to avoid the sectioning step and thus reduce the slicing induced distortion as well as increase the 3D imaging speed.

CHAPTER 3   METHODOLOGY

Based on the literature review detailed in Chapter 2, the following conclusions can be made concerning the use of quantitative MRI to study neurodegenerative diseases such as MS:

- While structural MRI is the current method to diagnose MS, (e.g. one diagnosis criteria is the number of hyperintense lesions on FLAIR images), neurodegenerative diseases are characterized by several pathophysiological processes that can be monitored by quantitative MRI (such as demyelination, inflammation, neuroaxonal loss and degeneration can be observed with quantitative T1, T2*, MTR or diffusion MRI).

- Despite being sensitive to subtle pathophysiological mechanisms, quantitative MRI techniques often lack specificity: several types of change in the brain can affect the same quantitative metric (for example, demyelination and iron content affect T2* while demyelination and inflammation affect T1). The combination of several quantitative metrics can help to unmix the genuine contribution of each mechanism.

- Quantitative MRI often requires a long scan time (typically >30 min) and complex post processing method that limits its suitability to be used in a clinical context. Few commercial solutions proposing quantitative MRI solutions approved for clinics emerged in the last years. For example, Synthetic MRI, faster than "research" quantitative MRI (<10 min) but providing lower resolution images.

- The main challenges of these quantitative MRI sequences suited for clinics is their repeatability and reproducibility (intra- and inter-scanner), also called precision. To be able to compare quantitative measurements across subjects, scanners and center, we need a high precision on the quantification.

- To be able to do histological measurements with MRI, we need to go one step further. Even if a technique is precise: comparable across time, scanners and centers, there might still be a systematic bias between the measurement and the reality. To move forward from precision to accuracy, we need to validate or calibrate quantitative MRI with gold standard histological data.

Those points led me to formulate the following research questions:

"What is the potential of multimodal quantitative MRI to decipher subtle neurodegenerative mechanisms of MS, in a research and clinical setups. And what does it take to bring multimodal quantitative MRI to in-vivo histology?"

The main objective of my Ph. D. is to answer these questions by 1) developing methods to combine and analyze multimodal quantitative MRI in research and 2) clinical setups focused on MS, 3) validating the precision of the quantitative biomarkers in actual clinical conditions and 4) evaluating and testing a protocol to improve the accuracy of histological measurements derived from quantitative MRI. The specific objectives are:

Objective 1: Assess the sensitivity of multimodal research quantitative MRI metrics to detect subtle pathological changes in MS. **Hypothesis 1:** T1, T2* and DWI techniques are sensitive enough to detect early changes in MS patients.

Objective 2: Assess the sensitivity of clinical grade multimodal quantitative MRI metrics to differentiate two close neurodegenerative conditions. **Hypothesis 2:** A combination of SyMRI-derived quantitative biomarkers can differentiate MS from a close neurodegenerative condition: Hereditary Diffuse Leukoencephalopathy with Spheroids (HDLS).

Objective 3: Assess the repeatability and reproducibility of SyMRI quantitative maps over an exhaustive set of MRI vendors and field strength available in clinics. **Hypothesis 3:** Multi-scanner studies can be performed using SyMRI-derived quantitative biomarkers without correction.

Objective 4: Propose and test a calibration protocol to assess the accuracy of quantitative MRI techniques to histological measurements such as myelin content. **Hypothesis 4:** Label-free histology techniques (vibrational and/or autofluorescence) can be efficiently used as a myelin gold standard validation protocol.

3.1 Structure of the dissertation

Chapter 4 presents my research in advanced quantitative MRI techniques to study subtle changes in early MS patients. More specifically, I investigated the relation between cortical demyelination and structural changes in the neural networks of the patients. This study involved the use of high resolution T1 and T2* images, high angular resolution DWI, tractography and graph theory; and led to a publication in the scientific journal HBM (Human Brain Mapping) (Gabriel Mangeat et al., 2018).

G. Mangeat, A. Badji, R. Ouellette, C.A. Treaba, E. Herranz, T. Granberg, C. Louapre, N. Stikov, J.A. Sloane, P. Bellec, C. Mainero, J. Cohen-Adad. Changes in structural network connectivity in early-stage multiple sclerosis are associated with cortical demyelination. Human Brain Mapping, 2018, 39:2133-2146.

Chapter 5 presents my work in assessing clinical quantitative MRI to distinguish two close neurodegenerative conditions hardly distinguishable by clinicians: MS and HDLS. This work involved the development of quantitative biomarkers based on SyMRI acquisitions, as well as machine learning, data augmentation and validation pipeline. The study was published in the scientific journal JON (Journal Of Neuroimaging) (Gabriel Mangeat et al., 2020).

G. Mangeat, R. Ouellette, M. Wabartha, B. De Leener, M. Plattén, V. Danylaité Karrenbauer, M. Warntjes, N. Stikov, C. Mainero, J. Cohen-Adad, T. Granberg. Machine Learning and Multiparametric Brain MRI to Differentiate Hereditary Diffuse Leukodystrophy with Spheroids from Multiple Sclerosis. Journal of Neuroimaging. 2020, 30 (5): 674–82.

Chapter 6 presents my work on the repeatability and reproducibility of SyMRI-derived biomarkers. This work was done during a 4 months fellowship in the Karolinska University Hospital, Stockholm, Sweden, at my co-supervisor (Tobias Granberg) laboratory. We performed more than 200 scans with 9 different MRI from 3 vendors and 2 field strengths to assess the precision of the measurements. This study has just been submitted in the journal Neuroimage as a Technical Note.
G. Mangeat, R. Ouellette, M. Plattén, S. Petersson, H. Van Loo, A. Badji, N. Stikov, T. Granberg, J. Cohen-Adad. Repeatability and reproducibility of quantitative synthetic MRI across vendors and field strengths. Neuroimage, 2021. Submitted.

Chapter 7 presents my work related to the histological validation. A validation protocol has been established and tested, involving the scan of two pigs in vivo then ex vivo. Their spinal cord was

then extracted to perform histological analyses using the hyperspectral auto-fluorescence technique under a confocal microscope. This work was published in the peer reviewed international conference ISMRM.

G. Mangeat, H. Nami, N. Pinon, A. Foias, N. Stikov, T. Granberg, J. Cohen-Adad, (2019), Stain-free histology to validate quantitative MRI, ISMRM. E-Poster presentation.

In addition, I have worked closely with a colleague R. Ouellette (Ph. D. student of my co-supervisor Dr T. Granberg) on a study aiming to validate the myelin estimation of SyMRI by using ex-vivo histology techniques on Human samples with MS. My contribution to this work and our conclusions are presented here.

Finally, some valuable but unpublished work on stain-free hyperspectral auto-fluorescence, CARS, and SEM techniques for optical histology of myelin are summarized.

3.2 Additional publications, and research awards

The present dissertation introduces three original articles and one conference presentation that have been published/submitted during my Ph.D. project. Several additional publications have resulted from this project, as part of collaborations, or presented at international conferences. The following sections are listing this additional work:

3.2.1 Peer-reviewed articles

1. R. Ouellette, **G. Mangeat**, M. Plattén, Y. Forslin, Å. Bergendal, C. Andrada Treaba, V. Barletta, M. Warntjes, J. Cohen-Adad, S. Fredrikson, M. Kristoffersen Wiberg, F. Piehl, C. Mainero, and T. Granberg Multiple sclerosis demyelination beyond lesions: an in vivo and ex vivo study. 2021, *In manuscript.*

2. V. Barletta, E. Herranz, C. Treaba, A. Mehndiratta, R. Ouellette, **G. Mangeat**, T. Granberg, J. Sloane, E. Klawiter, J. Cohen-Adad, C. Mainero. Quantitative 7-Tesla imaging of cortical myelin changes in early multiple sclerosis. Multiple Sclerosis Journal. 2021, *submitted.*

3. R. Ouellette, **G. Mangeat**, I. Polyak, M. Warntjes, Y. Forslin, Å. Bergendal, M. Plattén, M. Uppman, C.A. Treaba, J. Cohen-Adad, F. Piehl, M.K. Wiberg, S. Fredrikson, C. Mainero, T. Granberg. Validation of Rapid Magnetic Resonance Myelin Imaging in

Multiple Sclerosis. Annals of Neurology. 2020, 87(5):710-724. doi: https://doi.org/10.1002/ana.25705

4. E. Herranz, C. Louapre, C. A. Treaba, S. T Govindarajan, R. Ouellette, **G. Mangeat**, M. L. Loggia, J. Cohen-Adad, E. C Klawiter, J. A. Sloane, C. Mainero. Profiles of cortical inflammation in multiple sclerosis by 11 C-PBR28 MR-PET and 7 Tesla imaging. Multiple Sclerosis Journal. 2020, 26(12):1497-1509. doi: 10.1177/1352458519867320

5. T. Granberg, Q. Fan, C.A. Andrada Treaba, R. Ouellette, E. Herranz; **G. Mangeat**, C. Louapre, J. Cohen-Adad, E. C. Klawiter, J. A. Sloane, C. Mainero, In vivo characterization of cortical and white matter neuroaxonal pathology in early multiple sclerosis, Brain, 2017.

3.2.2 Peer-reviewed conferences presentations

1. **G. Mangeat,** R. Ouellette, M. Plattén, S. Petersson, H. Van Loo, A. Badji, N. Stikov, J. Cohen-Adad, T. Granberg; Repeatability and reproducibility of quantitative synthetic MRI across vendors and field strengths; Organisation for Human Brain Mapping, 2020.

2. V. Barletta, E. Herranz, A. Treaba, A. Mehndiratta, R. Ouellette, **G. Mangeat**, J. Sloane, N. Mercaldo, J. Cohen-Adad, C. Mainero. In vivo characterization of cortical lesion demyelination and remyelination in early multiple sclerosis by quantitative 7 Tesla MRI. 2019. MULTIPLE SCLEROSIS JOURNAL (ECTRIMS). 25:124:124

3. **G. Mangeat**, R. Ouellette, M. Wabartha, V.D. Karrenbauer, M. Warntjes, N. Stikov, C. Mainero, J. Cohen-Adad, T. Granberg, (2018) Machine learning and rapid multi-parametric relaxometry can differentiate demyelinating disorders with high accuracy. ISMRM. Oral presentation.

4. **G. Mangeat**, R. Ouellette, M. Plattén, M. Warntjes, L.E. Nordin, N. Stikov, T. Granberg, J.Cohen-Adad, (2018) Accuracy and precision of Synthetic MRI. ISMRM. Poster presentation.

5. E. Herranz, C. A Treaba, C. Louapre, S. T Govindarajan, R. Ouellette, **G. Mangeat**, M. L Loggia, J. A Sloane, C. Mainero. The contribution of microglial activation to cortical demyelination in multiple sclerosis: a multimodal C-11-PBR28 MR-PET and quantitative

7 Tesla imaging study. 2019. MULTIPLE SCLEROSIS JOURNAL (ECTRIMS). 24:218:219

6. R. Ouellette, C.A. Treaba, T. Granberg, V. Barletta, E. Herranz, **G. Mangeat**, A. Mehndiratta, S. Tauhid, F. Yousuf, B. De Leener, S. Dupont, J.A. Sloane R. Bakshi, J. Cohen-Adad, C. Mainero, Characterization of multiple sclerosis grey and white matter pathology in the brain and spinal cord at 7 Tesla MRI. 2018. ECTRIMS. Poster.

7. R. Ouellette, M. Warntjes, Y. Forslin, Å. Bergendal, I. Polyak, **G. Mangeat**, M. Plattén, M. Uppman, J. Cohen-Adad, F. Piehl, M. Kristoffersen Wiberg, S. Fredrikson, C. Mainero, T. Granberg. Clinical and histological validation of rapid magnetic resonance myelin imaging in multiple sclerosis. 2018. ECTRIMS. Poster.

3.2.3 Research awards and funding

1. Invited speaker at the international conference ARSEP, in Paris (equivalent of French MS society, travel and expenses paid). **G. Mangeat**, T. Granberg, C. Mainero, J. Cohen-Adad, (2019) Changes in structural network and cortical demyelination in early multiple sclerosis assessed by 7T MRI. Annual MRI workshop of ARSEP.

2. NSERC travel fellowship, BESC-SEEMS, *Supplément pour études à l'étranger Michael-Smith*, $6k, 2020.

3. MITACS travel fellowship, *Globalink scholarship for abroad training*, $6k, 2019.

4. FRQNT Ph.D. fellowship, *Bourse de doctorat en recherche (BX2),* $70k, money declined, ranked 1st out of 24, 2019.

5. NSERC Ph.D. fellowship, *Bourse d'études supérieures du Canada Alexander-Graham-Bell- doctorat (BESC D)*", $70k, ranked 9th out of 160, 2019.

6. *Genie en Image* Prize, 1st place for the best scientific image of Polytechnique (Figure 2.1), $500, 2018.

CHAPTER 4 ARTICLE 1: CHANGES IN STRUCTURAL NETWORK ARE ASSOCIATED WITH CORTICAL DEMYELINATION IN EARLY MULTIPLE SCLEROSIS

Title: Changes in structural network are associated with cortical demyelination in early multiple sclerosis

Authors: Gabriel Mangeat (1,3), Atef Badji (1,2), Russell Ouellette (3,5), Constantina A. Treaba (3,4), Elena Herranz (3,4), Tobias Granberg (3,4,5), Céline Louapre (3,4), Nikola Stikov (1,6), Jacob A. Sloane (4,7), Pierre Bellec (2), Caterina Mainero (3,4,*), Julien Cohen-Adad (1,2,*)

Affiliations:

(1) Institute of Biomedical Engineering, Polytechnique Montreal, Montreal, QC, Canada

(2) Functional Neuroimaging Unit, CRIUGM, Université de Montréal, Montreal, QC, Canada

(3) Department of Radiology, Athinoula A. Martinos Center for Biomedical Imaging, MGH, Charlestown, MA, USA

(4) Harvard Medical School, Boston, MA, USA

(5) Department of Clinical Neuroscience, Karolinska Institutet, Stockholm, Sweden

(6) Montreal Health Institute, Montreal, QC, Canada

(7) Department of Neurology, Beth Israel Deaconess Medical Center, Boston, MA, USA

(*) Both last co-authors have jointly supervised this work

4.1 Abstract

The aim of this study was to investigate the interplay between structural connectivity and cortical demyelination in early multiple sclerosis.

27 multiple sclerosis patients and 18 age-matched controls underwent two MRI scanning sessions. The first was done at 7T and involved acquiring quantitative T1 and T2* high-resolution maps to estimate cortical myelination. The second was done on a Connectome scanner and consisted of acquiring high angular resolution diffusion-weighted images to compute white matter structural connectivity metrics: strength, clustering and local efficiency. To further investigate the interplay between structural connectivity and cortical demyelination, patients were divided into four groups according to disease-duration: 0–1 year, 1–2 years, 2–3 years and >3 years. ANOVA and Spearman's correlations were used to highlight relations between metrics.

ANOVA detected a significant effect between disease duration and both cortical myelin ($p = 2 \times 10^{-8}$) and connectivity metrics ($p < 10^{-4}$). We observed significant cortical myelin loss in the shorter disease-duration cohorts (0–1 year, p=0.0015), and an increase in connectivity in the longer disease-duration cohort (2–3 years, strength: p=0.01, local efficiency: p=0.002, clustering: p=0.001). Moreover, significant covariations between myelin estimation and white matter connectivity metrics were observed: Spearman's Rho correlation coefficients of 0.52 (p=0.0003), 0.55 (p=0.0001) and 0.53 (p=0.0001) for strength, local efficiency, and clustering, respectively.

An association between cortical myelin loss and changes in white matter connectivity in early multiple sclerosis was detected. These changes in network organization might be the result of compensatory mechanisms in response to the ongoing cortical diffuse damage in the early stages of multiple sclerosis.

4.2 Introduction

Multiple sclerosis (MS) is an inflammatory and neurodegenerative disease of the central nervous system characterized by white matter (WM) demyelination (Noseworthy et al., 2000) (Poonawalla et al., 2008). Indeed, it has traditionally been regarded as a primarily WM disease. However, thanks to advances in immunopathology and magnetic resonance imaging (MRI), it is becoming clear that there is also extensive involvement of deep and cortical gray matter (GM) in multiple sclerosis (Pirko et al., 2007) (Kilsdonk et al., 2016)(Pitt et al., 2010)(Kilsdonk et al., 2016). The hallmark of the cortical pathology is demyelination, frequently associated with microglial activation, axonal transection and neuronal and synaptic loss ((Peterson et al., 2001)(Wegner et al., 2006)(Peterson et al., 2001). Over the past decade, a number of MRI studies have attempted to clarify the role of cortical demyelination from the earliest stages of multiple sclerosis, but conventional MRI methods lack the necessary sensitivity (Lucchinetti et al., 2011). This lack of sensitivity of MRI to cortical demyelination in the early stages of the disease is due, in part, to the different pathophysiology of the GM compared with the WM lesions, their small size, and the relatively weak MRI contrast between demyelinated cortex and adjacent normal-appearing cortical tissue (Trapp et al., 1998) (Wegner et al., 2006). Advances in ultra-high-field MRI have demonstrated that dedicated imaging protocols, including gradient echo (GRE) T_2* protocols, can significantly improve *in vivo* visualization of cortical demyelinating lesions in multiple sclerosis (Mainero et al., 2009) (Cohen-Adad et al., 2011), and that the use of quantitative T_2* to map cortical integrity as a function of cortical depth can reveal changes in myelin content beyond visible focal cortical lesions (Mainero et al., 2015)(Govindarajan et al., 2015). These findings have been corroborated by histopathological-MRI correlations in *ex vivo* samples from patients with multiple sclerosis imaged at 7T (Kilsdonk et al., 2016)(Pitt et al., 2010)(Kilsdonk et al., 2016)). Despite its sensitivity to myeloarchitecture, T_2* is influenced by several confounds, such as B0 field inhomogeneities (Hernando et al., 2012), fiber orientation with respect to B0 (Cohen-Adad et al., 2012), and iron levels in tissue (Fukunaga et al., 2010). Hence, combining T_2* with another measure sensitive to myelin would allow greater confidence in assessing the degree of myelination. The MRI longitudinal relaxation time, T_1, has been shown to be closely related to myelin content *in vivo* (Koenig et al., 1990) and *ex vivo* (Mottershead et al., 2003) (Schmierer et al., 2004), showing for example a high correlation (r = 0.89) with myelin content in fixed brain tissue (Schmierer et al.,

2008) (Stüber et al., 2014). Recently, high-resolution T_1 maps were used to study the myeloarchitecture of the entire cortical ribbon (Sereno et al., 2013) (Lutti et al., 2014).

In the present study, we combined T_2* and T_1 cortical mapping in order to extract the shared myelin-related signal and thus create a composite map called the combined myelin estimation (CME) map. The CME map has been shown to be more specific to myelin than either T_2* or T_1 maps alone (G. Mangeat, Govindarajan, Mainero, et al., 2015; G. Mangeat, Louapre, et al., 2015)

Growing understanding of normal brain network organization has made it possible to measure network changes in neurological diseases such as multiple sclerosis (Stam, 2014). The development of sophisticated post-processing methods, such as diffusion tensor imaging (DTI)-based fiber tractography, has driven the development of structural connectivity techniques, which serve to define and quantify anatomical links between GM regions via WM fiber pathways (Guye et al., 2010). DTI-based evaluation of structural network connectivity showed that a reduction of network efficiency in multiple sclerosis patients correlated significantly with physical disability, disease duration and total WM lesion load (Li et al., 2013; Shu et al., 2011).

The pathological interactions (involving demyelination, axonal injury and repair, for example) in the early stages of multiple sclerosis are still largely unknown (Llufriu et al., 2017). Thus, characterization of the brain's structural network might improve our understanding of the early pathophysiology of this disease. Network science and graph theory applied to diffusion MRI data offer powerful tools for mapping and predicting patterns in pathophysiological progression (Fornito et al., 2015), while quantitative T_1 and T_2* provide robust estimators of cortical myelin content (Cohen-Adad et al., 2012; Deistung et al., 2013; Mainero et al., 2015)(Dinse et al., 2013; Lutti et al., 2014)(Cohen-Adad et al., 2012; Deistung et al., 2013; Mainero et al., 2015)(Dinse et al., 2013; Lutti et al., 2014).

In this study, we set out to investigate the potential interplay between cortical demyelination and abnormalities in structural connectivity. We hypothesized that cortical demyelination is associated with disrupted structural connectivity in early multiple sclerosis.

4.3 Methods

4.3.1 Subjects

This cross-sectional study included 27 subjects with relapsing-remitting multiple sclerosis (RRMS) (age=39.0±7.8 years, 22 females; mean disease duration 2.5±1.0 years; median Expanded Disability Status Scale (EDSS) score=1 (range 0–4); mean Multiple Sclerosis Severity Scale (MSSS) score = 3.6±2.2)) and 18 healthy controls (age=38.0±11.2 years, 10 females). Table 1 in the Supplementary Material shows the demographics and clinical characteristics of all the participants with multiple sclerosis.

The general inclusion criteria were: age between 18 and 60 years, no significant medical history (other than multiple sclerosis for the patients) and absence of MRI contraindications. The patients' eligibility criteria included a diagnosis of RRMS (Polman et al., 2011) (Lublin et al., 2014) with a disease duration ≤ 5 years, use of stable disease-modifying treatment or no treatment for at least 3 months, no clinical relapse within the 3 months prior to enrolment, and no corticosteroid use for at least 1 month prior to enrolment.

Informed consent was obtained from each participant in this study, and the protocol was approved by the local ethics committee.

4.3.2 MRI data acquisition

All participants were scanned on a 3T whole-body scanner (Siemens Healthcare, MAGNETOM CONNECTOM, maximum gradient strength per channel=300mT/m, 64-channel head coil) to obtain measures of structural connectivity from diffusion-weighted images (DWIs, single refocusing spin echo echo-planar imaging sequence, 1.5 mm isotropic, TR=8800 ms, TE=57 ms, δ=12.9 ms, Δ=21.8 ms, 3 shells: 1k/5k/10k s/mm^2, number of directions: 64/128/128, total TA=53 min). In addition to the diffusion protocol, a T$_1$-weighted image was acquired at 3T for cortical surface reconstruction using a multi-echo MPRAGE (magnetization prepared rapid acquisition GRE) sequence (1 mm isotropic, TR=2530, TE=[1.15, 3.03, 4.89, 6.75] ms, TI=1100 ms) (van der Kouwe et al., 2008). Finally, a FLAIR (fluid-attenuated inversion recovery) image (1 mm isotropic, TR/TE/TI=5000/393/1800 ms) was acquired at 3T in order to segment the WM lesions. The diffusion volumes of three multiple sclerosis patients could not be used due to strong motion

artifacts (N=2) or technical issues during the diffusion scan (N=1). Hence, a total of 24 multiple sclerosis patients and 18 healthy controls (HC) were further considered for the 3T analysis.

Most of these participants underwent another scanning session a maximum of one week later. This was performed on a 7T whole-body scanner (Siemens Healthcare, Erlangen, Germany) using a 32-channel receive head coil. The protocol included a GRE sequence to compute T_2* maps (0.5 mm isotropic, TR=3680 ms, TE=3.12+3.32*[1..6] ms, 6 echoes, TA=40 min) and a dual magnetization-prepared rapid GRE sequence (MP2RAGE, (José P. Marques et al., 2010)) to compute T_1 maps (0.75 mm isotropic, TR/TE/TI=5000/2.93/[900-3200] ms, flip angles=4° and 5°, TA=10 min). Not all the baseline participants could be scanned: two multiple sclerosis patients and one healthy control did not fit inside the coil, while two patients and four healthy controls dropped out of the study. Furthermore, the scans of a further five multiple sclerosis patients had to be discarded due to strong motion artifacts either during the T_1 or the T_2* acquisitions. Hence, a total of 18 multiple sclerosis patients and 13 healthy controls were included in the 7T analysis.

Lesions were manually segmented on the basis of the consensus of two experienced raters (A.C.T. and C.M.). Cortical lesions were segmented on 7T images and classified as intracortical or leukocortical as previously detailed (Louapre et al., 2015). WM lesions were identified first on 3T FLAIR images (TA = 6:32 min) and then under the complementary guidance of 7T T_2* images.

4.3.3 Quantitative MRI analysis

4.3.3.1 Surface-based analysis

The cortical surface of each subject was extracted using FreeSurfer 5.3.0 (http://freesurfer.net) from the 3T T_1-weighted images after correction for gradient non-linearity-induced distortions. We used the 3T rather than the 7T images because the 7T scanner produced more B1+ inhomogeneities, potentially yielding more errors in the segmentations. Each surface reconstruction was carefully inspected and topographical errors caused by lesions were semi-manually corrected with lesion in-painting. The 7T quantitative T_1 and T_2* volumes were also corrected for gradient non-linearity distortions and then registered to the subject's surface using rigid (6 degrees of freedom, DOF) and affine (12 DOF) surface registration methods. Finally, T_1 and T_2* volumes were sampled at mid-

cortical depth along the cortex and projected to the FreeSurfer average (*fsaverage*) space. Cortical thickness was computed to correct both metrics for partial volume effects on a per-vertex level.

4.3.3.2 Combination of 7T quantitative maps

A spatial ICA (independent component analysis) was applied to the data to extract the myelin-specific signal shared by both metrics. This procedure produces a composite map, the CME map, that contains the myelin information from both the T_2* and T_1 maps Figure 4.1. The CME map has been suggested to be more specific to myelin content than the T_2* and T_1 maps separately ((Badji et al., 2016; Gabriel Mangeat et al., 2016)(G. Mangeat, Govindarajan, Mainero, et al., 2015)(Badji et al., 2016; Gabriel Mangeat et al., 2016). In this study we used CME maps to study the cortical demyelination occurring in multiple sclerosis.
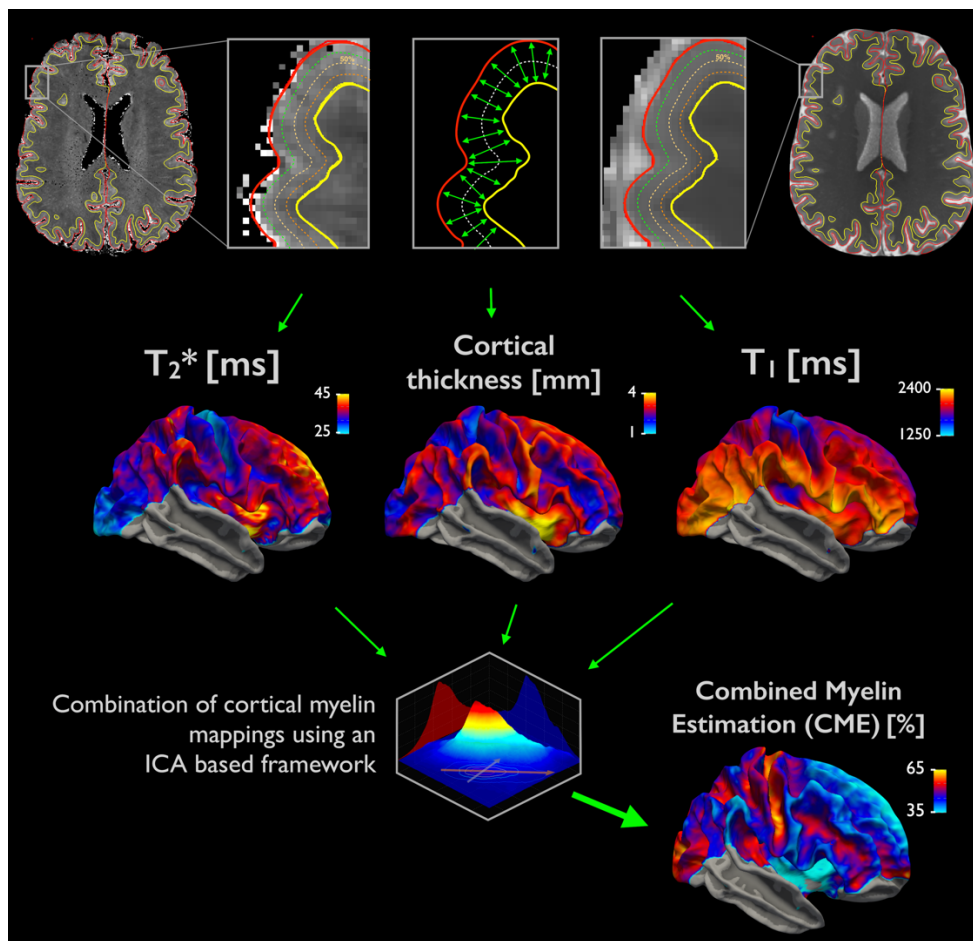
Figure 4.1 Cortical myelin estimation framework from T1 and T2* quantitative metrics at 7T. Combined myelin estimation (CME) was used aimed to estimate a cortical myelination trough

combination of T1 and T2* metrics. First, quantitative T1 and T2* data were acquired at 7T. Using the FreeSurfer pipeline, data were sampled at the mid-cortical depth and then registered to a common surface template. An independent component analysis (ICA) was then used to extract the myelin information shared by T1 and T2* as previously described in (G. Mangeat, Louapre, et al., 2015). Figure modified from (G. Mangeat, Louapre, et al., 2015).

4.3.3.3 Scan-rescan reproducibility of the 7T framework

To assess the reliability of the CME map as a biomarker of cortical demyelination, the scan-rescan reproducibility of the 7T metrics was assessed in four healthy volunteers. This was done by acquiring the 7T scan twice on the same day, with a short interval between the two imaging sessions during which the subjects were repositioned. The surface-based pipeline applied to the scan and the rescan datasets was exactly the same. For T_1, T_2* and the CME metrics, the absolute difference in diffusion metrics was calculated by subtracting map 1 from map 2. The within-subject coefficient of variation was calculated according to the following equation: standard deviation (scan 1 and scan 2) / mean (scan 1 and scan 2). The spatial correlations between the scan and rescan maps were computed. The results are presented in Supplementary Materials 4.

4.3.4 Reconstruction of structural networks

4.3.4.1 Whole-brain tractography

Standard preprocessing of the diffusion-weighted images included correction for gradient nonlinearity, eddy current distortions and subject motion. DSI-Studio (http://dsi-studio.labsolver.org) was used to perform probabilistic fiber tractography using GQI (generalized q-sampling imaging) reconstruction (Wang et al., 2015). Diffusion-weighted images were reconstructed with a diffusion sampling length ratio of 1.25, as recommended in the literature (Yeh et al., 2010). This length ratio defines the radius of the diffusion spins included in the ODF (orientation distribution function) estimation. Then, whole-brain tractography was conducted with whole-brain seeding. A default step size (0.75 mm), angular threshold (60°) and quantitative anisotropy threshold (0.045–0.060%) were used.

4.3.4.2   Anatomical parcellation

Due to the high anatomical variability of the cortical ribbon across individuals ((Hutton et al., 2008)(G. Mangeat, Govindarajan, Mainero, et al., 2015)(Hutton et al., 2008), available volumetric Brodmann atlases, such as the Montreal Neurological Institute (MNI) atlas, did not properly fit the cortical ribbon of our subjects after a 12-DOF registration. To overcome this problem, we here propose a new method able to produce volumetric GM parcellation accurately registered to each subject's cortical ribbon. First, the PALS-B12 Brodmann area (BA) surface atlas (Van Essen, 2005) was projected onto each subject's native space using FreeSurfer (~130,000 DOF deformation). The PALS-B12 BA (Van Essen, 2005) was chosen in view of previous studies that showed homogenous myeloarchitecture within functional areas (Abdollahi et al., 2014; Bock et al., 2009; Nieuwenhuys, 2013). Second, the surface atlases were converted to volumetric atlases and expanded to fill the entire cortical depth (Figure 4.2 B). These steps are further detailed in Supplementary Material 3, and the script that was used to generate these results is shared as open source (https://github.com/neuropoly/surface_based_tools/tree/master/atlas_generation).   Figure   4.2 illustrates the overall framework used to compute the connectivity matrix.
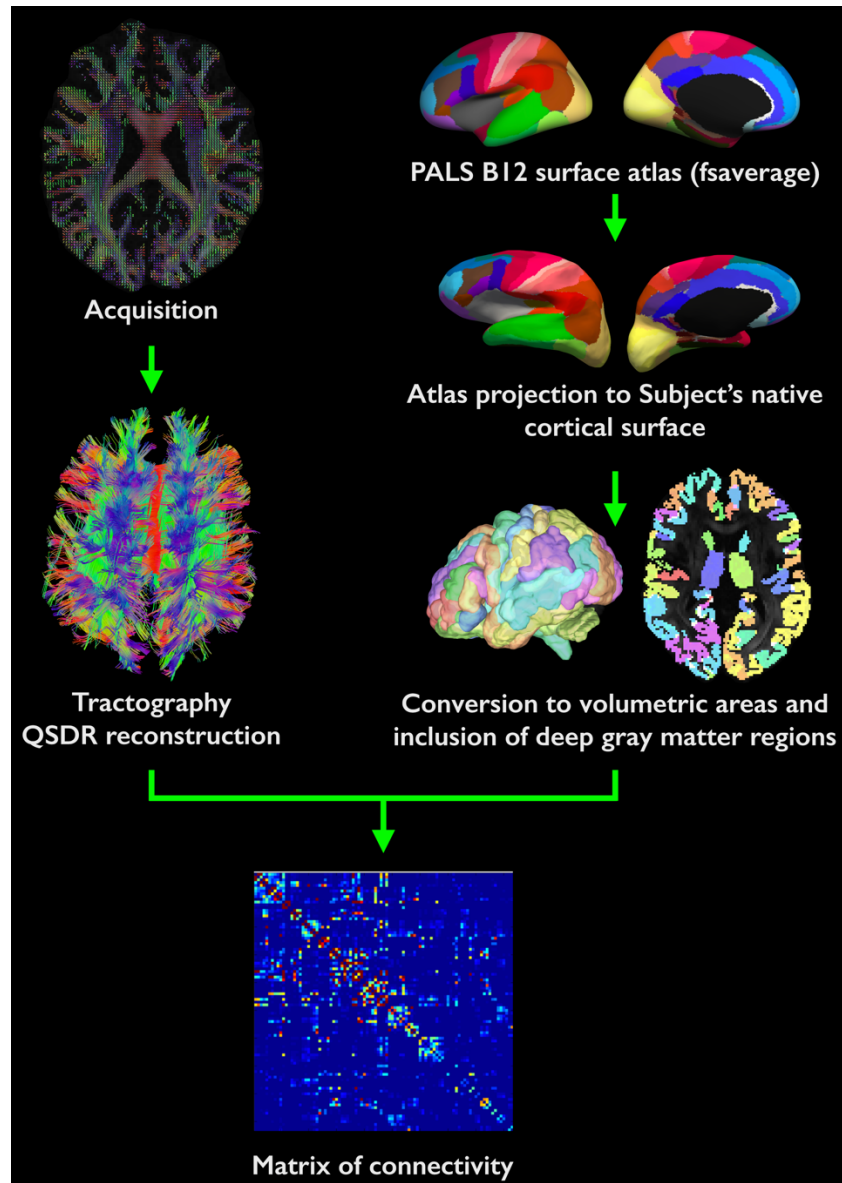
Figure 4.2 Cortical-based connectomics from 300mT/m diffusion imaging. A: Diffusion images were acquired on a 3T scanner with 3 shells (b-values 1k, 5k, 10k s/mm2), then whole-brain tractography was conducted using GQI reconstruction in DSI-studio. B: The PALS-B12 Brodmann atlas was projected onto the subject's space, then converted to a volumetric atlas in order to build the matrix of connectivity across ROIs.

4.3.4.3 Matrix stability analysis

To assess the reliability of the connectivity data and improve the structural coherence of the parcellation, a bootstrap analysis was performed, using BASC (bootstrap analysis of stable clusters, (Bellec et al., 2010), to estimate the stability of the connectivity matrices across subjects; BASC proceeds by repeating a clustering operation (here, a hierarchical agglomerative clustering with Ward's criterion (Ward, 1963)) 1000 times, and computes the frequency with which each pair of regions was assigned to the same cluster, called pairwise stability. The set of all pairwise stability measures form a region × region matrix, which is in turn fed into a clustering procedure to derive consensus clusters. The consensus clusters are composed of regions with a high average probability of being assigned to a certain cluster across all replications, hence the name consensus. The number of clusters was determined to maximize the intra-cluster stability while keeping an optimal functional distribution. Here, the random sub-sampled dataset was composed of 13 healthy controls, 13 multiple sclerosis patients, 1000 iterations (Bellec et al., 2010). The stable clusters were then used as a basis for further network and statistical analyses.

4.3.4.4 Network analysis

Connectivity matrices were computed by multiplying fiber counts and mean fractional anisotropy (FA) in order to avoid a fiber count bias in low FA areas (Betzel et al., 2014). Graph analysis was performed using the Brain Connectivity Toolbox (https://sites.google.com/site/bctnet/) in order to express node properties of the WM structural network. Whole-brain graph theory measures include node strength, local efficiency and clustering (Mohan et al., 2016).

Node **strength** is defined as the sum of the weights (w_{ij}) of all the connections between a particular node and the remaining nodes in the network. The average node strength of the network is the overall arithmetic average of the strength of all the individual nodes in the network.

$$Strength\ of\ i, k_i^w = \sum_{j \epsilon N} w_{ij}$$

The **local efficiency** of a node ($E_{loc,i}$) corresponds to the efficiency of information transfer among the neighbors of a particular node. The local efficiency is directly proportional to the clustering

coefficient of the node and is calculated from the functional distance matrix. It is calculated in the subgraph of the direct neighbors of i:

$$E_{loc}^w = \frac{1}{2} \sum_{j \in N} \frac{\sum_{j,h \in N, j \neq i} (w_{ij} w_{ih} [d_{jh}^w N_i]^{-1})^{1/3}}{k_i(k_i - 1)}$$

where $E_{loc,i}$ is the local efficiency of the node i, and d_{jh} (N_i) is the shortest path between j and node h that contains only direct neighbors of node i.

The **clustering** coefficient of a node (C_i) represents the degree of local connectivity of the node with its neighbors. Random networks have low average clustering compared with complex networks, the latter having higher clustering associated with locally specialized processing (Bullmore & Sporns, 2009).

This metric is calculated by estimating the number of triangles around the node i:

$$C_i = \frac{1}{k_i(k_i - 1)} \sum_{j,h \in N} \frac{(w_{ij} + w_{ih})}{2} a_{ij} a_{ih} a_{jh}$$

where k_i denotes the strength of node i, defined as $S_i = \sum_j w_{ij}$, and a_{ij} is an element of the underlying binary adjacency matrix.

4.3.5 Statistical analysis

4.3.5.1 Prediction of clinical measures

Multiple linear regressions were run using CME (whole GM average), strength, local efficiency, clustering (whole WM average) and age as regressors, and EDSS, MSSS and disease duration as dependent variables. The accuracy of the regressions was assessed using leave-one-out cross-validation (Cook & Weisberg, 1982; Good & Hardin, 2003; Kunter et al., 2005).

4.3.5.2 Disease duration analysis

In the light of a recent study showing associations between cortical volumetric measures and connectome metrics across disease duration (Fleischer et al., 2016), we decided to further analyze our data by dividing the patients into four groups on the basis of their disease duration: 0–1 year (n=4, mean age 35.0±8.4, four females), 1–2 years (n=6, mean = 35.7±8.2, five females), 2–3 years (n=6, 39.8±8.0, four females), 3+ years (n=8, 42.6±5.0, six females).

The healthy controls were also divided into four groups that matched the average age of each of the patient groups: group 1: n=8, mean age 31.5±2.0, four females, group 2: n=10, mean age 32.5±4.2, six females, group 3: n=10, mean age 36.1±6.8, seven females, group 4: n=12, mean age 38.8±8.7, eight females. The stratification was done using the method of nearest neighbor matching with replacement (King et al., 2011; Stuart, 2010) of type N+4:N (Magnoni et al., 2015).

4.3.5.2.1 Disease duration analysis: whole-brain analysis

The patient groups were compared with their respective age-matched healthy control groups to assess the initial direction of the changes in network connectivity and myelin loss within the cortex.

For each metric (cortical myelin content, strength, local efficiency and clustering respectively) and for each group, box plots as well as mean values and standard deviation were computed. For each cluster and each group, the variation rate, corresponding to the percentage normalized difference between multiple sclerosis patients and healthy controls, was calculated as follows: 100 * (metric_MS - metric_HC) / metric_HC.

ANOVAs were performed to determine whether disease duration had a significant effect. For each metric, a one-way ANOVA was computed as follows: the observations were the variation rate for each cluster (n=11) and the category was the disease duration group (n=4). For each metric and

each group, the difference between multiple sclerosis patients and healthy controls was tested using a general linear model, including age and gender as regressors.

4.3.5.2.2 Disease duration analysis: cortical cluster-based analysis

Student's *t*-tests were computed between the multiple sclerosis and matched healthy control groups. Moreover, bilateral *t*-tests on variation rates, paired for clusters, were computed between adjacent disease duration groups: G1-G2, G2-G3, G3-G4. An additional *t*-test was computed between the groups showing the maximum variation: G1-G3. Significance thresholds were corrected for multiple comparisons within metrics.

The spatial relation between the variation rate of cortical myelin content and the variation rate of each of the connectivity metrics in stable clusters (node strength, clustering and local efficiency) was tested using Spearman's Rho correlation coefficients.

4.4 Results

4.4.1 Clustering and parcellation

The bootstrap analysis of the consensus clustering identified 15 stable clusters, which are shown in Figure 4.3. Interestingly, most clusters were associated with a distinct functional area, for example cluster #3 with the right visual cortex, and cluster #4 with the motor cortex (for a list of all the clusters, see the table in Supplementary Material 5). **Moreover, the stability of clusters is high (>95%), which reveals a good reproducibility in cluster assignment.**

Only the clusters with both CME and connectivity metrics were further considered for statistical analyses, therefore, clusters corresponding to the deep nuclei where CME could not be computed were discarded. Note that deep GM clusters were essential to compute the connectivity metrics as they are important hubs of the network. Moreover, clusters where CME was unreliably computed due to excessive susceptibility artifacts in the temporal lobe (J. P. Marques & Bowtell, 2005) were also discarded. The remaining clusters were numbered 1 to 11.
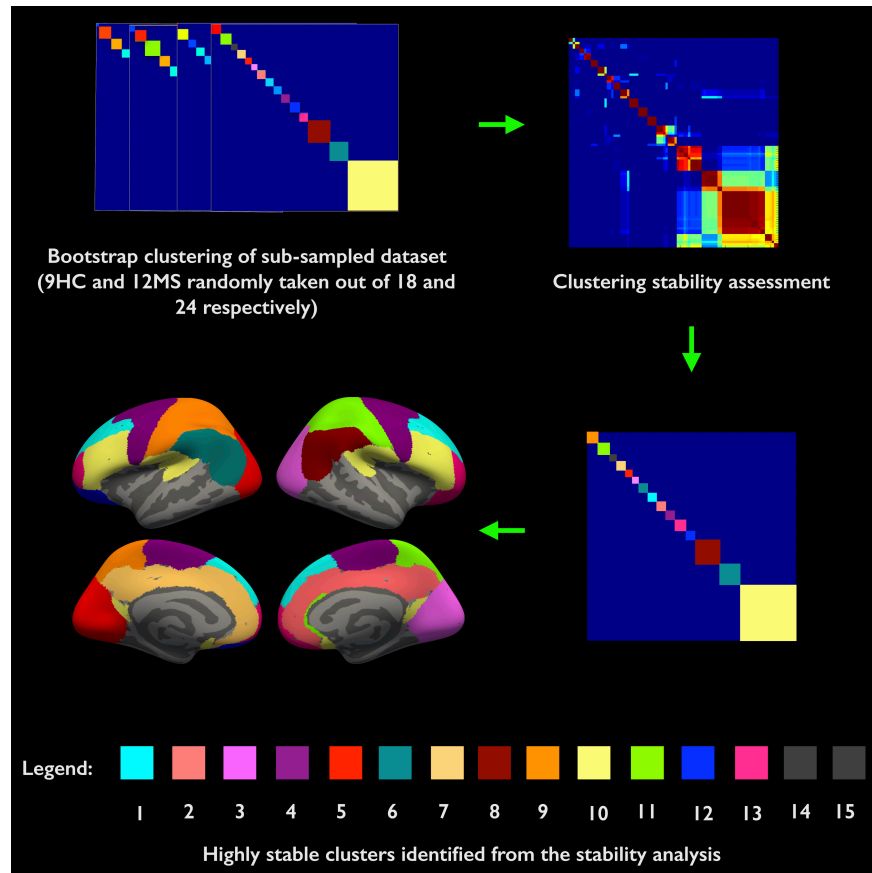
Figure 4.3 Stability of the matrices after a bootstrap analysis, implemented in BASC (Bellec et al., 2010). BASC proceeds by repeating a clustering operation (here, a hierarchical agglomerative clustering with Ward's criterion (Ward, 1963)) 1000 times, and computes the frequency with which each pair of regions was assigned to the same cluster, called pairwise stability. The set of all pairwise stability measures forms a region × region matrix, which is in turn fed into a clustering procedure to derive consensus clusters. The consensus clusters are composed of regions with a high average probability of being assigned to a certain cluster across all replications, hence the name consensus. Here, the random sub-sampled dataset was composed of 13 healthy controls (HC) and 13 multiple sclerosis patients (MS) subjects. The stability analysis generated 15 highly stable GM regions. Each color corresponds to a different cluster presented in Table 2 in Supplementary Materials.

4.4.2 Statistical analysis

4.4.2.1 Prediction analyses

Figure 4.4 shows the results of the regression analyses for EDSS, MSSS and disease duration. The global accuracy (calculated for all data, shown as blue in Figure 4.4) was 0.5 (EDSS), 1.2 (MSSS) and 0.7 years (disease duration), corresponding to an absolute mean error of 20.1% (EDSS), 17.3% (MSSS) and 13.6% (disease duration). The cross-validated accuracy (calculated for leave-one-out data, shown as red in Figure 4.4) was 0.7 (EDSS), 1.6 (MSSS) and 1 year (disease duration), corresponding to an absolute mean error of 29.1% (EDSS), 25.6% (MSSS) and 20.9% (disease duration). The Pearson correlation coefficients between each independent variable and their regressions were respectively: r=0.67, $p<10^{-16}$ for EDSS, r=0.67, $p<10^{-16}$ for MSSS and r=0.71, $p<10^{-16}$ for the disease duration.

We note that EDSS and MSSS show an error evenly distributed around the identity axis (magenta dashed line) while disease duration seems to be overestimated for low values (0–1) years, well estimated from 1 to 4 years, and underestimated after 4 years. The overestimation of the patients with a disease duration of 0–1 years could be due to the fact that they are affected by definite multiple sclerosis, which is, by definition, clinically and/or radiologically severe, as they already fulfill dissemination in space and dissemination in time criteria.
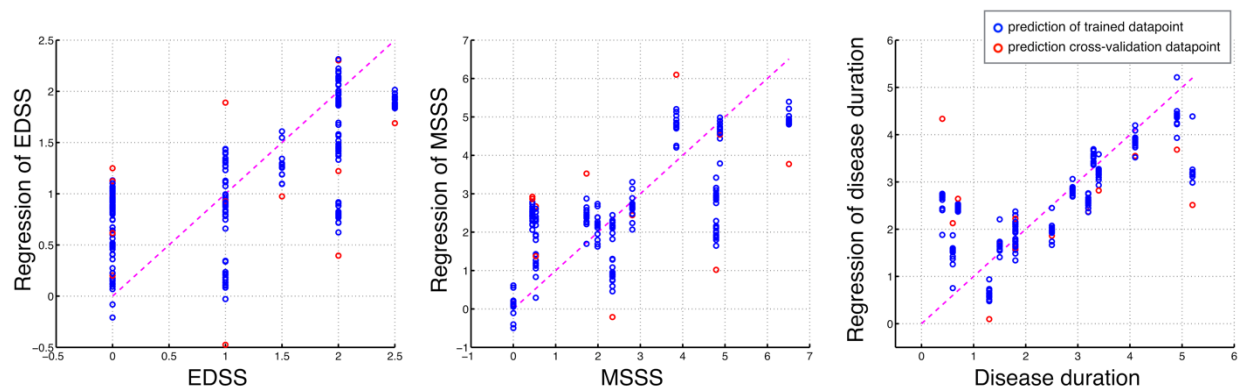
Figure 4.4 Results of the prediction analyses of clinical measures. Multiple linear regressions were run using CME (whole GM average), strength, local efficiency, clustering (whole WM average) and age as regressors, and EDSS, MSSS and disease duration as dependent variables. The predicted values of EDSS, MSSS and disease duration are plotted in the y axes while the true corresponding values are in the x axes. Leave-one-out bootstraps assessed the robustness of the predictions. In order to highlight the variability of the predicted values across the different

training datasets, the data used in the training (blue dots) and the data not used in the training (red dots) were plotted in the graph at each cross-validation step. Hence, each red dot corresponds to one patient. All EDSS and MSSS scores are well predicted (r=0.67, p<10-16, r=0.67, p<10-16 respectively) while disease duration is very well predicted (r=0.71, p<10-16).

4.4.2.2 Disease duration analysis: whole-brain

After dividing the multiple sclerosis patients by disease duration, clinical scores and lesion volumes were calculated for each group, as shown in Table 4.1.

Figure 4.5 shows box plots and mean values for cortical myelin content and connectivity values for each of the groups, i.e. the four multiple sclerosis and the four healthy control groups Interestingly, the variation of MRI metrics values across the multiple sclerosis groups follows the same trends across the metrics, with group 1 showing the lowest values and group 3 showing the highest. The ANOVAs showed that disease duration has an effect on CME ($p=2\times10^{-8}$), on for strength ($p=9\times10^{-5}$); on local efficiency ($p=8\times10^{-7}$), and on clustering ($p=6\times10^{-6}$). Supplementary material 2 includes more details about each of these values and also gives clinical scores and lesion volumes in the four patient groups.

Table 4.1 Clinical scores and lesion volumes averaged for each disease duration group. GM lesions were subdivided into intracortical (IC) and leukocortical (LC) lesions. Note that IC lesion volume + LC lesion volume = GM lesion volume.

	Group 1	Group 2	Group 3	Group 4
Disease duration [years]	0–1	1–2	2–3	3+
EDSS	2 ± 0.8	0.9 ± 0.7	1.3 ± 1.1	2.1 ± 0.8
MSSS	5.7 ± 2.5	2.4 ± 1.7	3 ± 2.3	4.1 ± 1.6

| Lesion volume [mm³] | WM : 425 ± 190
 GM : 75 ± 58
 IC : 59 ± 67
 LC : 16 ± 28 | WM : 626 ± 308
 GM : 475 ± 473
 IC : 314 ± 395
 LC : 160± 261 | WM : 445 ± 449
 GM : 97 ± 67
 IC : 64 ± 66
 LC : 32 ± 28 | WM : 1780 ± 1340
 GM : 457 ± 716
 IC : 333 ± 544
 LC : 124 ± 182 |
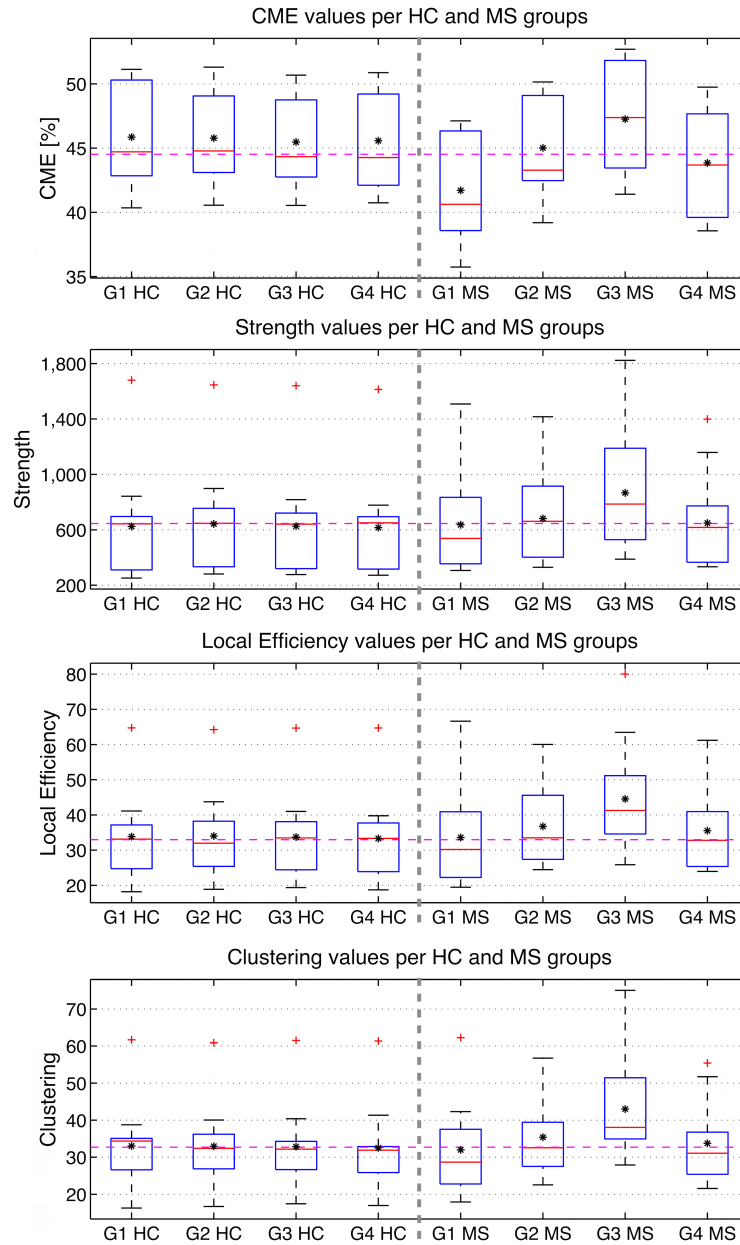
Figure 4.5 Box plots and mean values for cortical myelin content and connectivity values of strength, local efficiency and clustering for each group. The black stars represent group means and the purple dashed lines represent the global healthy control (HC) means. Interestingly, the variation of metric values across the multiple sclerosis (MS) groups follows the same trends across metrics, with group 1 showing the lowest values and group 3 showing the highest.

4.4.2.3 Disease duration analysis: cortical cluster-based

To further investigate the interplay between CME, connectivity changes and disease duration, the variation rates (i.e. relative changes between multiple sclerosis patients and healthy controls) were computed for each stable cluster identified by the structural connectivity clustering. Figure 4.6 shows the outcome of this analysis for each disease duration group. Each stable cluster is represented by a specific marker (see legend in the top-right of the figure; the color coding is consistent with Table 4.1 Clinical scores and lesion volumes averaged for each disease duration group. GM lesions were subdivided into intracortical (IC) and leukocortical (LC) lesions. Note that IC lesion volume + LC lesion volume = GM lesion volume. and Figure 4.3). Significance thresholds were corrected for multiple comparisons within metrics.

The first graph in Figure 4.6A shows the variation of the CME metric as a function of disease duration. We can observe a large reduction in cortical myelin content in year 0–1 (G1): (*t*-test controls vs patients: p=0.0015), −10% to −15% in the motor, premotor, somatosensory and prefrontal areas, as well as about −5% in the visual, supramarginal and inferior parietal areas. In years 1–2 (G2), loss of CME is still noticeable, although not significant (*t*-test controls vs patients: p=0.4), however the variation rate is significantly higher than that recorded for the G1 (*t*-test paired per cluster variation rate_0–1 vs variation rate_1–2: p=0.0004). In years 2–3 (G3), CME continues to increase significantly in multiple sclerosis patients (*t*-test paired per cluster variation rate_1–2 vs variation rate_2–3: p=0.004), **with the largest changes (>5%) in the visual (3, 5 in** Figure **4.6A) and cingulate regions (2).** Then, CME decreases in years 3+ (*t*-test paired per cluster variation rate_2–3 vs variation rate_3+: p=8×10^{-6}), showing a significant loss compared with healthy controls (*t*-test controls vs patients: p=0.04). To summarize these results, cortical myelin, as measured with CME, was largely decreased at the time of diagnosis (year 0–1); thereafter an increase in myelin content relative to G1 is observed in years 1–3, followed by a decrease in years 3+.

Interestingly, similar trends were observed for the connectivity metrics, as shown in Figure 4.6B (from left to right: strength, local efficiency and clustering). While the overall evolution is similar to that observed with the CME, a notable difference is that, instead of a relative decrease in the metric (negative variation rate), only positive variation rates are observed. As seen with the CME, the 2–3 years group shows the highest connectivity metric values, recording significantly higher values compared with G1 (0–1 years) (p=0.0006, p=0.0001 and p=0.0001 for strength, local

efficiency and clustering) and G2 (1–2 years) (p=0.004, p=0.007 and p=0.02 for strength, local efficiency and clustering), as well as a significant increase compared with the healthy control values (respectively, p=0.01, p=0.002 and p=0.001). Loss of cortical myelin and increase in connectivity metric values thus appear to be synchronized, suggesting that the two phenomena are associated. This hypothesis will be developed further in the discussion.
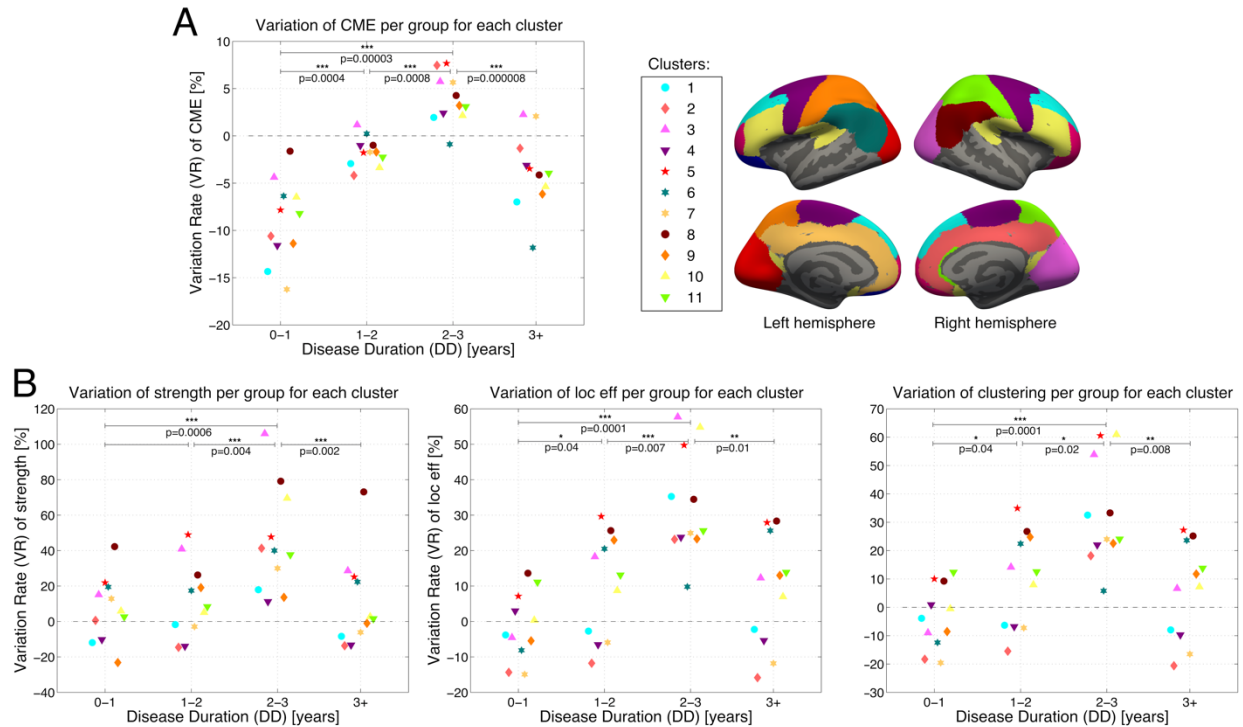
Figure 4.6 Percentage of variation of the four multiple sclerosis groups compared with matched healthy control (HC) groups. A negative variation means a lower value in the MS group and a positive variation means a higher value in the MS group. Each stable cluster is represented by a specific marker and the color code of Figure 4.3 has been conserved. Paired t-tests were used to assess the evolution of the metrics across groups, p-values were corrected for multiple comparisons within metrics. A) variation of the CME metric as a function of disease duration. We can observe a large reduction in cortical myelin content at year 0–1 (G1): (t-test HC vs MS: p=0.0015), −10% to −15% in the motor, premotor, somatosensory and prefrontal areas, as well as about −5% in the visual, supramarginal and inferior parietal areas. At years 1–2 (G2), a loss of CME is still noticeable although not significant (t-test HC vs MS: p=0.4), however the variation rate is significantly higher than that for the 0–1 group (t-test paired per cluster VR_0-1 vs VR_1–

2: p=0.0004). At years 2–3 (G3), CME continues to increase significantly in MS patients (t-test paired per cluster VR_1–2 vs VR_2–3: p=0.004) and then decreases at years 3+ (t-test paired per cluster VR_2–3 vsVR_3+: p=8×10-6) and show a significant loss compared to HC values (t-test HC vs MS: p=0.04). The three graphs in B) show from left to right: the variations rates of strength, local efficiency and clustering across the disease duration groups. The key observation is that the overall evolution is similar to that observed with the CME, with the notable difference that instead of a decrease in the metric (negative VR), only positive VRs are observed, highlighting an increase of the connectomic metrics in MS, especially in the occipito-parietal areas. As seen for the CME, G3 (the 2–3 years group) shows the highest values in connectivity metrics, showing significantly higher values compared with G1 (0–1 year, p=0.0006, p=0.0001 and p=0.0001 for strength, local efficiency and clustering) and G2 (1–2 years, p=0.004, p=0.007 and p=0.02 for strength, local efficiency and clustering) as well as significant increases compared with HC (respectively, p=0.01, p=0.002 and p=0.001 for strength, local efficiency and clustering).

As shown in Figure 4.7, Spearman's correlation coefficients, across the clusters in each group, confirm the relationship between the variation rate of cortical myelin and that of each of the connectivity metrics. The three connectivity metrics were found to be positively correlated with the cortical myelin variation rate, yielding Spearman's Rho correlation coefficients of 0.52 (p=0.0003), 0.55 (p=0.0001) and 0.53 (p=0.0001) for strength, local efficiency and clustering, respectively.
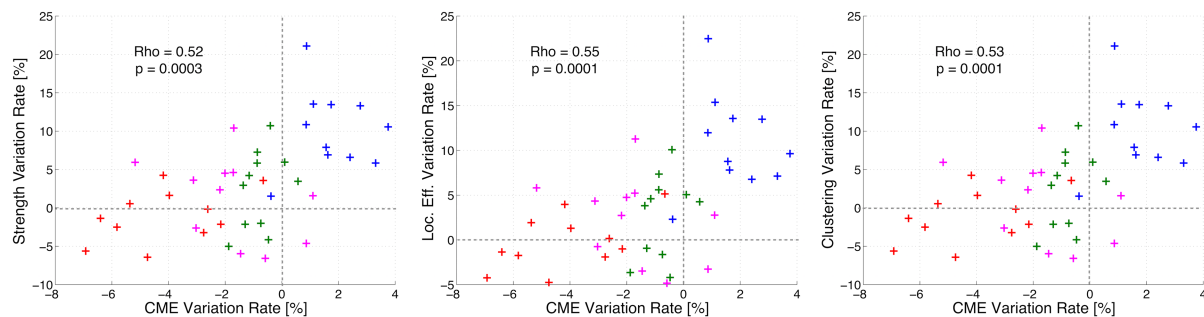
Figure 4.7 Spatial relation between cortical myelin variation rates (expressed as percentage values) and variation rates of connectivity metrics. Colors represent the different disease duration

groups (0–1 year group: red; 1–2 years group: green; 2–3 years group: blue; 3+ years group: purple). Each colored dot represents a stable cluster. The key observation is that the variation of strength, local efficiency and clustering reveal a positive correlation with the cortical myelin variation. The Spearman's Rho coefficients are 0.52 (p=0.0003), 0.55 (p=0.0001) and 0.53 (p=0.0001) for strength, local efficiency, and clustering, respectively.

4.5 Discussion

In this study, we combined ultra-high field (7T) MRI and ultra-high gradient strength (300mT/m, 3T) diffusion MRI to characterize myelin integrity in the cortex and WM of early-stage multiple sclerosis patients.

We developed an integrative framework to study topological alterations in both structural connectivity and cortical demyelination in these patients, and found that myelin-sensitive image contrasts, namely the CME map, together with diffusion-based graph theory metrics, can be helpful for characterizing, *in vivo*, microstructural tissue changes that accompany early cortical lesion pathology in multiple sclerosis.

We showed that WM connectivity metrics combined with CME can be used to predict disease duration, and MSSS and EDSS scores with good accuracy (respectively 13.6%, 17.3% and 20.1%). Moreover, we observed significant cortical myelin loss even in the subgroup with the shortest disease duration (0–1 year, p=0.00025), and an increase in connectivity in two later diagnosed cohorts (disease duration=1–2 and 2–3 years, strength: p>0.05, local efficiency: p>0.01, clustering: p>0.01, corrected for multiple comparisons). Interestingly, similar trends were observed between CME and WM connectivity metrics (Spearman's Rho correlation coefficients of 0.52 (p=0.0003), 0.55 (p=0.0001) and 0.53 (p=0.0001), for strength, local efficiency, and clustering, respectively), suggesting a possible interplay between the two phenomena.

Connectivity metrics and CME showed the highest values at 2-3 years disease duration, which suggests a possible role for compensation mechanisms in both remyelination and restructuring of the WM network, as will be further discussed below.

4.5.1 Compensation mechanisms

With regard to the variation of CME across disease duration, remyelination of lesions has frequently been observed in multiple sclerosis (Brück et al., 2003; Patrikios et al., 2006). Recently, Strijbis and colleagues (Strijbis et al., 2017) confirmed evidence (Albert et al., 2007)(Chang et al., 2012)(Albert et al., 2007) that remyelination is present in multiple sclerosis, and extended the previous authors' findings by showing that there is more remyelination in the GM than in the WM (75% vs 50% of total lesion lengths). In their work, conducted in a large, high-quality post-mortem multiple sclerosis sample, they scored remyelination in cortical lesions using a semi-quantitative scoring method (Strijbis et al., 2017).

The above-described increase in connectivity points to a structural reorganization in early-stage multiple sclerosis patients compared with healthy controls. This reorganization could be a mechanism of the brain, serving to compensate for the damage occurring in the early stages of the disease. Similar results were found in functional MRI (fMRI) studies, showing increased connectivity in the default-mode network and the frontoparietal network in multiple sclerosis patients, as well as in patients with clinically isolated syndrome (De Stefano et al., 2003; Meijer et al., 2017) .

While studies with fMRI demonstrated functional changes in all multiple sclerosis phenotypes, increasingly sophisticated structural connectivity techniques are now making it possible to detect compensatory mechanisms. Fleischer and colleagues (Fleischer et al., 2016), for example, showed that increased recruitment of brain networks might have an adaptive role.

4.5.2 Spatial distribution of myelin and connectivity changes

Our results show that the CME and connectivity values are overall higher in the occipital-parietal areas (see Figure 4.6), hence we could speculate that these regions are more prone to compensatory mechanisms. This hypothesis is strengthened by previous studies suggesting that visual recovery after acute episodes of optic neuritis in MS patients might be associated with cortical reorganization at the level of the occipital cortex (Gallo et al., 2015; Toosy et al., 2002; Werring et al., 2000). Additionally, evidence of frontal and parietal compensatory mechanisms has also been provided by functional studies and linked to improved cognitive functions (Mainero et al., 2004; Staffen et al., 2002; Sundgren et al., 2015). Despite the fact that the trends observed in the current study seem

to align with past literature, the current number of patients is still relatively small and hence those observations need to be confirmed/infirmed in larger studies.

4.5.3 Comparison with previous studies

As we have done in the present study, Fleischer et al. (Fleischer et al., 2016) evaluated the reorganization of structural networks in early-stage multiple sclerosis patients in relation to GM pathology. In their study, they evaluated the reorganization of structural networks through a topological analysis of WM and GM connectivity and reported that both WM and GM networks present an increase in local connectivity in the early disease stages, after which this declines as the disease progresses. Although their findings support the trends observed in our research, important methodological differences between the two studies need to be considered. In the study of Fleischer *et al.* (2017), GM changes were assessed using voxel-based morphometry, whereas in the present study, changes in the GM were evaluated using relaxation properties (T1 and T2*), which provide a more specific marker of demyelination (Cohen-Adad et al., 2012) (Filippi et al., 2014; Mainero et al., 2015) (G. Mangeat, Govindarajan, Kinkel, et al., 2015) (G. Mangeat, Govindarajan, Kinkel, et al., 2015), notably because tissue atrophy can also be caused by other factors, such as cell degeneration or adjacent tissue necrosis. Furthermore, Fleischer *et al.* built a connectivity matrix from diffusion images that had first been registered into the standard MNI-152 space and used the Automated Anatomical Labelling atlas for defining regions of interest; in our work, on the other hand, we used the BA surface atlas (Van Essen, 2005) that we projected into each subject's native space to build a subject-specific cortical atlas.

Figure A3 in the supplementary materials compares the two methods. Visual quality checks of the volumetric 12-DOF registration of cortical atlases to the subject's space revealed registration errors of several millimeters in many cortical areas, plus some areas overfill into adjacent gyri, while no such error was noticeable using the surface-based method.

Additionally, we used a method called bootstrap analysis of stable clusters to extract the stable features of a random clustering of our matrices of connectivity (Bellec et al., 2010). This method

has already been applied to fMRI datasets and has several benefits (Bellec et al., 2008) (Kelly et al., 2012). For instance, it can be used to investigate stable networks, both at the level of individual subjects and at the level of a group, and provides a measure of network stability (Bellec et al., 2010). This measure of stability could thus be used to select the number of stable networks for subsequent analyses (Bellec et al., 2010) as it was in our study of interplay between CME and connectivity across disease durations.

4.5.4 Causality

Although an association between cortical demyelination and increased structural connectivity was observed in the present study, we do not have elements allowing us to draw conclusions on the causality of these two events. The question thus remains, does demyelination influence structural reorganization, or vice versa? Longitudinal studies could help to address this issue, although it may be speculated, in accordance with (Fleischer et al., 2016) (2017), that cortical myelin loss is a feature of the early stage of the disease, and is followed by an increase in local connectivity that may be interpreted as a primordial response of the brain to disseminated damage, serving to maintain brain homeostasis.

4.5.5 Limitations

Although T_2* and T_1 are more specific to myelin content when used in combination as opposed to separately (G. Mangeat, Govindarajan, Mainero, et al., 2015; Gabriel Mangeat et al., 2016) (G. Mangeat, Govindarajan, Mainero, et al., 2015; Gabriel Mangeat et al., 2016), the use of CME maps as a measure of actual myelin requires further validation, particularly with respect to their accuracy. For example, CME could be partly affected by diffuse cortical inflammation.

Another limitation is the possible tractography bias induced by the WM focal lesions. The aim was to measure the loss of connectivity due to WM lesions, but their presence can sometimes hamper tractography results. Indeed, FA has been reported to decrease in focal multiple sclerosis lesions (Schneider et al., 2017), which might hamper our ability to reconstruct proper connectivity matrices using tractography. To minimize this undesirable effect, we set a threshold angle in order to discard any tracts with abrupt changes of direction. Other methods, such as masking diffusion

volumes with WM lesion masks could also be applied. In our work, we studied a cohort of early multiple sclerosis patients with a fairly low WM lesion load, therefore the problem of tractography errors due to WM lesions was less of a concern.

4.5.6 Perspectives

The combination of fMRI and brain connectivity metrics should allow a more comprehensive understanding of how structural changes in brain networks are associated with cortical demyelination in the early stages of multiple sclerosis.

The results of our study have important implications for future studies. A major goal will be to investigate how these adaptive processes correlate with underlying WM lesional pathology, as well as with clinical measures such as the EDSS score (Meyer-Moock et al., 2014). Moreover, histopathology validation (i.e. myelin staining) would further help to assess the morphological disruption of brain tissues at different stages of the disease. Larger sample sizes and longitudinal measurements will also help in further addressing questions regarding disruption of structural connectivity and cortical demyelination.

4.6 Acknowledgments

4.7 References

Abdollahi, R. O., Kolster, H., Glasser, M. F., Robinson, E. C., Coalson, T. S., Dierker, D., Jenkinson, M., Van Essen, D. C., & Orban, G. A. (2014). Correspondences between retinotopic areas and myelin maps in human visual cortex. NeuroImage, 99, 509–524.

Albert, M., Antel, J., Brück, W., & Stadelmann, C. (2007). Extensive cortical remyelination in patients with chronic multiple sclerosis. *Brain Pathology* , *17*(2), 129–138.

Badji, A., Mangeat, G., Ouellette, R., Treaba, C. A., Granberg, T., & Herranz, E. (2016). Changes in structural network connectivity in early-stage multiple sclerosis are associated with cortical demyelination. *ISMRM*.

Bellec, P., Marrelec, G., & Benali, H. (2008). A BOOTSTRAP TEST TO INVESTIGATE CHANGES IN BRAIN CONNECTIVITY FOR FUNCTIONAL MRI. *Statistica Sinica*, *18*(4), 1253–1268.

Bellec, P., Rosa-Neto, P., Lyttelton, O. C., Benali, H., & Evans, A. C. (2010). Multi-level bootstrap analysis of stable clusters in resting-state fMRI. *NeuroImage*, *51*(3), 1126–1139.

Betzel, R. F., Byrge, L., He, Y., Goñi, J., Zuo, X.-N., & Sporns, O. (2014). Changes in structural and functional connectivity among resting-state networks across the human lifespan. *NeuroImage*, *102 Pt 2*, 345–357.

Bock, N. A., Kocharyan, A., Liu, J. V., & Silva, A. C. (2009). Visualizing the entire cortical myelination pattern in marmosets with magnetic resonance imaging. *Journal of Neuroscience Methods*, *185*(1), 15–22.

Brück, W., Kuhlmann, T., & Stadelmann, C. (2003). Remyelination in multiple sclerosis. *Journal of the Neurological Sciences*, *206*(2), 181–185.

Bullmore, E., & Sporns, O. (2009). Complex brain networks: graph theoretical analysis of structural and functional systems. *Nature Reviews. Neuroscience*, *10*(3), 186–198.

Chang, A., Staugaitis, S. M., Dutta, R., Batt, C. E., Easley, K. E., Chomyk, A. M., Yong, V. W., Fox, R. J., Kidd, G. J., & Trapp, B. D. (2012). Cortical remyelination: a new target for repair therapies in multiple sclerosis. *Annals of Neurology*, *72*(6), 918–926.

Cohen-Adad, J., El Mendili, M.-M., Lehéricy, S., Pradat, P.-F., Blancho, S., Rossignol, S., & Benali, H. (2011). Demyelination and degeneration in the injured human spinal cord detected with diffusion and magnetization transfer MRI. *NeuroImage*, *55*(3), 1024–1033.

Cohen-Adad, J., Polimeni, J. R., Helmer, K. G., Benner, T., McNab, J. A., Wald, L. L., Rosen, B. R., & Mainero, C. (2012). T_2* mapping and B_0 orientation-dependence at 7 T reveal cyto- and myeloarchitecture organization of the human cortex. *NeuroImage*, *60*(2), 1006–1014.

Cook, R. D., & Weisberg, S. (1982). Criticism and Influence Analysis in Regression. *Sociological Methodology*, *13*, 313–361.

Deistung, A., Schäfer, A., Schweser, F., Biedermann, U., Turner, R., & Reichenbach, J. R. (2013). Toward in vivo histology: a comparison of quantitative susceptibility mapping (QSM) with magnitude-, phase-, and R2*-imaging at ultra-high magnetic field strength. *NeuroImage*, *65*, 299–314.

De Stefano, N., Matthews, P. M., Filippi, M., Agosta, F., De Luca, M., Bartolozzi, M. L., Guidi, L., Ghezzi, A., Montanari, E., Cifelli, A., Federico, A., & Smith, S. M. (2003). Evidence of early cortical atrophy in MS: relevance to white matter changes and disability. *Neurology*, *60*(7), 1157–1162.

Dinse, J., Waehnert, M., Tardif, C. L., Schäfer, A., Geyer, S., Turner, R., & Bazin, P.-L. (2013). A histology-based model of quantitative T1 contrast for in-vivo cortical parcellation of high-resolution 7 Tesla brain MR images. *Medical Image Computing and Computer-Assisted Intervention: MICCAI ... International Conference on Medical Image Computing and Computer-Assisted Intervention*, *16*(Pt 2), 51–58.

Filippi, M., Evangelou, N., Kangarlu, A., Inglese, M., Mainero, C., Horsfield, M. A., & Rocca, M. A. (2014). Ultra-high-field MR imaging in multiple sclerosis. *Journal of Neurology, Neurosurgery, and Psychiatry*, *85*(1), 60–66.

Fleischer, V., Gröger, A., Koirala, N., Droby, A., Muthuraman, M., Kolber, P., Reuter, E., Meuth, S. G., Zipp, F., & Groppa, S. (2016). Increased structural white and grey matter network connectivity compensates for functional decline in early multiple sclerosis. *Multiple Sclerosis* . https://doi.org/10.1177/1352458516651503

Fornito, A., Zalesky, A., & Breakspear, M. (2015). The connectomics of brain disorders. *Nature Reviews. Neuroscience*, *16*(3), 159–172.

Fukunaga, M., Li, T.-Q., van Gelderen, P., de Zwart, J. A., Shmueli, K., Yao, B., Lee, J., Maric, D., Aronova, M. A., Zhang, G., Leapman, R. D., Schenck, J. F., Merkle, H., & Duyn, J. H. (2010). Layer-specific variation of iron content in cerebral cortex as a source of MRI contrast. *Proceedings of the National Academy of Sciences of the United States of America*, *107*(8), 3834–3839.

Gallo, A., Bisecco, A., Bonavita, S., & Tedeschi, G. (2015). Functional plasticity of the visual system in multiple sclerosis. *Frontiers in Neurology*, *6*, 79.

Good, P. I., & Hardin, J. W. (2003). *COMMON ERRORS IN STATISTICS (AND HOW TO AVOID THEM)* (Wiley (ed.)). Wiley.

Govindarajan, S. T., Cohen-Adad, J., Sormani, M. P., Fan, A. P., Louapre, C., & Mainero, C. (2015). Reproducibility of T2 * mapping in the human cerebral cortex in vivo at 7 tesla MRI. *Journal of Magnetic Resonance Imaging: JMRI*, *42*(2), 290–296.

Guye, M., Bettus, G., Bartolomei, F., & Cozzone, P. J. (2010). Graph theoretical analysis of structural and functional connectivity MRI in normal and pathological brain networks. *Magma* , *23*(5-6), 409–421.

Hernando, D., Vigen, K. K., Shimakawa, A., & Reeder, S. B. (2012). R*(2) mapping in the presence of macroscopic B₀ field variations. *Magnetic Resonance in Medicine: Official Journal of the Society of Magnetic Resonance in Medicine / Society of Magnetic Resonance in Medicine*, *68*(3), 830–840.

Hutton, C., De Vita, E., Ashburner, J., Deichmann, R., & Turner, R. (2008). Voxel-based cortical thickness measurements in MRI. *NeuroImage*, *40*(4), 1701–1710.

Kelly, C., Toro, R., Di Martino, A., Cox, C. L., Bellec, P., Castellanos, F. X., & Milham, M. P. (2012). A convergent functional architecture of the insula emerges across imaging modalities. *NeuroImage*, *61*(4), 1129–1142.

Kilsdonk, I. D., Jonkman, L. E., Klaver, R., van Veluw, S. J., Zwanenburg, J. J. M., Kuijer, J. P. A., Pouwels, P. J. W., Twisk, J. W. R., Wattjes, M. P., Luijten, P. R., Barkhof, F., & Geurts, J. J. G. (2016). Increased cortical grey matter lesion detection in multiple sclerosis with 7 T MRI: a post-mortem verification study. *Brain: A Journal of Neurology*, *139*(Pt 5), 1472–1481.

King, G., Nielsen, R., Coberley, C., Pope, J. E., & Wells, A. (2011). *Comparative Effectiveness of Matching Methods for Causal Inference*∗. https://gking.harvard.edu/files/psparadox.pdf

Koenig, S. H., Brown, R. D., 3rd, Spiller, M., & Lundbom, N. (1990). Relaxometry of brain: why white matter appears bright in MRI. *Magnetic Resonance in Medicine: Official Journal of the Society of Magnetic Resonance in Medicine / Society of Magnetic Resonance in Medicine*, *14*(3), 482–495.

Kunter, M. H., Nachtsheim, C. J., Neter, J., & Li, W. (2005). *Applied linear statistical models* (McGraw-Hill (ed.)). McGraw-Hill.

Li, Y., Jewells, V., Kim, M., Chen, Y., Moon, A., Armao, D., Troiani, L., Markovic-Plese, S., Lin, W., & Shen, D. (2013). Diffusion tensor imaging based network analysis detects alterations of neuroconnectivity in patients with clinically early relapsing-remitting multiple sclerosis. *Human Brain Mapping*, *34*(12), 3376–3391.

Llufriu, S., Martinez-Heras, E., Solana, E., Sola-Valls, N., Sepulveda, M., Blanco, Y., Martinez-Lapiscina, E. H., Andorra, M., Villoslada, P., Prats-Galino, A., & Saiz, A. (2017). Structural networks involved in attention and executive functions in multiple sclerosis. *NeuroImage. Clinical*, *13*, 288–296.

Louapre, C., Govindarajan, S. T., Giannì, C., Langkammer, C., Sloane, J. A., Kinkel, R. P., & Mainero, C. (2015). Beyond focal cortical lesions in MS: An in vivo quantitative and spatial imaging study at 7T. *Neurology*, *85*(19), 1702–1709.

Lublin, F. D., Reingold, S. C., Cohen, J. A., Cutter, G. R., Sørensen, P. S., Thompson, A. J., Wolinsky, J. S., Balcer, L. J., Banwell, B., Barkhof, F., Bebo, B., Jr, Calabresi, P. A., Clanet, M., Comi, G., Fox, R. J., Freedman, M. S., Goodman, A. D., Inglese, M., Kappos, L., … Polman, C. H. (2014). Defining the clinical course of multiple sclerosis: the 2013 revisions. *Neurology*, *83*(3), 278–286.

Lucchinetti, C. F., Popescu, B. F. G., Bunyan, R. F., Moll, N. M., Roemer, S. F., Lassmann, H., Brück, W., Parisi, J. E., Scheithauer, B. W., Giannini, C., Weigand, S. D., Mandrekar, J., & Ransohoff, R. M. (2011). Inflammatory cortical demyelination in early multiple sclerosis. *The New England Journal of Medicine*, *365*(23), 2188–2197.

Lutti, A., Dick, F., Sereno, M. I., & Weiskopf, N. (2014). Using high-resolution quantitative mapping of R1 as an index of cortical myelination. *NeuroImage*, *93 Pt 2*, 176–188.

Magnoni, S., Mac Donald, C. L., Esparza, T. J., Conte, V., Sorrell, J., Macrì, M., Bertani, G., Biffi, R., Costa, A., Sammons, B., Snyder, A. Z., Shimony, J. S., Triulzi, F., Stocchetti, N., & Brody, D. L. (2015). Quantitative assessments of traumatic axonal injury in human brain: concordance of microdialysis and advanced MRI. *Brain: A Journal of Neurology*, *138*(Pt 8), 2263–2277.

Mainero, C., Benner, T., Radding, A., van der Kouwe, A., Jensen, R., Rosen, B. R., & Kinkel, R. P. (2009). In vivo imaging of cortical pathology in multiple sclerosis using ultra-high field MRI. *Neurology*, *73*(12), 941–948.

Mainero, C., Caramia, F., Pozzilli, C., Pisani, A., Pestalozza, I., Borriello, G., Bozzao, L., & Pantano, P. (2004). fMRI evidence of brain reorganization during attention and memory tasks in multiple sclerosis. *NeuroImage*, *21*(3), 858–867.

Mainero, C., Louapre, C., Govindarajan, S. T., Giannì, C., Nielsen, A. S., Cohen-Adad, J., Sloane, J., & Kinkel, R. P. (2015). A gradient in cortical pathology in multiple sclerosis by in vivo quantitative 7 T imaging. *Brain: A Journal of Neurology*, *138*(Pt 4), 932–945.

Mangeat, G., Govindarajan, S. T., Kinkel, R. P., Mainero, C., & Cohen-Adad, J. (2015). Multivariate combination of magnetization transfer ratio and quantitative T, to detect subpial demyelination in multiple sclerosis. *ISMRM*.

Mangeat, G., Govindarajan, S. T., Mainero, C., & Cohen-Adad, J. (2015). Multivariate combination of magnetization transfer, T2* and B0 orientation to study the myelo-architecture of the in vivo human cortex. *NeuroImage*, *119*, 89–102.

Mangeat, G., Louapre, C., Herranz, E., Treaba, C. A., Ouellette, R., Sloane, J. A., Klawiter, E. C., Cohen-Adad, J., & Mainero, C. (2015). Multivariate combination of quantitative T2* and T1 at 7T MRI detects in vivo subpial demyelination in the early stages of MS. *Mult Scler*, *23*, 485.

Mangeat, G., Ouellette, R., Treaba, C. A., Granberg, T., Herranz, E., Louapre, C., Stikov, N., Sloane, J. A., Klawiter, E. C., Mainero, C., & Cohen-Adad, J. (2016). Association between cortical demyelination and structural connectomics in early multiple sclerosis. *ISMRM*.

Marques, J. P., & Bowtell, R. (2005). Application of a Fourier-based method for rapid calculation of field inhomogeneity due to spatial variation of magnetic susceptibility. *Concepts in Magnetic Resonance. Part B, Magnetic Resonance Engineering*, *25*(1), 65–78.

Marques, J. P., Kober, T., Krueger, G., van der Zwaag, W., Van de Moortele, P.-F., & Gruetter, R. (2010). MP2RAGE, a self bias-field corrected sequence for improved segmentation and T1-mapping at high field. *NeuroImage*, *49*(2), 1271–1281.

Meijer, K. A., Eijlers, A. J. C., Douw, L., Uitdehaag, B. M. J., Barkhof, F., Geurts, J. J. G., & Schoonheim, M. M. (2017). Increased connectivity of hub networks and cognitive impairment in multiple sclerosis. *Neurology*, *88*(22), 2107–2114.

Meyer-Moock, S., Feng, Y.-S., Maeurer, M., Dippel, F.-W., & Kohlmann, T. (2014). Systematic literature review and validity evaluation of the Expanded Disability Status Scale (EDSS) and the Multiple Sclerosis Functional Composite (MSFC) in patients with multiple sclerosis. *BMC Neurology*, *14*, 58.

Mohan, A., De Ridder, D., & Vanneste, S. (2016). Graph theoretical analysis of brain connectivity in phantom sound perception. *Scientific Reports*, *6*, 19683.

Mottershead, J. P., Schmierer, K., Clemence, M., Thornton, J. S., Scaravilli, F., Barker, G. J., Tofts, P. S., Newcombe, J., Cuzner, M. L., Ordidge, R. J., McDonald, W. I., & Miller, D. H. (2003). High field MRI correlates of myelin content and axonal density in multiple sclerosis. *Journal of Neurology*, *250*(11), 1293–1301.

Nieuwenhuys, R. (2013). The myeloarchitectonic studies on the human cerebral cortex of the Vogt-Vogt school, and their significance for the interpretation of functional neuroimaging data. *Brain Structure & Function*, *218*(2), 303–352.

Noseworthy, J. H., Lucchinetti, C., Rodriguez, M., & Weinshenker, B. G. (2000). Multiple sclerosis. *The New England Journal of Medicine*, *343*(13), 938–952.

Patrikios, P., Stadelmann, C., Kutzelnigg, A., Rauschka, H., Schmidbauer, M., Laursen, H., Sorensen, P. S., Brück, W., Lucchinetti, C., & Lassmann, H. (2006). Remyelination is extensive in a subset of multiple sclerosis patients. *Brain: A Journal of Neurology*, *129*(Pt 12), 3165–3172.

Peterson, J. W., Bö, L., Mörk, S., Chang, A., & Trapp, B. D. (2001). Transected neurites, apoptotic neurons, and reduced inflammation in cortical multiple sclerosis lesions. *Annals of Neurology*, *50*(3), 389–400.

Pirko, I., Lucchinetti, C. F., Sriram, S., & Bakshi, R. (2007). Gray matter involvement in multiple sclerosis. *Neurology*, *68*(9), 634–642.

Pitt, D., Boster, A., Pei, W., Wohleb, E., Jasne, A., Zachariah, C. R., Rammohan, K., Knopp, M. V., & Schmalbrock, P. (2010). Imaging Cortical Lesions in Multiple Sclerosis With Ultra–High-Field Magnetic Resonance Imaging. *Archives of Neurology*, *67*(7), 812–818.

Polman, C. H., Reingold, S. C., Banwell, B., Clanet, M., Cohen, J. A., Filippi, M., Fujihara, K., Havrdova, E., Hutchinson, M., Kappos, L., Lublin, F. D., Montalban, X., O'Connor, P., Sandberg-Wollheim, M., Thompson, A. J., Waubant, E., Weinshenker, B., & Wolinsky, J. S. (2011). Diagnostic criteria for multiple sclerosis: 2010 revisions to the McDonald criteria. *Annals of Neurology*, *69*(2), 292–302.

Poonawalla, A. H., Hasan, K. M., Gupta, R. K., Ahn, C. W., Nelson, F., Wolinsky, J. S., & Narayana, P. A. (2008). Diffusion-tensor MR imaging of cortical lesions in multiple sclerosis: initial findings. *Radiology*, *246*(3), 880–886.

Schmierer, K., Scaravilli, F., Altmann, D. R., Barker, G. J., & Miller, D. H. (2004). Magnetization transfer ratio and myelin in postmortem multiple sclerosis brain. *Annals of Neurology*, *56*(3), 407–415.

Schmierer, K., Wheeler-Kingshott, C. A. M., Tozer, D. J., Boulby, P. A., Parkes, H. G., Yousry, T. A., Scaravilli, F., Barker, G. J., Tofts, P. S., & Miller, D. H. (2008). Quantitative magnetic resonance of postmortem multiple sclerosis brain before and after fixation. *Magnetic Resonance in Medicine: Official Journal of the Society of Magnetic Resonance in Medicine / Society of Magnetic Resonance in Medicine*, *59*(2), 268–277.

Sereno, M. I., Lutti, A., Weiskopf, N., & Dick, F. (2013). Mapping the Human Cortical Surface by Combining Quantitative T1 with Retinotopy. *Cerebral Cortex* , *23*(9), 2261–2268.

Shu, N., Liu, Y., Li, K., Duan, Y., Wang, J., Yu, C., Dong, H., Ye, J., & He, Y. (2011). Diffusion tensor tractography reveals disrupted topological efficiency in white matter structural networks in multiple sclerosis. *Cerebral Cortex* , *21*(11), 2565–2577.

Staffen, W., Mair, A., Zauner, H., Unterrainer, J., Niederhofer, H., Kutzelnigg, A., Ritter, S., Golaszewski, S., Iglseder, B., & Ladurner, G. (2002). Cognitive function and fMRI in patients with multiple sclerosis: evidence for compensatory cortical activation during an attention task. *Brain: A Journal of Neurology*, *125*(Pt 6), 1275–1282.

Stam, C. J. (2014). Modern network science of neurological disorders. *Nature Reviews. Neuroscience*, *15*(10), 683–695.

Strijbis, E. M. M., Kooi, E.-J., van der Valk, P., & Geurts, J. J. G. (2017). Cortical Remyelination Is Heterogeneous in Multiple Sclerosis. *Journal of Neuropathology and Experimental Neurology*, *76*(5), 390–401.

Stuart, E. A. (2010). Matching methods for causal inference: A review and a look forward. *Statistical Science: A Review Journal of the Institute of Mathematical Statistics*, *25*(1), 1–21.

Stüber, C., Morawski, M., Schäfer, A., Labadie, C., Wähnert, M., Leuze, C., Streicher, M., Barapatre, N., Reimann, K., Geyer, S., Spemann, D., & Turner, R. (2014). Myelin and iron concentration in the human brain: a quantitative study of MRI contrast. *NeuroImage*, *93 Pt 1*, 95–106.

Sundgren, M., Nikulin, V. V., Maurex, L., Wahlin, Å., Piehl, F., & Brismar, T. (2015). P300 amplitude and response speed relate to preserved cognitive function in relapsing–remitting multiple sclerosis. *Clinical Neurophysiology: Official Journal of the International Federation of Clinical Neurophysiology*, *126*(4), 689–697.

Toosy, A. T., Werring, D. J., Bullmore, E. T., Plant, G. T., Barker, G. J., Miller, D. H., & Thompson, A. J. (2002). Functional magnetic resonance imaging of the cortical response to photic stimulation in humans following optic neuritis recovery. *Neuroscience Letters*, *330*(3), 255–259.

Trapp, B. D., Peterson, J., Ransohoff, R. M., Rudick, R., Mörk, S., & Bö, L. (1998). Axonal transection in the lesions of multiple sclerosis. *The New England Journal of Medicine*, *338*(5), 278–285.

van der Kouwe, A. J. W., Benner, T., Salat, D. H., & Fischl, B. (2008). Brain morphometry with multiecho MPRAGE. *NeuroImage*, *40*(2), 559–569.

Van Essen, D. C. (2005). A Population-Average, Landmark- and Surface-based (PALS) atlas of human cerebral cortex. *NeuroImage*, *28*(3), 635–662.

Wang, Y., Sun, P., Wang, Q., Trinkaus, K., Schmidt, R. E., Naismith, R. T., Cross, A. H., & Song, S.-K. (2015). Differentiation and quantification of inflammation, demyelination and axon injury or loss in multiple sclerosis. *Brain: A Journal of Neurology*, *138*(Pt 5), 1223–1238.

Wegner, C., Esiri, M. M., Chance, S. A., Palace, J., & Matthews, P. M. (2006). Neocortical neuronal, synaptic, and glial loss in multiple sclerosis. *Neurology*, *67*(6), 960–967.

Werring, D. J., Bullmore, E. T., Toosy, A. T., Miller, D. H., Barker, G. J., MacManus, D. G., Brammer, M. J., Giampietro, V. P., Brusa, A., Brex, P. A., Moseley, I. F., Plant, G. T., McDonald, W. I., & Thompson, A. J. (2000). Recovery from optic neuritis is associated with a change in the distribution of cerebral response to visual stimulation: a functional magnetic resonance imaging study. *Journal of Neurology, Neurosurgery, and Psychiatry*, *68*(4), 441–449.

Yeh, F.-C., Wedeen, V. J., & Tseng, W.-Y. I. (2010). Generalized q-sampling imaging. *IEEE Transactions on Medical Imaging*, *29*(9), 1626–1635.

CHAPTER 5   ARTICLE 2: MACHINE LEARNING AND MULTI-PARAMETRIC BRAIN MRI TO DIFFERENTIATE HEREDITARY DIFFUSE LEUKODYSTROPHY WITH SPHEROIDS FROM MULTIPLE SCLEROSIS

Title: Machine learning and multi-parametric brain MRI to differentiate hereditary diffuse leukodystrophy with spheroids from multiple sclerosis

Authors: Gabriel, Mangeat (1); Russell, Ouellette (2,3); Maxime, Wabartha (1); Benjamin, De Leener (4); Michael, Plattén (2,3,5); Virginija, Danylaité Karrenbauer (2,6); Marcel, Warntjes (7,8); Nikola, Stikov (1,9); Caterina, Mainero (10,11); Julien, Cohen-Adad (1,12); Tobias, Granberg (2,3);

Affiliations:

(1) NeuroPoly Lab, Institute of Biomedical Engineering, Polytechnique Montreal, Montreal, QC, Canada

(2) Department of Clinical Neuroscience, Karolinska Institutet, Stockholm, Sweden

(3) Department of Neuroradiology, Karolinska University Hospital, Stockholm, Sweden

(4) Department of Computer Sciences and Software Engineering, Polytechnique Montreal, Montreal, QC, Canada

(5) School of Engineering Sciences in Chemistry, Biochemistry and Health, Royal Institute of Technology, Stockholm, Sweden

(6) Department of Neurology, Karolinska University Hospital, Stockholm, Sweden

(7) Center for Medical Imaging Science and Visualization, CMIV, Linköping, Sweden

(8) SyntheticMR, Linköping, Sweden

(9) Montreal Heart Institute, Montreal, QC, Canada

(10) Athinoula A. Martinos Center for Biomedical Imaging, Dept. of Radiology, MGH, Charlestown, MA, USA

(11) Harvard Medical School, Boston, MA, USA

(12) Functional Neuroimaging Unit, CRIUGM, Université de Montréal, Montreal, QC, Canada

5.1 Abstract

Background and Purpose: Hereditary diffuse leukoencephalopathy with spheroids (HDLS) and multiple sclerosis (MS) are demyelinating and neurodegenerative disorders that can be hard to distinguish clinically and radiologically. HDLS is a rare disorder compared to MS, which has led to occurrent misdiagnosis of HDLS as MS. That is problematic since their prognosis and treatment differ. Both disorders are investigated by MRI, which could help to identify patients with high probability of having HDLS, which could guide targeted genetic testing to confirm the HDLS diagnosis.

Methods: Here, we present a machine learning method based on quantitative MRI that can achieve a robust classification of HDLS vs. MS. Four HDLS and fourteen age-matched MS patients underwent a quantitative brain MRI protocol (synthetic MRI) at 3 Tesla (T) (scan time <7 min). We also performed a repeatability analysis of the predicting features to assess their generalizability by scanning a healthy control with five scan-rescans at 3T and 1.5T.

Results: Our predicting features were measured with an average confidence interval of 1.7% (p=0.01), at 3T and 2.3% (p=0.01) at 1.5T. The model gave a 100% correct classification of the cross-validation data when using five to eleven predicting features. When the maximum measurement noise was inserted in the model, the true positive rate of HDLS was 97.2% while the true positive rate of MS was 99.6%.

Conclusions: This study suggests that computer-assistance in combination with quantitative MRI may be helpful in aiding the challenging differential diagnosis of HDLS vs. MS.

5.2 Introduction

Hereditary diffuse leukoencephalopathy with spheroids (HDLS), a primary microgliopathy (Takuya Konno et al., 2018) sometimes referred to as adult-onset leukoencephalopathy with axonal spheroids and pigmented glia (Adams et al., 2018), is a neurodegenerative condition caused by mutations in the colony-stimulating factor 1 receptor (CSF1R) gene. HDLS was first described in 1984 (Axelsson et al., 1984) and is characterized by microglial dysfunction, demyelination, axonal degeneration with spheroids and gliosis (Axelsson et al., 1984; Baba et al., 2006; Freeman et al., 2009; Granberg, Hashim, et al., 2016; C. Sundal et al., 2015). HDLS is a rare condition, but is likely underdiagnosed since its symptomatology and radiological features overlap with other neurodegenerative diseases (Axelsson et al., 1984; Freeman et al., 2009; Granberg, Hashim, et al., 2016; Karle et al., 2013; C. Sundal et al., 2015; Christina Sundal, Lash, et al., 2012; Christina Sundal, Van Gerpen, et al., 2012). Multiple sclerosis (MS) is a relatively common neurological disorder of the central nervous system in young adults, characterized by heterogeneous pathological processes that include demyelination, neuroaxonal degeneration and inflammation with an unknown cause (Thompson, Baranzini, et al., 2018). Because HDLS and MS are both characterized by demyelination, axonal loss, neurodegeneration and scarring, they can be hard to distinguish either clinically, biochemically, with conventional imaging or even volumetry. HDLS can, therefore be misdiagnosed as MS due to their clinical, radiological and biochemical similarities (Saitoh et al., 2013; C. Sundal et al., 2015). Correctly diagnosing patients is especially important since the prognosis and treatment differ greatly. HDLS is a lethal disorder and the immunomodulating therapies currently used for MS may only provide adverse events for HDLS patients.

MS and HDLS have, however, underlying differences in the pathophysiology and degree of tissue disruption (Baba et al., 2006). Non-invasive in-vivo quantification of these underlying differences with MRI could thus prove helpful in improving the differential diagnostics. Among MRI techniques of interest, quantitative MRI is becoming increasingly popular as a tool that can enable clinicians to compare examinations longitudinally and between patients (Vaughn et al., 2013). Quantitative MRI has also shown the potential to relate the type and integrity of tissues, making it possible to study subtle pathological mechanisms (Cohen-Adad et al., 2012; Mainero et al., 2015), to achieve accurate diagnosis (A. Hagiwara, Hori, Yokoyama, Nakazawa, et al., 2017; A.

Hagiwara, Hori, Yokoyama, Takemura, et al., 2017) and to study diffuse changes in normal-appearing tissues (Wattjes et al., 2015). However, quantitative MRI often comes with limitations such as long scan times and/or complex post-processing. Of potential interest, synthetic MRI (SyMRI) provides clinically approved quantitative proton density (PD), T1 and T2 maps as well as rapid myelin estimation for diagnostic imaging (REMyDI) via a single acquisition (Akifumi Hagiwara et al., 2017). In addition to the advantages associated with the single acquisition (e.g., no co-registration required), synthetic MRI has been validated as a time-efficient imaging method for a number of clinical applications (Granberg, Uppman, et al., 2016; A. Hagiwara, Hori, Yokoyama, Nakazawa, et al., 2017; A. Hagiwara, Hori, Yokoyama, Takemura, et al., 2017; Akifumi Hagiwara et al., 2017; Kim et al., 2017; Vågberg et al., 2013; J. B. M. Warntjes et al., 2008). Another advantage of the multi-parametric maps is that it provides an opportunity to robustly compare datasets, which is ideal for applications of machine learning approaches.

Here, we aimed to develop a classification method based on SyMRI tissue quantification and volumetry of the brain to differentiate HDLS from MS. The confidence of the classifying features was first assessed using a scan-rescan protocol at 1.5T and 3T. Secondly, a feature selection process was performed prior to training a classifier model. Thirdly, the robustness of the model was tested under noisy conditions in order to assess the generalizability of the method.

5.3   Methods

5.3.1   Data acquisition

5.3.1.1   Repeatability study

The quantitative National Institute of Standards and Technology/The International Society of Magnetic Resonance in Medicine (NIST/ISMRM) system MRI phantom (Keenan et al., 2016) and a 29-year-old healthy male control underwent five scans each on a Siemens Aera 1.5T and a Siemens Prisma[Fit] 3T scanner (Siemens Medical Systems, Erlangen, Germany) with a standard 20-channel head coil. The three first scans were performed without reposition and the two last with repositioning (3+1+1 protocol), yielding three data sets per scanner without repositioning and three with repositioning (including the last scan of the first 3). The acquisition parameters for the multi-

dynamic multi-echo (MDME) sequence in the control were: 30 axial slices in the control, resolution $0.7x0.7x4.0$ mm^3 with a 1 mm slice gap, flip angle 120°; repetition time 4480/4630 ms; echo times 22/23 and 97/101 ms (Aera/Prisma^{Fit}); 4 averages with different slice acquisition order, resulting in four different effective inversion times (150/580/2000/4130 ms); GeneRalized Autocalibrating Partial Parallel Acquisition (GRAPPA) factor 2/3 (Aera/Prisma^{Fit}); acquisition time 6:24/5:55 min (Warntjes et al. 2008). For the phantom, the number of slices was increased to 40 to cover the entire phantom, resulting in a repetition time of 5780 and an acquisition time of 8:24 for both scanners. The software SyMRI 11.0 Beta 4 was used to calculate the quantitative PD, T1, T2 and REMyDI maps. REMyDI is an estimation of the myelin volume fraction based on a non-linear combination of the PD, T1 and T2 maps, as previously described (J. B. M. Warntjes et al., 2017; M. Warntjes et al., 2016). The REMyDI technique has recently been validated *ex vivo* and *in vivo* in MS (Ouellette et al., 2020). Since all quantitative maps are based on the same acquisition, they are inherently aligned.

5.3.1.2 Clinical application study

For the prospective study, we enrolled 4 HDLS patients (age 50±5 years, 2 females) with c.2562T>A p.Asn854Lys CSF1R mutation and 14 aged-matched MS patients (age 50±9 years, 11 females; 1 primary progressive MS, 4 relapsing-remitting MS, 9 secondary progressive MS, median Expanded disability status scale (EDSS) score 3.75, range 1-8.5). The MS patients were diagnosed and subtyped according to the contemporary criteria (Lublin, 2014; Polman et al., 2011). HDLS is a rare condition relative to MS (ratio about 1:10,000 MS (Axelsson et al., 1984; C. Sundal et al., 2015; Thompson, Baranzini, et al., 2018), limiting the availability of patients to be enrolled in the study. The clinical phenotype of the patients with HDLS have previously been thoroughly detailed, interestingly 2 of the patients with HDLS had been mis-diagnosed as MS and none exhibited brain calcifications on computed tomography (C. Sundal et al., 2015). Despite unbalanced classes, more MS patients increase the confidence markers for detecting an effect between HDLS and MS, such as the t-statistic. In addition, all the classifications measures used were corrected for the unbalanced classes of patients. Table 5.1 details the demographics of the patients. All participants underwent brain imaging on the same Siemens Trio 3T scanner (Siemens Healthcare, Erlangen, Germany) using the same multi-dynamic multi-echo sequence and a 12-

channel head coil. Acquisition parameters were: 30 axial slices, resolution 0.9x0.9x4.0 mm^3 with a 1 mm slice gap, flip angle 120°; repetition time 4260 ms; echo times 22 and 100 ms; 4 averages (150/580/2000/4130 ms effective inversion times); GRAPPA factor 2; acquisition time 6:50 min. The quantitative PD, T1, T2 and REMyDI maps were obtained using SyMRI in the same way as for the healthy control.

Table 5.1 Demographics of all patients. HDLS: Hereditary Diffuse Leukoencephalopathy with Spheroids, MS: Multiple Sclerosis, WM: White Matter, DMT: Disease Modifying Therapy, EDSS: Expanded Disability Status Scale. ID: Identification, SP: Secondary Progressive, RR: Relapsing-Remitting, M: Male, F: Female. NON-tissue volumes, volumes not classified as WM, GM nor CSF by the Synthetic MRI software, were added for comparison with the WM lesion volumes. Note that except for the NON-tissue volumes, no demographic data presented in this table were included in the predictive model.

ID	Sex	Age [years]	Disease duration [years]	WM lesion volume [milliliters]	NON-tissue volume [milliliters]	MS subtype	DMT	DMT drug	EDSS
HDLS 1	F	55	15	0.6	58.3				
HDLS 2	M	56	5	25.2	88.6				
HDLS 3	M	47	4	0.4	67.4				
HDLS 4	F	44	5	0.5	54.3				
MS 1	F	66	11	3.4	59.4	PPMS	0	0	6
MS 2	M	46	20	23.5	77.1	SPMS	1	Rituximab	8.5
MS 3	F	45	7	2.0	55.4	SPMS	0	0	3
MS 4	F	49	18	72.0	70.0	SPMS	1	Fingolimod	6

MS 5	F	60	34	4.8	60.6	SPMS	1	Interferon beta	5
MS 6	F	53	35	14.2	64.4	SPMS	0	0	3.5
MS 7	F	33	6	3.3	55.8	RRMS	0	0	1
MS 8	F	39	6	1.0	50.0	RRMS	0	0	1
MS 9	M	41	11	8.0	59.2	RRMS	0	0	2
MS 10	F	58	18	15.9	74.4	SPMS	1	Interferon beta	4
MS 11	F	48	34	23.9	78.3	SPMS	1	Cortisone	6
MS 12	F	56	36	2.6	52.6	SPMS	1	Rituximab	6
MS 13	F	49	35	6.3	66.2	RRMS	1	Glatiramer acetate	1
MS 14	M	64	21	1.2	54.1	SPMS	1	Interferon beta	1

5.3.2 ROI processing

5.3.2.1 Tissue masks

Grey matter (GM), white matter (WM) and cerebrospinal fluid (CSF) masks were automatically generated using the SyMRI software based on the combination of the quantitative T1, T2 and PD maps.(West et al., 2012) In more detail, a Bloch simulation was used to predict the T1, T2 and PD values of the GM, WM or CSF compartments in healthy human brain tissue. Then, the inverse solution can be used to predict the tissue from the measures T1, T2 and PD values. For example, the intracranial mask is defined as the middle ground of 0% PD in bone and 100% PD in CSF. The volume that cannot be classified as GM, WM or CSF was per default assigned a fourth tissue class

called NON-WM/GM/CSF that mainly includes lesioned tissue. The relaxometry-based volumetry included within-voxel partial volume correction and was performed offline within less than 10 seconds on a standard laptop.(Saccenti et al., 2019) In addition, actual lesion volumes in patients were segmented by a radiologist (T.G.) in ITK-SNAP.(Yushkevich et al., 2006) based on synthetic T2-weighted

 Fluid-Attenuated Inversion Recovery and PD-, T1- and T2-weighted images automatically generated in SyMRI with default settings. Note that the manual lesion volume has been reported in the demographic Table 5.1, but was not used as a predicting feature in order to keep the predicting pipeline as fast and unbiased as possible without the need for manual intervention.

5.3.3 Classification

The quantitative maps (T1, T2, R1, R2, PD, REMyDI) were averaged in GM and WM ($=6\times2$ features). Moreover, we computed the volume fractions of each tissue: GM, WM, CSF and NON (=4 features). This step reduces all the data of one subject to 16 features. The features underwent a feature selection process and were inputted in a model in order to output a diagnosis. A Linear Discriminant Analysis (LDA) was chosen to perform the classification task in order to avoid overfitting to the data (Fisher, 1936; Huberty & Olejnik, 2006; Ye et al., 2005). Note that since the predictive model is based on a linear combination of the features, having a T1 and a R1 measurement of the same ROI is not redundant. Figure 5.1 shows an example of the acquired data and summarizes the methodology.
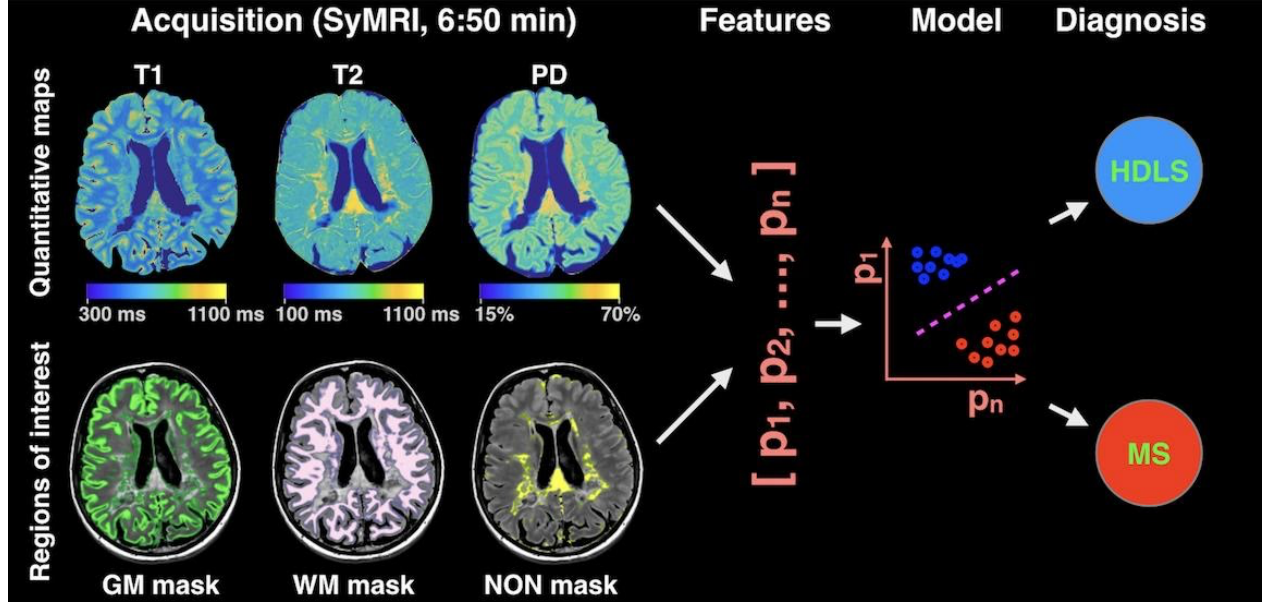
Figure 5.1: Illustration of the methodology. Left: Example of the acquired data in a multiple sclerosis (MS) patient; In the top row, an example of the quantitative T1, T2 and PD maps are displayed; In the bottom row the corresponding white matter, grey matter and NON-masks overlaid on a T2-weighted Fluid-Attenuated Inversion Recovery image. The predicting features are calculated from the quantitative maps and the regions of interest. Finally, the trained model uses the selected features as input and outputs the diagnoses, MS or HDLS. P_X: Predicting feature number X.

5.3.4 Feature selection

To determine what and how many features to use, we performed a bootstrap random feature selection (10,000 iterations). At each iteration, a subset of features was randomly chosen and leave-one-out cross-validation was performed to calculate the average accuracy of the prediction as detailed in the formula below. The average accuracy is the average per-class effectiveness of a classifier and was used here to remove the effect of the unbalanced classes (Sokolova & Lapalme, 2009).

Equation 5.1: $\mathrm{AA} = \frac{1}{2} * \left(\frac{\mathrm{TP_{HDLS}}}{\mathrm{N_{HDLS}}} + \frac{\mathrm{TP_{MS}}}{\mathrm{N_{MS}}} \right)$

Where AA is the average accuracy, TP_X is the True Positive rate for class X and N_X is the number of subjects in class X. The importance of each feature was then estimated by computing the frequency of the features used in the best predictive models (average accuracy = 100%).

5.3.5 Cross-validation

Leave-one-out bootstrap analyses were used to cross-validate the classifications. Confusion matrices were then computed to assess the performances of the classification. A confusion matrix displays the entire classification performance in the sense that any classification measure can be computed out of the confusion matrix.

5.3.6 Mean model and noise analysis

The models showing a 100% correct classification of the cross-validation data were averaged to propose one mean model. This mean model was then trained with artificially augmented data: original features + measurement noise (computed from the repeatability analysis). By doing so, the robustness of the mean model to various noise conditions was tested. Adding the repeatability noise to our model enables us to estimate the generalisability of our prediction method to other centers or scanners.

5.4 Results

5.4.1 Confidence of the predicting features

Figure 5.2A shows the five scan-rescans of the healthy control and the NIST phantom at 3T. Only T1 maps are displayed for visualization purposes. Figure 5.2B shows the confidence intervals (CI) of the measured features.

Overall, the quantitative measurements were found to be robust with relatively small 99% CIs. The average 99% CI, or repeatability error was 1.7% at 3T and 2.3% at 1.5T; while the maximum 99% CI was 3.3% at 3T (NON-volume fraction) and 5.6% at 1.5T (CSF volume fraction). The minimum 99% CI, was 0.3% for the PD map averaged in the grey matter. The quantitative measures remained robust at 1.5T, although we notice a slight increase in the 99% CIs compared to 3T. A two-sample

F-test for equal variances revealed that the variability across the scan-rescans was significantly lower at 3T compared to 1.5T for the CSF volume fraction only (**$p<0.01$). As the clinical study was performed at 3T, we choose to be conservative and use the maximum 3T repeatability error of 3.3% to create artificial data and test the performance of the classification model with artificial noise (in section 5.4.3).

Feature	Unit	Aera 1.5 T			PrismaFit 3 T		
		Value	95% CI	99% CI	Value	95% CI	99% CI
T1 WM	ms	679	1.0%	1.7%	792	0.9%	1.5%
T1 GM	ms	1400	1.3%	2.2%	1557	0.9%	1.5%
T2 WM	ms	70.2	0.7%	1.2%	62.1	1.1%	1.9%
T2 GM	ms	101	0.7%	1.1%	84.1	0.7%	1.2%
PD WM	%	62.2	0.4%	0.6%	61.3	0.3%	0.6%
PD GM	%	78.2	0.4%	0.6%	79.2	0.2%	0.3%
My WM	%	15.9	1.9%	3.2%	16.8	1.4%	2.3%
My GM	%	10.6	2.9%	4.9%	10.5	1.5%	2.5%
R1 WM	s^{-1}	1.47	1.0%	1.7%	1.26	0.9%	1.5%
R1 GM	s^{-1}	0.71	1.4%	2.2%	0.64	0.9%	1.5%
R2 WM	s^{-1}	12.9	0.7%	1.2%	16.1	1.1%	1.9%
R2 GM	s^{-1}	9.90	0.7%	1.1%	11.9	0.7%	1.2%
WM v.f.	%	34.6	2.1%	3.4%	34.6	1.7%	2.7%
GM v.f.	%	51.1	2.2%	3.6%	52.3	1.1%	1.8%
CSF v.f. **	%	10.7	3.4%	**5.6%**	9.8	0.9%	1.5%
NON v.f.	%	3.6	1.9%	3.1%	3.3	2.0%	**3.3%**

Figure 5.2 Confidence of the predicting features. A) Example of T1 maps of the five scan-rescans of the healthy control and the NIST phantom at 3T. B) 95% and 99% confidence intervals (CI) of all 16 predicting features. The CIs were computed across the five scan-rescans. A 99% CI of y% means that if we take a measurement A, there is a 99% chance that the true value of the feature is

contained in the interval [A - y/2 %, A + y/2 %]. A two-sample F-test for equal variances revealed that the variability across scan rescan was significantly lower at 3T compared to 1.5T only for the CSF volume fraction (**p<0.01). The maximum 99% CI, or repeatability error was 5.6% at 1.5T (CSF volume fraction) and 3.3% at 3T (NON-tissue volume fraction, i.e. the volume that cannot be classified as grey matter (GM), white matter (WM) or CSF, which mainly includes lesioned tissues). v.f.: Volume Fraction, My: REMyDI map.

5.4.2 Diagnosis prediction

5.4.2.1 Feature selection

A bootstrap random feature selection was first used to assess the number of features to use. At each iteration, a subset of features was randomly chosen and leave-one-out cross-validation was performed to calculate the average accuracy of the prediction. Figure 5.3A shows a graph of the maximum average accuracy depending on the number of features used in the predictive model. 100% correct classification of the cross-validation data can be observed when using between 5 to 11 features. With too few features (<5), the predictions underperform, notably, when using only one feature, the averaged accuracy of the prediction is 50%, which is the same as the random classifier would give. This supports the fact that the classification cannot be made by observing only one feature. With too many features (>11), the models tend to overfit, leading to less accurate classification of the cross-validation data. Out of the 10,000 subsets of features tested by the bootstrap algorithm, 42 led to a 100% correct classification of the cross-validation data.

5.4.2.2 Feature importance

To study the relative importance of the features, we computed the proportion of the features used in these 42 successful models. Since we only selected the models showing a 100% correct classification of the cross-validation data, any confusion matrix-based metric (e.g. average accuracy, precision, true positive rate, true negative rate, etc.) would have led to the same selection of models. Figure 5.3B shows the proportion of the features used in the successful models. Interestingly, the REMyDI map, reflecting myelin content, in the grey matter was nearly always used. Moreover, we can distinguish that some other features were also commonly used, such as the R2 map averaged in the gray matter, the white matter volume fraction and the NON-volume

fraction. We notice that no feature is completely discarded, meaning that all of them carry useful information for the classification. Table 5.2 shows the median, mean and standard deviation of each feature, computed within the MS and HDLS groups, as well as the result of a Student t-test. When analyzed alone, no feature can detect a difference between both conditions. Highlighting the relevance of combining several quantitative measurements to achieve a robust classification.
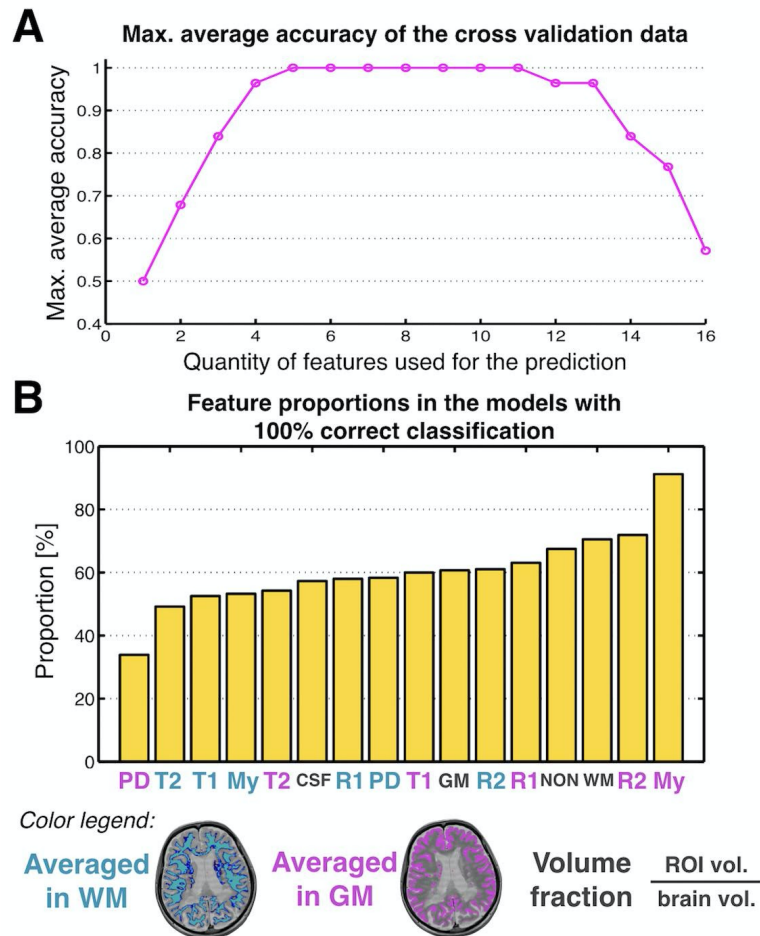
Figure 5.3 Selection of features. A) Graph of the maximum average accuracy depending on the number of features used in the predictive model. 100% average accuracy was achieved when using between 5 and 11 features. B) The proportion of features used in the successful models (100% correct classification). Interestingly, the REMyDI map (My) in the grey matter was nearly always used. Moreover, other commonly used features include the R2 map averaged in the gray matter, the white matter volume fraction or the NON-tissue volume fraction. WM: White Matter,

GM: Grey Matter, CSF: CerebroSpinal fluid, vol.: volume, My: REMyDI map, ROI: Region Of Interest.

Table 5.2 Group median, mean and standard deviation per class, for each feature. Group median, mean and standard deviation per class, for each feature. A Student t-test was performed to determine whether it could discriminate between the two groups. The last line (Combined) refers to the combination of nine features displayed as an example in Figure 5.4A. No feature, taken alone, was able to discriminate between the two groups, highlighting the relevance of combining several features to classify both conditions. *The combined metric is significantly different between the two groups. WM: White Matter, GM: Grey Matter, v.f.: Volume Fraction, My: REMyDI map, ms: milliseconds, SD: Standard Deviation.

Feature	Unit	Median HDLS	Mean HDLS	SD HDLS	Median MS	Mean MS	SD MS	p-value
T1 WM	ms	750	749	10.2	745	745	19.1	0.73
T1 GM	ms	1504	1503	4.65	1500	1507	26.47	0.80
T2 WM	ms	75.1	76.6	4.82	74.0	74.3	2.14	0.22
T2 GM	ms	92.3	93.9	5.35	89.5	90.9	3.49	0.23
PD WM	%	60.8	60.9	0.63	60.3	60.2	1.07	0.27
PD GM	%	78.6	78.7	0.27	79.0	79.0	0.43	0.19
My WM	%	24.7	24.6	0.85	25.3	25.4	1.44	0.31
My GM	%	3.82	3.80	0.07	3.62	3.66	0.15	0.10
R1 WM	s^{-1}	1.37	1.36	0.02	1.35	1.36	0.04	0.84
R1 GM	s^{-1}	0.70	0.70	0.002	0.70	0.70	0.01	0.75
R2 WM	s^{-1}	13.9	13.9	0.16	13.8	13.8	0.32	0.84

R2 GM	s^{-1}	11.4	11.4	0.10	11.4	11.4	0.15	0.68
WM v.f.	%	40.2	40.4	2.47	41.2	39.8	5.91	0.85
GM v.f.	%	32.0	31.9	4.85	34.0	33.2	4.00	0.60
CSF v.f.	%	20.3	18.9	5.17	18.0	19.5	8.28	0.91
NON v.f.	%	8.09	8.81	1.79	7.42	7.54	0.97	0.10
Combined	-	1.03	0.97	0.28	-1.20	-1.16	0.39	$*2.7_{x}10^{-8}$

5.4.2.3 Representation of the predictions

In order to visually assess the results of the classifications, we displayed the projections of the datasets on the direction of maximum separation (in Figure 5.4 and Figure 5.5). This direction is a vector determined by the LDA algorithm and expressed in an n-dimensional space (with n being the number of features used). Perpendicular to the direction of maximum separation, there is a separating hyperplane (purple dashed line in Figure 5.4 and Figure 5.5), which defines the virtual border of the classification: a data point on the positive side of the hyperplane will be predicted as being HDLS, while a data point on the negative side will be predicted as being MS. An increased distance of the data points from the separation plane represents a more robust classification.
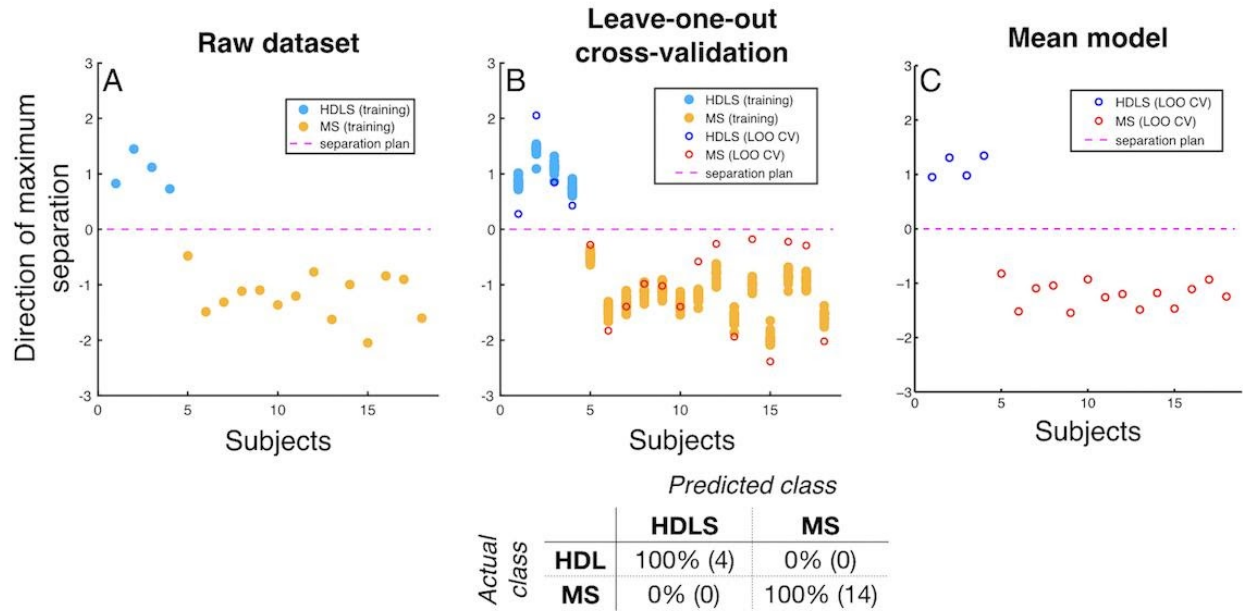
Figure 5.4 Example of classification models. The datasets are projected on to the direction of maximum separation (in the feature space). The panel (A) shows the raw classification of a model containing nine features (Proton density (PD) and REMyDI maps in white matter (WM); T1, R1, R2, PD and REMyDI in grey matter; WM and NON-tissue volume fractions). We notice a fairly low within-class variability compared to the inter-class distance, which is a sign of robust classification. The panel (B) shows the results of the cross-validation tests; the circles represent the data unknown to the model (cross-validation data) while the dots represent the training data. We observe that in some cases, while staying on the correct side, the cross-validation points tend to be closer to the line. The mean model (panel C) is the average (bagging) of the 42 models that presented a 100% correct cross-validation. We notice a lower within-class variability and a higher inter-class distance than the model in panels A-B, suggesting that the mean model is more robust than the single model displayed in panels A-B. LOO: Leave-One-Out, CV: Cross Validation.

5.4.2.4   Example of the classification

Figure 5.4A, B shows an example of a classification model containing nine features: PD and REMyDI maps in WM; T1, R1, R2, PD and REMyDI in GM; WM and NON-volume fractions. We notice a fairly low within-class variability compared to the inter-class distance, which is a sign of robust classification. Figure 5.4C shows the data points separated by the mean model. The mean model is the average (bagging) of the 42 models that presented a 100% correct cross-validation. We notice a lower within-class variability and a higher inter-class distance than the model in the middle panel, suggesting that the mean model is more robust than the single model displayed in the left panel. Despite the fairly low HDLS sample size and the unbalanced classes, the probability of measuring the observed class separation, assuming that the two conditions are not distinguishable were reasonably low: $p < 10^{-7}$ and $p < 10^{-11}$ for the distributions presented in Figure 5.4, left and right panels respectively. These results increase the confidence of the proposed classification models. Moreover, the hypothesis of having a quantitative measure along the direction of maximum separation that display equal variance in the HDLS and MS groups can not be discarded (two-sample F-tests for equal variances, $p = 0.78$ and $p = 0.97$ in Figure 5.4, left and right panels respectively).

5.4.3   Generalization of the predictions

As a first step towards the generalization of our results, we tested our classification model under noisy conditions. To do so, we used the upper bound of the maximum 99% CI of our feature measurement at 3T (3.3% error, Figure 5.2), representing a worst-case scenario, in order to create artificial noisy data. For each subject, we created 100 artificial noisy subjects and retrained the mean model (presented in Figure 5.4) with these artificial data points. Figure 5.5A shows the classification of the original subjects performed by the mean model after being re-trained with artificial data. We notice that the clusters of each class tend to be closer to the separation plan, but the classification remains 100% accurate and fairly robust.

Figure 5.5B, C and D show the classification of artificially noisy datasets performed by the re-trained mean model. For each subject, 100 artificial noisy subjects were tested. The level of noise displayed is 1%, 3.3% and 5%, respectively in Figure 5.5B, 5C and 5D. We observe that with 1%

noise, the classification is still perfect. With 3.3% noise, representing the maximal repeatability noise we measured at 3T, some misclassifications are observed, the true positive detection rate (TPDR) of HDLS being 97.2%, while the TPDR of MS being 99.6%. Additionally, we computed the classification when the repeatability noise is at 5%, to represent a hypothetically less robust data set. In this case, the TDPRs decrease: HDLS 92.0% and MS 97.0%.
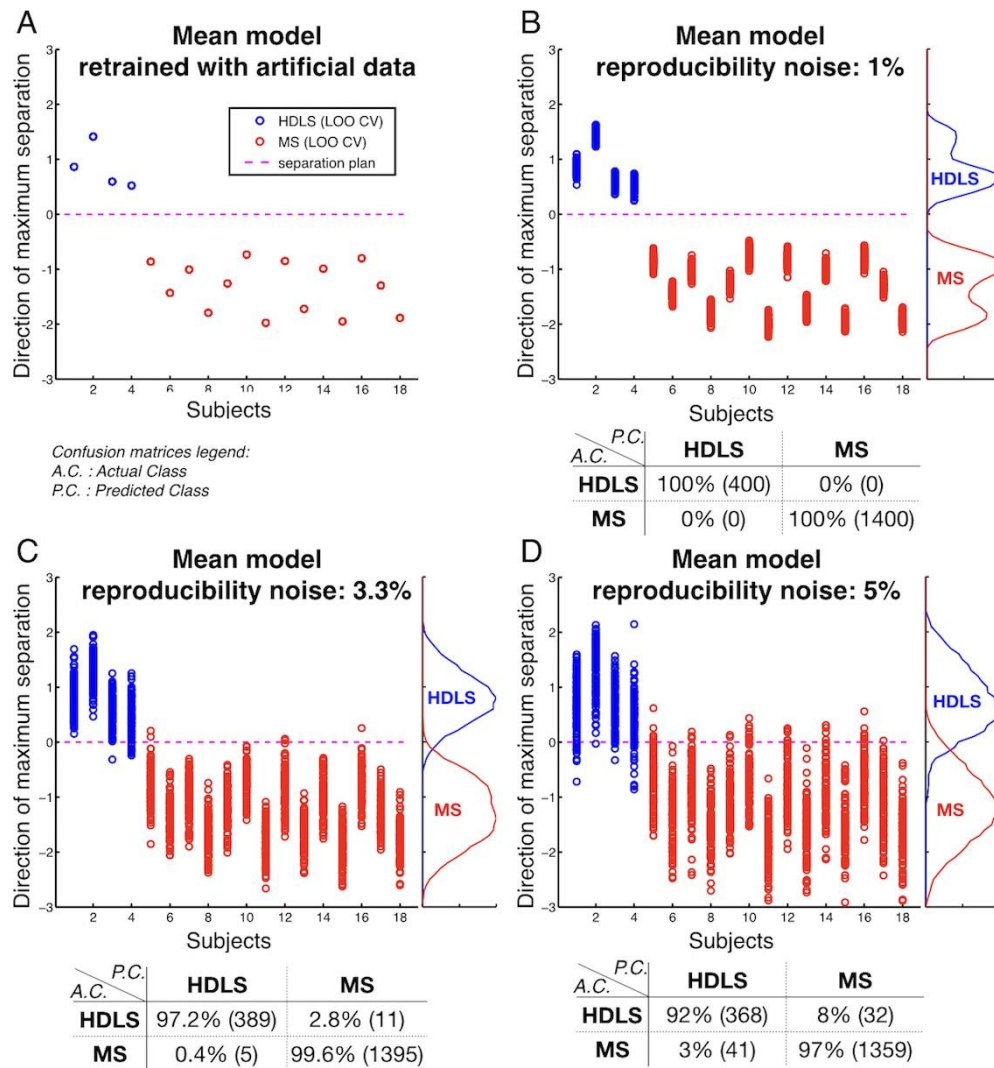
Figure 5.5 A) Classification of the original data performed by the mean model re-trained with artificial noisy data, variability noise: 3.3%, leave-one-out cross-validation displayed only. B, C and D) Classification of artificial noisy data by the mean model re-trained with artificial noisy data, variability noise respectively: 1%, 3.3% and 5%, leave-one-out cross-validation displayed only. We observe that with 1% noise, the classification is still perfect. With 3.3% noise (maximal repeatability noise we measured at 3T) some misclassifications are observed, while the overall

classification remains robust: the true positive detection rate (TPDR) of HDLS being 97.2%, while the TPDR of MS being 99.6%.

5.5 Discussion

This study presents a quantitative MRI based method that is able to differentiate HDLS from MS, which is otherwise clinically and radiologically challenging to distinguish. In our cohort, two patients with HDLS had previously been misdiagnosed with MS since they fulfilled the diagnostic criteria for MS both radiologically and clinically. We have previously shown in the same cohort, that neither structured neuroradiological assessments nor volumetric analysis has been able to accurately differentiate the patients with HDLS from those with MS (Granberg, Hashim, et al., 2016). Furthermore, CT examinations revealed that none of the patients had HDLS-typical calcifications in the brain parenchyma (T. Konno et al., 2017). Their correct diagnosis was only made after they participated in a genetic study revealing mutations in their CSF1R gene (Rademakers et al., 2011; Christina Sundal, Lash, et al., 2012; Christina Sundal, Van Gerpen, et al., 2012). Our new findings suggest quantitative MRI and that computer-assistance may be helpful in aiding the diagnostics of these disorders. Indeed, quantitative MRI allows the study of slight diffuse alterations in normal-appearing tissues, that, when combined in one model, can be specific to the underlying pathology. The imaging method used here, SyMRI, is clinically approved and offers robust repeatability and reproducibility, combined with a relatively short scan time (<7 min) and fast automated post-processing. Thus, no manual interventions or processing are required to perform the classification based on these automatically generated features, making the method suitable for fast clinical screening of potential HDLS candidates. Such a screening tool could potentially be applied both at the time of MS diagnosis and/or any point of re-evaluation or routine MRI follow-up. For example, due to lack of MS treatment response or if the patient presents HDLS features, such as the two misdiagnosed HDLS patients in this study, that were re-diagnosed after several years of an MS diagnosis. Additional tests such as targeted genetic testing could then be run to confirm the HDLS diagnosis. A recent multi-vendor study of SyMRI suggests that the method is generalizable also across multiple vendors (Akifumi Hagiwara et al., 2019), which also needs further confirmation.

5.5.1 Classification method and dataset

Here, a simple linear classification method was chosen over non-linear methods to minimize the degrees of freedom. Other non-linear methods such as quadratic discriminant analysis and random forest classification trees were tested, but the non-linearities led to overfitting of the training dataset, inducing larger cross-validation errors. While advanced algorithms could lead to a more robust classification, they also have more degrees of freedom, thus requiring a larger dataset to avoid overfitting. Artificial data augmentation or slice-based analysis could be used to test non-linear algorithms with a small dataset. Ultimately, collecting a multi-center international dataset would open the door to more generalizable models.

5.5.2 Interpretation of the results

An interesting tool to start understanding the mechanisms of the classification is the feature selection. Knowing that some features are more useful than others for the classification is a valuable hint to help to focus on additional investigations. Here, the feature analysis shows that the myelin map (REMyDI) averaged in the grey matter was the most commonly used feature to achieve a 100% correct classification. This suggests that HDLS with c.2562T>A p.Asn854Lys CSF1R mutation tends to have less cortical demyelination than MS. This study thus provides a better understanding of CSF1R dysfunction in the role of the demyelination process in HDLS. While cortical thinning/volumetrics have been shown to be focally and diffusely altered in MS, this has not been so apparent in HDLS (Granberg, Hashim, et al., 2016). Since our results suggest that the cortical demyelination processes might differ in both diseases, future studies should evaluate whether there are detectable cortical lesions in HDLS with advanced MRI (i.e. double inversion recovery, phase-sensitive inversion recovery or ideally 7T). It also supports the choice of adding cortical lesions to the dissemination in space classification in the latest revision of the diagnostic MS criteria (Thompson, Banwell, et al., 2018).

5.5.3 Feature ROIs

In order to facilitate the reproducibility of the study, we chose to use the tissue masks that are automatically computed by the SyMRI software: GM, WM, CSF and NON and to average the

quantitative measurements in GM and WM only. A finer parcellation could have been used in order to explore the hypothesis that the spatial distribution of the pathologic processes can differentiate both diseases. However, as observed in the repeatability results, smaller areas can lead to lower SNR or higher repeatability noise. Indeed, the confidence intervals of the phantom quantitative spheres have been shown to be larger than the confidence intervals of the brain ROIs. Thus, if smaller areas are chosen as a predictive feature (e.g. anatomical or functional atlas, quantitative measurements in lesions or NON-volume, etc.), we suggest first assessing their stability and applying it in a larger sample size.

5.5.4 Limitations of the study

Despite convincing results showing a 100% correct diagnosis prediction of the cross-validation data, and a high group separation ($p < 10^{-11}$, Figure 5.4C), the sample size of the HDLS pool was fairly low due to the rareness of the disorder, hence increasing the chances of having a biased variability of the HDLS features. While section 3.3 tends to address this exact problem, a larger HDLS sample size would increase the confidence of the predictive analysis. In the current study, all six concurrently known patients with HDLS in the Stockholm region were offered participation but one had MRI contraindications and one declined participation. Future studies should thus focus on recruiting more HDLS to be scanned with the same quantitative MRI protocol, which seems achievable in a multi-center study since the reproducibility of the method is robust (Akifumi Hagiwara et al., 2019). It is also important to note that the disease duration for both the MS and HDLS populations were relatively high. This is reflective of the fact that the two HDLS patients that had been misdiagnosed as MS were discovered rather late through genetic screening and the MS patients were matched according to age and sex thereafter. Further validation of the algorithm in a cohort with lower disease duration is warranted. Another limitation is that different 3T models were used in the clinical and the repeatability portion of the study. Although it was the same scanner in both studies, it underwent an upgrade from a Trio to a Prisma^{Fit} due to clinical needs before the phantom arrived on site. All participants were scanned before the upgrade except for the healthy control and the phantom for the repeatability scans.

5.5.5 Conclusions

This study explored the feasibility of combining a clinically feasible quantitative MRI technique with machine learning in order to differentiate two demyelinating and neurodegenerative phenotypes, HDLS and MS, that are hard to distinguish clinically and with conventional neuroimaging. The machine learning method was able to distinguish MS from HDLS to 100%, even allowing an artificially added noise of 1%. Our prediction method could potentially be integrated into clinics since the used imaging technique is clinically approved, time-efficient and additionally produces traditional and conventional image contrasts, as well as robust volumetry (Granberg, Uppman, et al., 2016), without manual adjustments.

5.5.6 Future studies

Future studies will include a) similar approaches (machine learning combined with quantitative MRI) to differentiate the diagnosis of other mimicking neuroinflammatory/neurodegenerative diagnoses, such as MS, neuromyelitis optica spectrum disorder, migraine, ischemic brain lesions or other neuroinflammatory disorders. Application of the method to less rare pathologies would most likely produce a more generalizable algorithm due to larger pools of patients available. b) Study the relevance of similar approaches for routine screening and early diagnosis. c) Evaluating whether there are detectable cortical lesions in HDLS with advanced MRI. d) Functional and structural studies on monocytes and microglia, will help to understand the difference between MS and HDLS underlying neurodegenerative mechanisms.

5.6 Acknowledgments and Disclosures

5.7   References

Adams, S. J., Kirk, A., & Auer, R. N. (2018). Adult-onset leukoencephalopathy with axonal spheroids and pigmented glia (ALSP): Integrating the literature on hereditary diffuse leukoencephalopathy with spheroids (HDLS) and pigmentary orthochromatic leukodystrophy (POLD). *Journal of Clinical Neuroscience: Official Journal of the Neurosurgical Society of Australasia*, *48*, 42–49.

Axelsson, R., Röyttä, M., Sourander, P., Akesson, H. O., & Andersen, O. (1984). Hereditary diffuse leucoencephalopathy with spheroids. *Acta Psychiatrica Scandinavica. Supplementum*, *314*, 1–65.

Baba, Y., Ghetti, B., Baker, M. C., Uitti, R. J., Hutton, M. L., Yamaguchi, K., Bird, T., Lin, W., DeLucia, M. W., Dickson, D. W., & Wszolek, Z. K. (2006). Hereditary diffuse leukoencephalopathy with spheroids: clinical, pathologic and genetic studies of a new kindred. *Acta Neuropathologica*, *111*(4), 300–311.

Cohen-Adad, J., Polimeni, J. R., Helmer, K. G., Benner, T., McNab, J. A., Wald, L. L., Rosen, B. R., & Mainero, C. (2012). T_2* mapping and B_0 orientation-dependence at 7 T reveal cyto- and myeloarchitecture organization of the human cortex. *NeuroImage*, *60*(2), 1006–1014.

Fisher, R. A. (1936). The Use of Multiple Measurements in Taxonomic Problems. *Annals of Eugenics*, *7*, 179–188.

Freeman, S. H., Hyman, B. T., Sims, K. B., Hedley-Whyte, E. T., Vossough, A., Frosch, M. P., & Schmahmann, J. D. (2009). Adult onset leukodystrophy with neuroaxonal spheroids: clinical, neuroimaging and neuropathologic observations. *Brain Pathology* , *19*(1), 39–47.

Granberg, T., Hashim, F., Andersen, O., Sundal, C., & Karrenbauer, V. D. (2016). Hereditary diffuse leukoencephalopathy with spheroids - a volumetric and radiological comparison with multiple sclerosis patients and healthy controls. *European Journal of Neurology: The Official Journal of the European Federation of Neurological Societies*, *23*(4), 817–822.

Granberg, T., Uppman, M., Hashim, F., Cananau, C., Nordin, L. E., Shams, S., Berglund, J., Forslin, Y., Aspelin, P., Fredrikson, S., & Kristoffersen-Wiberg, M. (2016). Clinical Feasibility of Synthetic MRI in Multiple Sclerosis: A Diagnostic and Volumetric Validation Study. *AJNR. American Journal of Neuroradiology*, *37*(6), 1023–1029.

Hagiwara, A., Hori, M., Cohen-Adad, J., Nakazawa, M., Suzuki, Y., Kasahara, A., Horita, M., Haruyama, T., Andica, C., Maekawa, T., Kamagata, K., Kumamaru, K. K., Abe, O., & Aoki, S. (2019). Linearity, Bias, Intrascanner Repeatability, and Interscanner Reproducibility of Quantitative Multidynamic Multiecho Sequence for Rapid Simultaneous Relaxometry at 3 T: A Validation Study With a Standardized Phantom and Healthy Controls. *Investigative Radiology*, *54*(1), 39–47.

Hagiwara, A., Hori, M., Yokoyama, K., Nakazawa, M., Ueda, R., Horita, M., Andica, C., Abe, O., & Aoki, S. (2017). Analysis of White Matter Damage in Patients with Multiple Sclerosis via a Novel In Vivo MR Method for Measuring Myelin, Axons, and G-Ratio. *AJNR. American Journal of Neuroradiology*, *38*(10), 1934–1940.

Hagiwara, A., Hori, M., Yokoyama, K., Takemura, M. Y., Andica, C., Kumamaru, K. K., Nakazawa, M., Takano, N., Kawasaki, H., Sato, S., Hamasaki, N., Kunimatsu, A., & Aoki, S. (2017). Utility of a Multiparametric Quantitative MRI Model That Assesses Myelin and Edema for Evaluating Plaques, Periplaque White Matter, and Normal-Appearing White Matter in Patients with Multiple Sclerosis: A Feasibility Study. *AJNR. American Journal of Neuroradiology*, *38*(2), 237–242.

Hagiwara, A., Warntjes, M., Hori, M., Andica, C., Nakazawa, M., Kumamaru, K. K., Abe, O., & Aoki, S. (2017). Symri of the Brain: Rapid Quantification of Relaxation Rates and Proton Density, With Synthetic Mri, Automatic Brain Segmentation, and Myelin Measurement. *Investigative Radiology*, *52*(10), 647–657.

Huberty, C. J., & Olejnik, S. (Eds.). (2006). Two-Group Classification. In W. A. Shewhart & S. S. Wilks, *Applied MANOVA and Discriminant Analysis* (pp. 349–360). John Wiley & Sons, Inc.

Karle, K. N., Biskup, S., Schüle, R., Schweitzer, K. J., Krüger, R., Bauer, P., Bender, B., Nägele, T., & Schöls, L. (2013). De novo mutations in hereditary diffuse leukoencephalopathy with axonal spheroids (HDLS). *Neurology*, *81*(23), 2039–2044.

Keenan, K. E., Stupic, K. F., Boss, M. A., Russek, S. E., Chenevert, T. L., Prasad, P. V., Reddick, W. E., Cecil, K. M., Zheng, J., Hu, P., Jackson, E. F., & and Ad Hoc Committee for Standards in Quantitative MR. (2016). *Multi-site, multi-vendor comparison of T1 measurement using ISMRM/NIST system phantom*. ISMRM, Singapore. http://archive.ismrm.org/2016/3290.html

Kim, H. G., Moon, W.-J., Han, J., & Choi, J. W. (2017). Quantification of myelin in children using multiparametric quantitative MRI: a pilot study. *Neuroradiology*. https://doi.org/10.1007/s00234-017-1889-9

Konno, T., Broderick, D. F., Mezaki, N., Isami, A., Kaneda, D., Tashiro, Y., Tokutake, T., Keegan, B. M., Woodruff, B. K., Miura, T., Nozaki, H., Nishizawa, M., Onodera, O., Wszolek, Z. K., & Ikeuchi, T. (2017). Diagnostic Value of Brain Calcifications in Adult-Onset Leukoencephalopathy with Axonal Spheroids and Pigmented Glia. *AJNR. American Journal of Neuroradiology*, *38*(1), 77–83.

Konno, T., Kasanuki, K., Ikeuchi, T., Dickson, D. W., & Wszolek, Z. K. (2018). CSF1R-related leukoencephalopathy: A major player in primary microgliopathies. *Neurology*, *91*(24), 1092–1104.

Lublin, F. D. (2014). New multiple sclerosis phenotypic classification. *European Neurology*, *72 Suppl 1*, 1–5.

Mainero, C., Louapre, C., Govindarajan, S. T., Giannì, C., Nielsen, A. S., Cohen-Adad, J., Sloane, J., & Kinkel, R. P. (2015). A gradient in cortical pathology in multiple sclerosis by in vivo quantitative 7 T imaging. *Brain: A Journal of Neurology*, *138*(Pt 4), 932–945.

Ouellette, R., Mangeat, G., Polyak, I., Warntjes, M., Forslin, Y., Bergendal, Å., Plattén, M., Uppman, M., Treaba, C. A., Cohen-Adad, J., Piehl, F., Wiberg, M. K., Fredrikson, S., Mainero, C., & Granberg, T. (2020). Validation of rapid magnetic resonance myelin imaging in multiple sclerosis. *Annals of Neurology*. https://doi.org/10.1002/ana.25705

Polman, C. H., Reingold, S. C., Banwell, B., Clanet, M., Cohen, J. A., Filippi, M., Fujihara, K., Havrdova, E., Hutchinson, M., Kappos, L., Lublin, F. D., Montalban, X., O'Connor, P., Sandberg-Wollheim, M., Thompson, A. J., Waubant, E., Weinshenker, B., & Wolinsky, J. S. (2011). Diagnostic criteria for multiple sclerosis: 2010 revisions to the McDonald criteria. *Annals of Neurology*, *69*(2), 292–302.

Rademakers, R., Baker, M., Nicholson, A. M., Rutherford, N. J., Finch, N., Soto-Ortolaza, A., Lash, J., Wider, C., Wojtas, A., DeJesus-Hernandez, M., Adamson, J., Kouri, N., Sundal, C., Shuster, E. A., Aasly, J., MacKenzie, J., Roeber, S., Kretzschmar, H. A., Boeve, B. F., … Wszolek, Z. K. (2011). Mutations in the colony stimulating factor 1 receptor (CSF1R) gene cause hereditary diffuse leukoencephalopathy with spheroids. *Nature Genetics*, *44*(2), 200–205.

Saccenti, L., Andica, C., Hagiwara, A., Yokoyama, K., Takemura, M. Y., Fujita, S., Maekawa, T., Kamagata, K., Le Berre, A., Hori, M., Hattori, N., & Aoki, S. (2019). Brain tissue and myelin volumetric analysis in multiple sclerosis at 3T MRI with various in-plane resolutions using synthetic MRI. *Neuroradiology*, *61*(11), 1219–1227.

Saitoh, B.-Y., Yamasaki, R., Hayashi, S., Yoshimura, S., Tateishi, T., Ohyagi, Y., Murai, H., Iwaki, T., Yoshida, K., & Kira, J.-I. (2013). A case of hereditary diffuse leukoencephalopathy with axonal spheroids caused by a de novo mutation in CSF1R masquerading as primary progressive multiple sclerosis. *Multiple Sclerosis* , *19*(10), 1367–1370.

Sokolova, M., & Lapalme, G. (2009). A systematic analysis of performance measures for classification tasks. *Information Processing & Management*, *45*(4), 427–437.

Sundal, C., Baker, M., Karrenbauer, V., Gustavsen, M., Bedri, S., Glaser, A., Myhr, K.-M., Haugarvoll, K., Zetterberg, H., Harbo, H., Kockum, I., Hillert, J., Wszolek, Z., Rademakers, R., & Andersen, O. (2015). Hereditary diffuse leukoencephalopathy with spheroids with phenotype of primary progressive multiple sclerosis. *European Journal of Neurology: The Official Journal of the European Federation of Neurological Societies*, *22*(2), 328–333.

Sundal, C., Lash, J., Aasly, J., Øygarden, S., Roeber, S., Kretzschman, H., Garbern, J. Y., Tselis, A., Rademakers, R., Dickson, D. W., Broderick, D., & Wszolek, Z. K. (2012). Hereditary diffuse leukoencephalopathy with axonal spheroids (HDLS): a misdiagnosed disease entity. *Journal of the Neurological Sciences*, *314*(1-2), 130–137.

Sundal, C., Van Gerpen, J. A., Nicholson, A. M., Wider, C., Shuster, E. A., Aasly, J., Spina, S., Ghetti, B., Roeber, S., Garbern, J., Borjesson-Hanson, A., Tselis, A., Swerdlow, R. H., Miller, B. B., Fujioka, S., Heckman, M. G., Uitti, R. J., Josephs, K. A., Baker, M., … Wszolek, Z. K. (2012). MRI characteristics and scoring in HDLS due to CSF1R gene mutations. *Neurology*, *79*(6), 566–574.

Thompson, A. J., Banwell, B. L., Barkhof, F., Carroll, W. M., Coetzee, T., Comi, G., Correale, J., Fazekas, F., Filippi, M., Freedman, M. S., Fujihara, K., Galetta, S. L., Hartung, H. P., Kappos, L., Lublin, F. D., Marrie, R. A., Miller, A. E., Miller, D. H., Montalban, X., … Cohen, J. A. (2018). Diagnosis of multiple sclerosis: 2017 revisions of the McDonald criteria. *Lancet Neurology*, *17*(2), 162–173.

Thompson, A. J., Baranzini, S. E., Geurts, J., Hemmer, B., & Ciccarelli, O. (2018). Multiple sclerosis. *The Lancet*, *391*(10130), 1622–1636.

Vågberg, M., Lindqvist, T., Ambarki, K., Warntjes, J. B. M., Sundström, P., Birgander, R., & Svenningsson, A. (2013). Automated determination of brain parenchymal fraction in multiple sclerosis. *AJNR. American Journal of Neuroradiology*, *34*(3), 498–504.

Vaughn, J., Hagiwara, M., Katz, J., Roth, J., Devinsky, O., Weiner, H., & Milla, S. (2013). MRI characterization and longitudinal study of focal cerebellar lesions in a young tuberous sclerosis cohort. *AJNR. American Journal of Neuroradiology*, *34*(3), 655–659.

Warntjes, J. B. M., Leinhard, O. D., West, J., & Lundberg, P. (2008). Rapid magnetic resonance quantification on the brain: Optimization for clinical usage. *Magnetic Resonance in Medicine: Official Journal of the Society of Magnetic Resonance in Medicine / Society of Magnetic Resonance in Medicine*, *60*(2), 320–329.

Warntjes, J. B. M., Persson, A., Berge, J., & Zech, W. (2017). Myelin Detection Using Rapid Quantitative MR Imaging Correlated to Macroscopically Registered Luxol Fast Blue-Stained Brain Specimens. *AJNR. American Journal of Neuroradiology*, *38*(6), 1096–1102.

Warntjes, M., Engström, M., Tisell, A., & Lundberg, P. (2016). Modeling the Presence of Myelin and Edema in the Brain Based on Multi-Parametric Quantitative MRI. *Frontiers in Neurology*, *7*, 16.

Wattjes, M. P., Rovira, À., Miller, D., Yousry, T. A., Sormani, M. P., de Stefano, M. P., Tintoré, M., Auger, C., Tur, C., Filippi, M., Rocca, M. A., Fazekas, F., Kappos, L., Polman, C., Frederik Barkhof, Xavier Montalban, & MAGNIMS study group. (2015). Evidence-based guidelines: MAGNIMS consensus guidelines on the use of MRI in multiple sclerosis--establishing disease prognosis and monitoring patients. *Nature Reviews. Neurology*, *11*(10), 597–606.

West, J., Warntjes, J. B. M., & Lundberg, P. (2012). Novel whole brain segmentation and volume estimation using quantitative MRI. *European Radiology*, *22*(5), 998–1007.

Ye, J., Janardan, R., & Li, Q. (2005). Two-Dimensional Linear Discriminant Analysis. In L. K. Saul, Y. Weiss, & L. Bottou (Eds.), *Advances in Neural Information Processing Systems 17* (pp. 1569–1576). MIT Press.

Yushkevich, P. A., Piven, J., Hazlett, H. C., Smith, R. G., Ho, S., Gee, J. C., & Gerig, G. (2006). User-guided 3D active contour segmentation of anatomical structures: significantly improved efficiency and reliability. *NeuroImage*, *31*(3), 1116–1128.

CHAPTER 6   ARTICLE 3: REPEATABILITY AND REPRODUCIBILITY OF QUANTITATIVE SYNTHETIC MRI ACROSS VENDORS AND FIELD STRENGTHS

Title: Repeatability and reproducibility of quantitative synthetic MRI across vendors and field strengths

Authors: Gabriel Mangeat (1,2), Russell Ouellette (2,3), Michael Plattén (2,3,4), Sven Petersson (5,6), Hadrien Van Loo (5), Atef Badji (1,7), Nikola Stikov (1,8), Tobias Granberg* (2,3), Julien Cohen-Adad* (1,9)

Affiliations:

(1) NeuroPoly Lab, Institute of Biomedical Engineering, Polytechnique Montreal, Montreal, QC, Canada

(2) Department of Clinical Neuroscience, Karolinska Institutet, Stockholm, Sweden

(3) Department of Neuroradiology, Karolinska University Hospital, Stockholm, Sweden

(4) School of Engineering Sciences in Chemistry, Biochemistry and Health, Royal Institute of Technology, Stockholm, Sweden

(5) Medical Radiation Physics and Nuclear Medicine, Karolinska University Hospital, Stockholm, Sweden

(6) Department of Clinical Science Intervention and Technology, Karolinska Institutet, Stockholm, Sweden

(7) Division of Clinical Geriatrics, Department of Neurobiology, Care Sciences and Society, Karolinska Institutet, Stockholm, Sweden

(8) Montreal Heart Institute, Montreal, QC, Canada

(9) Functional Neuroimaging Unit, CRIUGM, Université de Montréal, Montreal, QC, Canada

(*) Both last co-authors have jointly supervised this work

6.1 Abstract

Background: Quantitative MRI can enable comparisons of scans longitudinally and between patients, studying subtle pathological mechanisms and achieving improved tissue-specificity such as myelin imaging. However, clinical implementations are often hampered by long scan times or complex post-processing. Synthetic MRI (SyMRI) provides clinically approved quantitative MRI but independent evaluations of its precision are scarce.

Aim: To assess the repeatability, reproducibility and precision of SyMRI-derived metrics.

Methods: Five healthy controls were scanned with SyMRI on six scanners (GE, Philips, Siemens; 1.5 and 3 T) on the same day. One of the controls was scanned on three additional scanner models. For every scan, five acquisitions were made with two repositionings (3+1+1 protocol), yielding a total of 165 SyMRI acquisitions. Quantitative PD, T1, T2 and Rapid Estimation of Myelin (REMyDI) maps were averaged across the white matter and grey matter.

Results: Intra-scanner coefficient of variation ranged from 0.10% for PD to 1.97% for T1 in the white matter and 0.10% for PD to 3.38% for REMyDI in the grey matter. The inter-scanner coefficients of variations were larger, from 1.60% and 1.08% for PD in the white and grey matter respectively to 4.84% and 20.2% for REMyDI in the white and grey matter respectively. We also observed that the field strength and the repositioning procedure do not have a significant impact on the repeatability.

Conclusions: SyMRI offers good repeatability within a single scanner. Despite finding relatively more variability across scanners, quantitative comparisons across scanners remain viable. To mitigate the inter-scanner variability, multi-center studies should ideally acquire calibration data using a travelling phantom.

6.2 Introduction

Magnetic Resonance Imaging (MRI) is an essential clinical tool for non-invasive studies of the human brain due to its ability to visualize a wide range of tissue properties with millimetric spatial resolution without ionizing radiation. Morphologic MRI images are widely used in clinics for diagnoses and in research for studying the physiology and pathophysiology of the human brain (Katti et al., 2011; Thompson et al., 2018). However, unlike the commonly used Hounsfield units of computed tomography, pixel intensities on conventional MRI are arbitrarily scaled and are substantially affected by several variable factors such as the homogeneity of the B0 and B1 fields, coil sensitivity profiles, RF amplification settings, calibration, or hardware differences in MRI vendor and model (Caverly, 2015; Gach et al., 2020; Giovannetti et al., 2007; Ibrahim and Tang, 2007; Lin et al., 2003). Quantitative MRI (qMRI) techniques aim to overcome this flaw by providing comparable measurements across patients, scanners, sites and over time (Stikov et al., 2014; Warntjes et al., 2008). Combining the morphological and quantitative information contained within MRI images opens the door to more accurate observations and diagnostics (Granberg et al., 2016a, 2016b; A. Hagiwara et al., 2017a, 2017b; Mangeat et al., 2020). qMRI also has the potential to describe subtle pathological mechanisms and achieve improved tissue-specificity (Cohen-Adad et al., 2012; Gupta et al., 2017; Mainero et al., 2015; Ouellette et al., 2020; Vaughn et al., 2013).

Quantitative relaxometry is a popular qMRI technique. The longitudinal relaxation time T1 (Lutti et al., 2014; Stikov et al., 2014; van der Kouwe et al., 2008), the transverse relaxation times T2 (Ben-Eliezer et al., 2015) and T2* (Cohen-Adad, 2014; Cohen-Adad et al., 2012, 2011; Stüber et al., 2014) and the proton density, PD, (Chong et al., 2016; Gracien et al., 2016; Mezer et al., 2016) are four MRI metrics characterizing underlying tissues. As a single voxel usually contains several tissue types, multi-exponential modeling can be applied to recover the relaxation parameters of each tissue. However, conventional multi-exponential relaxometry measurements are demanding in terms of scan time and complex processing (Does, 2018; Mackay et al., 1994). Despite rising research interest and clinical potential for qMRI, there remain comparable limitations regarding complex acquisition protocols, lack of clinical approval and/or post-processing that may often hamper (McGuire et al., 2017) their potential utility in clinics. Thus, there exists a need for fast, simple and clinically approved qMRI techniques (Granberg et al., 2016a, 2016b; A. Hagiwara et al., 2017a, 2017b; Mangeat et al., 2020). The more repeatable and reproducible the qMRI

techniques are across vendors, field strengths and centers, the more precise quantitative imaging metrics or biomarkers can be derived and proposed for diagnostic standards.

Of those qMRI applications that hold clinical potential, Synthetic MRI (SyMRI) provides quantitative PD, T1 and T2 maps as well as rapid myelin estimation for diagnostic imaging (REMyDI) via a single acquisition (Akifumi Hagiwara et al., 2017). In addition to the advantages associated with the single acquisition (e.g., no co-registration required), synthetic MRI has been validated as a time-efficient imaging method for a number of clinical applications (A. Hagiwara et al., 2017a, 2017b; Akifumi Hagiwara et al., 2017; Vågberg et al., 2013) and has been approved in several major healthcare markets for clinical use.

The repeatability and reproducibility of SyMRI have recently been assessed on 3 scanners for 3 vendors by Hagiwara et al. (Hagiwara et al., 2019). Here, we aimed to build upon this work by assessing the repeatability and reproducibility to measure the level of confidence of SyMRI derived metrics based on a total of 165 test-retest acquisitions with and without repositioning from 9 different scanner models from the 3 major MRI vendors, at 1.5 T and 3 T.

6.3 Methods

6.3.1 Acquisition

Five healthy controls (two females, three males, 30±1 years old) were scanned on six scanners (GE 450w 1.5 T, GE 750w 3 T, Philips Ingenia 1.5 T, Philips Ingenia 3 T, Siemens Aera 1.5 T and Siemens PrismaFit 3 T) on the same day, see Table 1. One of the healthy controls was scanned on four additional scanner models (Siemens AvantoFit 1.5 T, Siemens Skyra 3 T and Siemens Vida 3 T) within two weeks. For every scanning session, five test-retest acquisitions were made; the three first acquisitions were performed without reposition and the two last with repositioning (3+1+1 protocol), yielding a total of 165 acquisitions. The default acquisition parameters for the multi-dynamic multi-echo sequence (referred to as MDME, Syntac or MAGiC, depending on the vendor) were used for each scanner with a harmonization of the slice thickness (4 mm, 1 mm gap) and number of slices (32 slices). Detailed acquisition parameters are given in Table 6.1.

Table 6.1 Acquisition parameters of the SyMRI sequence for the nine scanners used in this study. FOV: Field Of View; TR: readout time; TE: echo time; TI: inversion time; N: number of healthy controls scanned.

Scanner	Field strength [T]	FOV [mm]	Matrix size [pixels]	TR [ms]	TE [ms]	N
GE 750w	3.0	230x184	512x512	4101	22, 89	5
Philips Ingenia	3.0	230x187	432x432	4833	13, 100	5
Siemens PrismaFit	3.0	230x187	260x320	4640	23, 101	5
Siemens Skyra	3.0	230x230	320x320	4640	23, 101	1
Siemens Vida	3.0	230x187	260x320	4640	23, 101	1
GE 450w	1.5	230x207	512x512	4057	21, 95	5
Philips Ingenia	1.5	230x190	432x432	4784	13, 100	5
Siemens Aera	1.5	230x187	260x320	4480	22, 97	5
Siemens AvantoFit	1.5	230x187	260x320	4440	21, 96	1

6.3.2 Processing

The software SyMRI 11.2.2 was used to calculate the quantitative PD, T1, T2 and REMyDI maps. REMyDI is an estimation of the myelin volume fraction based on a non-linear combination of the PD, T1 and T2 maps, as previously described (Warntjes et al., 2017, 2016). The REMyDI technique has recently been validated *ex vivo* and *in vivo* in MS (Ouellette et al., 2020). Since all quantitative maps are based on the same acquisition, they are inherently aligned.

6.3.3 Masks

Grey matter (GM) and white matter (WM) were also automatically generated using the SyMRI software in the healthy controls based on a linear combination of the quantitative T1, T2 and PD maps and known relaxometry values of GM/WM/CSF from healthy reference data as previously described (West et al., 2012). The relaxometry-based volumetry was performed offline within less than 10 seconds on a standard laptop (Saccenti et al., 2019).

6.3.4 Statistical analysis

For each acquisition, eight metrics were computed by averaging the four quantitative maps (PD, T1, T2 and REMyDI) across the two tissue masks, (GM and WM). For each subject, the absolute value of these metrics was then compared intra- and inter-scanner by calculating the Coefficient of Variation (CoV, Equation 6.1) (Carstensen, 2010). The CoVs were averaged across subjects to compute the CoVs per scanner and metric.

Equation 6.1: $\text{CoV}\,[\%] = 100 * \frac{\sigma}{\mu}$

Where σ is the standard deviation of a distribution and μ is the mean. The advantage of using the CoV compared to the standard deviation, is that we can compare CoVs of two distributions even if the measurement unit is different, making it suitable to compare different qMRI methods. In addition, the precision of a measurement method is often given as the CoV (Carstensen, 2010).

The repeatability of a measurement is defined as the upper limit of a prediction interval for the absolute difference between two measurements by the same method on the same item under *identical circumstances* (5725-2, 1994; Carstensen, 2010). Here, we defined the repeatability as the same metric from the same control subject acquired on the same MRI scanner. The repeatability was calculated according to Equation 6.2:

Equation 6.2: $\text{Repeatability} = 1.96 * \sqrt{2} * \sigma$

The distinction between repeatability and reproducibility is only a question of the sources of variation included in the definition of σ (5725-2, 1994; Carstensen, 2010). The reproducibility coefficient for a method is defined as the upper limits of a prediction interval for the absolute difference between two measurements by the same method on the same item under *different circumstances*, here, different scanners.

For the repositioning analysis we calculated the relative variation on the acquisition *N* compared to the measure made at the first acquisition, according to Equation 6.3:

Equation 6.3: $Variation\_acq\_N = 100 * \dfrac{|measure\_acq\_1 - measure\_acq\_N|}{measure\_acq\_1}$

Where *measure_acq_1* is the measure of a metric at the first acquisition and *measure_acq_N* in the repeated measure of the same metric at the acquisition *N*.

6.3.5 Ethics

This study was approved by the Regional Ethics board in Stockholm and written informed consent was obtained from all participants.

6.3.6 Data availability

The ethical approval and consent for this study did not cover sharing individual subjects' imaging data. Numeric output and aggregated data on a group level are available from the corresponding author, upon reasonable request.

6.4 3 Results

6.4.1 Quality control of the data

Figure 6.1 shows the T1 maps of one of the controls (29-year-old male); each column represents a different scanner and each line a different acquisition. Within the same field strength, no major differences across acquisitions could be visually observed on the T1 maps. As expected, T1 values were overall lower at 1.5 T than at 3 T. No overt artifacts were visible on the T1 and PD maps. Concerning the T2 maps, some volumes acquired with the GE scanners were hampered by eddy current artifacts inducing errors in the quantitative maps and, therefore, in the automatic brain segmentation. After a quality check of the brain segmentation done by a trained rater (G.M.) with guidance of a radiologist (T.G.), some volumes had to be discarded (19 volumes from the GE 450w).
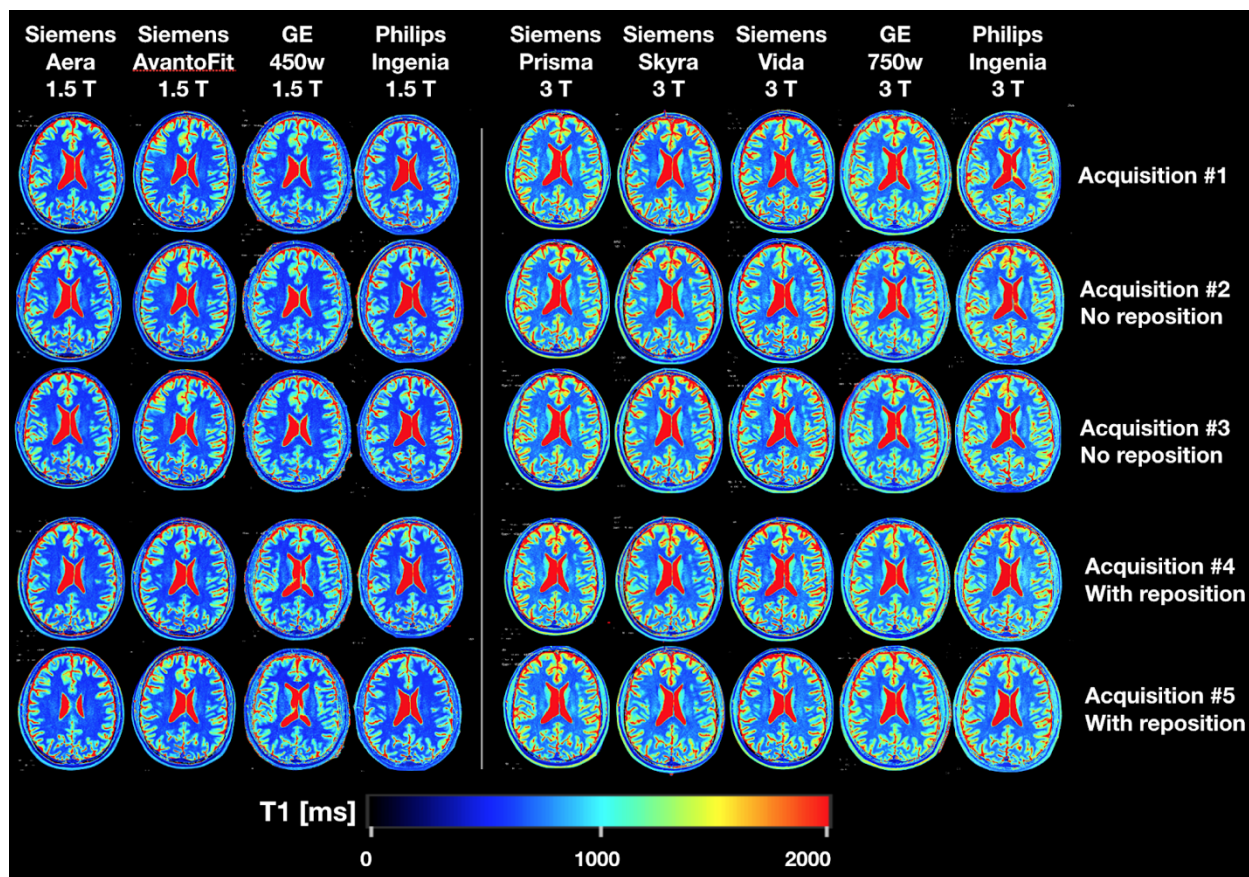
Figure 6.1 T1 mapping for each of the test-retests of one 29-year-old male healthy control. Left panel: 1.5 T scanners, right panel: 3 T scanners. Within the same field strength, no major differences across acquisitions could be visually observed on the T1 maps. As expected, T1 values were overall lower at 1.5 T than at 3 T.

6.4.2 Comparison of the quantitative metrics

Figure 6.2 shows every quantitative value obtained for each of the eight metrics of interest. Overall, we notice good intra-scanner repeatabilities and larger inter-scanner variabilities, compared to the reference CoV lines (1% and 5%). For T1 and T2, the reference CoV lines are split as different values are expected whether a 3 T or 1.5 T scanner is used.
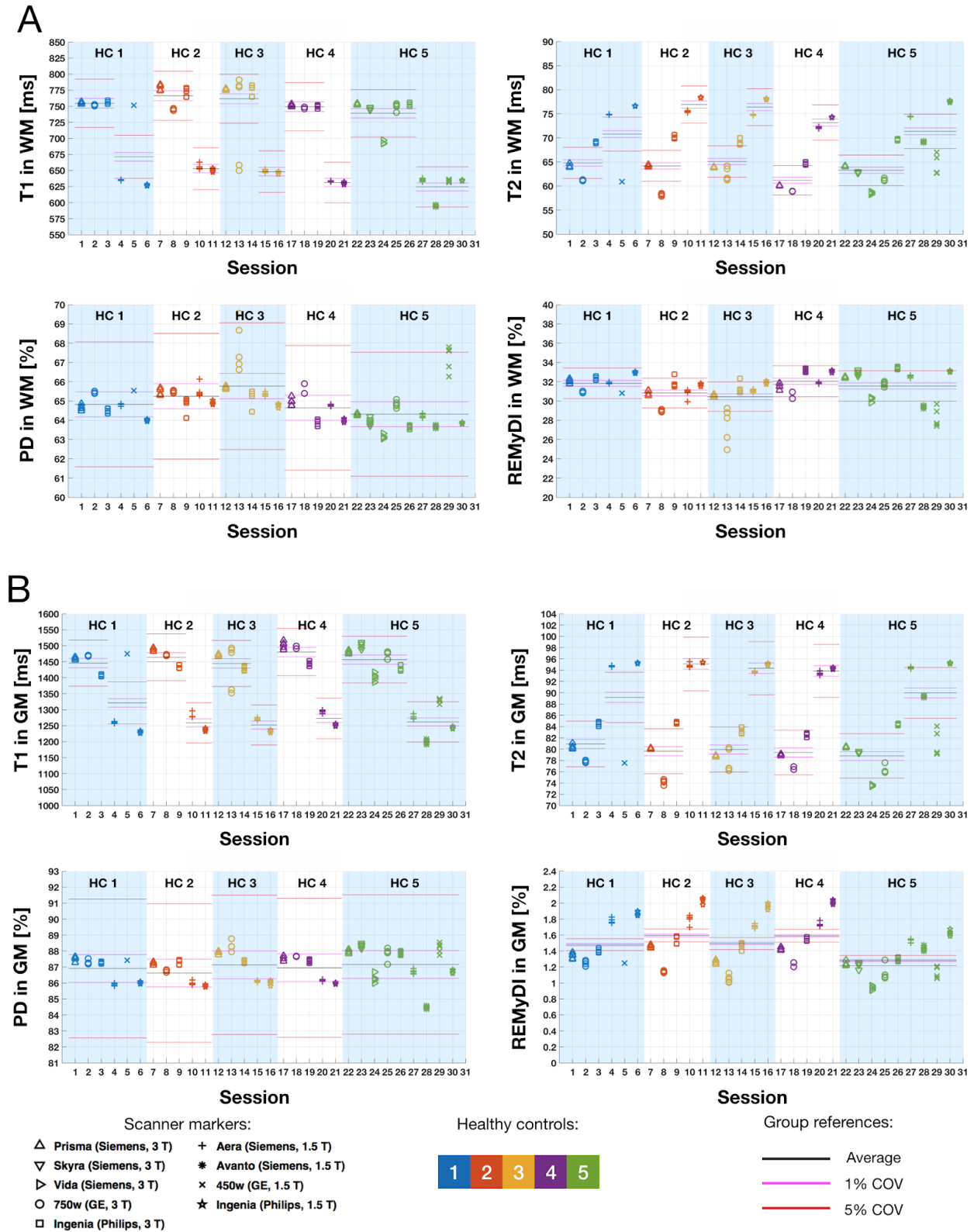
Figure 6.2 Values of the four quantitative metrics T1, T2, PD and REMyDI in WM (A) and GM (B). Each acquisition is displayed on the graph with different markers for different scanners. For

every subject, the average of the metric value is displayed with a black line and the +/-1% and +/-5% CoVs are displayed with purple and red lines respectively. For T1 and T2, as we expect different values at 1.5 and 3 T, the reference CoV lines were split per field strength. PD: proton density; REMyDI: Rapid Estimation of Myelin; WM: white matter; GM: grey matter; COV: coefficient of variation; HC: healthy control.

6.4.3 Coefficients of variation of the quantitative metrics

Table 2 shows the CoVs for the eight metrics of interest (T1, T2, PD and REMyDI in WM and GM). The CoVs were calculated according to Equation 6.1. For T1 and T2, as we expect to measure a different value at 3T than at 1.5T, the CoVs were calculated per field strength, then averaged. We observe a low intra-scanner CoV ranging from 0.10% to 1.97% for the four maps averaged in the white matter and 0.11% to 3.38% for maps averaged in the GM. The inter-scanner CoVs are numerically larger. We observe that for each metric (column) the inter-scanner CoVs are about 5 to 10 times larger than the mean intra-scanner CoVs. REMyDI in GM is an outlier; as the mean myelin estimation in the GM is low compared to its variation, it leads to a larger CoV.

Table 6.2 Average intra- and inter-scanner CoVs for the four quantitative metrics T1, T2, PD and REMyDI in WM and GM. PD: proton density; REMyDI: Rapid Estimation of Myelin; WM: white matter; GM: grey matter; CoV: coefficient of variation.

	T1 in WM	T2 in WM	PD in WM	REMyDI in WM	T1 in GM	T2 in GM	PD in GM	REMyDI in GM	Mean
Intra-scanner	CoV [%]	CoV [%]	CoV [%]	CoV [%]	CoV [%]	CoV [%]	CoV [%]	CoV [%]	CoV [%]
GE 750w 3 T	1.97	0.57	0.48	1.66	1.10	0.83	0.18	3.38	1.27
Philips Ingenia 3 T	0.44	0.38	0.32	0.88	0.34	0.30	0.10	1.90	0.58
Siemens PrismaFit 3 T	0.24	0.22	0.18	0.53	0.33	0.21	0.12	1.69	0.44
Siemens Skyra 3 T	0.20	0.16	0.26	0.64	0.50	0.13	0.13	2.58	0.58
Siemens Vida 3 T	0.28	0.30	0.15	0.64	0.74	0.16	0.26	2.24	0.60
GE 450w 1.5 T	0.16	1.45	0.44	1.57	0.24	1.27	0.16	2.93	1.03
Philips Ingenia 1.5 T	0.20	0.11	0.10	0.29	0.26	0.11	0.08	1.48	0.33
Siemens Aera 1.5 T	0.27	0.12	0.18	0.53	0.35	0.20	0.09	1.64	0.42
Siemens AvantoFit 1.5 T	0.17	0.14	0.10	0.39	0.49	0.14	0.09	1.72	0.41
Intra-scanner mean	0.44	0.38	0.25	0.79	0.48	0.37	0.14	2.17	0.63
Inter-scanner	3.36	5.83	1.60	4.84	2.84	4.48	1.08	20.19	5.53

6.4.4 Repeatability and reproducibility

Table 3 shows the repeatability and reproducibility coefficients for the eight metrics of interest. Overall we again observed good repeatability and reproducibility 5 to 10 times lower. In terms of the different metrics, we observe that PD is the most reproducible, followed by T1, T2 and REMyDI. We note an outlier for T1 in WM measured with GE 750W (40.1 ms of repeatability compared to a mean of 8.7 ms).

Table 6.3 Mean value, repeatability and reproducibility coefficients for the eight metrics of interest (T1, T2, PD and REMyDI in WM and GM). For T1 and T2, the mean values and reproducibility coefficients were first computed per field strength, then averaged. We observe good repeatability, for example, when we measure T1 in the gray matter with the Siemens Prisma, we measure 1480 ms with a repeatability of 7.74 ms, meaning that if we take a new measure, it should be comprised between 1473 ms and 1488 ms. Overall better repeatability than reproducibility is observed. PD: proton density; REMyDI: Rapid Estimation of Myelin; WM: white matter; GM: grey matter; Repeat.: repeatability; Repro.: reproducibility.

Intra-scanner	T1 in WM [ms]		T2 in WM [ms]		PD in WM [%]		REMyDI in WM [%]		T1 in GM [ms]		T2 in GM [ms]		PD in GM [%]		REMyDI in GM [%]	
	Mean	Repeat.	Mean	Repeat.	Mean	Repeat.	Mean	Repeat.	Mean	Repeat.	Mean	Repeat.	Mean	Repeat.	Mean	Repeat.
GE 750w 3 T	745	40.1	60.4	1.0	65.8	0.9	30.0	1.3	1469	18.7	76.6	1.8	87.6	0.5	1.16	0.1
Philips Ingenia 3 T	762	9.4	68.5	0.7	64.4	0.6	32.4	0.8	1428	7.7	83.8	0.7	87.4	0.2	1.45	0.1
Siemens PrismaFit 3 T	763	5.2	63.3	0.4	65.0	0.3	31.5	0.5	1480	7.7	79.7	0.5	87.6	0.3	1.35	0.1
Siemens Skyra 3 T	747	4.2	62.8	0.3	63.9	0.5	32.9	0.6	1500	10.2	79.4	0.3	88.3	0.3	1.22	0.1
Siemens Vida 3 T	693	5.3	58.5	0.5	63.1	0.3	30.2	0.5	1401	13.2	73.6	0.3	86.3	0.6	0.94	0.1
GE 450w 1.5T	692	2.8	62.5	2.6	66.4	0.8	29.5	1.2	1401	6.0	79.2	2.9	87.8	0.4	1.19	0.1
Philips Ingenia 1.5T	638	3.6	77.0	0.2	64.3	0.2	32.5	0.3	1238	6.0	95.0	0.3	86.1	0.2	1.90	0.1
Siemens Aera 1.5T	642	4.8	74.3	0.3	65.0	0.3	31.6	0.5	1277	7.3	94.2	0.5	86.2	0.2	1.71	0.1
Siemens AvantoFit 1.5T	595	2.9	69.2	0.3	63.7	0.2	29.4	0.3	1199	8.6	89.4	0.3	84.5	0.2	1.43	0.1
Intra-scanner mean	697	8.7	66.3	0.7	64.6	0.5	31.1	0.7	1377	9.5	83.4	0.8	86.9	0.3	1.37	0.1
Inter-scanner repro.	697	64.9	66.3	10.7	64.6	2.9	31.1	4.2	1377	108.3	83.4	10.4	86.9	2.6	1.37	0.8

6.4.5 Effect of the repositioning

For each scanning session on each scanner, three acquisitions without repositioning and two acquisitions with repositioning were acquired. Taking the first acquisition as a reference, we

compared the effect of repositioning on the quantitative results. Figure 3 shows the deviation from the first acquisition in percent computed with Equation 6.3. For each metric, we observed a slightly higher mean deviation for the acquisitions made with repositioning. However, the difference was never significant (p > 0.05 for T1, T2, PD and REMyDI).
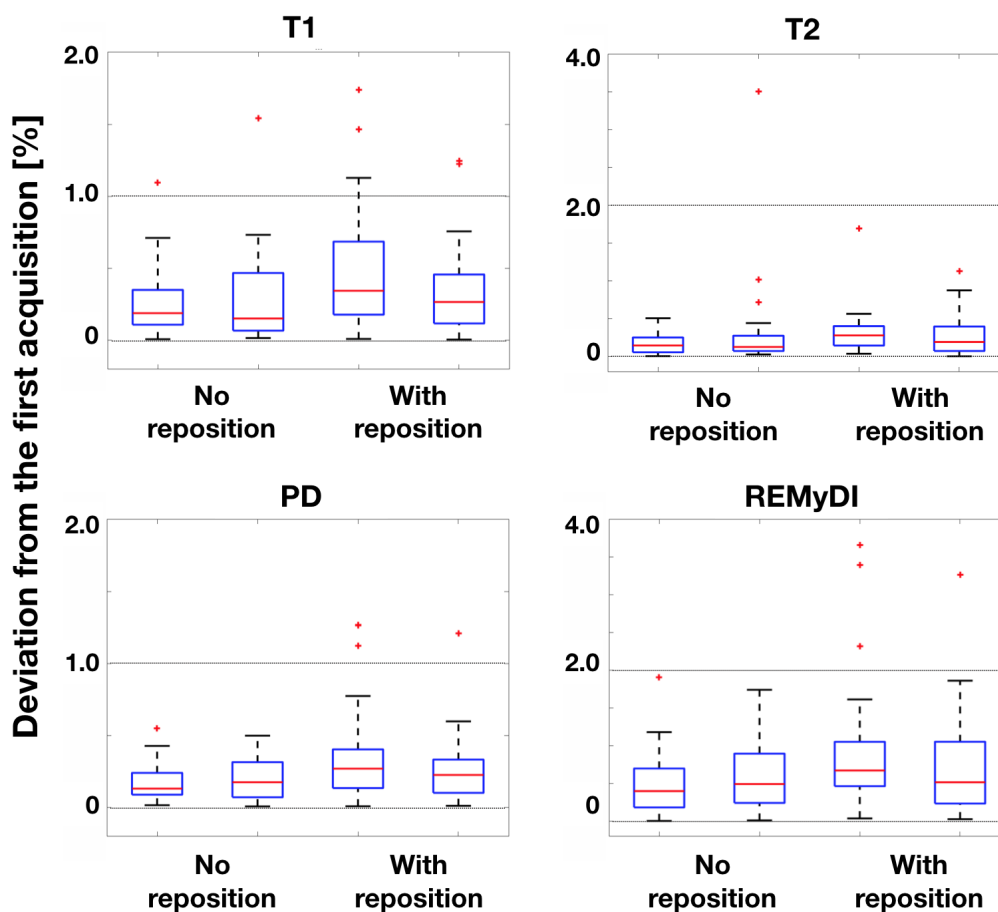
Figure 6.3 Deviation from the first acquisition in percent, computed using Equation 6.3. The four boxes correspond to the four rescans (two with reposition and two without). For each metric, we observed a slightly higher mean deviation for the acquisitions made with reposition. However, the difference was never significant (p > 0.05 for T1, T2, PD and REMyDI). The outlier measures can be observed in more detail in Figure 2. PD: proton density; REMyDI: Rapid Estimation of Myelin.

6.4.6 Effect of the field strength

Each control subject was, at the least, scanned with three 1.5 T and three 3 T MRI scanners. Figure 4 shows a comparison between the CoV measured at 1.5 vs. 3 T. The CoVs are used here as they are comparable across metrics and field strength. We observe that the mean CoVs tended to be higher for metrics acquired at 1.5 T than for metrics acquired at 3 T. However, this difference was never significant ($p > 0.05$ for T1, T2, PD and REMyDI), highlighting that in our current setup, using a 3 T MRI scanner did not lead to significantly more precise measures.
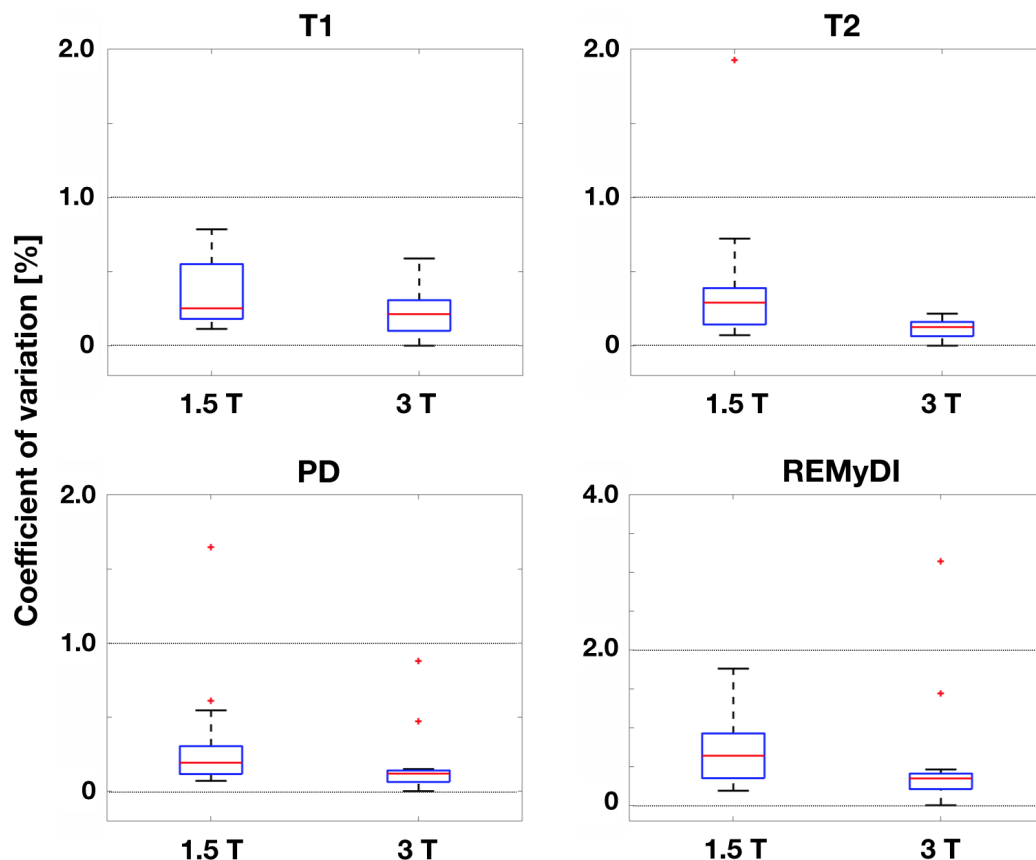
Figure 6.4 Comparison between the CoVs measured at 1.5 and 3 T. We observe that mean CoVs tended to be higher for metrics acquired at 1.5 T than at 3 T. However, this difference was never significant ($p > 0.05$ for T1, T2, PD and REMyDI). PD: proton density; REMyDI: Rapid Estimation of Myelin.

6.5 Discussion

In this study, we performed 165 acquisitions on 9 scanners from 3 vendors to assess the repeatability and reproducibility of the SyMRI quantitative protocol. Overall, the intra-scanner repeatability was good, with mean intra-scanners coefficients of variation ranging from 0.1% for the PD in GM to 3.4% for REMyDI in GM. The inter-scanner reproducibility always resulted in higher coefficients of variation, approximately 5 to 10 times the mean intra-scanner coefficients of variation, depending on the metric. Similarly, the reproducibility values were 5 to 10 times the repeatability.

One of the main goals of this work was to determine if SyMRI could be used for multicenter studies to obtain comparable data, where different parts of the cohort of subjects are scanned with different scanners. Our study suggests that it might be possible, but it depends on the scanners, the metric or biomarker studied and the effect size to be observed. For example, if one wants to study the metric T1 in GM in a group of patients scanned with a scanner A and compare it to a group of healthy controls scanned with a scanner B; our results suggest that if the group difference is significant but lower than 108 ms, it is likely to be due to a technical bias or reproducibility bias. While if the difference is significant and higher than 108 ms, it might be due to an actual physiological effect. Of course, this kind of situation is not ideal because of the bias introduced, but it opens the door to making studies at the global level, which can drastically increase the amount of data available.

6.5.1 Choice of the metrics

In this study, eight different metrics were evaluated (T1, T2, PD and REMyDI averaged in WM and GM). These were selected based on the ability from the SyMRI software to automatically generate this output. From a clinical perspective, this subdivision is reasonable seeing that these different tissue properties tend to provide different types of pathophysiological information and different disorders tend to involve GM and WM to different extents. One technical advantage of using these particular regions of interest is their large size in terms of number of voxels. Averaging the quantitative measurements on a large ROI permits an increase in the confidence of the estimation of the metrics or biomarkers. In addition to the increased confidence, large ROIs are less sensitive to segmentation errors. Since the masks of the GM and WM are also automatically

generated and any variance in the mask generation will affect the quantification of the metric. Smaller ROIs would be potentially more sensitive to segmentation errors. As this study focused on the repeatability and reproducibility of the quantification, we chose large ROIs to minimise the effect of the variance of the segmentation, while these of course are inherently connected based on the relaxometry output.

6.5.2 Repositioning

Fully repositioning the subject between two repeatability acquisitions is necessary to make the two acquisitions as independent as possible. We observed a slightly higher deviation from the first acquisition for acquisitions after repositioning than for acquisitions without repositioning, which was expected. However, this difference was not statistically significant, highlighting that the effects of the repositioning are low compared to the quantification error between two acquisitions.

6.5.3 Limitations

Despite fairly good repeatability and reproducibility observed using the SyMRI protocol in 9 different scanners, we faced some limitations. First, for the acquisitions with the GE 450W 1.5T (20/25 volumes) and some acquisitions of the GE 750W 3T (5/25 volumes), some images were hampered by eddy currents artifacts inducing errors in the quantitative maps and in the automatic brain segmentation. This resulted in a discarding of 19 volumes from the GE 450w. Eddy currents affect the coils, and lead to a gradually smaller signal at T2 relaxation, inducing to the second echo a lower signal than expected. As the signal difference between echoes is used to measure T2, this artifact causes errors in the T2 measurements. This suggests that scanners should be properly prepared and calibrated to be used with quantitative sequences such as SyMRI. The fact that SyMRI is a closed commercial software, gives less freedom to process the data than an open source software would. For example, if data were acquired with poorly calibrated scanners, the scans would be rendered worthless, since it is impossible to change the fitting parameters. Conversely, restricting the access to the fitting parameters plays an important role in ensuring the reproducibility. While the simultaneous multiparametric acquisition has the advantage to produce maps inherently aligned, it is still naturally sensitive to head motion since there is no motion correction in the acquisition. While the sequence can be performed with a short acquisition time

(<7 min), it comes at the cost of large slice thickness (4 mm) and a necessary 1 mm slice gap to avoid inter-slice cross-talk in the 2D based SyMRI acquisitions. That being said, 3D prototype sequences for SyMRI are being developed to mitigate this problem (Fujita et al., 2020a, 2020b). Using the CoV to compare the variability of the different biomarkers is convenient because it is expressed in percentage units and it is thus comparable across metrics. However, the CoV can be a misleading metric because it depends on the dynamic range and can be arbitrarily modulated by adding an offset to a measurement (Lévy et al. 2018). This effect is noticeable in Table 6.2, where a low average value of REMyDI in the GM induces a relatively high CoV despite a good repeatability. It is thus important to compute the repeatability and reproducibility measurements which are not affected by this bias of dynamic range.

6.5.4 Conclusions

- Quantitative imaging metrics from SyMRI provides a very good repeatability within a single scanner (mean CoV = 0.63 %) but shows more variability across scanners (mean CoV = 5.5 %), as also suggested by (Hagiwara et al., 2019).

- It is possible to perform large scale multicenter qMRI analyses using the SyMRI protocol. As the inter-scanner variability is 5 to 10 times higher than the intra-scanner variability, we need to expect a higher effect size (Sawilowsky, 2009), than if the study were made with one scanner.

6.5.5 Future studies

To mitigate the inter-scanner variability, multi-center studies should ideally acquire calibration data using a travelling phantom. After such calibration, the data from different scanners could be compared with higher reliability, thus allowing multi-center quantitative studies. Future studies will look at methods to calibrate multi-centric SyMRI data and assess the multi-centric test-retest variability of other metrics and 3D versions of SyMRI.

6.6 References

5725-2, I. (1994). Accuracy (trueness and precision) of measurement methods and results-Part 2: Basic method for the determination of repeatability and reproducibility of a standard measurement method. In *ISO Standards*. International Organization for Standardization.

Ben-Eliezer, N., Sodickson, D. K., & Block, K. T. (2015). Rapid and accurate T2 mapping from multi-spin-echo data using Bloch-simulation-based reconstruction. *Magnetic Resonance in Medicine: Official Journal of the Society of Magnetic Resonance in Medicine / Society of Magnetic Resonance in Medicine*, *73*(2), 809–817.

Carstensen, B. (2010). Repeatability, Reproducibility and Coefficient of Variation. In J. W. &. Sons (Ed.), *Comparing Clinical Measurement Methods* (pp. 107–114).

Caverly, R. H. (2015). MRI Fundamentals: RF Aspects of Magnetic Resonance Imaging (MRI). *IEEE Microwave Magazine*, *16*(6), 20–33.

Chong, A. L., Chandra, R. V., Chuah, K. C., Roberts, E. L., & Stuckey, S. L. (2016). Proton Density MRI Increases Detection of Cervical Spinal Cord Multiple Sclerosis Lesions Compared with T2-Weighted Fast Spin-Echo. *AJNR. American Journal of Neuroradiology*, *37*(1), 180–184.

Cohen-Adad, J. (2014). What can we learn from T2* maps of the cortex? *NeuroImage*, *93 Pt 2*, 189–200.

Cohen-Adad, J., Benner, T., Greve, D., Kinkel, R. P., Radding, A., Fischl, B., Rosen, B. R., & Mainero, C. (2011). In vivo evidence of disseminated subpial T2* signal changes in multiple sclerosis at 7 T: a surface-based analysis. *NeuroImage*, *57*(1), 55–62.

Cohen-Adad, J., Polimeni, J. R., Helmer, K. G., Benner, T., McNab, J. A., Wald, L. L., Rosen, B. R., & Mainero, C. (2012). T2* mapping and B0 orientation-dependence at 7 T reveal cyto- and myeloarchitecture organization of the human cortex. *NeuroImage*, *60*(2), 1006–1014.

Does, M. D. (2018). Inferring brain tissue composition and microstructure via MR relaxometry. *NeuroImage*. https://doi.org/10.1016/j.neuroimage.2017.12.087

Fujita, S., Hagiwara, A., Otsuka, Y., Hori, M., Takei, N., Hwang, K.-P., Irie, R., Andica, C., Kamagata, K., Akashi, T., Kunishima Kumamaru, K., Suzuki, M., Wada, A., Abe, O., & Aoki, S. (2020). Deep Learning Approach for Generating MRA Images From 3D Quantitative Synthetic MRI Without Additional Scans. *Investigative Radiology*, *55*(4), 249–256.

Fujita, S., Hagiwara, A., Takei, N., Hwang, K.-P., Fukunaga, I., Kato, S., Andica, C., Kamagata, K., Yokoyama, K., Hattori, N., Abe, O., & Aoki, S. (2020). Accelerated Isotropic Multiparametric Imaging by High Spatial Resolution 3D-QALAS With Compressed Sensing: A Phantom, Volunteer, and Patient Study. *Investigative Radiology*. https://doi.org/10.1097/RLI.0000000000000744

Gach, H. M., Curcuru, A. N., Mutic, S., & Kim, T. (2020). B0 field homogeneity recommendations, specifications, and measurement units for MRI in radiation therapy. *Medical Physics*, *47*(9), 4101–4114.

Giovannetti, G., Viti, V., Positano, V., Santarelli, M. F., Landini, L., & Benassi, A. (2007). Coil sensitivity map-based filter for phased-array image reconstruction in Magnetic Resonance Imaging. *International Journal of Biomedical Engineering and Technology*, *1*(1), 4–17.

Gracien, R.-M., Reitz, S. C., Hof, S. M., Fleischer, V., Zimmermann, H., Droby, A., Steinmetz, H., Zipp, F., Deichmann, R., & Klein, J. C. (2016). Changes and variability of proton density and T1 relaxation times in early multiple sclerosis: MRI markers of neuronal damage in the cerebral cortex. *European Radiology*, *26*(8), 2578–2586.

Granberg, T., Hashim, F., Andersen, O., Sundal, C., & Karrenbauer, V. D. (2016). Hereditary diffuse leukoencephalopathy with spheroids - a volumetric and radiological comparison with multiple sclerosis patients and healthy controls. *European Journal of Neurology: The Official Journal of the European Federation of Neurological Societies*, *23*(4), 817–822.

Granberg, T., Uppman, M., Hashim, F., Cananau, C., Nordin, L. E., Shams, S., Berglund, J., Forslin, Y., Aspelin, P., Fredrikson, S., & Kristoffersen-Wiberg, M. (2016). Clinical Feasibility of Synthetic MRI in Multiple Sclerosis: A Diagnostic and Volumetric Validation Study. *AJNR. American Journal of Neuroradiology*, *37*(6), 1023–1029.

Gupta, A., Al-Dasuqi, K., Xia, F., Askin, G., Zhao, Y., Delgado, D., & Wang, Y. (2017). The Use of Noncontrast Quantitative MRI to Detect Gadolinium-Enhancing Multiple Sclerosis Brain Lesions: A Systematic Review and Meta-Analysis. *AJNR. American Journal of Neuroradiology*, *38*(7), 1317–1322.

Hagiwara, A., Hori, M., Cohen-Adad, J., Nakazawa, M., Suzuki, Y., Kasahara, A., Horita, M., Haruyama, T., Andica, C., Maekawa, T., Kamagata, K., Kumamaru, K. K., Abe, O., & Aoki, S. (2019). Linearity, Bias, Intrascanner Repeatability, and Interscanner Reproducibility of Quantitative Multidynamic Multiecho Sequence for Rapid Simultaneous Relaxometry at 3 T: A Validation Study With a Standardized Phantom and Healthy Controls. *Investigative Radiology*, *54*(1), 39–47.

Hagiwara, A., Hori, M., Yokoyama, K., Nakazawa, M., Ueda, R., Horita, M., Andica, C., Abe, O., & Aoki, S. (2017). Analysis of White Matter Damage in Patients with Multiple Sclerosis via a Novel In Vivo MR Method for Measuring Myelin, Axons, and G-Ratio. *AJNR. American Journal of Neuroradiology*, *38*(10), 1934–1940.

Hagiwara, A., Hori, M., Yokoyama, K., Takemura, M. Y., Andica, C., Kumamaru, K. K., Nakazawa, M., Takano, N., Kawasaki, H., Sato, S., Hamasaki, N., Kunimatsu, A., & Aoki, S. (2017). Utility of a Multiparametric Quantitative MRI Model That Assesses Myelin and Edema for Evaluating Plaques, Periplaque White Matter, and Normal-Appearing White Matter in Patients with Multiple Sclerosis: A Feasibility Study. *AJNR. American Journal of Neuroradiology*, *38*(2), 237–242.

Hagiwara, A., Warntjes, M., Hori, M., Andica, C., Nakazawa, M., Kumamaru, K. K., Abe, O., & Aoki, S. (2017). Symri of the Brain: Rapid Quantification of Relaxation Rates and Proton Density, With Synthetic Mri, Automatic Brain Segmentation, and Myelin Measurement. *Investigative Radiology*, *52*(10), 647–657.

Ibrahim, T. S., & Tang, L. (2007). Insight into RF power requirements and B1 field homogeneity for human MRI via rigorous FDTD approach. *Journal of Magnetic Resonance Imaging: JMRI*, *25*(6), 1235–1247.

Katti, G., Ara, S. A., & Shireen, A. (2011). *Magnetic resonance imaging (MRI) – A review*. http://citeseerx.ist.psu.edu/viewdoc/download?doi=10.1.1.829.7053&rep=rep1&type=pdf

Lévy, S., Guertin, M.-C., Khatibi, A., Mezer, A., Martinu, K., Chen, J.-I., Stikov, N., Rainville, P., & Cohen-Adad, J. (2018). Correction: Test-retest reliability of myelin imaging in the human spinal cord: Measurement errors versus region- and aging-induced variations. *PloS One*, *13*(6), e0199796.

Lin, F.-H., Chen, Y.-J., Belliveau, J. W., & Wald, L. L. (2003). A wavelet-based approximation of surface coil sensitivity profiles for correction of image intensity inhomogeneity and parallel imaging reconstruction. *Human Brain Mapping*, *19*(2), 96–111.

Lutti, A., Dick, F., Sereno, M. I., & Weiskopf, N. (2014). Using high-resolution quantitative mapping of R1 as an index of cortical myelination. *NeuroImage*, *93 Pt 2*, 176–188.

Mackay, A., Whittall, K., Adler, J., Li, D., Paty, D., & Graeb, D. (1994). In vivo visualization of myelin water in brain by magnetic resonance. *Magnetic Resonance in Medicine: Official Journal of the Society of Magnetic Resonance in Medicine / Society of Magnetic Resonance in Medicine*, *31*(6), 673–677.

Mainero, C., Louapre, C., Govindarajan, S. T., Giannì, C., Nielsen, A. S., Cohen-Adad, J., Sloane, J., & Kinkel, R. P. (2015). A gradient in cortical pathology in multiple sclerosis by in vivo quantitative 7 T imaging. *Brain: A Journal of Neurology*, *138*(Pt 4), 932–945.

Mangeat, G., Ouellette, R., Wabartha, M., De Leener, B., Plattén, M., Danylaité Karrenbauer, V., Warntjes, M., Stikov, N., Mainero, C., Cohen-Adad, J., & Granberg, T. (2020). Machine Learning and Multiparametric Brain MRI to Differentiate Hereditary Diffuse Leukodystrophy with Spheroids from Multiple Sclerosis. *Journal of Neuroimaging: Official Journal of the American Society of Neuroimaging*, *30*(5), 674–682.

McGuire, S. A., Wijtenburg, S. A., Sherman, P. M., Rowland, L. M., Ryan, M., Sladky, J. H., & Kochunov, P. V. (2017). Reproducibility of quantitative structural and physiological MRI measurements. *Brain and Behavior*, *7*(9), e00759.

Mezer, A., Rokem, A., Berman, S., Hastie, T., & Wandell, B. A. (2016). Evaluating quantitative proton-density-mapping methods. *Human Brain Mapping*, *37*(10), 3623–3635.

Ouellette, R., Mangeat, G., Polyak, I., Warntjes, M., Forslin, Y., Bergendal, Å., Plattén, M., Uppman, M., Treaba, C. A., Cohen-Adad, J., Piehl, F., Kristoffersen Wiberg, M., Fredrikson, S., Mainero, C., & Granberg, T. (2020). Validation of Rapid Magnetic Resonance Myelin Imaging in Multiple Sclerosis. *Annals of Neurology*, *87*(5), 710–724.

Saccenti, L., Andica, C., Hagiwara, A., Yokoyama, K., Takemura, M. Y., Fujita, S., Maekawa, T., Kamagata, K., Le Berre, A., Hori, M., Hattori, N., & Aoki, S. (2019). Brain tissue and myelin volumetric analysis in multiple sclerosis at 3T MRI with various in-plane resolutions using synthetic MRI. *Neuroradiology*, *61*(11), 1219–1227.

Sawilowsky, S. S. (2009). New effect size rules of thumb. *Journal of Modern Applied Statistical Methods: JMASM*, *8*(2), 597–599.

Stikov, N., Boudreau, M., Levesque, I. R., Tardif, C. L., Barral, J. K., & Pike, G. B. (2014). On the accuracy of T1 mapping: Searching for common ground. *Magnetic Resonance in Medicine: Official Journal of the Society of Magnetic Resonance in Medicine / Society of Magnetic Resonance in Medicine*. https://doi.org/10.1002/mrm.25135

Stüber, C., Morawski, M., Schäfer, A., Labadie, C., Wähnert, M., Leuze, C., Streicher, M., Barapatre, N., Reimann, K., Geyer, S., Spemann, D., & Turner, R. (2014). Myelin and iron concentration in the human brain: a quantitative study of MRI contrast. *NeuroImage*, *93 Pt 1*, 95–106.

Thompson, A. J., Banwell, B. L., Barkhof, F., Carroll, W. M., Coetzee, T., Comi, G., Correale, J., Fazekas, F., Filippi, M., Freedman, M. S., Fujihara, K., Galetta, S. L., Hartung, H. P., Kappos, L., Lublin, F. D., Marrie, R. A., Miller, A. E., Miller, D. H., Montalban, X., … Cohen, J. A. (2018). Diagnosis of multiple sclerosis: 2017 revisions of the McDonald criteria. *Lancet Neurology*, *17*(2), 162–173.

Vågberg, M., Lindqvist, T., Ambarki, K., Warntjes, J. B. M., Sundström, P., Birgander, R., & Svenningsson, A. (2013). Automated determination of brain parenchymal fraction in multiple sclerosis. *AJNR. American Journal of Neuroradiology*, *34*(3), 498–504.

van der Kouwe, A. J. W., Benner, T., Salat, D. H., & Fischl, B. (2008). Brain morphometry with multiecho MPRAGE. *NeuroImage*, *40*(2), 559–569.

Vaughn, J., Hagiwara, M., Katz, J., Roth, J., Devinsky, O., Weiner, H., & Milla, S. (2013). MRI characterization and longitudinal study of focal cerebellar lesions in a young tuberous sclerosis cohort. *AJNR. American Journal of Neuroradiology*, *34*(3), 655–659.

Warntjes, J. B. M., Leinhard, O. D., West, J., & Lundberg, P. (2008). Rapid magnetic resonance quantification on the brain: Optimization for clinical usage. *Magnetic Resonance in Medicine: Official Journal of the Society of Magnetic Resonance in Medicine / Society of Magnetic Resonance in Medicine*, *60*(2), 320–329.

Warntjes, J. B. M., Persson, A., Berge, J., & Zech, W. (2017). Myelin Detection Using Rapid Quantitative MR Imaging Correlated to Macroscopically Registered Luxol Fast Blue-Stained Brain Specimens. *AJNR. American Journal of Neuroradiology*, *38*(6), 1096–1102.

Warntjes, M., Engström, M., Tisell, A., & Lundberg, P. (2016). Modeling the Presence of Myelin and Edema in the Brain Based on Multi-Parametric Quantitative MRI. *Frontiers in Neurology*, *7*, 16.

West, J., Warntjes, J. B. M., & Lundberg, P. (2012). Novel whole brain segmentation and volume estimation using quantitative MRI. *European Radiology*, *22*(5), 998–1007.

6.7   Acknowledgments

CHAPTER 7   FROM PRECISION TO ACCURACY: COMPLEMENTARY WORK ON HISTOLOGY VALIDATION

7.1   Stain-free histology to validate quantitative MRI
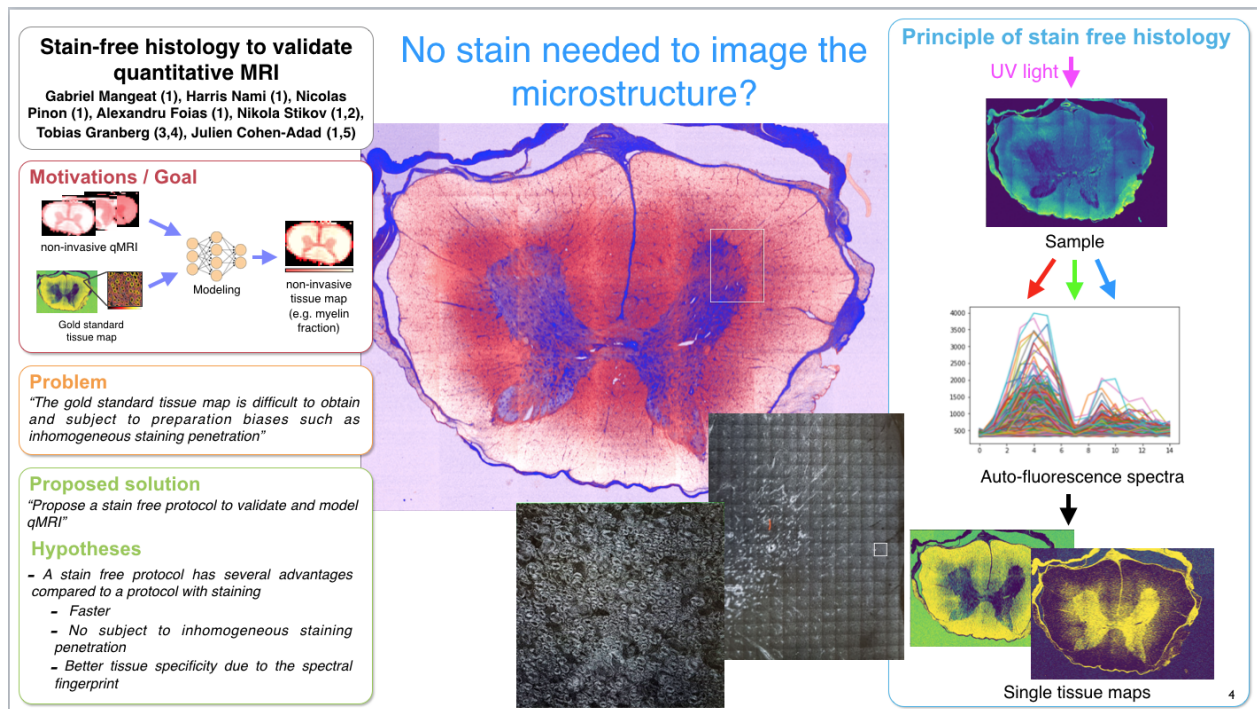
Figure 7.1 Cover page of the digital poster presented at the international conference ISMRM 2019.

7.2   Synopsis

Quantitative MRI (qMRI) is reproducible but often lacks calibration and/or specificity to the underlying microstructure. Light transmission optical histology of stained tissue is a popular method for validation; however, it is hampered by calibration issues and inhomogeneous penetration of staining agents. We propose a method to validate quantitative MRI metrics using stainless histology by utilizing the innate autofluorescence spectra of tissues when excited with an ultraviolet laser. We demonstrate a proof-of-concept application of a qMRI validation pipeline on a pig spinal cord section with in vivo and ex vivo qMRI followed by histological autofluorescence microscopy to quantify myelin content.

7.3   Purpose

Quantitative MRI (qMRI) is designed to measure intrinsic MR properties of tissues with high repeatability and accuracy across different scanners, sites and over time. However, qMRI is often hampered by poor tissue-specificity as it only provides indirect measures of the underlying microstructure. T1 and T2 relaxations times, proton density (PD) and magnetization transfer (MT) are commonly used in studies of the central nervous system. However, these techniques do not directly relate to histopathological features such as the density and volume of axons, neuronal somas and glial cells, nor do they directly relate to myelin content. This disconnect makes it difficult to interpret the underlying processes of qMRI measures. Efforts in linking qMRI to histology measurements (e.g., electron microscopy, immunostaining techniques) are often hampered by histology biases such as issues related to the specificity of the staining technique and inhomogeneous penetration of the staining agents (Vincze et al., 2008).

In this study, we establish a fast and accurate qMRI validation protocol based on a staining-free, high resolution (~300 nm) single-photon multi-spectral UV-autofluorescence, adapted from Christensen *et al* (Christensen et al., 2014). In short, tissues are discriminated against based on their specific auto-fluorescence spectra. In addition, we propose a proof-of-concept application on a pig spinal cord section in order to perform validation of multiple qMRI technique's abilities to quantify myelin.

7.4 Methods

7.4.1 qMRI acquisitions

A pig (24 kg) was scanned *in vivo* on a 3T Siemens Skyra with a 24-channel spine coil. The following axial qMRI protocol was used: MTR/MTsat (0.8×0.8×5.0 mm, TR 35 ms, TE 3.13 ms, FA 9°), Synthetic MR (Warntjes et al., 2008) (0.8×0.8×5.0 mm, TR 4000 ms, TE1 25 ms, TE2 99 ms, TI 100 ms, FA 150°) and Diffusion-weighted imaging (0.9×0.9×5.0 mm, TR 3300 ms, TE 89 ms, 30 directions).

7.4.2 Tissue extraction

After the scan, the pig was sacrificed by euthanyl injection. The cervical area of the spinal cord was extracted within 2 h and fixed by immersion in a 3% paraformaldehyde and 3% glutaraldehyde solution. After 4 days, the sample was scanned on the same MRI using a custom solenoid coil, with a higher resolution protocol: MTR/MTsat (0.24×0.24×3.0 mm, TR 45 ms, TE 4.52 ms, FA 9°), Synthetic MR (0.24×0.24×3 mm, TR 4000.0 ms, TE1 30 ms, TE2 106 ms, TI 100 ms, FA 150°) and Diffusion-weighted imaging (voxel size 0.7×0.7×3 mm, TR 2200 ms, TE 92 ms, 6 directions). Figure 7-2 illustrates the whole procedure.

7.4.3 Histology acquisition

A 300 μm thick slice was mounted on a coverslip and scanned using a confocal laser-scanning microscope, Olympus FV1000. A 405 nm laser was used for the UV-autofluorescence excitation and multi-spectral detection was performed on 16 channels in the wavelength range of 410-650 nm. The in-plane resolution limit was 300 nm, with a 40× apochromatic objective of NA=0.95 (in the air). The integration time per pixel was 20 μs and 5 averages were recorded for each frame. An automatic mosaic scan mode was used to cover the full spinal cord section.

7.4.4 Processing

The 16 spectral channels from the microscopy were used to unmix the fluorescence signal of myelin from surrounding tissue. Thereafter, the ground truth myelin volume fraction could be

computed. The Spinal Cord Toolbox (De Leener et al., 2017) was used to compute the following quantitative MRI maps: MTR, MTsat, FA and MD. The software SyMRI (Warntjes et al., 2008) was used to compute the quantitative T1, T2 and PD maps.

Figure 1: Methodology of the proposed qMRI validation protocol

A: *in vivo* MRI

MTR — 55 % / 25 %
MTsat — 7 / 1
...
Siemens Skyra 3T
Low resolution *in vivo* qMRI (800 µm)

B: *ex vivo* MRI

Euthanyl injection
Spine extraction + fixation by immersion
MRI with custom-made receive-only solenoid coil
MTR — 55 % / 25 %
MTsat — 7 / 1
...
High resolution qMRI maps (250 µm)

C: *ex vivo* Histology

Olympus FV1000
mosaic image
High resolution multispectral image
Myelin unmixed image
Ground truth microstructural maps

Figure 7.2 Proof-of-concept application of the qMRI validation protocol, performed on a pig spinal cord tissue section. A) in vivo scan using a Siemens Skyra 3T MRI scanner to acquire images of the cervical region of the spinal cord at 0.8×0.8×5 mm. B) Surgical extraction of the cervical spinal cord and histological fixation. Then a higher resolution ex vivo qMRI scan was performed to take into account the tissue changes induced by the fixation process. C) Staining-free histology procedure using the tissue UV-autofluorescence and spectral unmixing.

7.4.5 Histology processing

Once the series of hyperspectral images acquired, there are several options to recover the independent underlying tissue maps. 1) The unsupervised tissue estimation (Figure 7-5, middle panel) consists of extracting the orthogonal component of the signal, here with a PCA. This produces maps of distinct features of the microstructure, but their identification remains challenging. 2) The supervised tissue estimation (Figure 7-5, right panel) consists of predicting a

given stain map from the series of spectral channels. The model can then be reused to predict the stain map from a hyperspectral dataset. Note that the stain map can also be replaced by a tissue segmentation at high resolution.

7.5 Results

Figure 7.3 shows the qMRI maps of the spinal cord at the C6 level, *in vivo* and *ex vivo*. We observe a qMRI shift between *in vivo* and *ex vivo* for the T1, T2, PD and MT0 maps, while similar ranges of qMRI values are observed in MTR, MTsat and FA maps.

Figure 7.4 shows a successful unmixing of the myelin signal from the image background (non-myelin). We can observe a high-resolution image before and after the spectral deconvolution, taken in the dorsal column of C6. A similar process will be used to extract other cellular features, such as axons and glia.

Figure 7.5 shows the different machine learning methods: supervised and unsupervised, to extract the individual tissue maps from the set on hyperspectral images.

Figure 7.6 shows the correlation matrix between all the imaging modalities performed in this study.

Figure 2: qMRI maps of the spinal cord at the C6 level
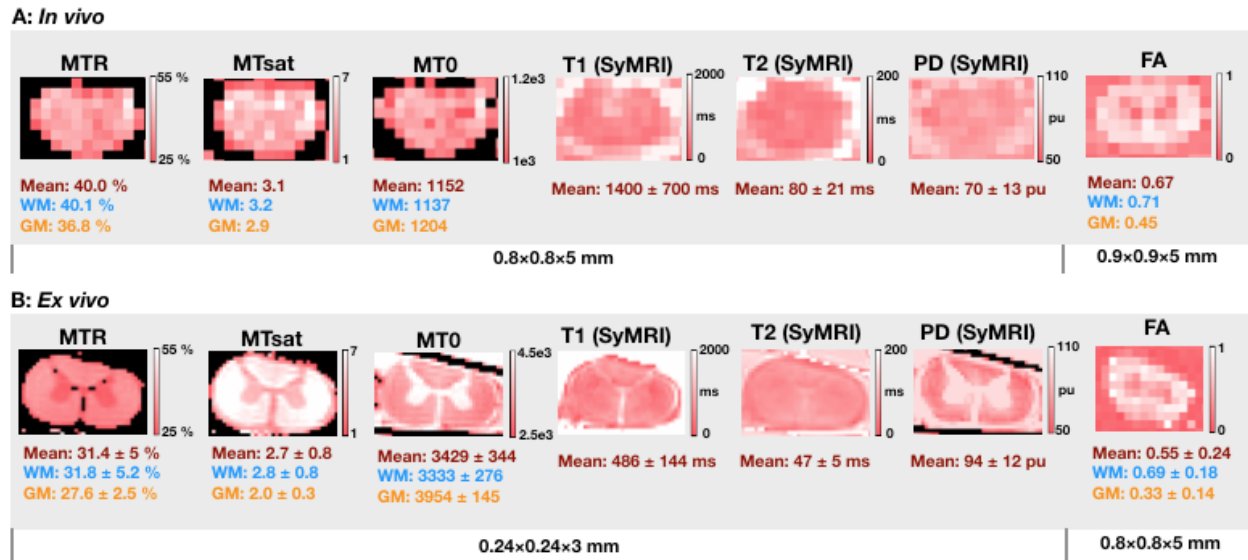
Figure 7.3 Quantitative MRI maps of the spinal cord section C6, in vivo (top line) and ex vivo (bottom line). A common pattern is noticeable amongst the myelin-sensitive maps (MTR, MTsat, T1). The in vivo qMRI maps were registered to the SCT-template (De Leener et al., 2017) in order to extract quantitative measures across ROIs (Lévy et al., 2015): here mean spinal cord, Grey Matter (GM) and White Matter (WM). We observe a qMRI shift between in vivo and ex vivo for the T1, T2, PD and MT0 maps, while similar ranges of qMRI values are observed in MTR, MTsat and FA maps.
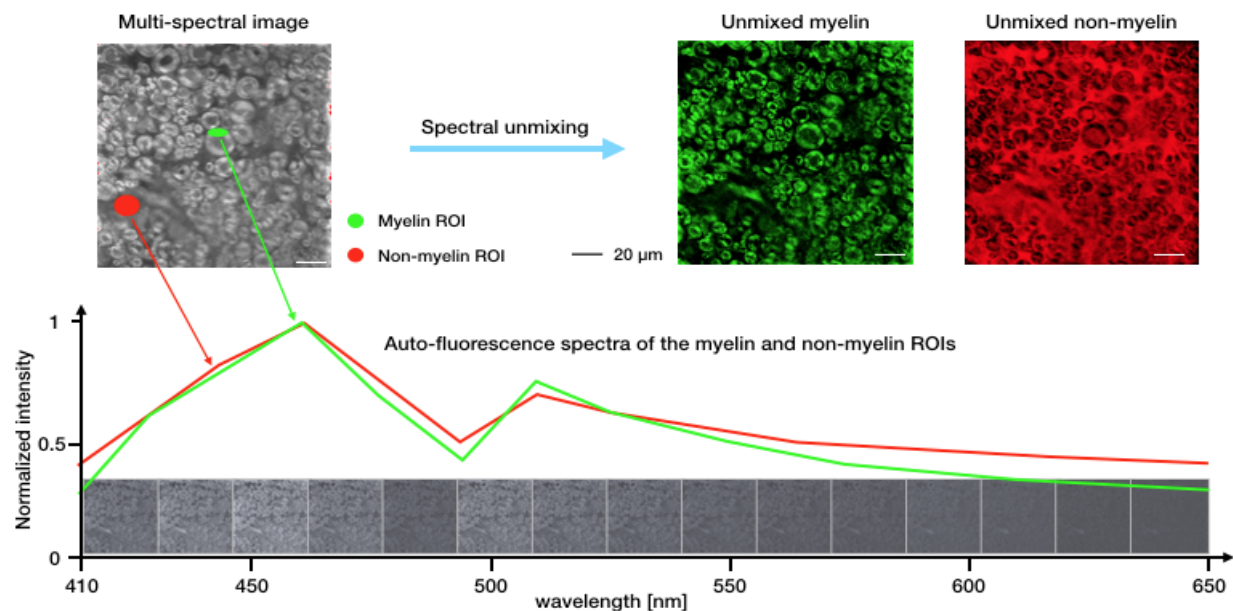
Figure 7.4 Principle of the multispectral unmixing method. The sample is excited with a 405nm laser that produces autofluorescence of the phospholipids. The signal emitted by the tissue is spectrally recorded on 16 channels (from 410 to 650 nm). When two tissues have a different spectral signature, it is possible to separate their respective contribution to the multispectral image. Here we choose two tissue compartments: myelin and non-myelin, and we obtained their spectral signature from ROI visually placed on myelin (green) and non-myelin (red) tissues respectively. The unmixed images of myelin and glia are shown in the upper right corner.
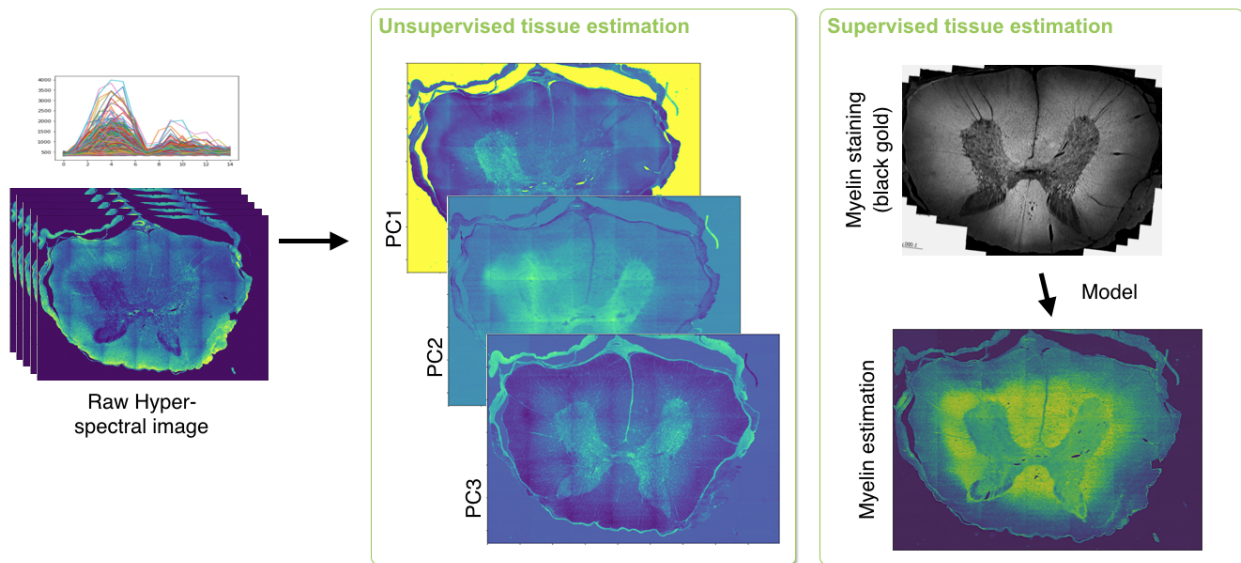
Figure 7.5 The 3 first components of the PCA explained 99.7% of the variance of the hyper-spectral data. Distinct features are visible on each of the PC maps (see teaser slide), supporting the idea that the endogenous fluorescence of the tissues provides multiple biomarkers of the microstructure. Concerning the supervised method, the model (linear Bayesian) was trained on 10 features, ~ 1.3 million of datapoint (WM + GM mask). The stain map and the predicted myelin map correlated at r=0.72, p<1e-16.
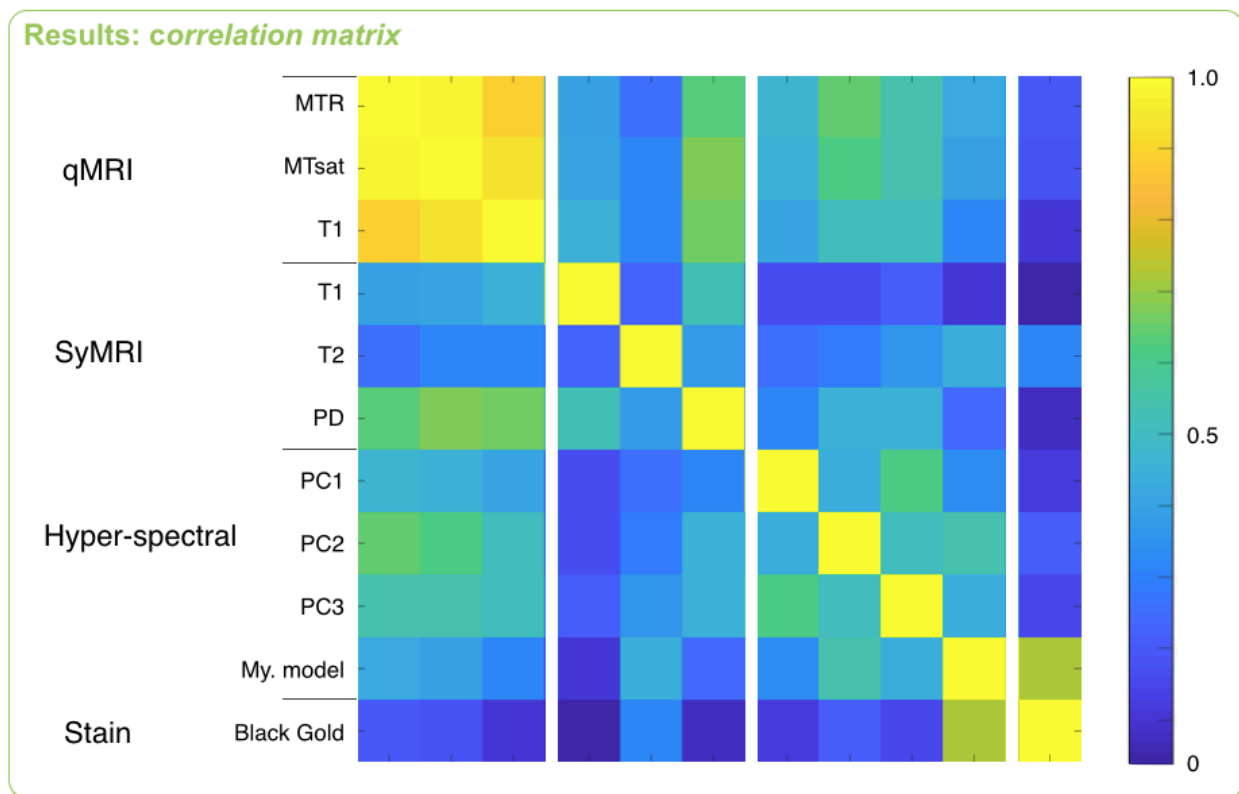
Figure 7.6 We note that the unsupervised tissue estimation correlates fairly well with the qMRI (e.g. PC2 correlates with MTR, MTsat and T1 with r = 0.64, 0.62 and 0.51 respectively). The myelin stain "Black Gold" shows a fairly low correlation with both the MRI and hyper-spectral histology. This is partly due to staining biases, such as the agglomeration of the stain to the tissue, causing holes and bright spots. Another staining will have to be investigated. Interestingly, we note that the myelin model is a better estimation of all the qMRI maps than the myelin staining himself, supporting the relevance of a stain-free method.

7.5.1 Discussion and conclusion

We proposed a qMRI validation protocol involving a fast and staining-free histology method for quantifying myelin content. While the first results are promising, future work is required to further optimize the protocol, including 1) Addition of a fresh post-mortem MRI scan immediately after tissue-extraction and before the fixation process; 2) Development of an agar-gadolinium-based sample holder to lower Gibbs artifacts and fasten the histology slicing step; 3) Development of a protocol to make cryogenic sections of the fresh tissues, in order to avoid the potential biases dues

to fixation and save time. 4) Improvement of the hyperspectral protocol (more channels, multi-laser excitations, etc) in order to optimize the tissue map predictions. 5) Adding more micro-structural satins to the validation process, such as Luxol Fast Blue or Nile-RED stains to predict the myelin, for example.

7.5.2 Acknowledgements

7.6 Validation of Rapid Magnetic Resonance Myelin Imaging in Multiple Sclerosis

This section will present my contribution to a project made in collaboration with a colleague R. Ouellette (Ph. D. student of my co-supervisor Dr. T. Granberg) on a study aiming to validate the myelin estimation of SyMRI by using ex-vivo histology techniques on Human samples with MS.

R. Ouellette, **G. Mangeat,** I. Polyak, M. Warntjes, Y. Forslin, Å. Bergendal, M. Plattén, M. Uppman, C.A. Treaba, J. Cohen-Adad, F. Piehl, M.K. Wiberg, S. Fredrikson, C. Mainero, T. Granberg. Validation of Rapid Magnetic Resonance Myelin Imaging in Multiple Sclerosis. Annals of Neurology. 2020, 87(5):710-724. doi: https://doi.org/10.1002/ana.25705

7.6.1 Abstract of the original study

Objective: Magnetic resonance imaging (MRI) is essential for multiple sclerosis diagnostics but is conventionally not specific to demyelination. Myelin imaging is often hampered by long

scanning times, complex postprocessing, or lack of clinical approval. This study aimed to assess the specificity, robustness, and clinical value of Rapid Estimation of Myelin for Diagnostic Imaging, a new myelin imaging technique based on time-efficient simultaneous T1/T2 relaxometry and proton density mapping in multiple sclerosis.

Methods: Rapid myelin imaging was applied using 3T MRI ex vivo in 3 multiple sclerosis brain samples and in vivo in a prospective cohort of 71 multiple sclerosis patients and 21 age/sex-matched healthy controls, with scan–rescan repeatability in a subcohort. Disability in patients was assessed by the Expanded Disability Status Scale and the Symbol Digit Modalities Test at baseline and 2-year follow-up.

Results: Rapid myelin imaging correlated with myelin-related stains (proteolipid protein immunostaining and Luxol fast blue) and demonstrated good precision. Multiple sclerosis patients had, relative to controls, lower normalized whole-brain and normal-appearing white matter myelin fractions, which correlated with baseline cognitive and physical disability. Longitudinally, these myelin fractions correlated with follow-up physical disability, even with correction for baseline disability.

Interpretation: Rapid Estimation of Myelin for Diagnostic Imaging provides robust myelin quantification that detects diffuse demyelination in normal-appearing tissue in multiple sclerosis, which is associated with both cognitive and clinical disability. Because the technique is fast, with automatic postprocessing and US Food and Drug Administration/CE clinical approval, it can be a clinically feasible biomarker that may be suitable to monitor myelin dynamics and evaluate treatments aiming at remyelination.

7.6.2 Contribution

For this study, I was in charge of the processing and analysis of the large-scale histology images and the ex-vivo qMRI images. More specifically, I created and optimized the pipeline to register the ex-vivo qMRI images on the corresponding histology. This was particularly challenging due to the non-linear deformations induced by the slicing and staining steps. Figure 7.7 shows the different processing steps to achieve the registration. Figure 7.8 shows the registered ex-vivo images and their correlations to the qMRI modality of interest.
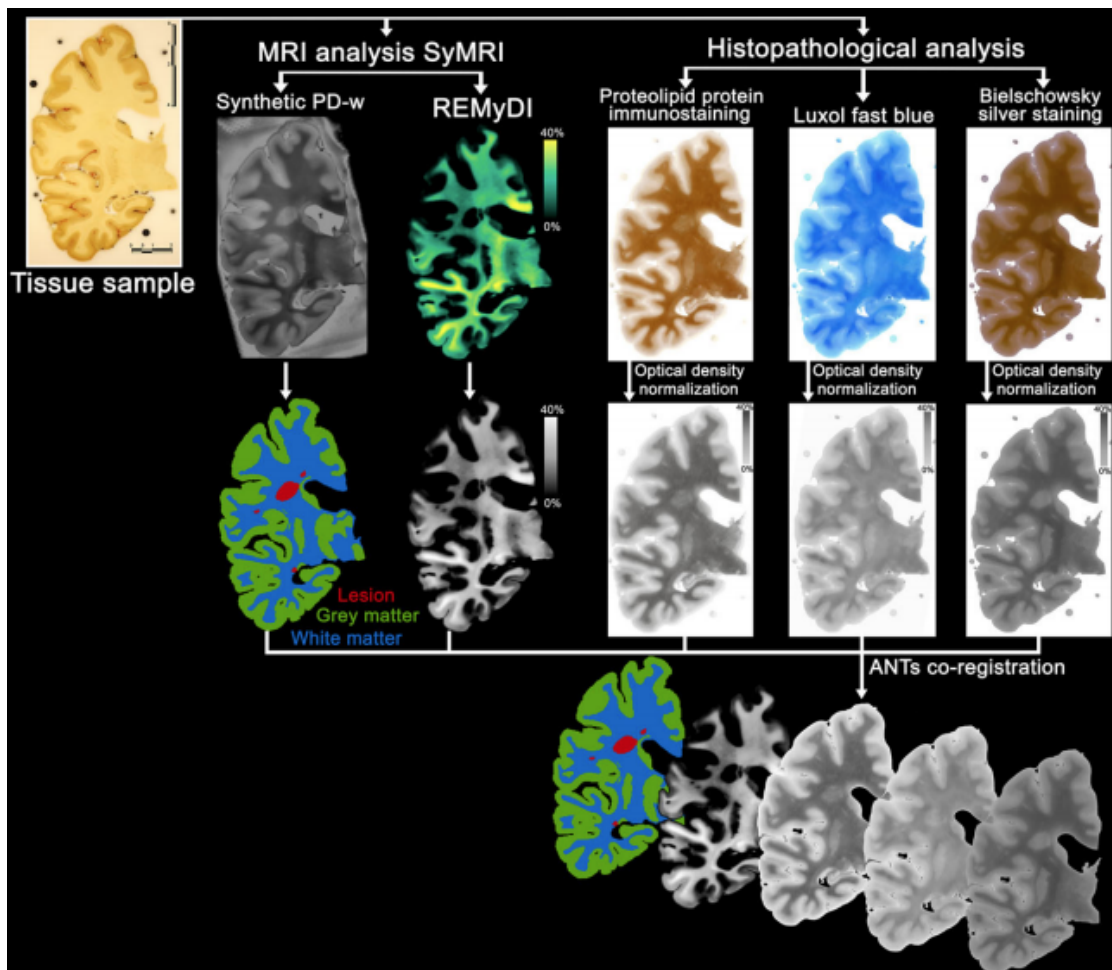
Figure 7.7 extracted and adapted from (Ouellette et al., 2020). Overview of the ex-vivo image processing: The coronal frontotemporal multiple sclerosis tissue sample was similarly scanned to obtain proton density (PD)–weighted images for tissue segmentation and REMyDI for myelin quantification. The sample was then histopathologically processed and stained using proteolipid protein immunostaining, Luxol fast blue, and Bielschowsky silver staining. Magnetic resonance imaging (MRI) and histologically stained sections were registered by ANTsRegistration. Scale bar is shown in centimetres. ANTs = Advanced Normalization Tools; w = weighted images.
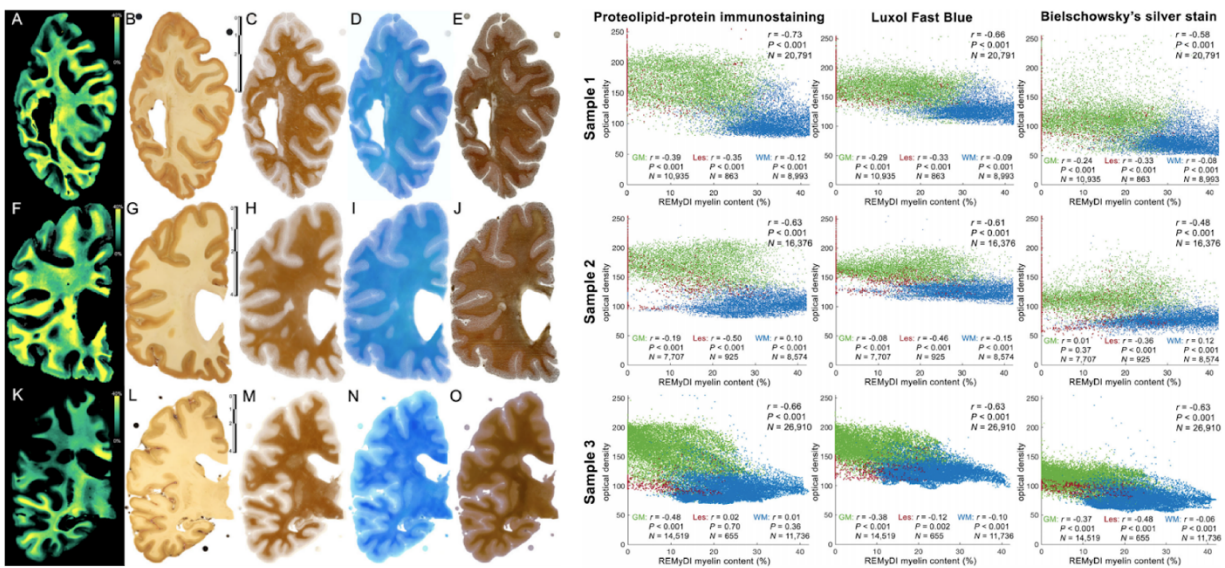
Figure 7.8 Extracted and adapted from (Ouellette et al., 2020). Left panel: Whole-section coronal 10μm-thick tissue sections. Top row (A–E): Parietal coronal hemispheric brain tissue sample from a 71-year-old donor with secondary progressive multiple sclerosis (SPMS). Middle row (F–J): Frontal coronal hemispheric brain tissue sample from a 46-year-old donor with SPMS. Bottom row (K–O): Frontotemporal coronal hemispheric brain tissue sample from a 56-year-old donor with SPMS. First column (A, F, K): REMyDI myelin maps. Second column (B, G, L): Tissue samples before histological processing. Scale bars in centimeters. Third column (C, H, M): Proteolipid protein immunostaining. Fourth column (D, I, N): Luxol fast blue staining. Fifth column (E, J, O): Bielschowsky silver staining (some cutting artifacts can be appreciated in E and J). Right panel: Comparative correlations of individual Rapid Estimation of Myelin for Diagnostic Imaging (REMyDI) myelin quantification with myelin-specific histopathological stainings. Three multiple sclerosis brain tissue samples' voxelwise Pearson correlations of the REMyDI myelin maps with the histological stain uptake optical densities for proteolipid protein immunostaining, Luxol fast blue, and Bielschowsky silver staining. Tissue segmentation is identified as gray matter (GM) in green, white matter (WM) in blue, and lesions (Les) in red, alongside the respective tissue voxel count (N).

7.6.3 Discussion and conclusions

In this study, the associations of REMyDI myelin quantification with the myelin stains were generally numerically higher than with the axonal stain, suggesting that REMyDI is more reflective of myelin content than axons. However, axon-related and myelin-related stains are expected to be highly correlated due to the colocalization of myelin around the axons as well as the concomitant processes of demyelination and axonal loss. This study highlights that REMyDI can be a decent estimator of the myelin content in the brain, especially considering the speed of the acquisition. However, a large unexplained variance still remains between REMyDI and the three OD stains. Both REMyDI and the OD stains contain biases to the estimation of myelin and further studies need to be performed to confirm the accuracy of REMyDI to measure the concentration of myelin in the brain.

7.7 Additional unpublished work on histology techniques for myelin imaging

7.7.1 Example of stain free histology with autofluorescence.

Figure 7.9 shows a mosaic autofluorescence image of a pig cervical spinal cord section, imaged with a confocal microscope, in ~1h. A 10 x objective was used to image a large field of view (6 x 5 mm) in a short amount of time. We observe a good contrast between the myelin sheets and the background (purple zoom). However, only the large axons are visible due to the resolution limitations at 10 x. We notice that other structures than myelin seem to be producing an autofluorescence signal, especially in the grey matter (red zoom). Finally, we observe a shading artifact amongst the different tiles which is due to the slight imperfections in the sectioning leading to subtle misalignments between the imaging z-plane and the sample surface. The following paragraph will present an approach to correct this artifact.
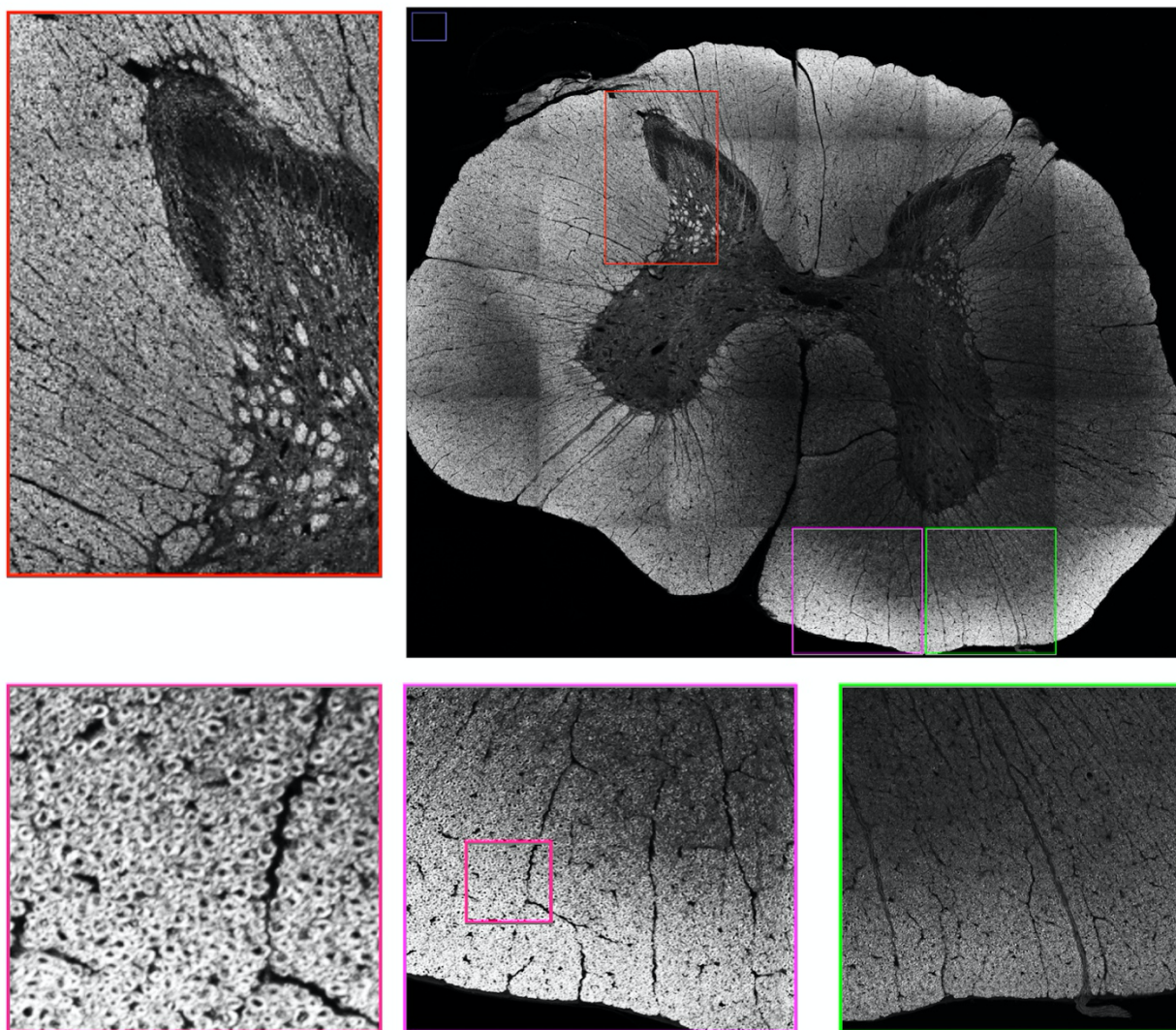
Figure 7.9 Mosaic autofluorescence image of a pig cervical spinal cord section, imaged with a confocal microscope, in ~1h. Excitation wavelength: 405 nm, 10 x objective.

The shading artifact can be mitigated by using the Gaussian blurring technique. It consists in dividing the original image by the blurred image in order to normalize every pixel by its local intensity. Figure 7.10 shows an example of the gaussian blurring correction. Overall, we observe a flatter image with very small tile boundary artifacts (purple zoom). For example, on Figure 7.10, the red and green zoom were showing different mean intensities on the original image and a similar average intensity on the corrected image. However, this correction technique cannot fix everything. We still observe some intensities artifacts at the edges of the different tissues. In addition, if the

original shading is too strong: saturated pixels on one side of the tile and/or no intensity at another side, the image will not be properly recovered.
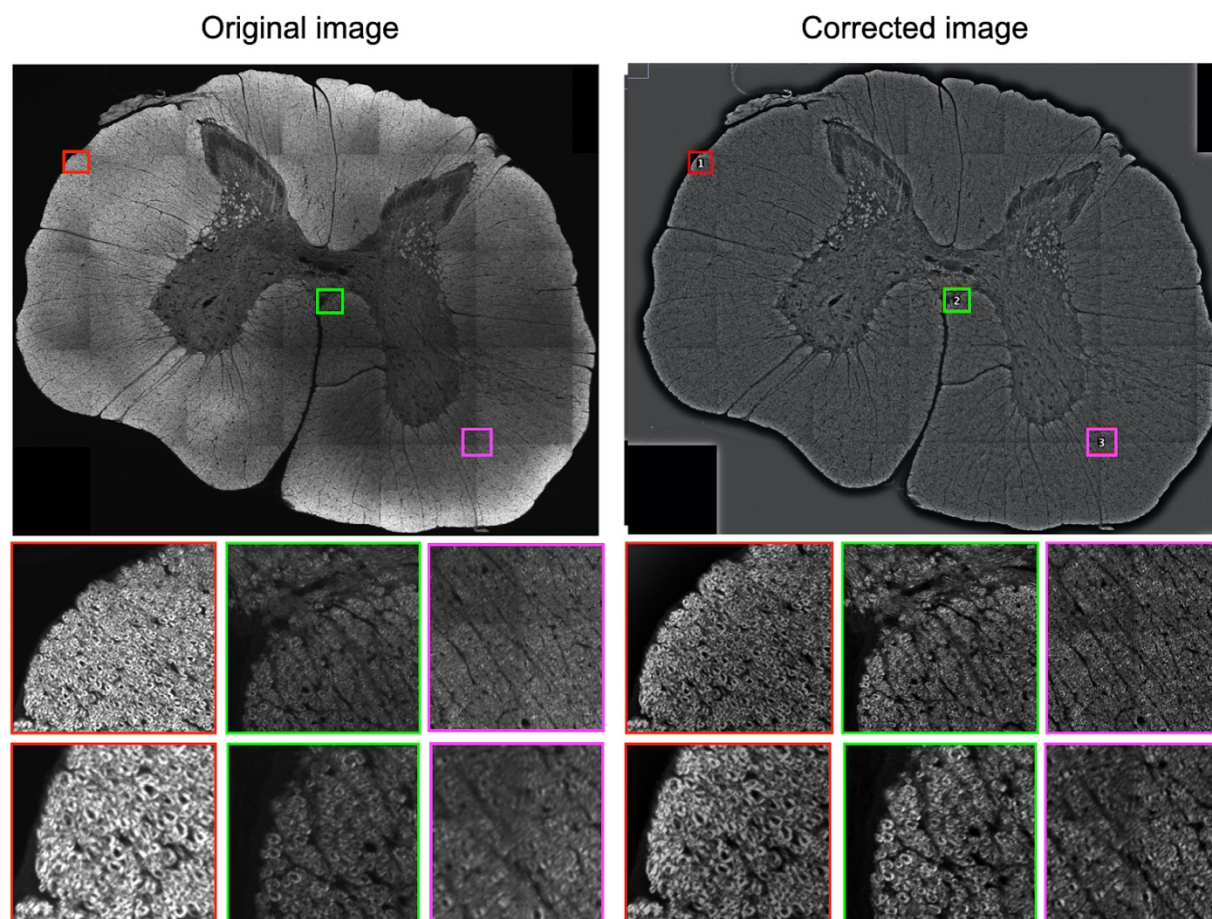
Figure 7.10 Image with shading artifacts (left) and image corrected with a gaussian blurring (kernel of 100 pixels). We observe a flatter corrected image with very small tile boundary artifacts (purple zoom). The red and green zoom were showing different mean intensities on the original image and a similar average intensity on the corrected image.

The shading correction can be applied automatically to the whole hyperspectral stack in order to correct each hyperspectral channel one by one. Figure 7.11 shows the correction applied to the 5 first channels of an hyperspectral image. Here, the image to be blurred needs to be the mean of all the channels, otherwise we would lose the relative intensity across spectral channels.
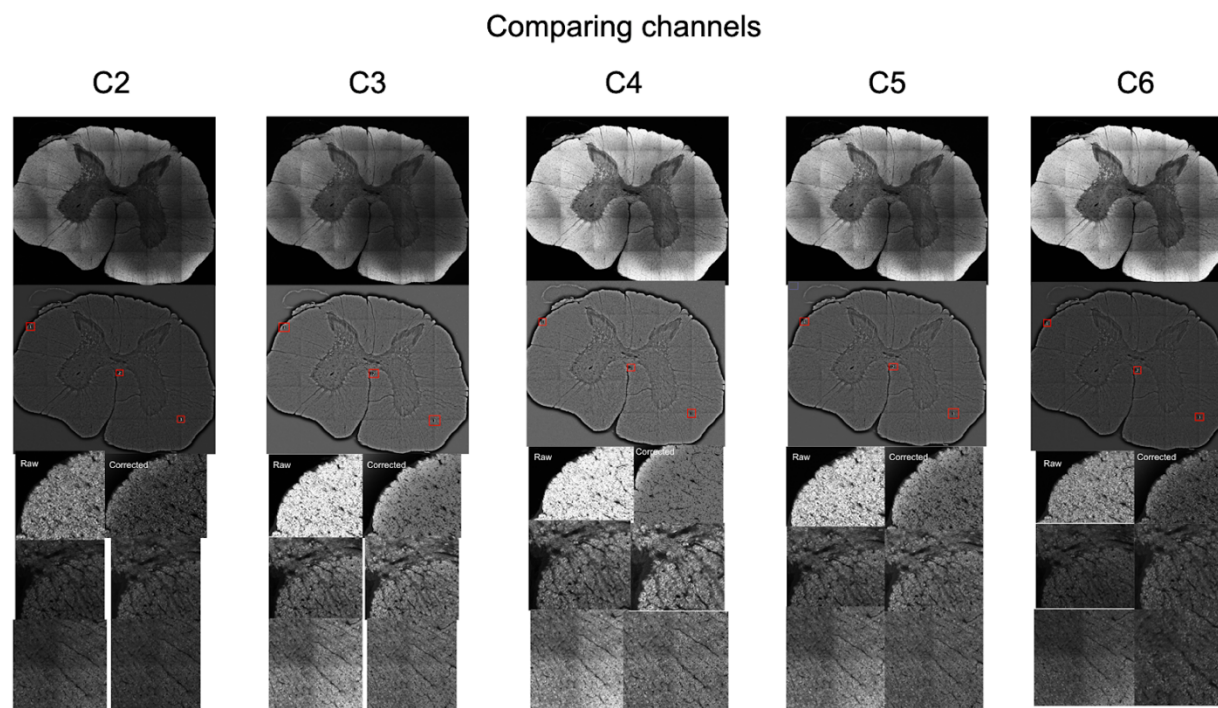
Figure 7.11 Gaussian blurring correction applied to the 5 first channels of an hyperspectral image. The blurred image needs to be the mean of all the channels, otherwise we would lose the relative intensity across spectral channels.

The 10 x hyperspectral autofluorescence imaging technique is sensitive to myelin, fast, and can produce large field of view imaging (6 x 5 mm) in a reasonable amount of time (~1 h). Some imaging artifacts are present but can be mitigated with post processing corrections. The main problem is that the resolution provided by the 10 x objective is barely enough to resolve the largest axons (> 10 micrometers). To resolve smaller axons, a higher magnification is needed, such as 40 x or 60 x. However, imaging at high resolution comes with several costs. First, for the same field of view, we need 16 times more time to image at 40 x and 36 times more time to image at 60 x, than at 10 x. Secondly, as the imaging plan is thinner, the shading artifacts are stronger and often not fixable due to saturation and shot noise limit observed on the same image.

7.7.2 Example of high-resolution histology with fluorescent stain

Figure 7.12 shows a test of a large field of view, high resolution imaging of a rat spinal cord stained with the fluorescent myelin stain Nile-Red. Only one channel was used, and the high quantum efficiency of the Nile-Red allowed to increase the imaging speed. Imaging the full field of view (4.25 x 5 mm) at 40 x was below 8 hours. We can see that the corrected image is not perfectly flat in intensity. The bottom left was very noisy due to the low signal intensity. A compromise had to be taken between low SNR of some pixels and avoiding the saturation of other pixels.
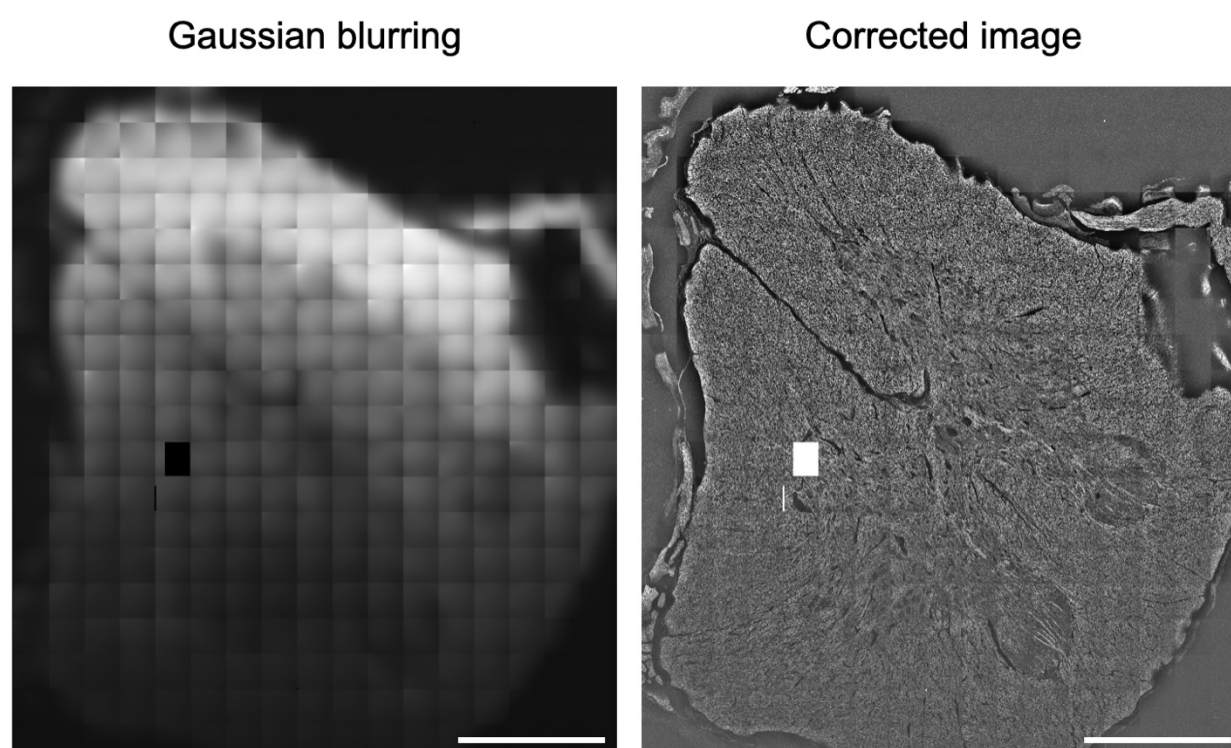
Figure 7.12 Confocal image of a rat spinal cord stained with the Nile-Red myelin stain. The scale bar is 1 millimeter. The imaging parameters were: 40 x apochromatic objective of NA=0.95 (in the air), 17x20 tiles (4.25 x 5 mm), imaging time <8 h, excitation laser: 405 nm. The white rectangle is a loss of data due to some corruptions in the encoding.

Figure 7.13 shows a magnification of the rat spinal cord image, at the junction between the white and the grey matter. The red zoom panel shows that the myelinated axons are well contrasted: the myelin sheets appear bright white while the background and axon remain black. However, the

purple zoom panel shows that some grey matter structures seem to be highlighted by the stain. The green arrows are showing two glial cells and the orange arrows are highlighting a transected blood vessel. This suggests that the Nile-Red stain is not 100% specific to the myelin sheets, at least in the grey matter.
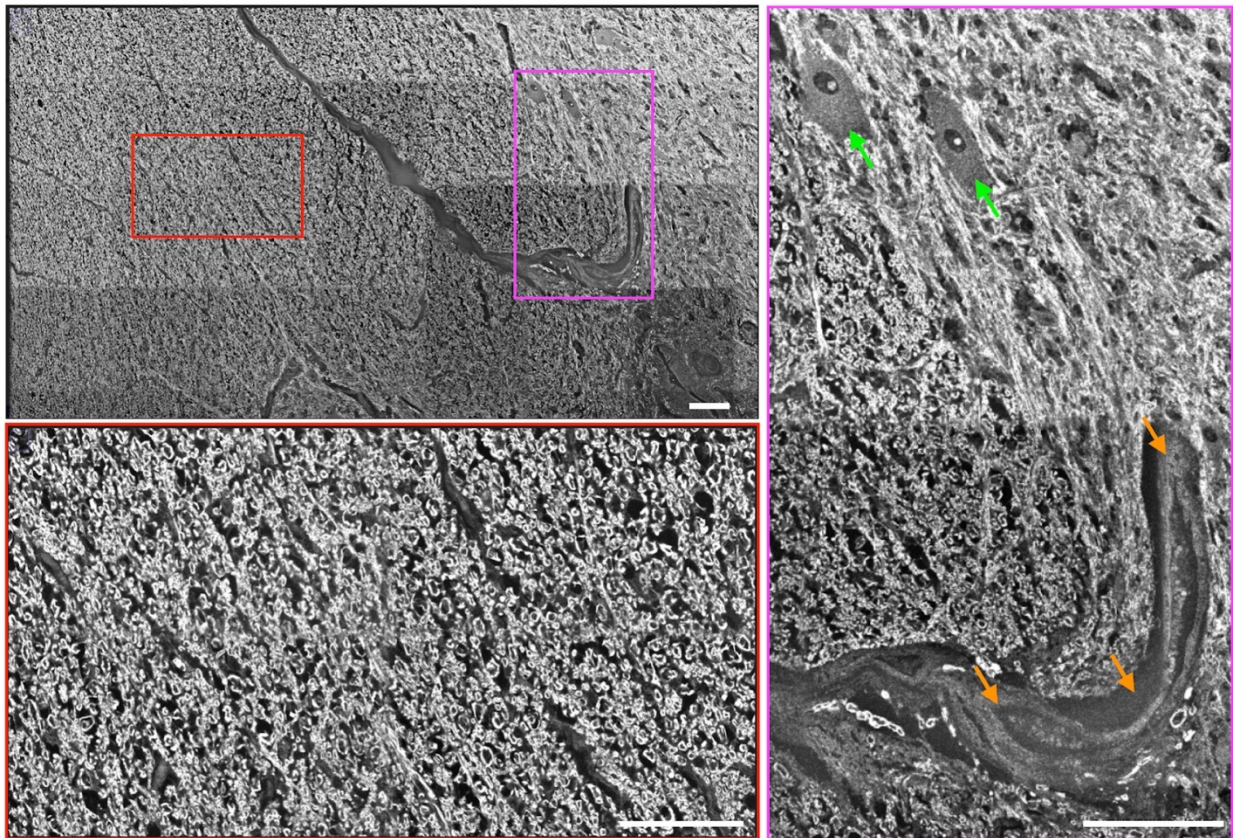
Figure 7.13 Confocal image of a rat spinal cord stained with the Nile-Red myelin stain. The scale bar is 100 micrometers. The imaging parameters were: 40 x apochromatic objective of NA=0.95 (in the air). The red zoom shows well contrasted myelinated axons of the white matter. The purple zoom shows that some grey matter structures are highlighted by the stain. The green arrows are showing two glial cells and the orange arrows are a transected blood vessel.

Figure 7.14 shows a comparison between a 40 x and a 60 x image of a rat spinal cord stained with the Nile-Red myelin stain. The green arrow shows a myelinated axon with a diameter of 0.9 micrometers. While it is well resolved on the 60 x image, it is barely visible on the 40 x image,

suggesting that a large part of the submicrometric axons could not be properly detected with the 40 x protocol.

40 x	60 x
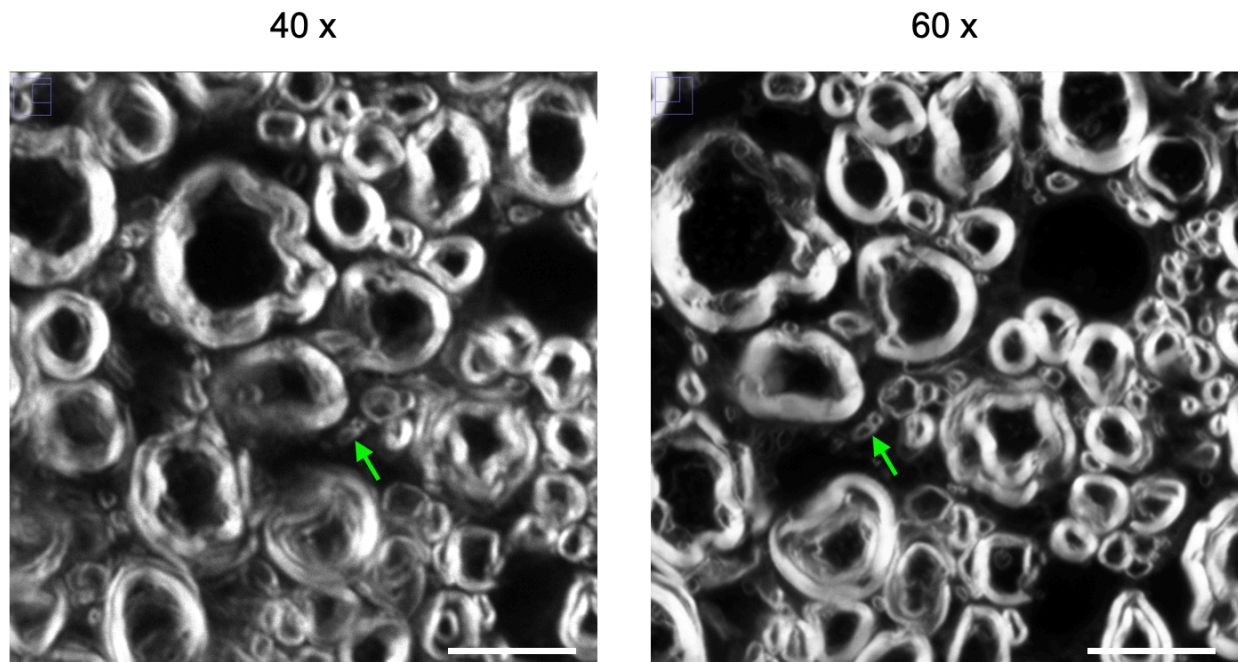
Figure 7.14 Comparison between a 40 x (NA=0.95, air) and a 60 x (NA=1.4, oil) image of a rat spinal cord stained with the Nile-Red myelin stain. The scale bar is 10 micrometers. The green arrow shows a myelinated axon with a diameter of 0.9 micrometers. While it is well resolved on the 60 x image, it is barely visible on the 40 x image.

7.7.3 Discussion and conclusions.

Here, two myelin histology techniques based on confocal microscopy were investigated: the hyperspectral autofluorescence and the Nile-Red fluorescent staining. The autofluorescence has the advantage of being a stain-free protocol, which makes it simpler and not subject to potential staining artifacts. Despite every channel of the hyperspectral stack already showing a high sensitivity to myelin, the spectral information can help to gain in specificity. However, this comes at the cost of a longer acquisition due to the multiple channels to acquire, the cross-channels bleaching, and the low quantum efficiency of the endogenous fluorescence. This long acquisition time makes it not suitable to use hyperspectral autofluorescence to image at high resolution (> 40 x) a full millimetric field of view. The Nile-Red fluorescent stain offers a much better quantum efficiency and unlock the possibility to acquire, relatively quickly, high resolution images at large

fields of view. In the white matter, it offers a very good contrast between the myelin sheets and the axons and background. In the grey matter, other structures were also stained, like glial cells and blood vessels. To image myelin in the white matter as part of a qMRI validation protocol, both hyperspectral autofluorescence and the Nile-Red fluorescent stain could be used at 10 x. The Nile-Red would be a more expensive and more challenging protocol, but the imaging time would be shorter so more samples could potentially be scanned. The hyperspectral autofluorescence would be simpler, cheaper, less biased, but would require more imaging and post-processing time.

7.8   References

Christensen, P. C., Brideau, C., Poon, K. W. C., Döring, A., Yong, V. W., & Stys, P. K. (2014). High-resolution fluorescence microscopy of myelin without exogenous probes. *NeuroImage*, *87*, 42–54.

De Leener, B., Lévy, S., Dupont, S. M., Fonov, V. S., Stikov, N., Louis Collins, D., Callot, V., & Cohen-Adad, J. (2017). SCT: Spinal Cord Toolbox, an open-source software for processing spinal cord MRI data. *NeuroImage*, *145*(Pt A), 24–43.

Lévy, S., Benhamou, M., Naaman, C., Rainville, P., Callot, V., & Cohen-Adad, J. (2015). White matter atlas of the human spinal cord with estimation of partial volume effect. *NeuroImage*, *119*, 262–271.

Ouellette, R., Mangeat, G., Polyak, I., Warntjes, M., Forslin, Y., Bergendal, Å., Plattén, M., Uppman, M., Treaba, C. A., Cohen-Adad, J., Piehl, F., Kristoffersen Wiberg, M., Fredrikson, S., Mainero, C., & Granberg, T. (2020). Validation of Rapid Magnetic Resonance Myelin Imaging in Multiple Sclerosis. *Annals of Neurology*, *87*(5), 710–724.

Vincze, A., Mázló, M., Seress, L., Komoly, S., & Abrahám, H. (2008). A correlative light and electron microscopic study of postnatal myelination in the murine corpus callosum. *International Journal of Developmental Neuroscience: The Official Journal of the International Society for Developmental Neuroscience*, *26*(6), 575–584.

Warntjes, J. B. M., Leinhard, O. D., West, J., & Lundberg, P. (2008). Rapid magnetic resonance quantification on the brain: Optimization for clinical usage. *Magnetic Resonance in Medicine: Official Journal of the Society of Magnetic Resonance in Medicine / Society of Magnetic Resonance in Medicine*, *60*(2), 320–329.

CHAPTER 8   GENERAL DISCUSSION

8.1   Execution of the project: timeline, collaborations and opportunities.

My PhD project started in Fall 2017, after finishing a Master on quantitative MRI, I wished to 1) investigate and work on new quantitative MRI techniques, 2) apply my research to a clinical context, 3) be involved in the histology and microscopy procedures to validate quantitative MRI. My first project was done in collaboration with Dr Caterina Mainero, MD, PhD, neurologist and associate professor at HMS/HST/Martinos center for biomedical imaging, Charlestown, USA. The goal was to combine several qMRI techniques to investigate their relevance to detect subtle pathological features in early MS patients. On the one hand, I combined high resolution 7 Tesla T1 and T2* mapping in order to extract a marker of cortical myelination (CME). And on the other hand, I computed the high angular resolution tractography from diffusion MRI images acquired on a Connectome scanner (300mT/m) and extracted graph theory and connectivity markers from the same cohort of subjects. This study enabled us to discover a new association between cortical pathology and brain network reorganization at an early stage of MS. This work, Presented on Chapter 4, was published in the journal Human Brain Mapping (Gabriel Mangeat et al., 2018). A year after the publication, I have been personally invited by the ARSEP (French MS society) to present these findings in Paris.

I always keep in mind that these advanced MRI techniques should, ultimately, be translated to the patient's bed. Thus, I have initiated a collaboration with Dr. Tobias Granberg, MD, PhD, clinician and neuro-radiologist at Karolinska Institutet in Sweden, who became my official PhD co-supervisor in 2018. He was using qMRI as part of his clinical routine protocol, which triggered my interest. Indeed, the SyMRI protocol had recently been CE-marked in Sweden (equivalent to FDA approved in the US). I have investigated several approaches to extract useful biomarkers from these clinical qMRI images. More specifically, I worked on biomarkers capable of distinguishing two neurodegenerative conditions hardly distinguishable by clinicians: MS and HDLS. I found that a machine learning based model could give specific markers of the physical processes underlying the myelin losses, which is of great interest to aid the differential diagnosis of those two symptomatically close neurodegenerative conditions. This work, presented in Chapter 5, was completed during my internship in Stockholm, Sweden, in Fall 2019 and published in the Journal of Neuroimaging (Gabriel Mangeat et al., 2020).

In parallel with this study, I started my work on histology. I investigated several options: 1) I worked with Prof. Frédéric Lesage, from Polytechnique who was working on a CARS serial histology setup, aiming to perform automatic serial and label free histology. 2) I worked with Prof. Mark Lavertu, from Polytechnique, who has a high-end hyperspectral confocal microscopy platform. 3) I worked with Irene Londono, expert in staining protocols and Lab assistant of Prof. Isabelle Villemure, from Polytechnique. I really enjoyed applying my knowledge in physics to these projects. After investigating the different histology options, I proposed a protocol aiming to compare qMRI and histology with the least possible biases. With the aid of Prof. Sylvain Martel, from Polytechnique, I realised a protocol involving *in-vivo* and *ex-vivo* qMRI scans of a pig, extraction of the spinal cord, *ex-vivo* qMRI scans of the extracted tissues, fixation, slicing, and microscopy of the same tissues. I tried the protocol two times with two different pigs, every time trying to optimise the quality of the the microscopy and the qMRI images. This work, Presented in Chapter 7, was presented at the international conference ISMRM 2019. I Initially planned to pursue this work by improving the histology protocol, e.g. adding and comparing more specific myelin labelling techniques. However, soon after my return from Sweden, the global pandemic stroke and the lockdown forced me to stop my current microscopy activities.

Thus, I have decided to focus my work on the processing of a valuable dataset that I had just acquired during my stay in Sweden. Indeed, the Karolinska Institutet owns dozens of MRI scanners from the three vendors available on the market: Siemens, GE and Phillips, and for each field strength available in clinics (1.5 tesla and 3 tesla). Karolinska Institutet thus offered a unique opportunity to test the repeatability and reproducibility of our tools under various clinical environments. During my internship, I recruited 5 healthy controls and performed more than 200 scans with 9 different MRI from 3 vendors and 2 field strengths to assess the repeatability and reproducibility of the measurements. This work enables clinicians to assess the possibility to compare images and biomarkers acquired from different scanners. More particularly, it provides estimates of the expected technical variability of such multicentric protocols. This work, presented in Chapter 6, has just been submitted in the journal Neuroimage.

Despite all of these studies being individually discussed in their respective chapters, here are some general discussion points that I found necessary to elaborate.

8.2 Importance of the reproducibility in qMRI

The name quantitative MRI genuinely implies that we can rely on the absolute values of the measurements because they are quantitative. However, as presented in Chapter 6, this is not always the case and some techniques are more repeatable than others. The importance of reproducibility in qMRI is critical when an algorithm or a protocol directly relies on the quantitative values of an image, such as the algorithm presented in Chapter 5. In this study, the repeatability was estimated with several scan-rescans so that the algorithm could take into account a reasonable variability of the predicting features. However, the repeatability and reproducibility study performed in Chapter 6 was more comprehensive in terms of number of different MRI scanners and subjects involved. The repeatability results of both studies are coherent. A great advantage of the study presented in Chapter 6 is that it permits to assess if the diagnosis algorithm of Chapter 5 could be directly applied to multicentric qMRI images, or at least, to any of the 9 scanners tested. The answer is: *"Yes, almost!".* In Chapter 5, I have shown that with 5% of reproducibility error, the algorithm is not 100% accurate, but shows that the true positive rate of HDLS was 97.2%, and the true positive rate of MS was 99.6%, which is still helpful if considered as an aid to the diagnosis. In comparison, in Chapter 6, I have shown that the reproducibility error amongst the 9 scanners is under 5% for all biomarkers except T1 in WM (5.83%) and REMyDI in GM (20.19%). Suggesting that the algorithm could still be of interest to aid the diagnosis even when using multicentric data. Some work to optimize the diagnosis algorithm knowing the actual variability could be done (e.g. adding a higher weight to the features with the best reproducibility). Such developments are opening the door to multicentric diagnosis algorithms. An automatic pre-assessment of a patient condition could help reduce the workload of radiologists and thus make hospitals and governments save money and time.

8.3 Comparing qMRI methods

The repeatability of a technique measures its agreement with itself under various experimental conditions (e,g, different acquisitions or different machines). In addition, we saw in this thesis that several different qMRI techniques are designed to measure the same tissue properties, like T1, T2 of the myelin concentration. However, some of the results might seems contradictory and one might wonder if these techniques are equals of even comparable amongst themselves. For example, in

Chapter 6, Table 6.3 shows that the myelin estimation REMyDI measures a myelin content in the GM below 2%, which is about 15 times less than in the WM. Those results are not consistent with the one presented in Figure 7.8, where the histology shows a myelin measurement about 50% lower in the GM than in the WM and *ex-vivo* REMyDI show myelin measurement about 25% lower in the GM than in the WM. In addition, the CME results presented in Chapter 4 estimate the cortical myelin at about 40%, which is largely overestimated compared to the measurements of SyMRI. Another example is the measure of the longitudinal relaxation time T1. Figure 7.6 show that the T1 measured with SyMRI and the T1 measured with the VFA protocol only correlates with a coefficient of r=0.5, which highlight a large un-explained variance between the two measurements of the same MR property. These inconsistent results could have different causes, such as: unperfect specificity of the measurements, some protocols are optimized for *in-vivo* but not for not *ex-vivo*, or even some protocols are optimized for WM measurements rather than GM. Several studies have investigated the question of comparing different MR protocols to measure a unique tissue property. For example, Stikov et al., 2014, reported a discrepancy in the T1 values in the brain using three most common T1 mapping techniques. In addition, Mancini et al., 2020 performed an extensive meta-analysis of qMRI derived myelin estimates, and also conclude that all the measurements techniques are not equals in terms of specificity to myelin. In the future, SyMRI derived measures should be included in one of these comparison studies to give the community an idea of how it compares to other more established qMRI methods. For now, it is important to keep in mind that absolute qMRI measures strongly depends on the method and that comparisons of a tissue property should always consider the biases induces by the measuring technique.

8.4 Choice of the histology techniques

Inhomogeneous stain penetration in tissues, stain agglomeration or endogenous background attenuation are hampering the specificity of stained images and are thus lowering their ability to be used as *"gold standard references"*. The rationale of investigating CARS and hyperspectral autofluorescence is that those two techniques do not require any staining and are thus not prone to staining artifacts. The CARS microscope was unfortunately experiential and under assembly for a longer period of time than expected. Some tests of axon imaging were made, but strong image artifacts, such as galvanometers fringes, or background resonant signal made the images not

suitable for our histology needs. However, the hyperspectral autofluorescence tests were much more conclusive. As seen on Chapter 7, we observed a good contrast between the background and the tissues of interest, such as the myelin sheaths. The quality of these images is in part due to the ease of manipulation and various options given by the Olympus FV 1000 microscope which made it easy to find the optimal imaging parameters, such as the excitation wavelength, number of reception channels, bandwidth of the reception channels, resolution, etc. Several compromises had to be made between the duration of the scan, the size of the image, the resolution (spatial specificity) and the number of spectral channels (tissue specificity). One optimal set of parameters that optimizes the contrast of myelin sheets vs background is presented in Chapter 7. However, different parameters would need to be found to image different tissues, such as collagen or axons. This being said, there is still one major limitation in using hyperspectral autofluorescence for large scale histology: the higher is the resolution, the higher is the spectral difference between tissues and the better is the unmixing result. The corollary being that we need a high resolution to get a specific tissue unmixing. Combining high resolution and a large field of view opens the door to new challenges.

8.5 Field of view versus resolution

Imaging with a sub-micrometric resolution over a centimetric field of view is extremely challenging. For example, if we are imaging a green light of 514 nm and our confocal microscope is equipped with an oil immersion objective with an NA of 1.45, then the (theoretical) limit of resolution will be 177 nm, which is good to image axons and their myelin sheaths, as presented in Chapter 7. However, if we need to image a whole human spinal cord section of 5 x 7 cm, the imaging will present some challenges: 1) it will be about 384,000 x 284,000 pixels, or 109 gigapixels, 2) it will be composed of 188 x 134 tiles (providing each tile has a resolution of 2048 x 2048 pixels), and 3) the imaging plane in such conditions would have a thickness of about 500 nanometers, implying that if the planarity tolerance between the sample and the microscope stage is below 500 nm, we will observe intensity gradient artifacts through the tile. Lowering the resolution would attenuate those challenges but reduce our ability to detect the details of the microstructure. A compromise has to be found between the practical feasibility of a histology technique and its sensitivity to the microstructure.

8.6 Validating the accuracy of qMRI

As seen in the previous paragraph, obtaining a high-resolution quantitative histology image is quite challenging. However, alternative approaches could be used to validate the accuracy of qMRI: either using low resolution quantitative images (such as 10 x hyperspectral autofluorescence images or Nile-Red images, as discussed in Chapter 7), or high resolution un-quantitative images. The idea of the later approach is to obtain images with the highest possible resolution (e.g. SEM or optical) and to segment the tissues of interest. This is the idea of the software AxonDeepSeg (Zaimi et al., 2018) which offers impressive performance in segmenting the myelin of the white matter. The main advantage of this technique is its specificity: no other structure than myelin rings would be segmented. Another advantage of this technique is that several metrics can be extracted from the segmentation, such as axon diameter, myelin thickness, g-ratio, myelin density, etc. Some disadvantages of this technique are 1) it will be less sensitive than a staining approach, as some small axons and axons with improbable shapes won't be segmented, 2) it requires high resolution images, thus a long imaging time and 3) it is only working in the spinal cord, where the sections are perpendicular to the axons.

In summary, a qMRI validation study could consider different approaches depending on the aim, the budget and the time. 1) Traditional OD stains (e.g. LFB) can be used to produce images with large fields of view at a relatively low cost, but their actual specificity and sensitivity is difficult to assess, often leading to large unexplained variance between histology and qMRI. 2) Automatic segmentation of high-resolution images is very specific, and its sensitivity and specificity are easily measurable, but the technique is cost and time consuming. 3) Low resolution fluorescent imaging, whether it is endogenous or exogenous, offers a good compromise: the protocol is relatively fast to set up and low-resolution images can be acquired quickly. It is possible to zoom afterward on some selected spots to measure the relative intensity of the unwanted tissues and have a clear idea of the sensitivity, specificity or potential sources of bias hampering the ability of our *"gold standard"* to be used as a reference imaging technique.

CHAPTER 9   CONCLUSIONS AND RECOMMENDATIONS

The quantitative MRI community is seeking for repeatability, reproducibility, accuracy, specificity, and speed of imaging, while the neuropathology community is seeking for meaningful biomarkers of disease progression. The objective of this project was to assess how multimodal quantitative MRI can measure subtle neurodegenerative changes in MS, in research and in a clinical context, with a high repeatability, reproducibility and accuracy.

The first contribution was to show that the combination of high resolution 7 tesla T1 and T2* mapping and high angular resolution tractography from diffusion MRI images acquired on a Connectome scanner (300mT/m) could be used to monitor an interplay between cortical pathology and brain network reorganization at an early stage of MS. More specifically, significant covariations between cortical myelin estimation and white matter graph theory connectivity metrics were observed. This study contributes to the knowledge in the neuropathology of MS and opens the door to follow-up studies investigating the causality of the observed interplay. The main limitation of this study was the state-of-the-art experimental setup needed to monitor the interplay: 7 tesla MRI, Connectome MRI and 4 hours of scan per subject.

The second contribution was to show that a fast quantitative MRI protocol combined with machine learning could give insights, not perceptible by radiologists, to aid the challenging differential diagnosis of MS and the rare neurodegenerative condition HDLS. Indeed, quantitative T1, T2, PD and REMyDI maps from the SyMRI protocol can be combined to compute discriminant biomarkers of the HDLS pathology. This study contributes to the field of clinical radiology and demonstrates the feasibility of computer-assistance tools based on quantitative MRI, to help differentiate subtle pathological mechanisms. The main limitation of this study was the low availability of patients with the rare neurodegenerative condition HDLS.

The third contribution was a comprehensive assessment of the repeatability and reproducibility of the quantitative biomarkers used in the previous study, using 9 different MRI from 3 vendors (Siemens, GE and Phillips) and 2 field strengths (1.5 tesla and 3 tesla). We found that most of the biomarkers can be measured with an excellent repeatability and decent reproducibility in clinical conditions. This study demonstrates the possibility and the relevance to use quantitative MRI in clinics. The recommendation can be made to incorporate fast quantitative MRI sequences to routine

scans of neurodegenerative conditions, like MS, as these scans can be compared across platforms and can be used to draw better diagnoses and more personalised patient assessment.

The last contribution was to propose and evaluate a histology validation protocol to assess the accuracy and specificity of quantitative MRI. I developed a protocol based on stain-free histology techniques, in-vivo and ex-vivo quantitative MRI scans of pigs and demonstrated that hyperspectral auto-fluorescence imaging could be used to assess MRI based myelin imaging techniques. This study contributed to the field of quantitative MRI, by proposing and assessing alternative gold standard myelin imaging techniques. The main limitation of this study is the high resolution needed to obtain a good myelin specificity, which limits the maximum sample size. Future research directions could be focused on low resolution stain-free myelin histology techniques.

This 3.5 years PhD project gave me the opportunity to develop my critical thinking, optimise my strategy to answer scientific questions and brought to light my dedication to tackle technical problems. I really enjoyed working in the bridge between the technical fields of quantitative MRI and advanced optics, and the applied field of clinical radiology. Achieving my project within an incredible multidisciplinary team of professors, physicists, mathematicians, neurologists and radiologists largely contributed to this modest but meaningful contribution to science.

CHAPTER 10   BIBLIOGRAPHY

Azevedo, F. A. C., Carvalho, L. R. B., Grinberg, L. T., Farfel, J. M., Ferretti, R. E. L., Leite, R. E. P., Jacob Filho, W., Lent, R., & Herculano-Houzel, S. (2009). Equal numbers of neuronal and nonneuronal cells make the human brain an isometrically scaled-up primate brain. *The Journal of Comparative Neurology*, *513*(5), 532–541.

Ben-Eliezer, N., Sodickson, D. K., & Block, K. T. (2015). Rapid and accurate T2 mapping from multi-spin-echo data using Bloch-simulation-based reconstruction. *Magnetic Resonance in Medicine: Official Journal of the Society of Magnetic Resonance in Medicine / Society of Magnetic Resonance in Medicine*, *73*(2), 809–817.

Berry, I., Barker, G. J., Barkhof, F., Campi, A., Dousset, V., Franconi, J. M., Gass, A., Schreiber, W., Miller, D. H., & Tofts, P. S. (1999). A multicenter measurement of magnetization transfer ratio in normal white matter. *Journal of Magnetic Resonance Imaging: JMRI*, *9*(3), 441–446.

Betzel, R. F., Avena-Koenigsberger, A., Goñi, J., He, Y., de Reus, M. A., Griffa, A., Vértes, P. E., Mišic, B., Thiran, J.-P., Hagmann, P., van den Heuvel, M., Zuo, X.-N., Bullmore, E. T., & Sporns, O. (2016). Generative models of the human connectome. *NeuroImage*, *124*(Pt A), 1054–1064.

Bjarnason, T. A., Vavasour, I. M., Chia, C. L. L., & MacKay, A. L. (2005). Characterization of the NMR behavior of white matter in bovine brain. *Magnetic Resonance in Medicine: Official Journal of the Society of Magnetic Resonance in Medicine / Society of Magnetic Resonance in Medicine*, *54*(5), 1072–1081.

Blystad, I., Håkansson, I., Tisell, A., Ernerudh, J., Smedby, Ö., Lundberg, P., & Larsson, E.-M. (2016). Quantitative MRI for Analysis of Active Multiple Sclerosis Lesions without Gadolinium-Based Contrast Agent. *AJNR. American Journal of Neuroradiology*, *37*(1), 94–100.

Bonnier, G., Maréchal, B., Fartaria, M. J., Falkowskiy, P., Marques, J. P., Simioni, S., Schluep, M., Du Pasquier, R., Thiran, J.-P., Krueger, G., & Granziera, C. (2017). The Combined Quantification and Interpretation of Multiple Quantitative Magnetic Resonance Imaging Metrics Enlightens Longitudinal Changes Compatible with Brain Repair in Relapsing-Remitting Multiple Sclerosis Patients. *Frontiers in Neurology*, *8*, 506.

Bullmore, E., & Sporns, O. (2009). Complex brain networks: graph theoretical analysis of structural and functional systems. *Nature Reviews. Neuroscience*, *10*(3), 186–198.

Cercignani, M., Basile, B., Spanò, B., Comanducci, G., Fasano, F., Caltagirone, C., Nocentini, U., & Bozzali, M. (2009). Investigation of quantitative magnetisation transfer parameters of lesions and normal appearing white matter in multiple sclerosis. *NMR in Biomedicine*, *22*(6), 646–653.

Cheng, J.-X., & Xie, X. S. (2015). Vibrational spectroscopic imaging of living systems: An emerging platform for biology and medicine. *Science*, *350*(6264), aaa8870.

Chen, J. T.-H., Easley, K., Schneider, C., Nakamura, K., Kidd, G. J., Chang, A., Staugaitis, S. M., Fox, R. J., Fisher, E., Arnold, D. L., & Trapp, B. D. (2013). Clinically feasible MTR is sensitive to cortical demyelination in MS. *Neurology*, *80*(3), 246–252.

Chong, A. L., Chandra, R. V., Chuah, K. C., Roberts, E. L., & Stuckey, S. L. (2016). Proton Density MRI Increases Detection of Cervical Spinal Cord Multiple Sclerosis Lesions Compared with T2-Weighted Fast Spin-Echo. *AJNR. American Journal of Neuroradiology*, *37*(1), 180–184.

Christensen, P. C., Brideau, C., Poon, K. W. C., Döring, A., Yong, V. W., & Stys, P. K. (2014). High-resolution fluorescence microscopy of myelin without exogenous probes. *NeuroImage*, *87*, 42–54.

Chung, K., Wallace, J., Kim, S.-Y., Kalyanasundaram, S., Andalman, A. S., Davidson, T. J., Mirzabekov, J. J., Zalocusky, K. A., Mattis, J., Denisin, A. K., Pak, S., Bernstein, H., Ramakrishnan, C., Grosenick, L., Gradinaru, V., & Deisseroth, K. (2013). Structural and molecular interrogation of intact biological systems. *Nature*, *497*(7449), 332–337.

Cohen-Adad, J. (2014). What can we learn from T2* maps of the cortex? *NeuroImage*, *93 Pt 2*, 189–200.

Cohen-Adad, J., Benner, T., Greve, D., Kinkel, R. P., Radding, A., Fischl, B., Rosen, B. R., & Mainero, C. (2011). In vivo evidence of disseminated subpial T2* signal changes in multiple sclerosis at 7 T: a surface-based analysis. *NeuroImage*, *57*(1), 55–62.

Cohen-Adad, J., Polimeni, J. R., Helmer, K. G., Benner, T., McNab, J. A., Wald, L. L., Rosen, B. R., & Mainero, C. (2012). T$_2$* mapping and B$_0$ orientation-dependence at 7 T reveal cyto- and myeloarchitecture organization of the human cortex. *NeuroImage*, *60*(2), 1006–1014.

Compston, A., & Coles, A. (2008). Multiple sclerosis. *The Lancet*, *372*(9648), 1502–1517.

Deistung, A., Schäfer, A., Schweser, F., Biedermann, U., Turner, R., & Reichenbach, J. R. (2013). Toward in vivo histology: a comparison of quantitative susceptibility mapping (QSM) with magnitude-, phase-, and R2*-imaging at ultra-high magnetic field strength. *NeuroImage*, *65*, 299–314.

Does, M. D. (2018). Inferring brain tissue composition and microstructure via MR relaxometry. *NeuroImage*. https://doi.org/10.1016/j.neuroimage.2017.12.087

Douglas Fields, R. (2009). *The Other Brain: From Dementia to Schizophrenia, How New Discoveries about the Brain Are Revolutionizing Medicine and Science*. Simon and Schuster.

Duboisset, J., Berto, P., Gasecka, P., Bioud, F.-Z., Ferrand, P., Rigneault, H., & Brasselet, S. (2015). Molecular orientational order probed by coherent anti-Stokes Raman scattering (CARS) and stimulated Raman scattering (SRS) microscopy: a spectral comparative study. *The Journal of Physical Chemistry. B*, *119*(7), 3242–3249.

Evans, C. L., Potma, E. O., Puoris'haag, M., Côté, D., Lin, C. P., & Xie, X. S. (2005). Chemical imaging of tissue in vivo with video-rate coherent anti-Stokes Raman scattering microscopy. *Proceedings of the National Academy of Sciences of the United States of America*, *102*(46), 16807–16812.

Filippi, M., Cercignani, M., Inglese, M., Horsfield, M. A., & Comi, G. (2001). Diffusion tensor magnetic resonance imaging in multiple sclerosis. In *Neurology* (Vol. 56, Issue 3, pp. 304–311). https://doi.org/10.1212/wnl.56.3.304

Filippi, M., Rocca, M. A., Barkhof, F., Brück, W., Chen, J. T., Comi, G., DeLuca, G., De Stefano, N., Erickson, B. J., Evangelou, N., Fazekas, F., Geurts, J. J. G., Lucchinetti, C., Miller, D. H., Pelletier, D., Popescu, B. F. G., Lassmann, H., & Attendees of the Correlation between

Pathological MRI findings in MS workshop. (2012). Association between pathological and MRI findings in multiple sclerosis. *Lancet Neurology*, *11*(4), 349–360.

Fleischer, V., Gröger, A., Koirala, N., Droby, A., Muthuraman, M., Kolber, P., Reuter, E., Meuth, S. G., Zipp, F., & Groppa, S. (2016). Increased structural white and grey matter network connectivity compensates for functional decline in early multiple sclerosis. *Multiple Sclerosis* . https://doi.org/10.1177/1352458516651503

Fooladi, M., Riyahi Alam, N., Sharini, H., Firouznia, K., Shakiba, M., & Harirchian, M. H. (2020). Multiparametric qMTI Assessment and Monitoring of Normal Appearing White Matter and Classified T1 Hypointense Lesions in Relapsing-Remitting Multiple Sclerosis. *IRBM*, *41*(3), 151–160.

Fornito, A., Zalesky, A., & Breakspear, M. (2015). The connectomics of brain disorders. *Nature Reviews. Neuroscience*, *16*(3), 159–172.

Frank, J., Wagenknecht, T., McEwen, B. F., Marko, M., Hsieh, C.-E., & Mannella, C. A. (2002). Three-dimensional imaging of biological complexity. *Journal of Structural Biology*, *138*(1-2), 85–91.

Fukunaga, M., Li, T.-Q., van Gelderen, P., de Zwart, J. A., Shmueli, K., Yao, B., Lee, J., Maric, D., Aronova, M. A., Zhang, G., Leapman, R. D., Schenck, J. F., Merkle, H., & Duyn, J. H. (2010). Layer-specific variation of iron content in cerebral cortex as a source of MRI contrast. *Proceedings of the National Academy of Sciences of the United States of America*, *107*(8), 3834–3839.

Fu, Y., Huff, T. B., Wang, H.-W., Wang, H., & Cheng, J.-X. (2008). Ex vivo and in vivo imaging of myelin fibers in mouse brain by coherent anti-Stokes Raman scattering microscopy. *Optics Express*, *16*(24), 19396–19409.

Fu, Y., Wang, H., Huff, T. B., Shi, R., & Cheng, J.-X. (2007). Coherent anti-Stokes Raman scattering imaging of myelin degradation reveals a calcium-dependent pathway in lyso-PtdCho-induced demyelination. *Journal of Neuroscience Research*, *85*(13), 2870–2881.

Galbusera, R., Parmar, K., Boillat, Y., Fartaria, M. J., Todea, A.-R., Brien, K. O., Smolinski, A., Kappos, L., van der Zwaag, W., & Granziera, C. (2020). Laminar analysis of the cerebellar cortex shows widespread damage in early MS patients: A pilot study at 7T MRI. *Multiple Sclerosis Journal - Experimental, Translational and Clinical*, *6*(4), 2055217320961409.

Giacomini, P. S., Levesque, I. R., Ribeiro, L., Narayanan, S., Francis, S. J., Pike, G. B., & Arnold, D. L. (2009). Measuring demyelination and remyelination in acute multiple sclerosis lesion voxels. *Archives of Neurology*, *66*(3), 375–381.

Girard, O. M., Prevost, V. H., Varma, G., Cozzone, P. J., Alsop, D. C., & Duhamel, G. (2015). Magnetization transfer from inhomogeneously broadened lines (ihMT): Experimental optimization of saturation parameters for human brain imaging at 1.5 Tesla. *Magnetic Resonance in Medicine: Official Journal of the Society of Magnetic Resonance in Medicine / Society of Magnetic Resonance in Medicine*, *73*(6), 2111–2121.

Gracien, R.-M., Reitz, S. C., Hof, S. M., Fleischer, V., Zimmermann, H., Droby, A., Steinmetz, H., Zipp, F., Deichmann, R., & Klein, J. C. (2016). Changes and variability of proton density and T1 relaxation times in early multiple sclerosis: MRI markers of neuronal damage in the cerebral cortex. *European Radiology*, *26*(8), 2578–2586.

Granberg, T., Uppman, M., Hashim, F., Cananau, C., Nordin, L. E., Shams, S., Berglund, J., Forslin, Y., Aspelin, P., Fredrikson, S., & Kristoffersen-Wiberg, M. (2016). Clinical Feasibility of Synthetic MRI in Multiple Sclerosis: A Diagnostic and Volumetric Validation Study. *AJNR. American Journal of Neuroradiology*, *37*(6), 1023–1029.

Griffa, A., Baumann, P. S., Thiran, J.-P., & Hagmann, P. (2013). Structural connectomics in brain diseases. *NeuroImage*, *80*, 515–526.

Hagiwara, A., Hori, M., Yokoyama, K., Nakazawa, M., Ueda, R., Horita, M., Andica, C., Abe, O., & Aoki, S. (2017). Analysis of White Matter Damage in Patients with Multiple Sclerosis via a Novel In Vivo MR Method for Measuring Myelin, Axons, and G-Ratio. *AJNR. American Journal of Neuroradiology*, *38*(10), 1934–1940.

Hagiwara, A., Hori, M., Yokoyama, K., Takemura, M. Y., Andica, C., Kumamaru, K. K., Nakazawa, M., Takano, N., Kawasaki, H., Sato, S., Hamasaki, N., Kunimatsu, A., & Aoki, S. (2017). Utility of a Multiparametric Quantitative MRI Model That Assesses Myelin and Edema for Evaluating Plaques, Periplaque White Matter, and Normal-Appearing White Matter in Patients with Multiple Sclerosis: A Feasibility Study. *AJNR. American Journal of Neuroradiology*, *38*(2), 237–242.

Hagiwara, A., Hori, M., Yokoyama, K., Takemura, M. Y., Andica, C., Tabata, T., Kamagata, K., Suzuki, M., Kumamaru, K. K., Nakazawa, M., Takano, N., Kawasaki, H., Hamasaki, N., Kunimatsu, A., & Aoki, S. (2017). Synthetic MRI in the Detection of Multiple Sclerosis Plaques. *AJNR. American Journal of Neuroradiology*, *38*(2), 257–263.

Hagiwara, A., Warntjes, M., Hori, M., Andica, C., Nakazawa, M., Kumamaru, K. K., Abe, O., & Aoki, S. (2017). Symri of the Brain: Rapid Quantification of Relaxation Rates and Proton Density, With Synthetic Mri, Automatic Brain Segmentation, and Myelin Measurement. *Investigative Radiology*, *52*(10), 647–657.

Harrison, D. M., Li, X., Liu, H., Jones, C. K., Caffo, B., Calabresi, P. A., & van Zijl, P. (2016). Lesion Heterogeneity on High-Field Susceptibility MRI Is Associated with Multiple Sclerosis Severity. *AJNR. American Journal of Neuroradiology*. https://doi.org/10.3174/ajnr.A4726

Hartung, D. M., Bourdette, D. N., Ahmed, S. M., & Whitham, R. H. (2015). The cost of multiple sclerosis drugs in the US and the pharmaceutical industry: Too big to fail? *Neurology*, *84*(21), 2185–2192.

Henkelman, R. M., Huang, X., Xiang, Q. S., Stanisz, G. J., Swanson, S. D., & Bronskill, M. J. (1993). Quantitative interpretation of magnetization transfer. *Magnetic Resonance in Medicine: Official Journal of the Society of Magnetic Resonance in Medicine / Society of Magnetic Resonance in Medicine*, *29*(6), 759–766.

Henkelman, R. M., Stanisz, G. J., & Graham, S. J. (2001). Magnetization transfer in MRI: a review. *NMR in Biomedicine*, *14*(2), 57–64.

Hines, C. D. G., Agni, R., Roen, C., Rowland, I., Hernando, D., Bultman, E., Horng, D., Yu, H., Shimakawa, A., Brittain, J. H., & Others. (2012). Validation of MRI biomarkers of hepatic steatosis in the presence of iron overload in the ob/ob mouse. *Journal of Magnetic Resonance Imaging: JMRI*, *35*(4), 844–851.

Imitola, J., Côté, D., Rasmussen, S., Xie, X. S., Liu, Y., Chitnis, T., Sidman, R. L., Lin, C. P., & Khoury, S. J. (2011). Multimodal coherent anti-Stokes Raman scattering microscopy reveals

microglia-associated myelin and axonal dysfunction in multiple sclerosis-like lesions in mice. *Journal of Biomedical Optics*, *16*(2), 021109.

Jang, J., Nam, Y., Choi, Y., Shin, N. Y., An, J. Y., Ahn, K. J., Kim, B. S., Lee, K. S., & Kim, W. (2020). Paramagnetic Rims in Multiple Sclerosis and Neuromyelitis Optica Spectrum Disorder: A Quantitative Susceptibility Mapping Study with 3-T MRI. *Journal of Clinical Neurology* , *16*(4), 562–572.

Karampampa, K., Gustavsson, A., Miltenburger, C., Kindundu, C. M., & Selchen, D. H. (2012). TREATMENT EXPERIENCE, BURDEN, AND UNMET NEEDS (TRIBUNE) IN MULTIPLE SCLEROSIS STUDY: THE COSTS AND UTILITIES OF MS PATIENTS IN CANADA. *J Popul Ther Clin Pharmacol, 19(1)*, 11–25.

Kilsdonk, I. D., Jonkman, L. E., Klaver, R., van Veluw, S. J., Zwanenburg, J. J. M., Kuijer, J. P. A., Pouwels, P. J. W., Twisk, J. W. R., Wattjes, M. P., Luijten, P. R., Barkhof, F., & Geurts, J. J. G. (2016). Increased cortical grey matter lesion detection in multiple sclerosis with 7 T MRI: a post-mortem verification study. *Brain: A Journal of Neurology*, *139*(Pt 5), 1472–1481.

Kobelt, G., Thompson, A., Berg, J., Gannedahl, M., Eriksson, J., MSCOI Study Group, & European Multiple Sclerosis Platform. (2017). New insights into the burden and costs of multiple sclerosis in Europe. *Multiple Sclerosis* , *23*(8), 1123–1136.

Kocevar, G., Stamile, C., Hannoun, S., Cotton, F., Vukusic, S., Durand-Dubief, F., & Sappey-Marinier, D. (2016). Graph Theory-Based Brain Connectivity for Automatic Classification of Multiple Sclerosis Clinical Courses. *Frontiers in Neuroscience*, *10*, 478.

Koenig, S. H., Brown, R. D., 3rd, Spiller, M., & Lundbom, N. (1990). Relaxometry of brain: why white matter appears bright in MRI. *Magnetic Resonance in Medicine: Official Journal of the Society of Magnetic Resonance in Medicine / Society of Magnetic Resonance in Medicine*, *14*(3), 482–495.

Kolind, S. H., & Deoni, S. C. (2011). Rapid three-dimensional multicomponent relaxation imaging of the cervical spinal cord. *Magnetic Resonance in Medicine: Official Journal of the Society of Magnetic Resonance in Medicine / Society of Magnetic Resonance in Medicine*, *65*(2), 551–556.

Kolind, S., Matthews, L., Johansen-Berg, H., Leite, M. I., Williams, S. C. R., Deoni, S., & Palace, J. (2012). Myelin water imaging reflects clinical variability in multiple sclerosis. *NeuroImage*, *60*(1), 263–270.

Lang, H. L. E., Jacobsen, H., Ikemizu, S., Andersson, C., Harlos, K., Madsen, L., Hjorth, P., Sondergaard, L., Svejgaard, A., Wucherpfennig, K., Stuart, D. I., Bell, J. I., Jones, E. Y., & Fugger, L. (2002). A functional and structural basis for TCR cross-reactivity in multiple sclerosis. *Nature Immunology*, *3*(10), 940–943.

Lashkari, A., Davoodi-Bojd, E., Fahmy, L., Li, L., Nejad-Davarani, S. P., Chopp, M., Jiang, Q., & Cerghet, M. (2020). Impairments of white matter tracts and connectivity alterations in five cognitive networks of patients with multiple sclerosis. *Clinical Neurology and Neurosurgery*, *201*, 106424.

Laule, C., Kozlowski, P., Leung, E., Li, D. K. B., Mackay, A. L., & Moore, G. R. W. (2008). Myelin water imaging of multiple sclerosis at 7 T: correlations with histopathology. *NeuroImage*, *40*(4), 1575–1580.

Laule, C., Leung, E., Lis, D. K. B., Traboulsee, A. L., Paty, D. W., MacKay, A. L., & Moore, G. R. W. (2006). Myelin water imaging in multiple sclerosis: quantitative correlations with histopathology. *Multiple Sclerosis* , *12*(6), 747–753.

Levesque, I. R., Giacomini, P. S., Narayanan, S., Ribeiro, L. T., Sled, J. G., Arnold, D. L., & Pike, G. B. (2010). Quantitative magnetization transfer and myelin water imaging of the evolution of acute multiple sclerosis lesions. *Magnetic Resonance in Medicine: Official Journal of the Society of Magnetic Resonance in Medicine / Society of Magnetic Resonance in Medicine*, *63*(3), 633–640.

Levesque, I. R., & Pike, G. B. (2009). Characterizing healthy and diseased white matter using quantitative magnetization transfer and multicomponent T2 relaxometry: A unified view via a four-pool model. *Magnetic Resonance in Medicine: Official Journal of the Society of Magnetic Resonance in Medicine / Society of Magnetic Resonance in Medicine*, *62*(6), 1487–1496.

Levin, L. I., Munger, K. L., O'Reilly, E. J., Falk, K. I., & Ascherio, A. (2010). Primary infection with the Epstein-Barr virus and risk of multiple sclerosis. *Annals of Neurology*, *67*(6), 824–830.

Li, Y., Jewells, V., Kim, M., Chen, Y., Moon, A., Armao, D., Troiani, L., Markovic-Plese, S., Lin, W., & Shen, D. (2013). Diffusion tensor imaging based network analysis detects alterations of neuroconnectivity in patients with clinically early relapsing-remitting multiple sclerosis. *Human Brain Mapping*, *34*(12), 3376–3391.

Lutti, A., Dick, F., Sereno, M. I., & Weiskopf, N. (2014). Using high-resolution quantitative mapping of R1 as an index of cortical myelination. *NeuroImage*, *93 Pt 2*, 176–188.

MacKay, A. L., & Laule, C. (2016). Magnetic Resonance of Myelin Water: An in vivo Marker for Myelin. *Brain Plasticity (Amsterdam, Netherlands)*, *2*(1), 71–91.

Mackay, A., Whittall, K., Adler, J., Li, D., Paty, D., & Graeb, D. (1994). In vivo visualization of myelin water in brain by magnetic resonance. *Magnetic Resonance in Medicine: Official Journal of the Society of Magnetic Resonance in Medicine / Society of Magnetic Resonance in Medicine*, *31*(6), 673–677.

Mainero, C., Benner, T., Radding, A., van der Kouwe, A., Jensen, R., Rosen, B. R., & Kinkel, R. P. (2009). In vivo imaging of cortical pathology in multiple sclerosis using ultra-high field MRI. *Neurology*, *73*(12), 941–948.

Mainero, C., Govindarajan, S. T., Kinkel, P. R., Nielsen, A. S., & Cohen-Adad, J. (2012). A gradient in cortical T2* relaxation decay changes at 7 Tesla MRI in patients with multiple sclerosis. *ISMRM*, 6158.

Mainero, C., Louapre, C., Govindarajan, S. T., Giannì, C., Nielsen, A. S., Cohen-Adad, J., Sloane, J., & Kinkel, R. P. (2015). A gradient in cortical pathology in multiple sclerosis by in vivo quantitative 7 T imaging. *Brain: A Journal of Neurology*, *138*(Pt 4), 932–945.

Mancini, M., Karakuzu, A., Cohen-Adad, J., Cercignani, M., Nichols, T. E., & Stikov, N. (2020). An interactive meta-analysis of MRI biomarkers of myelin. *eLife*, *9*. https://doi.org/10.7554/eLife.61523

Manfredonia, F., Ciccarelli, O., Khaleeli, Z., Tozer, D. J., Sastre-Garriga, J., Miller, D. H., & Thompson, A. J. (2007). Normal-appearing brain t1 relaxation time predicts disability in early primary progressive multiple sclerosis. *Archives of Neurology*, *64*(3), 411–415.

Mangeat, G., Badji, A., Ouellette, R., Treaba, C. A., Herranz, E., Granberg, T., Louapre, C., Stikov, N., Sloane, J. A., Bellec, P., Mainero, C., & Cohen-Adad, J. (2018). Changes in structural network are associated with cortical demyelination in early multiple sclerosis. *Human Brain Mapping*, *39*(5), 2133–2146.

Mangeat, G., Govindarajan, S. T., Kinkel, P. R., Mainero, C., & Cohen-Adad, J. (2013). Magnetization transfer ratio (MTR) and T2 (star) analysis of subpial demyelination. *MULTIPLE SCLEROSIS JOURNAL*, *19*, 189–190.

Mangeat, G., Govindarajan, S. T., Mainero, C., & Cohen-Adad, J. (2015). Multivariate combination of magnetization transfer, T2* and B0 orientation to study the myelo-architecture of the in vivo human cortex. *NeuroImage*, *119*, 89–102.

Mangeat, G., Louapre, C., Herranz, E., Treaba, C. A., Ouellette, R., Sloane, J. A., Klawiter, E. C., Cohen-Adad, J., & Mainero, C. (2015). Multivariate combination of quantitative T2* and T1 at 7T MRI detects in vivo subpial demyelination in the early stages of MS. *Mult Scler*, *23*, 485.

Mangeat, G., Nami, H., Pinon, N., Foias, A., Stikov, N., Granberg, T., & Cohen-Adad, J. (2019). *Stain-free histology to validate quantitative MRI*. ISMRM, Paris.

Mangeat, G., Ouellette, R., Wabartha, M., De Leener, B., Plattén, M., Danylaité Karrenbauer, V., Warntjes, M., Stikov, N., Mainero, C., Cohen-Adad, J., & Granberg, T. (2020). Machine Learning and Multiparametric Brain MRI to Differentiate Hereditary Diffuse Leukodystrophy with Spheroids from Multiple Sclerosis. *Journal of Neuroimaging: Official Journal of the American Society of Neuroimaging*, *30*(5), 674–682.

Marrie, R. A. (2004). Environmental risk factors in multiple sclerosis aetiology. *Lancet Neurology*, *3*(12), 709–718.

Ma, S., Wang, N., Fan, Z., Kaisey, M., Sicotte, N. L., Christodoulou, A. G., & Li, D. (2020). Three-dimensional whole-brain simultaneous T1, T2, and T1ρ quantification using MR Multitasking: Method and initial clinical experience in tissue characterization of multiple sclerosis. *Magnetic Resonance in Medicine: Official Journal of the Society of Magnetic Resonance in Medicine / Society of Magnetic Resonance in Medicine*. https://doi.org/10.1002/mrm.28553

Mezer, A., Yeatman, J. D., Stikov, N., Kay, K. N., Cho, N.-J., Dougherty, R. F., Perry, M. L., Parvizi, J., Hua, L. H., Butts-Pauly, K., & Wandell, B. A. (2013). Quantifying the local tissue volume and composition in individual brains with magnetic resonance imaging. *Nature Medicine*, *19*(12), 1667–1672.

Min, W., Freudiger, C. W., Lu, S., & Xie, X. S. (2011). Coherent nonlinear optical imaging: beyond fluorescence microscopy. *Annual Review of Physical Chemistry*, *62*, 507–530.

Mohan, A., De Ridder, D., & Vanneste, S. (2016). Graph theoretical analysis of brain connectivity in phantom sound perception. *Scientific Reports*, *6*, 19683.

Morawski, M., Kirilina, E., Scherf, N., Jäger, C., Reimann, K., Trampel, R., Gavriilidis, F., Geyer, S., Biedermann, B., Arendt, T., & Weiskopf, N. (2018). Developing 3D microscopy with CLARITY on human brain tissue: Towards a tool for informing and validating MRI-based histology. *NeuroImage*, *182*, 417–428.

Mottershead, J. P., Schmierer, K., Clemence, M., Thornton, J. S., Scaravilli, F., Barker, G. J., Tofts, P. S., Newcombe, J., Cuzner, M. L., Ordidge, R. J., & Others. (2003). High field MRI correlates of myelin content and axonal density in multiple sclerosis. *Journal of Neurology*, *250*(11), 1293–1301.

Mulero, P., Midaglia, L., & Montalban, X. (2018). Ocrelizumab: a new milestone in multiple sclerosis therapy. *Therapeutic Advances in Neurological Disorders*, *11*, 1756286418773025.

Nieminen, M. T., Rieppo, J., Töyräs, J., Hakumäki, J. M., Silvennoinen, J., Hyttinen, M. M., Helminen, H. J., & Jurvelin, J. S. (2001). T2 relaxation reveals spatial collagen architecture in articular cartilage: a comparative quantitative MRI and polarized light microscopic study. *Magnetic Resonance in Medicine: Official Journal of the Society of Magnetic Resonance in Medicine / Society of Magnetic Resonance in Medicine*, *46*(3), 487–493.

Nigro, S., Passamonti, L., Riccelli, R., Toschi, N., Rocca, F., Valentino, P., Nisticò, R., Fera, F., & Quattrone, A. (2015). Structural "connectomic" alterations in the limbic system of multiple sclerosis patients with major depression. *Multiple Sclerosis* , *21*(8), 1003–1012.

Orton, S.-M., Herrera, B. M., Yee, I. M., Valdar, W., Ramagopalan, S. V., Sadovnick, A. D., Ebers, G. C., & Canadian Collaborative Study Group. (2006). Sex ratio of multiple sclerosis in Canada: a longitudinal study. *Lancet Neurology*, *5*(11), 932–936.

Ouellette, R., Mangeat, G., Polyak, I., Warntjes, M., Forslin, Y., Bergendal, Å., Plattén, M., Uppman, M., Treaba, C. A., Cohen-Adad, J., Piehl, F., Kristoffersen Wiberg, M., Fredrikson, S., Mainero, C., & Granberg, T. (2020). Validation of Rapid Magnetic Resonance Myelin Imaging in Multiple Sclerosis. *Annals of Neurology*, *87*(5), 710–724.

Pampel, A., Müller, D. K., Anwander, A., Marschner, H., & Möller, H. E. (2015). Orientation dependence of magnetization transfer parameters in human white matter. *NeuroImage*, *114*, 136–146.

Pitt, D., Boster, A., Pei, W., Bs, E. W., Bs, A. J., Zachariah BS, C. R., Rammohan, K., Knopp, M. V., & Schmalbrock, P. (2010). Imaging Cortical Lesions in Multiple Sclerosis With Ultra–High-Field Magnetic Resonance Imaging. *Arch Neurol*, "812–818."

Polman, C. H., Reingold, S. C., Banwell, B., Clanet, M., Cohen, J. A., Filippi, M., Fujihara, K., Havrdova, E., Hutchinson, M., Kappos, L., Lublin, F. D., Montalban, X., O'Connor, P., Sandberg-Wollheim, M., Thompson, A. J., Waubant, E., Weinshenker, B., & Wolinsky, J. S. (2011). Diagnostic criteria for multiple sclerosis: 2010 revisions to the McDonald criteria. *Annals of Neurology*, *69*(2), 292–302.

Quintá, H. R., Pasquini, L. A., & Pasquini, J. M. (2015). Three-dimensional reconstruction of corticospinal tract using one-photon confocal microscopy acquisition allows detection of axonal disruption in spinal cord injury. *Journal of Neurochemistry*, *133*(1), 113–124.

Rilling, J. K., Glasser, M. F., Jbabdi, S., Andersson, J., & Preuss, T. M. (2011). Continuity, divergence, and the evolution of brain language pathways. *Frontiers in Evolutionary Neuroscience*, *3*, 11.

Samsonov, A., Alexander, A. L., Mossahebi, P., Wu, Y.-C., Duncan, I. D., & Field, A. S. (2012). Quantitative MR imaging of two-pool magnetization transfer model parameters in myelin mutant shaking pup. *NeuroImage*, *62*(3), 1390–1398.

Schmierer, K., Scaravilli, F., Altmann, D. R., Barker, G. J., & Miller, D. H. (2004). Magnetization transfer ratio and myelin in postmortem multiple sclerosis brain. *Annals of Neurology*, *56*(3), 407–415.

Schmierer, K., Tozer, D. J., Scaravilli, F., Altmann, D. R., Barker, G. J., Tofts, P. S., & Miller, D. H. (2007). Quantitative magnetization transfer imaging in postmortem multiple sclerosis brain. *Journal of Magnetic Resonance Imaging: JMRI*, *26*(1), 41–51.

Schmierer, K., Wheeler-Kingshott, C. A. M., Tozer, D. J., Boulby, P. A., Parkes, H. G., Yousry, T. A., Scaravilli, F., Barker, G. J., Tofts, P. S., & Miller, D. H. (2008). Quantitative magnetic resonance of postmortem multiple sclerosis brain before and after fixation. *Magnetic Resonance in Medicine: Official Journal of the Society of Magnetic Resonance in Medicine / Society of Magnetic Resonance in Medicine*, *59*(2), 268–277.

Schneider, T., Brownlee, W., Zhang, H., Ciccarelli, O., Miller, D. H., & Wheeler-Kingshott, C. G. (2017). Sensitivity of multi-shell NODDI to multiple sclerosis white matter changes: a pilot study. *Functional Neurology*, *32*(2), 97–101.

Sereno, M. I., Lutti, A., Weiskopf, N., & Dick, F. (2013). Mapping the human cortical surface by combining quantitative T(1) with retinotopy. *Cerebral Cortex* , *23*(9), 2261–2268.

Shu, N., Liu, Y., Li, K., Duan, Y., Wang, J., Yu, C., Dong, H., Ye, J., & He, Y. (2011). Diffusion tensor tractography reveals disrupted topological efficiency in white matter structural networks in multiple sclerosis. *Cerebral Cortex* , *21*(11), 2565–2577.

Stewart, W. A., Mackay, A. L., Whittall, K. P., Moore, G. R. W., & Paty, D. W. (1993). Spin-spin relaxation in experimental allergic encephalomyelitis. Analysis of CPMG data using a non-linear least squares method and linear inverse theory. *Magnetic Resonance in Medicine: Official Journal of the Society of Magnetic Resonance in Medicine / Society of Magnetic Resonance in Medicine*, *29*(6), 767–775.

Stikov, N., Boudreau, M., Levesque, I. R., Tardif, C. L., Barral, J. K., & Pike, G. B. (2014). On the accuracy of T1 mapping: Searching for common ground. *Magnetic Resonance in Medicine: Official Journal of the Society of Magnetic Resonance in Medicine / Society of Magnetic Resonance in Medicine*. https://doi.org/10.1002/mrm.25135

Stikov, N., Perry, L. M., Mezer, A., Rykhlevskaia, E., Wandell, B. A., Pauly, J. M., & Dougherty, R. F. (2011). Bound pool fractions complement diffusion measures to describe white matter micro and macrostructure. *NeuroImage*, *54*(2), 1112–1121.

Stüber, C., Morawski, M., Schäfer, A., Labadie, C., Wähnert, M., Leuze, C., Streicher, M., Barapatre, N., Reimann, K., Geyer, S., Spemann, D., & Turner, R. (2014). Myelin and iron concentration in the human brain: a quantitative study of MRI contrast. *NeuroImage*, *93 Pt 1*, 95–106.

Tang, Y., Nyengaard, J. R., De Groot, D. M., & Gundersen, H. J. (2001). Total regional and global number of synapses in the human brain neocortex. *Synapse* , *41*(3), 258–273.

Tardif, C. L., Bedell, B. J., Eskildsen, S. F., Collins, D. L., & Pike, G. B. (2012). Quantitative magnetic resonance imaging of cortical multiple sclerosis pathology. *Multiple Sclerosis International*, *2012*, 742018.

Taso, M., Girard, O. M., Duhamel, G., Le Troter, A., Feiweier, T., Guye, M., Ranjeva, J.-P., & Callot, V. (2016). Tract-specific and age-related variations of the spinal cord microstructure: a multi-parametric MRI study using diffusion tensor imaging (DTI) and inhomogeneous magnetization transfer (ihMT). *NMR in Biomedicine*, *29*(6), 817–832.

Thompson, A. J., Banwell, B. L., Barkhof, F., Carroll, W. M., Coetzee, T., Comi, G., Correale, J., Fazekas, F., Filippi, M., Freedman, M. S., Fujihara, K., Galetta, S. L., Hartung, H. P., Kappos, L., Lublin, F. D., Marrie, R. A., Miller, A. E., Miller, D. H., Montalban, X., … Cohen, J. A. (2018). Diagnosis of multiple sclerosis: 2017 revisions of the McDonald criteria. *Lancet Neurology*, *17*(2), 162–173.

Thompson, A. J., Baranzini, S. E., Geurts, J., Hemmer, B., & Ciccarelli, O. (2018). Multiple sclerosis. *The Lancet*, *391*(10130), 1622–1636.

Tian, F., Yang, W., Mordes, D. A., Wang, J.-Y., Salameh, J. S., Mok, J., Chew, J., Sharma, A., Leno-Duran, E., Suzuki-Uematsu, S., Suzuki, N., Han, S. S., Lu, F.-K., Ji, M., Zhang, R., Liu, Y., Strominger, J., Shneider, N. A., Petrucelli, L., … Eggan, K. (2016). Monitoring peripheral nerve degeneration in ALS by label-free stimulated Raman scattering imaging. *Nature Communications*, *7*, 13283.

Tozer, D., Ramani, A., Barker, G. J., Davies, G. R., Miller, D. H., & Tofts, P. S. (2003). Quantitative magnetization transfer mapping of bound protons in multiple sclerosis. *Magnetic Resonance in Medicine: Official Journal of the Society of Magnetic Resonance in Medicine / Society of Magnetic Resonance in Medicine*, *50*(1), 83–91.

Vågberg, M., Lindqvist, T., Ambarki, K., Warntjes, J. B. M., Sundström, P., Birgander, R., & Svenningsson, A. (2013). Automated determination of brain parenchymal fraction in multiple sclerosis. *AJNR. American Journal of Neuroradiology*, *34*(3), 498–504.

van der Kouwe, A. J. W., Benner, T., Salat, D. H., & Fischl, B. (2008). Brain morphometry with multiecho MPRAGE. *NeuroImage*, *40*(2), 559–569.

Van Obberghen, E., Mchinda, S., le Troter, A., Prevost, V. H., Viout, P., Guye, M., Varma, G., Alsop, D. C., Ranjeva, J.-P., Pelletier, J., Girard, O., & Duhamel, G. (2018). Evaluation of the Sensitivity of Inhomogeneous Magnetization Transfer (ihMT) MRI for Multiple Sclerosis. *AJNR. American Journal of Neuroradiology*, *39*(4), 634–641.

Varma, G., Duhamel, G., de Bazelaire, C., & Alsop, D. C. (2015). Magnetization transfer from inhomogeneously broadened lines: A potential marker for myelin. *Magnetic Resonance in Medicine: Official Journal of the Society of Magnetic Resonance in Medicine / Society of Magnetic Resonance in Medicine*, *73*(2), 614–622.

Vaughn, J., Hagiwara, M., Katz, J., Roth, J., Devinsky, O., Weiner, H., & Milla, S. (2013). MRI characterization and longitudinal study of focal cerebellar lesions in a young tuberous sclerosis cohort. *AJNR. American Journal of Neuroradiology*, *34*(3), 655–659.

Vavasour, I. M., Laule, C., Li, D. K. B., Oger, J., Moore, G. R. W., Traboulsee, A., & MacKay, A. L. (2009). Longitudinal changes in myelin water fraction in two MS patients with active disease. *Journal of the Neurological Sciences*, *276*(1-2), 49–53.

Vincze, A., Mázló, M., Seress, L., Komoly, S., & Abrahám, H. (2008). A correlative light and electron microscopic study of postnatal myelination in the murine corpus callosum. *International*

Journal of Developmental Neuroscience: The Official Journal of the International Society for Developmental Neuroscience, *26*(6), 575–584.

Vrenken, H., Geurts, J. J. G., Knol, D. L., van Dijk, L. N., Dattola, V., Jasperse, B., van Schijndel, R. A., Polman, C. H., Castelijns, J. A., Barkhof, F., & Pouwels, P. J. W. (2006). Whole-brain T1 mapping in multiple sclerosis: global changes of normal-appearing gray and white matter. *Radiology*, *240*(3), 811–820.

Wang, H., Fu, Y., Zickmund, P., Shi, R., & Cheng, J.-X. (2005). Coherent anti-stokes Raman scattering imaging of axonal myelin in live spinal tissues. *Biophysical Journal*, *89*(1), 581–591.

Wang, H., Zhu, J., Reuter, M., Vinke, L. N., Yendiki, A., Boas, D. A., Fischl, B., & Akkin, T. (2014). Cross-validation of serial optical coherence scanning and diffusion tensor imaging: a study on neural fiber maps in human medulla oblongata. *NeuroImage*, *100*, 395–404.

Warntjes, J. B. M., Leinhard, O. D., West, J., & Lundberg, P. (2008). Rapid magnetic resonance quantification on the brain: Optimization for clinical usage. *Magnetic Resonance in Medicine: Official Journal of the Society of Magnetic Resonance in Medicine / Society of Magnetic Resonance in Medicine*, *60*(2), 320–329.

Warntjes, J. B. M., Persson, A., Berge, J., & Zech, W. (2017). Myelin Detection Using Rapid Quantitative MR Imaging Correlated to Macroscopically Registered Luxol Fast Blue-Stained Brain Specimens. *AJNR. American Journal of Neuroradiology*, *38*(6), 1096–1102.

Warntjes, M., Engström, M., Tisell, A., & Lundberg, P. (2016). Modeling the Presence of Myelin and Edema in the Brain Based on Multi-Parametric Quantitative MRI. *Frontiers in Neurology*, *7*, 16.

West, K. L., Kelm, N. D., Carson, R. P., Gochberg, D. F., Ess, K. C., & Does, M. D. (2018). Myelin volume fraction imaging with MRI. *NeuroImage*, *182*, 511–521.

What is MS? — MS Society of Canada. (n.d.). Retrieved September 30, 2017, from https://mssociety.ca/about-ms/what-is-ms

Widmaier, E., aff, ershel, & Strang, K. (2013). *Vander's Human Physiology: 13th Edition*. McGraw-Hill Higher Education.

Zaimi, A., Wabartha, M., Herman, V., Antonsanti, P.-L., Perone, C. S., & Cohen-Adad, J. (2018). AxonDeepSeg: automatic axon and myelin segmentation from microscopy data using convolutional neural networks. *Scientific Reports*, *8*(1), 3816.

Zhang, H., Schneider, T., Wheeler-Kingshott, C. A., & Alexander, D. C. (2012). NODDI: practical in vivo neurite orientation dispersion and density imaging of the human brain. *NeuroImage*, *61*(4), 1000–1016.

Zhang, L., Wen, B., Chen, T., Tian, H., Xue, H., Ren, H., Li, L., Fan, Q., & Ren, Z. (2020). A comparison study of inhomogeneous magnetization transfer (ihMT) and magnetization transfer (MT) in multiple sclerosis based on whole brain acquisition at 3.0 T. *Magnetic Resonance Imaging*, *70*, 43–49.

APPENDIX A   SUPPLEMENTARY MATERIALS OF CHAPTER 4

A1 Table with subject's details

Table A1 - Main demographics and clinical characteristics of all the participants with multiple sclerosis.

ID	Group	Age (years)	Gender (F/M)	Disease duration (years)	WM lesion volume (mm^3)	Cortical lesion volume (mm^3)	Intracortical / leukocortical volume (mm^3)
1	1	43	F	0.4	226	164.8	164.8/0
2	1	22	F	0.4	427	65.5	0/65.5
3	1	42	F	0.6	318	0	0/0
4	1	33	F	0.7	732	71	71/0
5	2	46	F	2	423	20.8	0/20.8
6	2	26	M	1.5	100	134.1	134.1/0
7	2	31	F	1.8	806	173.7	160.8/12.9
8	2	28	F	1.3	711	289.4	219.6/69.8
9	2	36	F	1.8	630	924.4	186.6/737.8
10	2	47	F	1.7	1090	1308.9	1185.1/123.8
11	2	32	F	1.8	N/A	N/A	N/A

12	3	33	M	2.5	161	85.5	64.7/20.8
13	3	31	M	2.5	169	87.7	9.1/78.6
14	3	55	F	2.7	485	85.3	85.3/0
15	3	37	F	2.9	1415	53.7	0/53.7
16	3	42	F	2.3	188	142	0/142
17	3	38	F	2.4	298	31.7	31.7/0
18	3	45	F	2.9	142	239.6	196.6/43
19	4	43	F	4.1	638	10.6	0/10.6
20	4	38	F	3.2	3408	276.1	80.7/195.4
21	4	47	F	3.3	702	163.8	163.8/0
22	4	42	M	3.6	1274	N/A	N/A
23	4	44	M	4.9	479	282.5	189.9/92.6
24	4	32	F	5.2	2376	276.1	247.7/28.4
25	4	47	F	5.1	1039	0	0/0
26	4	48	F	3.4	4310	2189.5	1649.9/539.6
27	4	47	F	3.2	N/A	N/A	N/A

A2 Averaged metric values across healthy controls and multiple sclerosis patients

Table A2: Averaged metric values across healthy controls and multiple sclerosis patients.

VR stands for variation rate and is defined in the Methods.

	Group 1	Group 2	Group 3	Group 4
DD [years]	0–1	1–2	2–3	3+
EDSS	2 ± 0.8	0.9 ± 0.7	1.3 ± 1.1	2.1 ± 0.8
MSSS	5.7 ± 2.5	2.4 ± 1.7	3 ± 2.3	4.1 ± 1.6
Lesion volume [mm3]	WM : 425 ± 190 GM : 75 ± 58	WM : 626 ± 308 GM : 475 ± 473	WM : 445 ± 449 GM : 97 ± 67	WM : 1780 ± 1340 GM : 457 ± 716
CME [%]	HC = 46.5 ± 4.2 MS = 42.2 ± 4.1 VR = -9.0 ± 4.1	HC = 46.4 ± 3.7 MS = 45.6 ± 4.2 VR = -1.7 ± 1.4	HC = 46.1 ± 3.7 MS = 47.8 ± 1.2 VR = 3.8 ± 2.4	HC = 46.7 ± 3.6 MS = 44.5 ± 2.4 VR = -3.8 ± 3.8
Strength	HC = 741 ± 62 MS = 721 ± 117 VR = 6.8 ± 17.4	HC = 753 ± 73 MS = 773 ± 110 VR = 12.0 ± 19.8	HC = 738 ± 80 MS = 980 ± 496 VR = 44.9 ± 28.0	HC = 724 ± 80 MS = 721 ± 165 VR = 10.1 ± 24.6
Local efficiency	HC = 36.8 ± 3.2 MS = 36.9 ± 7.3 VR = -1.4 ± 9.0	HC = 37.0 ± 3.9 MS = 39.4 ± 5.8 VR = 10.1 ± 13.9	HC = 36.8 ± 4.0 MS = 46.8 ± 23.0 VR = 32.9 ± 14.4	HC = 36.3 ± 3.9 MS = 38.1 ± 8.3 VR = 8.4 ± 14.9

Clustering	HC = 35.2 ± 2.9 MS = 34.6 ± 6.5 VR = -3.6 ± 10.6	HC = 35.2± 3.5 MS = 37.3 ± 5.5 VR = 9.8 ± 15.9	HC = 35.1 ± 3.4 MS = 46.3 ± 21.2 VR = 32.5 ± 17.4	HC = 34.7 ± 3.4 MS = 35.4 ± 7.8 VR = 5.5 ± 16.1

DD=disease duration; EDSS=Expanded Disability Status Scale score; CME=combined myelin estimation; HC=healthy controls; MS=multiple sclerosis patients; VR= variation rate (defined in the Methods)

A3 Procedure for cortical atlas registration

For this study we developed a procedure to obtain volumetric atlases accurately registered on subjects' cortical areas and other regions of interest (ROIs) (Figure 2B). We hope this might be of interest to others working with cortical volumetric ROIs. Here is the basic algorithm we used (using FreeSurfer functions), followed by the GitHub link to the actual code:

https://github.com/neuropoly/surface_based_tools/tree/master/atlas_generation.

Figure S3 shows an example of a cortical atlas registration performed using a standard 12-DOF method and by using the surface-based method described in the present study.

Cortical areas

mri_annotation2label : create labels from PALS-B12 (surface atlas in *fsaverage* space, can work with any surface atlas in any space)

loop on Subjects

    loop on PALS-B12 labels (BAs)

mri_label2label : convert labels from *fsaverage* space to subject's native space.

mri_label2vol : convert labels to expanded volumetric ROIs in the diffusion space.

    end loop Labels

end loop Subjects

Aseg areas (e.g. deep GM)

loop on Subjects

mri_label2vol : sending FreeSurfer Aseg to the diffusion space.

    loop on wanted Aseg labels (areas)

fslmaths : selecting wanted aseg labels
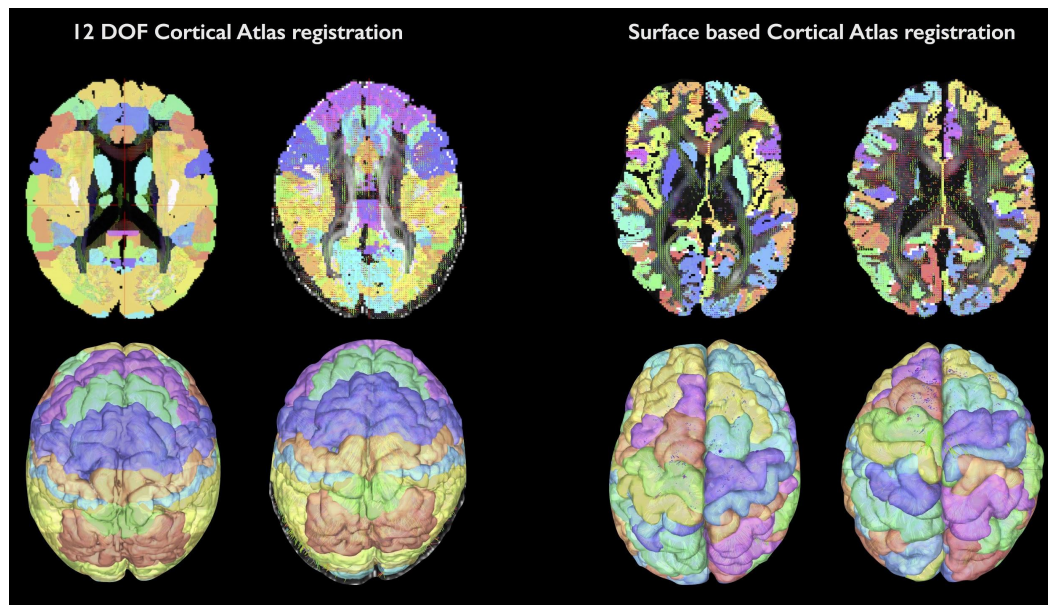
    end loop Labels

end loop Subjects

concatenate (optional)

loop on Subjects

mri_concat : concatenate all ROIs in one atlas file (per subject)

end loop Subjects

Figure A3 Example of a cortical atlas registrations performed using a standard 12-DOF (left) method and the surface-based method described herein (right). 12-DOF registration of cortical atlases (left) to the subject's native space revealed registration errors of several millimeters in many cortical areas, plus some areas overfill in adjacent gyri, the latter being our major concern. When using the surface-based method (right), no such error was detected and we noticed a visually good concordance between the BA registrations and their corresponding anatomical features (e.g. gyri or sulci delineation).

A4 Scan-rescan reproducibility of the 7T framework

Hemisphere: lh

Metric: T1

Ctrl050   1st SCAN: 2031.1911+/-260.2873   REPRO: 1934.498+/-473.629   Corr: 0.15921 variation: 4.7604 %

Ctrl052   1st SCAN: 2132.3487+/-349.0225   REPRO: 2134.9647+/-289.6866   Corr: 0.71722 variation: -0.12268 %

Ctrl053   1st SCAN: 1732.1028+/-335.5787   REPRO: 1683.112+/-376.065   Corr: 0.8995 variation: 2.8284 %

Ctrl054   1st SCAN: 1852.3211+/-376.607   REPRO: 1853.7937+/-360.2632   Corr: 0.88393 variation: -0.0795 %

Metric: T2*

Ctrl050   1st SCAN: 34.6742+/-5.7408   REPRO: 34.5047+/-5.5905   Corr: 0.67423   variation: 0.48861 %

Ctrl052   1st SCAN: 34.9842+/-6.2838   REPRO: 34.6868+/-5.7619   Corr: 0.64299   variation: 0.84991 %

Ctrl053   1st SCAN: 34.7246+/-6.6932   REPRO: 34.8308+/-6.6937   Corr: 0.7688   variation: -0.30566 %

Ctrl054   1st SCAN: 36.4677+/-6.8594   REPRO: 37.2872+/-7.2763   Corr: 0.67574   variation: -2.2471 %

Metric: CME

Ctrl050   1st SCAN: 48.3748+/-11.6424   REPRO: 49.5961+/-8.614   **Corr: 0.88983** variation: -2.5247 %

Ctrl052   1st SCAN: 47.448+/-9.2496   REPRO: 47.7079+/-11.1854   **Corr: 0.86964** variation: -0.54761 %

Ctrl053   1st SCAN: 52.5408+/-9.299   REPRO: 53.1292+/-8.6513   **Corr: 0.94929**   variation: -1.1198 %

Ctrl054   1st SCAN: 49.6959+/-9.0245   REPRO: 49.3365+/-8.5935   **Corr: 0.92462** variation: 0.72313 %

Hemisphere: rh

Metric: T1

Ctrl050   1st SCAN: 2069.8004+/-287.8106   REPRO: 1933.4422+/-510.4251   Corr: 0.10094 variation: 6.588 %

Ctrl052   1st SCAN: 2161.8799+/-292.8631   REPRO: 2149.2409+/-299.1076   Corr: 0.63545 variation: 0.58463 %

Ctrl053   1st SCAN: 1720.6884+/-380.1549   REPRO: 1654.476+/-410.7913   Corr: 0.87498 variation: 3.848 %

Ctrl054   1st SCAN: 1902.367+/-457.3429   REPRO: 1920.789+/-369.1687   Corr: 0.73438 variation: -0.96837 %

Metric: T2*

Ctrl050   1st SCAN: 35.6193+/-6.0186   REPRO: 35.3818+/-6.0688   Corr: 0.67344   variation: 0.66662 %

Ctrl052   1st SCAN: 35.4964+/-6.9356   REPRO: 35.5714+/-6.4377   Corr: 0.60299   variation: -0.21147 %

Ctrl053   1st SCAN: 34.6841+/-7.1886   REPRO: 34.8867+/-6.9543   Corr: 0.78564   variation: -0.58432 %

Ctrl054   1st SCAN: 36.1339+/-7.1971   REPRO: 36.2008+/-7.2355   Corr: 0.63617   variation: -0.18514 %

Metric: CME

Ctrl050   1st SCAN: 48.5944+/-11.4684   REPRO: 49.6895+/-8.0247   **Corr: 0.87199**
variation: -2.2535 %

Ctrl052   1st SCAN: 47.9068+/-9.4721   REPRO: 47.1847+/-11.8584   **Corr: 0.83628**
variation: 1.5074 %

Ctrl053   1st SCAN: 52.4134+/-9.4058   REPRO: 53.1829+/-8.7527   **Corr: 0.94005**
variation: -1.468 %

Ctrl054   1st SCAN: 49.5855+/-8.8139   REPRO: 49.0964+/-9.3425   **Corr: 0.88979**
variation: 0.98649 %

Reproducibility measurements were performed at the end of the whole processing pipeline in order to take into account any error that might have been induced by the distortion correction, the surface registration, the quantitative estimation, and the surface sampling. Correlations were computed across the 160k vertices of each surface hemisphere. P-values of the correlations were extremely low ($<10-16$), partly due to the number of datapoints involved. The spatial correlation coefficient was an indicator of the reproducibility. In addition to the correlation, we computed the variation rate ((mean_surf_2 - mean_surf_1) /mean_surf_1*100) between the first and the reproducibility datasets. The reproducibility analysis revealed that CME shows, every time, the best spatial correlation across scans, on average, c = 0.90, $p<10^{-16}$ for CME rescans.

A5 Detailed stable clusters List

Table A5 List of stable clusters

Cluster ID	Cluster Name	Brodmann areas / regions	Color code
1	Pre 4Frontal Cortex	8 RL ,9 RL	
2	Right Cingulum	23R,24R,31R,32R	
3	Right Visual Cortex	17R,18R,19R	
4	Motor Cortex	4RL, 6RL	
5	Left visual Cortex	17L,18L,19L	
6	Left Supra marginal, Inferior parietal	22L,39L,40L,37L	
7	Left Cingulum	23L,24L,31L,32L	
8	Right Supra marginal, Inferior Parietal	22R, 39R,40R,37R, 20R,36R,38R,21R,thalamus, hypothalamus	
9	Left Somatosensoriel	1L,2L,3L,5L,7L	
10	opercularis, triangularis, insula, transverse temporal,	25RL,26RL,43RL,45RL,46RL, 47RL, 42RL, 27RL,35RL,30L,29L,44L,41L,29R,30R, amygdala	
11	Right Somatosensoriel	1R, 2R,3R,5R,7R	
12	Lateral Orbitofrontal Gauche	11L, putamen, thalamus, caudate	
13	Orbitofrontal	10 LR, putamen, caudate	
14	Temporal, thalamus, hippocampus	20L,21L,28L,36L,38L, thalamus, hippocampus	
15	Brain stem, Cerebellum	Brain stem, cerebellum	

APPENDIX B   SUPPLEMENTARY MATERIALS OF CHAPTER 5

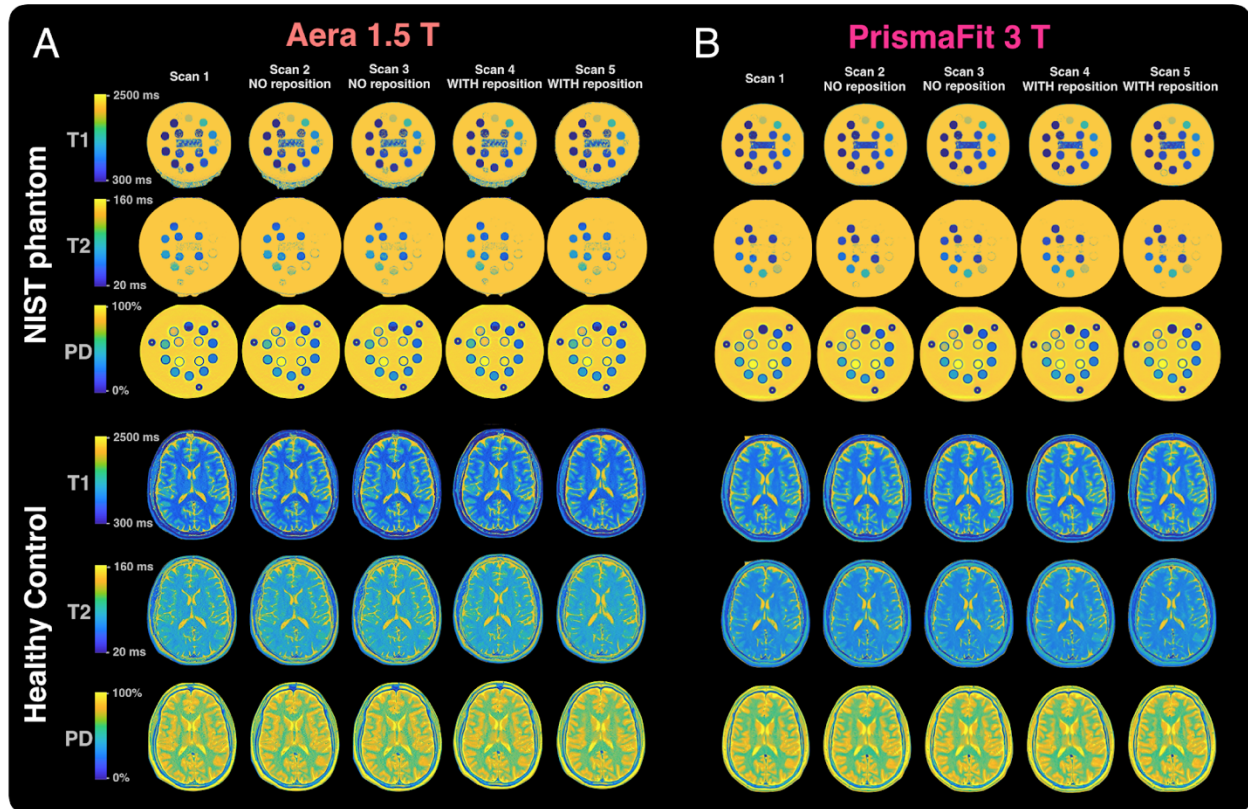**B1: Quality checks of the 5 scans re-scans of the NIST phantom and the healthy control**

Figure B1: T1, T2 and PD maps of the 5 scans re-scans of the NIST phantom and the healthy control, scanned at 1.5 T (A) and 3 T (B).

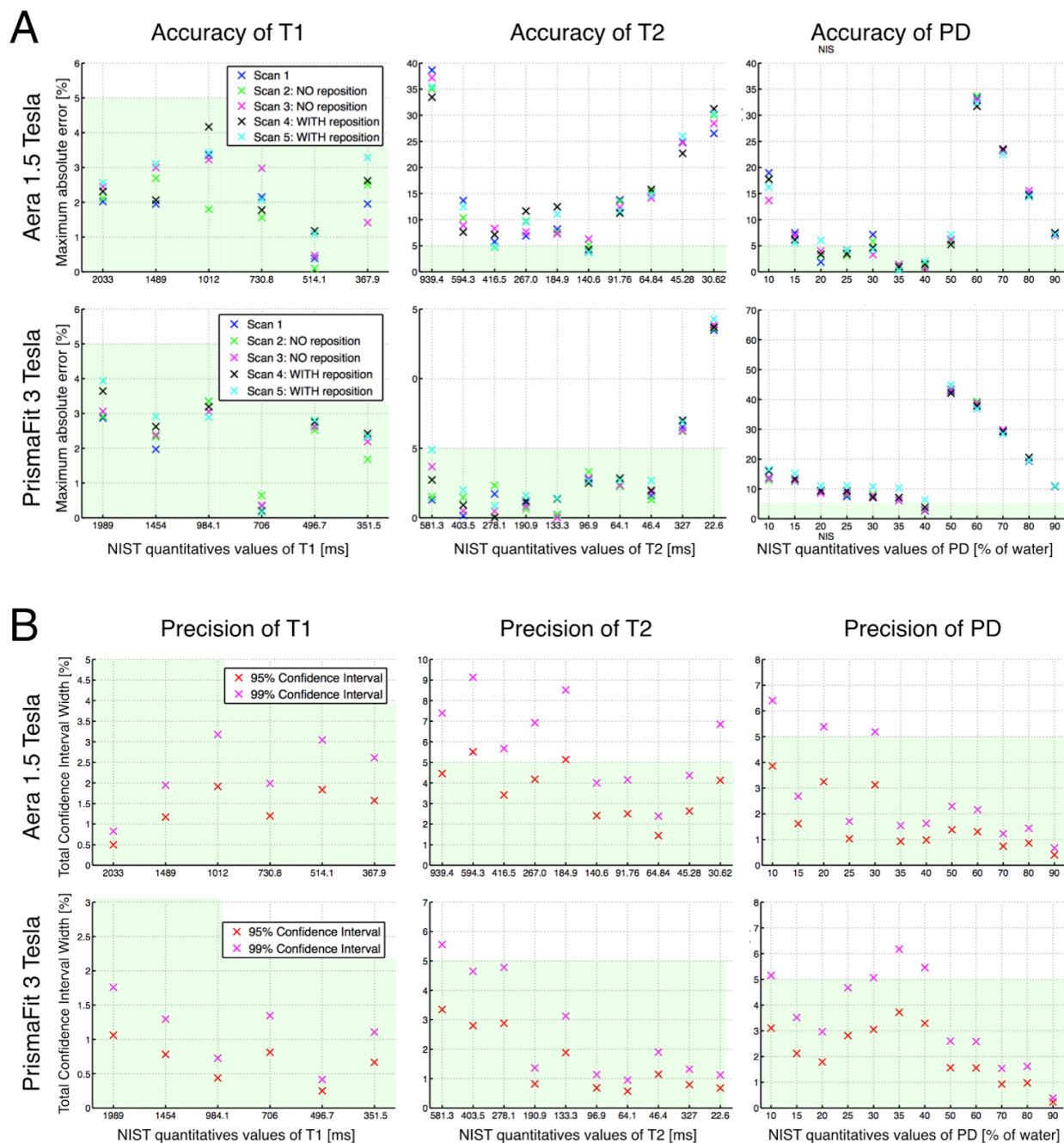**B2: Accuracy and precision of SyMRI quantification.**

Figure B2: A) Accuracy of SyMRI quantification. Each graph shows the accuracy of the five quantitative measurements related to the NIST quantitative phantom values, for two field strengths (1.5 and 3.0 T) and the three quantitative measurements (T1, T2 and PD). The accuracy was estimated with the formula Eq.1. The green areas show measurements with a <5% absolute error. B) Precision of SyMRI quantification. The precision of the quantitative measurements of

T1, T2 and PD in the NIST phantom, calculated over the 5 scan data points, for two field strengths (1.5 and 3.0 T). The total width of the 95% and 99% confidence intervals were calculated with the Eq.2. The green areas show measurements with a 5% confidence interval.